*Author:*
**Brooks, Sam**

*Title:*
**Supercooling brine in a helical coiled heat exchanger for ice slurry production**

*Experiments supercooling brine in heat exchangers to generate ice slurry hygienically and efficiently.*

# Supercooling brine in a helical coiled heat exchanger for ice slurry production

*Experiments supercooling brine in heat exchangers to generate ice slurry hygienically and efficiently.*

By

Sam Brooks

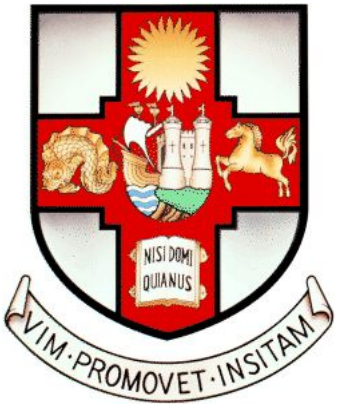


Department of Mechanical Engineering

University of Bristol

A dissertation submitted to the University of Bristol in accordance with the requirements of the degree of Doctor of Philosophy in the Faculty of Engineering.

June 2019

Word count: 35300

# Abstract

Ice slurries are formed from a combination of ice and water containing freezing point depressant. Despite the proven potential uses, they remain underutilised. Improving the efficiency of slurry production could increase adoption in many industries. Applications requiring greater hygiene have also developed in food production and medicine. Currently, scraped surface generators are the favoured generation method; a large body of work has focused on finding an effective replacement. This work presents a new method, utilising plastic pipes to slow ice growth and reduce adhesion.

A helical coiled heat exchanger (HCHX) arrangement with nylon pipe was used to cool an internal brine flow until ice nucleated. Initial results showed that ice slurry above 15% could be produced, at refrigeration temperatures from - 8 to - 13°C. Refrigeration temperatures that are warmer than scraped surface generators, indicating potential improved efficiency. Changing the flow direction, coil orientation, and fluctuating the flow rate in the pipe, failed to increase ice production. A control system, designed to set flow rate of the fluid, maintained ice fraction above 10%, despite rising refrigeration temperatures. A comparison between aluminium, silicone rubber, PTFE and nylon HCHXs was conducted. PTFE produced the highest ice fractions and production rates, possibly as a result of its high contact angle (hydrophobic) surface. Further experiments with silicone rubber pipe cooled in a tube-in-tube heat exchanger were conducted. The pipe was flattened in order to help remove ice formed in the tube. Small improvements in ice production were observed.

Successful improvements noted in previous chapters were combined with a smaller HCHX. Fluid phase was recirculated in the heat exchanger to generate ice fractions up to 23.5% after 6000 seconds of operation. Possible designs for implementing this method in a working generator with a refrigeration loop were proposed. A working prototype of one of these methods would be required to confirm the improved efficiency over scraped surface generators. Nevertheless, this method does offer more hygienic ice slurry generation, which could be exploited in the food and drinks industry or medical cooling. Many remaining avenues of research still exist which could optimise ice production in plastic heat exchangers further.

# Acknowledgements

I would like to thank Prof. Joe Quarini for offering me the chance to pursue a PhD. He and Dr Mike Tierney have been a constant source of patient support and guidance throughout the PhD.

I would like to acknowledge the Engineering and Physical Science Research Council (EPSRC) for funding the research.

It was a pleasure working with Edward Lucas and Xiao Yun, their engineering knowledge and friendship have proved invaluable.

Additionally, I would like to thank all my friends and flatmates (Rosy, Alex, Tania and Andy) over the last few years who have provided support and much needed distractions from work.

Finally, I should thank my whole family (Mum, Dad, David and Misha) for their endless support and enthusiasm for everything I have undertaken. A special thanks to Jen for being there throughout and being a very effective spell checker.

# Author's Declaration

I declare that the work in this dissertation was carried out in accordance with the regulations of the University of Bristol. The work is original except where indicated by special reference in the text and no part of the dissertation has been submitted for any other academic award. Any views expressed in the dissertation are those of the author.

SIGNED:

Date:

# Publications

## Journal Papers

Brooks, S., Yun, X., Lucas, E., Quarini, G. and Tierney, M., Supercooling in a nylon helical coiled heat exchanger, an alternative ice slurry generation method, *Thermal Science and Engineering Progress*

Yun, X., Brooks, S. and Quarini, G., Phase transformation and the heat and mass transfer in the ice, water and brine system., *Special Issue of Heat Transfer Engineering dedicated to the 15th UK Heat Transfer Conference*(2019)

Yun, X., Brooks, S., Cheng, Y., Hales, A., Lucas, E., McBryde, D. and Quarini, G., Ice Formation in the Subcooled Brine Environment., *International Journal of Heat and Mass Transfer*, (2016)

Lucas, E., Brooks, S., Cheng, Y., Hales, A., McBryde, D., Yun, X. and Quarini, G., Noninvasive Monitoring by Ultrasound of Liquid Foodstuff to Ice Slurry Transitions Within Steel Ducts and Pipes., *Journal of Food Process Engineering* (2016)

# Conference Contributions

Brooks, S., Tierney, M., and Quarini, G., Ice slurry production control system for supercooled brine in nylon helical coiled heat exchanger., *12th IIR Conference on Phase-Change Materials and Slurries for Refrigeration and Air Conditioning*, Quebec, Canada (2018)

Brooks, S., Yun, X., Lucas, E., and Quarini, G., Effect of flow direction on ice fraction produced by cooling brine flow in helical coiled heat exchanger. *15th Tierney Transfer Conference*, London, (2017)

Brooks, S., Yun, X., Lucas, E., and Quarini, G., Effect of coil orientation on ice fraction produced by cooling brine flow in a helical coiled heat exchanger., *15th UK Heat Transfer Conference*, London, (2017)

Yun, X., Brooks, S., and Quarini, G., Phase transformation and the heat and mass transfer in the ice, water and brine system., *15th UK Heat Transfer Conference*, London, (2017)

# Contents

# List of Figures

# List of Tables

# Nomenclature

## Main Variables

**Greek Alphabet**

| Variable | Description | Units |
|---|---|---|
| $\alpha$ | Ratio of cross sectional area | $[dimensionless]$ |
| $\beta$ | Thermal expansion coefficient | $[K^{-1}]$ |
| $\gamma$ | Interfacal energy | $[Jm^{-2}]$ |
| $E$ | Young's modulus | $[Pa]$ |
| $\theta$ | Wetting angle | $[^{\circ}]$ |
| $\lambda$ | Pipe thickness ratio | $[dimensionless]$ |
| $\mu$ | Dynamic viscosity | $[Nsm^{-2}]$ |
| $\nu$ | Poisons ratio | $[dimensionless]$ |
| $\Pi$ | Transmural pressure | $[Pa]$ |
| $\rho$ | Density | $[kgm^{-3}]$ |
| $\tau$ | Time constant | $[s]$ |
| $\phi_{caf}$ | Cafetiere ice mass fraction | $[\%]$ |
| $\phi_m$ | Ice mass fraction | $[\%]$ |
| $\omega$ | Angular frequency | $[rads^{-1}]$ |

**Latin Alphabet**

| Variable | Description | Units |
|---|---|---|
| $a$ | Equation constants | $[dimensionless]$ |
| $A_{s,L}$ | Perimeter length | $[m]$ |
| $A_c$ | Cross section area | $[m^2]$ |
| $A_s$ | Surface area | $[m^2]$ |
| $b$ | Equation constants | $[dimensionless]$ |
| $C$ | Concentration of brine | $[wt.\%]$ |
| $c_p$ | Specific heat capacity | $[Jkg^{-1}K^{-1}]$ |
| $COP_{Carnot}$ | Carnot coefficient of performance | $[dimensionless]$ |
| $D$ | Diameter | $[m]$ |
| $f$ | Frequency of oscillations | $[s^{-1}]$ |
| $f_{sampling}$ | Frequency of sampling | $[s^{-1}]$ |
| $G$ | Gibbs function | $[J]$ |
| $\Delta G_V$ | Difference in volume free energy | $[Jm^{-3}]$ |
| $g$ | Gravitational constant | $[ms^{-2}]$ |
| $\Delta H$ | Change in enthalpy | $[J]$ |
| $\bar{h}$ | Average local heat transfer coefficients | $[Wm^{-2}K^{-1}]$ |
| $h$ | Local heat transfer coefficients | $[Wm^{-2}K^{-1}]$ |
| $h_{s,f}$ | Latent heat of fusion | $[Jkg^{-1}]$ |
| $k$ | Thermal conductivity | $[Wm^{-1}K^{-1}]$ |

| | | |
|---|---|---|
| $K_p$ | Flexural rigidity of the tube | $[Pa]$ |
| $L$ | Length | $[m]$ |
| $m$ | Mass | $[kg]$ |
| $\dot{m}$ | Mass flow rate | $[kgs^{-1}]$ |
| $\dot{m}_{\phi_m}$ | Ice production rate | $[kgs^{-1}]$ |
| $P$ | Pressure | $[Pa]$ |
| $Q_{lat,sl}$ | Specific latent heat capacity of ice in a slurry | $[Jkg^{-1}]$ |
| $r$ | Radius of nucleus | $[m]$ |
| $R$ | Thermal resistance | $[KW^{-1}]$ |
| $r^*$ | Critical nucleus radius | $[m]$ |
| $S$ | Entropy | $[JK^{-1}]$ |
| $S(\theta)$ | Wetting factor | $[dimensionless]$ |
| $T$ | Temperature | $[^\circ C]$ (or K) |
| $t$ | Time | $[s]$ |
| $U$ | Internal energy (Chapter 2 only) | $[J]$ |
| $\bar{U}$ | Average heat transfer coefficient | $[Wm^{-2}K^{-1}]$ |
| $V$ | Volume | $[m^3]$ |
| $W_a$ | Work of adhesion | $[Jm^{-2}]$ |
| $x_{fd,h}$ | Hydrodynamic entry length | $[m]$ |
| $x_{fd,t}$ | Thermal entry length | $[m]$ |

# Dimensionless Numbers

| **Variables** | **Description** | **Equation** |
|---|---|---|
| De | Internal flow Dean number | $De_D = Re_D \left(\frac{D}{D_{curve}}\right)^{0.5}$ |
| Nu | Nusselt number | $Nu_D = \frac{hD}{k}$ |
| Pr | Prandtl number | $Pr = \frac{c_p \mu}{k}$ |
| Ra | Rayleigh number | $Ra_D = \frac{g\beta(T_s - T_{\inf})D^3}{(\mu/\rho)^2} Pr_D$ |
| Re | Reynolds number | $Re_D = \frac{4\dot{m}}{\pi D \mu}$ |
| Wo | Womersley number | $Wo = D\left(\frac{\omega\rho}{\mu}\right)^{\frac{1}{2}}$ |

# Subscripts

| **Subscript** | **Description** |
|---|---|
| 0 | Original |
| 20 | 20% ice fraction produced |
| atm | Atmospheric pressure |
| Bath | Refrigeration bath |
| brine | Brine |
| coil | Helical coil |

| | |
|---|---|
| e | External pipe pressure |
| eff | Effective |
| end | End combined mixture (calorimetry) |
| eut | Eutectic |
| external | External applied pressure |
| f | Freezing/melting |
| H | Condenser refrigerant temperature |
| het | Heterogeneous nucleation |
| het, r | Heterogeneous nucleation of radius r |
| hom | Homogeneous nucleation |
| hom, r | Homogeneous nucleation of radius r |
| hot | hot fluid properties (calorimetry) |
| HX-Inlet | Outer pipe inlet (tube-in-tube HX) |
| HX-Outlet | Outer pipe outlet (tube-in-tube HX) |
| i | Inner |
| ice | Ice phase of slurry |
| in | Inlet HCHX |
| Inlet | Inner pipe inlet (tube-in-tube HX) |
| int | Internal pipe pressure |
| internal | Measured internal pressure ($\Delta P + P_{external}$) |
| L | Evaporator refrigerant temperature |
| Liq | Liquid phase |
| LS | Liquid-solid phase interface |
| n | Outlet HCHX when nucleation occurs |
| nuc | Nucleation of ice |
| o | Outer |
| off | Valve closed |
| on | Valve open |
| out | Outlet HCHX |
| Outlet | Inner pipe outlet (Tube-in-tube HX) |
| pipe | Pipe properties |
| pre | Predicted |
| pump | Pressure head from pump |
| S | Solid phase |
| s | Surface |
| slurry | Ice slurry properties |
| start | At beginning of experiments |
| V | Volume |
| w | Water |

# Abbreviations

| **Subscript** | **Description** |
|---|---|
| BCS | Basic Control System |
| BMU | Bottom Moving Up |
| CFD | Computational Fluid Dynamics |
| COP | Coefficent of Performance |
| CS | Control System |
| EM | Electromagnetic |
| HCHX | Helical Coiled Heat Exchanger |
| HX | Heat Exchanger |
| ICS | Improved Control System |
| FPD | Freezing Point Depressant |
| PTFE | Polytetrafluoroethylene (PTFE) |
| SS | Scraped Surface Generator |
| TMD | Top Moving Down |

# Chapter 1

# Introduction

A significant body of research over the last few years has focused on ice slurries and their uses. Formed from a combination of ice and water, usually mixed with a freezing point depressant, such as NaCl, ethalyne glycol, etc. Ice slurries have been used for many years, some records reveal it being used up to 2000 years ago; salt was combined with ice from glaciers and used as a cooling fluid (Hansen et al. (2001)). Ice slurries benefit from high cooling capacities due to the high latent heat of ice, but the slurry consistency enables it to be transported cheaply as a liquid (Egolf (2004)). Some of the more interesting applications include:

- **Secondary refrigerant**

  This is an area with the most potential, many systems using ice slurry as a secondary refrigerant are already operating in structures all over the world, including the CAPCOM and Herbis buildings in Osaka Japan, Kyoto Station, 'Techno-Mart 21' in Seoul Korea, Middlesex University, and Western Deep Level Gold Mine in South Africa (Bellas and Tassou (2005)). The ability to pump ice slurries easily along pipes and retain their cooling potential make them ideal for applications in large buildings. The number of refrigeration units is also reduced and can be replaced by a larger more efficient central unit which can be operated cheaply at night (J. Wang and Kusumoto (2001)).

- **Ice pigging**

  An extensive body of research at the University of Bristol has proven the

viability of using ice slurries to remove a variety of materials from fouled pipe, also known as ice pigging (Quarini (2002)).

- **Food preservation and processing**

  A wide range of research (K. Fikiin and A. Fikiin (2000) Pineiro et al. (2004) Gladis (1997)) and companies (such as Sunwell) have proven the benefits of using ice slurries to provide rapid uniform cooling of food.

- **Organ cooling during surgery**

  Recently, the high cooling capacity of ice slurries has seen them used in surgical application. Small amounts of small crystal slurry can be pumped to surround organs and tissue during surgery to limit damage and increase surgical working time (Kauffeld et al. (2010)).

The last two uses mentioned are of interest, ice slurry for these applications must meet more rigorous hygiene standards, especially in medical applications.

## 1.1 General Research Overview

The work in this thesis aims to explore an alternative ice generation method that could replace conventional scraped surface generators. It could not only offer greater efficiency but also better hygiene control, opening more potential uses for ice slurry. Ice is generated within a plastic heat exchanger (HX), utilising the low thermal conductivity and ice adhesion strengths of plastics. An initial patent filed by Kauffeld et al. (1995), showed it was possible to generate ice slurry from alcohol solution (wine) inside cooled plastic pipes. More recently, Winston et al. (2011) have filed a similar patent for a generator to dispense slushy drinks. Both authors utilised plastic pipes for the cooling of alcoholic drink because it offers greater hygiene control. No known published work exists about this method, offering a large area of potential

research.

## 1.2 Thesis Structure

Chapter 2 *(Literature Review)* begins with a review of how ice crystals nucleate and grow, including contributing factors. Properties of ice slurries are discussed, with focus on how ice fraction can be found in a slurry and pressure drops from moving a two-phase fluid. Current ice generation methods which have been investigated and are in use, are reviewed. Finally, ice adhesion to different surfaces and material types is explored.

Chapter 3 *(General Experimental Set-up)* discusses the benefit of a helical coiled heat exchanger over straight pipes. Details of the set-up used in most chapters is given, along with pictures and diagrams. Sources of error are discussed and summarised in a table at the end of the chapter.

Chapter 4 *(Initial HCHX Experiments)* outlines the initial experiments conducted with nylon pipe in a HCHX arrangement. Sodium chloride concentration (NaCl) is changed in each experimental set and the effect observed. Operation regions and ice production rates are then compared, crystal size and refrigeration temperatures are compared to a scraped surface generator.

Chapter 5 *(Optimisation Of Ice Fraction)* builds on the work of the previous chapter and aims to improve the ice fractions produced. Reversing the flow, changing the coil orientation and implementing a flow rate control system are all tested. The results of each are compared to the results in Chapter 4 to see if any modifications help improve ice production or widen the operation region.

Chapter 6 *(Pipe Material Investigation)* reports results of experiments conducted with different materials used in a HCHX arrangement. Nylon, PTFE, silicone rubber and aluminium pipes of similar size were all tested. Operation regions and production rates were compared to see if the material properties had an effect. Further experiments to quantify the time before ice nucleation or blocking occurred were also conducted. The results were used to try and predict regions of flow rate and temperature where ice would be produced.

Chapter 7 *(Utilisation Of Oscillations)* investigates if oscillations can be used to improve ice production with two experiment sets. Firstly, a pulsating flow is created by turning an inlet value on and off. Ice production rates are compared to a uniform flow rate flow such as that used previously. Secondly, a fluctuating pressure is applied to a flexible silicone rubber pipe using a tube-in-tube heat exchanger to break up ice forming in the pipe. Results are compared to control experiments with no fluctuations in a tube-in-tube heat exchanger.

Chapter 8 *(Future Of The Method)* brings together some of the most successful improvements from previous experiments into one extended test. Designs for potential ice slurry generators using plastic HCHX are presented, possible problems and benefits of each are discussed.

Chapter 9 *(Conclusion)* - presents areas of further work which could be investigated and concludes the work presented outlined in the thesis including any final comments or recommendations.

# Chapter 2

# Literature Review

## 2.1 Introduction

The first section of the chapter explores the freezing process, outlining how ice nucleates and grows to form stable crystals. This is followed by a review of ice slurry thermo-physical properties, including density, pressure drop and solid content determination; information which is vital for interpreting experimental results when working with ice slurries. Later, current engineering methods are reviewed, starting with current ice slurry generation methods. Finally, ice adhesion is reviewed, including how it can be limited to reduce energy needed for removal.

## 2.2 Freezing Phenomenon

Water or aqueous solutions go through three key stages to become ice: supersaturation, nucleation and crystal growth (Dorsey (1948), Brout (1963), Fletcher and Hasted (1971), and Franks (1982)). This section explores each of these stages in more details as well as factors effecting crystal size, growth and nucleation during the phase change process.

*Supersaturation* - A saturated system is when the solid and liquid states are at equilibrium, such as water at its freezing/melting point of 0 °C (at atmospheric pressure). Lowering the temperature further creates a supersaturated system, increasing the

energy available to initiate crystallisation. The higher the level of supersaturation (supercooling) the higher the driving potential force is for crystallisation. In aqueous solutions the solid particulates lower the solution equilibrium temperature.

Primary nucleation in a supersaturated solution occurs in two key ways, heterogeneous nucleation and homogeneous nucleation. Secondary nucleation occurs from the presence of crystals in the solution (also known as seeding) see § 2.2.3.

### 2.2.1 Homogeneous Nucleation

Homogeneous nucleation occurs within the main bulk of the fluid. For a nucleus to form there needs to be a reduction in temperature below the melting point, the lower this temperature the larger the change in Gibbs function and the greater the chance of nucleation occurring. Gibbs function, G, is defined in Equation 2.1. Equation 2.2 is the change in Gibbs function as particles move from liquid to solid phases.

$$G = U - TS + PV \tag{2.1}$$

$$\Delta G = - V_s(\Delta G_V) + A_{s,SL}\gamma_{SL} \tag{2.2}$$

Volume of the solid formed ($V_S$), surface area separating solid and liquid phases($A_{s,SL}$) and the interfacial energy ($\gamma$) are all used. Subscripts S corresponds to the solid phase, while SL represents properties at the solid-liquid interface. As the temperature, T, falls below the melting/freezing point, $T_f$, G for the solid phase begins to fall below that for liquid phase, $G_S < G_L$. This means the total volume free energy per unit volume ($\Delta G_V$ [J m$^{-3}$]) increases (see Equation 2.3).

$$\Delta G_V = \frac{\Delta H \Delta T}{T_f} \tag{2.3}$$

Where

$$\Delta T = T_f - T$$

The substance will subsequently try and change to a more stable solid phase with less Gibbs function. However, for an ice nucleus to form homogeneously significant cooling below $T_f$ is needed to create a stable nucleus.

A stable nucleus is achieved when the Gibbs function ($\Delta G$) is large enough to drive a phase change of sufficient volume that it can overcome the interfacial energy acting on the surface of the volume, see Figure 2.1. The simplest and most common geometry considered when discussing nucleation is a sphere; the optimum shape for nucleation where the maximum volume and lowest surface area can be achieved. Using this, a critical radius $r^*$ can be found for the minimum radius ice nucleus that can be maintained in an aqueous solution.

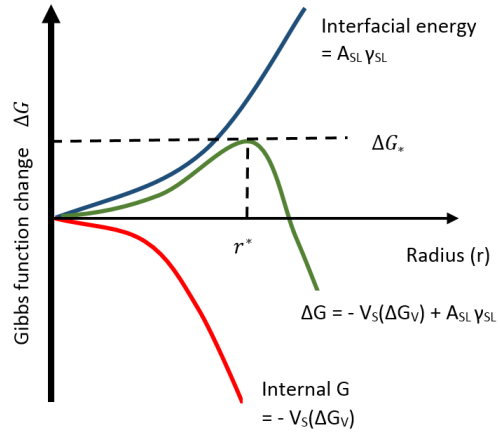


Figure 2.1: Graph illustrating the change in total, interfacial and volume free energies as the radius on the nucleus increases. From Franks (1982).

$$\Delta G = -V_s(\Delta G_V) + A_{s,SL}\gamma_{SL} \tag{2.4}$$

$$\Delta G_{hom} = -\frac{4}{3}\pi r^3(\Delta G_V) + 4\pi r^2\gamma_{SL} \tag{2.5}$$

$$\frac{d\Delta G_{hom}}{dr} = -4\pi r^2(\Delta G_V) + 8\pi r\gamma_{SL} = 0 \tag{2.6}$$

$$r^* = \frac{2\gamma_{SL}}{\Delta G_V} \tag{2.7}$$

It can be observed from Equation 2.7 that the critical radius size will decrease as supercooling ($\Delta T$) increases. Low temperatures are needed to drive homogeneous ice nucleation, often as low as -40 °C for pure water (Fletcher and Hasted (1971)). While heterogeneous nucleation can occur at temperatures between between -4 to -15°C.

The addition of freezing point depressants (FPD), such as NaCl, lowers the freezing temperature (discussed further in §2.3.1). The work of Wilson and Haymet (2009) shows that the addition of FPD lowers the homogeneous ($T_{hom}$) and heterogeneous ($T_{het}$) nucleation temperatures further:

$$\Delta T_{hom} \approx \lambda \Delta T_f \tag{2.8}$$

$$\Delta T_{het} \approx \lambda \Delta T_f \tag{2.9}$$

Where $\lambda \approx 2$, independent of the solute added.

Authors such as Koop et al. (2000) correlate water activity to homogeneous nucleation temperature. Water activity is affected by the addition of FPD, the pressure and the temperature (Zobrist et al. (2008)). Most of the work in this area relates to ice formation from water vapour (cloud formation) and not from liquids and

therefore is not presented here.

### 2.2.2 Heterogeneous Nucleation

Homogeneous nucleation is rarely how ice nucleates from liquid water, because of the low temperatures required. The far more common nucleation method is heterogeneous nucleation, where crystallisation occurs on foreign surfaces inside (or on the edge) of the solute. Using a foreign solid surface reduces the surface area of the solid-liquid interface reducing the interfacial energy. A stable nucleus can form at a lower critical energy with less supercooling.

A nucleus forming on a surface has a lower surface area in contact with the remaining fluid as part of it is already in contact with a solid surface. If the wetting angle, $\theta$, is known and the ice forms in a sphere then a wetting factor, $S(\theta)$, can be derived. A flatter nucleus forming closer to the surface will have a low $\theta$ and a low exposed surface area, resulting in a lower $\Delta G$ for nucleation to occur. The wetting factor takes account of this geometry change (see Equation 2.10). Figure 2.2 presents the wetting factor, $S(\theta)$, plotted against wetting angle. As the wetting angle tends to 180° the ice is forming in the bulk fluid (homogeneous nucleation). However, the wetting angle would normally be below 90°, meaning heterogeneous nucleation of a stable nucleus can occur at less than half the Gibbs function needed for homogeneous nucleation (Franks (1982)). Information on this and the derivation of Equation 2.10 can be found in Appendix A.

$$\begin{aligned} \Delta G_{het,r} &= \Delta G_{hom,r} S(\theta) \\ S(\theta) &= \frac{1}{4}(2 + cos(\theta))(1 - cos(\theta))^2) \end{aligned} \tag{2.10}$$

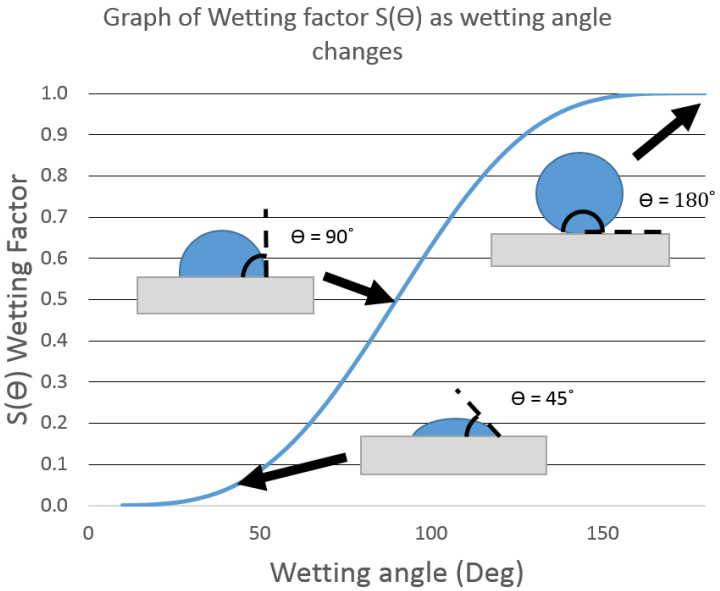


Figure 2.2: Graph of wetting factor,$S(\theta)$, against wetting angle, $\theta$, from 0 to 180° (where the nucleus would be fully detached)

Contact angle can be the difficult thing to find. Equation 2.11 is created by resolving $\gamma$, the interfacial energies between the different phases and a surface, displayed in Figure 2.3. I, II, III are the different phases of water and S is the surface.

$$cos(\theta) = \frac{\gamma_{S/III} - \gamma_{S/II}}{\gamma_{II/III}} \tag{2.11}$$

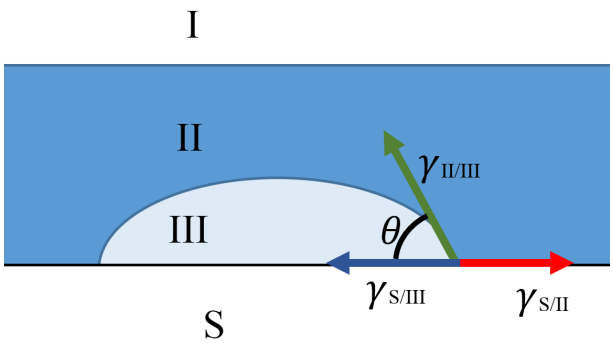


Figure 2.3: Interfacial energies, $\gamma$, for three different phases with an embryo forming on a flat surface. $\theta$ is the wetting angle; I, II, III are the different phases of water; s is the surface.

Phase I is gas (water vapour) and phase III is ice for freezing. Phase II can be either gas or liquid water depending on the nucleation taking place. A significant body of work investigates supercooled water droplets which nucleate on contact with a surface; for this nucleation, phase II can be considered a vapour. However, if the surface is submerged in fluid (e.g. the inside of a pipe) then phase II is a liquid (Schmelzer and Hellmuth (2013)). In lots of literature, the contact angle is assumed to not change when phase II is vapour or liquid ( Murase et al. (1994) and Chen et al. (2008)), in reality, it would be different. This assumption is likely made for two reasons; firstly it is very difficult to measure contact angle for an ice nucleus forming in water and easier to measure it for water freezing on a surface. Secondly, lots of experiments investigating heterogeneous ice nucleation use water drops rather than a submerged surface as it is easier to observe nucleation.

Leloux (1999) and Zobrist et al. (2008) investigated the effects of adding macromolecules to water to promote heterogeneous nucleation. Small macromolecules which could not dissolve in the solution are found to reduce the supercooling needed for nucleation to occur by promoting heterogeneous nucleation. Tap water is observed to nucleate faster than filtered water as there are particulates in it (Wettlaufer et al. (1997), Gilpin (1977), and Dorsey (1948)). Many other authors have aimed to prevent ice nucleation on surfaces using either special coatings or material preparations, this is discussed further in § 2.6.3.

Heterogeneous nucleation is the nucleation found predominately in ice slurry generators as it occurs at higher temperatures than homogeneous nucleation.

### 2.2.3 Initiating Nucleation in Supercooled Fluids

Different methods for initiating nucleation of supercooled water exist, some common methods and their reliability are discussed below.

**Pouring onto a cooled surface** - Pouring supercooled water out onto a cooled surface is found to not be effective unless the surface had ice crystals present from the air or previous tests (Dorsey (1948)). However, pouring supercooled water into a tank of water at 0 °C is proven effective (Bedecarrats et al. (2000)).

**Splashing or shaking** - Splashing or shaking the supercooled water can cause nucleation but with less supercooling more movement is needed to initiate this. A high level of supercooling is therefore required to achieve reliable nucleation (Dorsey (1948)).

**Electrical current** - Many authors have investigated using electrical current to initiate nucleation. Generally, it has been found to be beneficial for promoting heterogenous nucleation, though high electrical field strengths above $10^5$V m$^{-1}$ are required. (Zhang et al. (2016)).

**Spraying in a jet** - Spraying supercooled water on to a flat surface is found to occasionally work but water often froze in the nozzle of the jet (Dorsey (1948)).

**Hitting** - Sudden impacts like hitting or banging a sample's container only causes nucleation when bubbles and cavitation occurred as a result of the impacts. Gilpin (1977) found this method effective during tests with supercooled water.

**Ultrasonic waves** - Bedecarrats et al. (2010) used ultrasonic waves to initiate ice nucleation with relative success though it was difficult to implement consistently. However, Tanino (2000) and Mito et al. (2002) utilised it to successfully generate ice slurry from supercooled water. Zhang et al. (2001) and Zhang et al. (2008) increased the effectiveness of ultrasound by combining it with cavitation or the addition of air bubbles in a fluid flow.

**Seeding** - The most stable and reliable way to initiate nucleation is found to be with an existing ice crystal, seeding (Dorsey (1948) and Tanino (2000)).

### 2.2.4 Growth

For the nucleus to grow and become stable, more molecules of water need to diffuse through the solution and bond onto the surface of the nucleus. This bond causes heat (and solutes if any present) to be transferred to the bulk fluid surrounding the crystal. The rate at which this heat (and solutes) is removed from around the new nucleus affects the growth rate.

There are two main types of growth observed during ice crystal growth. Kapembwa and Rodriguez-Pascual (2014) investigated the growth rate of ice and its formation inside pure water and aqueous solutions. Ice grows initially in fast dendritic formations followed by slower layer growth. Dendritic growth is almost 10 times faster than layered growth though only occurs when water is supercooled by more than 2.8 °C. More details on each type of growth are provided below for both pure water and with freezing point depressant solutions.

*Dendritic ice growth* rate is dependent on the degree of supercooling and convection currents moving any solute molecules away from the ice-liquid interface. Often, the

speed of dendritic growth traps warmer and higher concentration fluid (produced during the phase change) around the ice. This leads to the formation of branches or 'tree' shaped crystals, as the fast-growing dendritic ice attempts to grow into areas of lower concentration and temperature. These snowflake like shapes have a large surface area making it vulnerable to interfacial energy which can slow down growth (Gilpin (1977) and Fletcher and Hasted (1971)). Growth stops or slows when the fluid is no longer supersaturated ($T_f \leq T$), slower layer growth takes over from here.

Recent work by Kong and H. Liu (2018) demonstrated that initially, a thin layer growth forms quickly on a cooled surface after heterogeneous nucleation. This is followed by dendritic crystals which grow away from the surface. This thin layer was seen on polymer and metal surfaces when pure water is supercooled below -3°C. Increased conductivity of the cooled nucleation surface and lower supercooling temperatures increase the growth rate of the thin layer and dendrite crystals (Kong and H. Liu (2015)).

Growth rate of dendritic ice in water was found to be proportional to ($\Delta T$) the degree of supercooling ($\Delta T = T_f - T$). The more a fluid is supercooled the faster the growth rate (Pruppacher (1967) and Lindenmeyer and Chalmers (1966)). Teraoka et al. (2002) investigated effects of concentration on ice growth from supercooled water-ethylene glycol. Width and length of the dendritic ice crystal grown, and speed of growth are not significantly affected by changing concentrations from 0-5 wt.%. However, as concentration increased thinner dendritic ice crystals formed, with more brine channels and pools found within the structure. Adding more solute slowed down the initial speed of growth but produced a slower and more consistent growth rate.

*Layer growth* forms following an initial fast dendritic growth (or sometimes even without dendritic growth). Ice begins to grow in layers around the cooled surfaces, acting as an insulating layer and slowing down growth rate. Wettlaufer et al. (1997) conducted experiments investigating the formation of ice on a cooled plate. Concentrations of 1-14wt.% NaCl and cooling fluid temperatures of -10 to -20 °C, were tested. As brine solidified a 'mushy layer' made up of ice and higher concentration brine begins to form on the leading edge of the freezing front. A mushy layer is a combination of ice particles with high concentration brine, which blocks a complete solid layer forming. The mushy layer grows and eventually reaches a critical height where ice begins to solidify, and the brine is expelled through vertical channels called 'brine channels'. These channels and the process observed is known as compositional convection and leads to a reduction in ice growth rate, due to warmer water molecules and a surplus of high concentration brine at the freezing front. The size of the ice layer and speed of its growth were heavily influenced by rate of heat removal, concentration and convection in the fluid. Kapembwa and Rodriguez-Pascual (2014) noted a similar effect and that approximately 3-16% of the heat generated by crystallisation was dissipated into the liquid but the majority was absorbed by the solid ice layer during ice formation.

### 2.2.5 Factors Affecting Ice Crystal Size in Slurries

The method of generation used influences the size and shape of ice crystals initially produced. However, during slurry storage and transport, other factors can change the crystal size (Pronk et al. (2005)).

*Attrition* - Larger ice crystals collide with each other, or solid surfaces, creating large stresses on the crystal, causing it to fracture into smaller parts.

*Agglomeration* - Smaller ice crystals adhere together to form larger crystals, this can be reduced by agitating (such as stirring) the fluid, which is done in ice slurry storage tanks.

*Ostwald ripening* - When ice slurries are stored for extended periods of time smaller crystals tend to dissolve and be redeposited on larger crystals, this process is called Otswald ripening. The ice crystals become more stable as larger crystals form, reducing the surface area and (Stamatiou et al. (2005)) thus reducing Gibbs function.

*Melting* - If the insulation is insufficient then melting of ice crystals occurs, especially close to the walls of the container.
Crystal size influences slurry properties, as discussed later in § 2.3.

## 2.3 Properties of Ice Slurries

There has been significant work conducted investigating the properties of ice slurries in pipes; however, the two-phase nature of ice slurries makes it challenging to consistently predict properties and behaviour.

### 2.3.1 Effect of Freezing Point Depressant

Adding a freezing point depressant (FPD) to water changes the thermo-physical properties of the solution. Many different FPD are used to make ice slurries, all with their own advantages and disadvantages. The effects of sodium chloride (NaCl) FPD have been predominately considered here, because it was used in all work outlined in this thesis.

The addition of FPD, as the name implies, lowers the freezing temperature below

the that of pure water, as the presence of solute ions interfere with pure ice crystal formation. Figure 2.4 demonstrates the effect of adding different FPD on the freezing temperature of aqueous solutions.

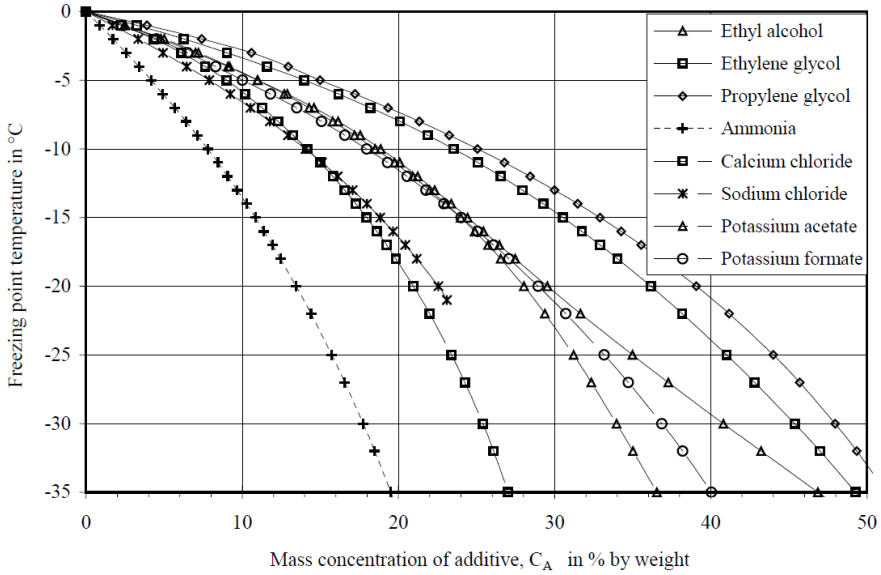


Figure 2.4: Graph of change in freezing temperature with addition of different freezing point depressants, taken from Kauffeld et al. (2005), created using equations by Melinder (1997).

If the temperature of the solution drops below the freezing temperature, a separation of the mixture occurs. Ice crystals form from the pure water component, leaving the FPD component behind, increasing the concentration of the remaining solution. This depresses the freezing temperature further as the equilibrium point for the remaining solution adjusts. The phase diagram for NaCl on Figure 2.5 includes a liquidus line, indicating the transition point from pure liquid to solid and liquid component. The solution does not fully solidify until the eutectic temperature, $T_{eut}$, is reached. The eutectic point marks where the solution is fully saturated with solute. Below the eutectic temperature hydrohalite ($NaCl.2H_2O$) forms (Cocks and Brower (1974)).

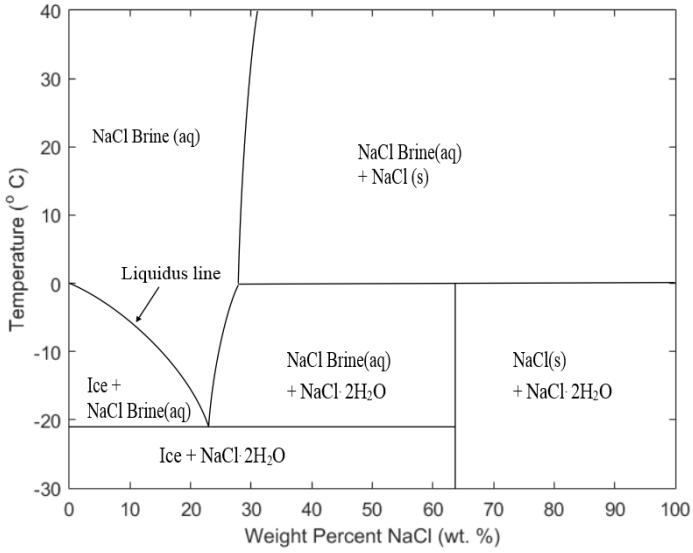


Figure 2.5: Binary phase change diagram for water ($H_2O$ and sodium chloride (NaCl) solutions. Replicated using information from Cocks and Brower (1974) and Oro et al. (2012).

### 2.3.2 NaCl Concentration and Ice Fraction

As mentioned previously an increase in mass of ice in a slurry increases the concentration (C) of NaCl, lowering the freezing point. Using data from Clark et al. (1985) for the liquidus line (see Figure 2.5) a polynomial relationship for $C(T)$ (concentration at a set temperature) can be found, see Equation 2.12.

$$C(T) = a_1\hat{T} + a_2\hat{T}^2 + a_3\hat{T}^3 \tag{2.12}$$

$$\hat{T} = T - T_0$$

$$T_{eut} < T < T_0$$

This equation is valid for $T_0$ = 0°C, $T_{eut}$ = -21.1°C, $a_1$ = -0.0177, $a_2$ = -4.14×$10^{-4}$

and $a_3$ = -4.52×$10^{-6}$. If temperature is known, this and Equation 2.13 below can be used to find an approximation of ice fraction.

$$\phi_m = 1 - \frac{C_{bulk}}{C(T)} \tag{2.13}$$

Where $C_{bulk}$ and $C(T)$ are starting and current solution concentration found using Equation 2.12 and the fluid is not in a supercooled state. Alternatively, for a known concentration the process can be reversed and Equation 2.14 used as an approximation for temperature.

$$T(C) = T_0 + b_3C^3 + b_2C^2 + b_1C \tag{2.14}$$
$$0 < C < C_{eut}$$

Where $b_1$ = -59.3K, $b_2$ = -8.45K and $b_3$ = -555K.

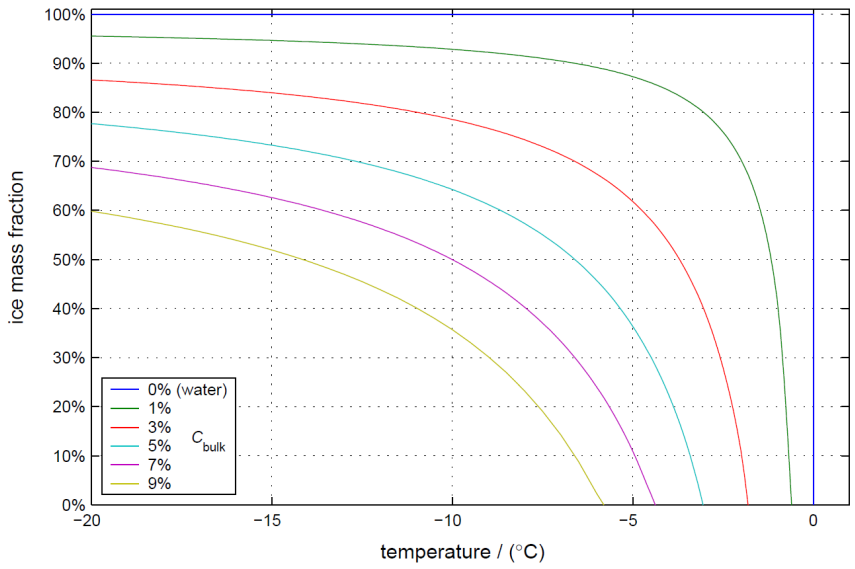


Figure 2.6: Graph of predicted ice mass fraction as a function of temperature for different starting NaCl solution concentrations, taken from Evans (2007).

Curves for different concentrations have been plotted and are illustrated on Figure

2.6. Comparable curves are presented by Melinder and Granryd (2005) for other FPD solutions. Using this method to relate ice fraction and slurry temperature is not very accurate, except at high sodium chloride starting concentrations ($\geq$ 10 wt.%) or lower temperatures (where the $d\phi_m/dT$ is smaller).

### 2.3.3 Density of Ice Slurry

The addition of NaCl to water (a single-phase solution) is known to increase density of the solution as well as acting as a FPD. When this solution begins to freeze a more complex two-phase solution is created. Density for an ice slurry can be estimated by considering the densities of the parts, using Equation 2.15, assuming the ice mass fraction ($\phi_m$) is known.

$$\rho_{slurry} = \frac{1}{\frac{\phi_m}{\rho_{ice}} + \frac{1-\phi_m}{\rho_{brine}}} \tag{2.15}$$

Density of the remaining brine component ($\rho_{brine}$) changes with temperature and concentration, which is also dependent on temperature (discussed in § 2.3.1). Density of ice ($\rho_{ice}$) increases proportionally as temperature decreases.

### 2.3.4 Rheology and Viscosity

An aqueous solution of NaCl will behave like a Newtonian fluid, with a linear relationship between shear stress and shear rate (or velocity gradient). Ice slurry rheology and viscosity is more complex and has been the subject of many scientific papers, with many different conclusions.

Ayel et al. (2003) reviewed research and experiments conducted by several authors looking at modelling the rheology of ice slurries. For low ice fractions, the flow can be considered a Newtonian fluid, the point at which this stops is uncertain but ranges

from 6-15% ice fraction. Above this range Bingham and Herschel-Buckley models for two-phase non-Newtonian fluids are most accurate. However, the dependence on temperature makes it difficult to accurately measure fluid properties like viscosity because the ice slurries can melt and stratify before or during the experiments (Ayel et al. (2003)). Christensen and Kauffeld (1997) presented an equation for viscosity of ice slurries which is generally accepted by most authors for ice fractions below 62.5%. Other studies challenge this work and indicate the equation overestimates the viscosity (Ayel et al. (2003) and Hansen et al. (2000)).

### 2.3.5 Two-phase Flow Characteristics

The different densities of phases found in an ice slurry means that different flow patterns are observed. Doron and Barnea (1996) first observed four distinct patterns in liquid-solid flows:

- Homogeneous flow - Liquid and Solid phases are completely mixed and solid particles uniformly distributed within the flow. This would occur in flows with significant mixing, such as high velocity turbulent flows.
- Heterogeneous flow - More particles are found on one half of the pipe than the other. Often found in lower speed (laminar) flows where buoyancy forces can take effect.
- Sliding bed flow - Particles cluster together forming a separate layer of slower solid particles and faster fluid.
- Stationary bed flow - Particles form a stationary layer, flow is still possible under or above the layer depending where it forms.

Figure 2.7 shows how these flows would look with ice slurries. Yamada et al. (2004) found that cohesion forces between particles in ice slurries has a big impact of the

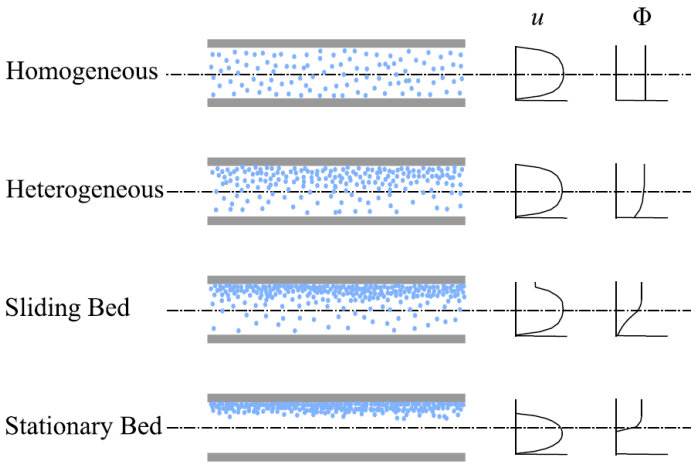


Figure 2.7: Diagram of slurry flow patterns in horizontal pipe, from A. Leiper (2012).

flow pattern and proposed three new classifications.

- Dispersed flow - Particles of ice remain relatively separate in the flow, similar to homogeneous
- Cluster flow - Particles form small clusters strong enough to maintain their shape in the flow.
- Column flow - The clusters form an axial cylinder shape of particles in the flow.

These flow patterns are observed at different flow rates and produce different pressure losses in the flow as shown by Figure 2.8.

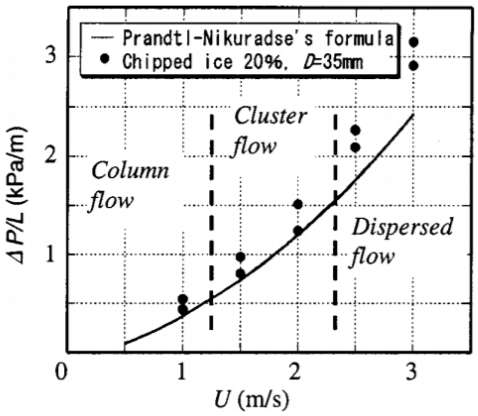


Figure 2.8: Pressure loss and flow patterns vs. velocity, from Yamada et al. (2004).

### 2.3.6 Thermal Properties

The high latent heat of fusion for ice means that ice slurries have large thermal storage capacity, giving them a higher cooling capacity than water at the same temperature. The thermal properties of ice slurry have been an area of considerable research, only a summary of properties at atmospheric pressure are provided in this section.

#### Heat capacity

The heat capacity of ice slurry at constant pressure ($c_{p,slurry}$) is dependent on that of its two phases, ice ($c_{p,ice}$) and FPD (NaCl) solution($c_{p,brine}$). Term $c_{p,slurry}$ can be found using Equation 2.16 (Dorsey (1940)).

$$c_{p,slurry} = \phi_m c_{p,ice} + (1 - \phi_m) c_{p,brine} \tag{2.16}$$

Values for $c_{p,ice}$ vary linearly with temperature of the ice ($T_{ice}$) and can be found using Equation 2.17, where $T_{ice}$ is measured in Kelvin (Dorsey (1940)).

$$c_{p,ice} = 2.12 + (7.8 \times 10^{-3}) T_i \qquad (-20 > T_{ice} > 0) \tag{2.17}$$

Values for $c_{p,brine}$ also vary with temperature and NaCl concentrations. Many different tests have been carried out to evaluate $c_p$ of water and aqueous NaCl solutions below and above 0 $°C$, Archer and Carter (2000) combine many of these and present experimental data and models for a range of solution concentrations at 250 - 300 K.

**Latent heat of fusion**

Latent heat of fusion ($h_{s,f}$) for ice in pure water with no solute is 334 kJ kg$^{-1}$. The specific latent heat capacity of ice in a slurry (assuming continuous phase change), $Q_{lat,sl}$, can be found using the mass fraction of ice ($\theta_m$) and Equation 2.18 below.

$$Q_{lat,sl} = h_{s,f}\phi_m \tag{2.18}$$

However, as discussed in § 2.3.1, the concentration of solute in the slurry liquid phase increases (and freezing point is depressed further) as ice fraction increases. $\phi_m$ and therefore $Q_{lat,sl}$ are both dependent on temperature and can be represented more accurately by Equation 2.19 (Hales (2015)).

$$\frac{dQ_{lat,sl}}{dT} = h_{s,f}\frac{d\phi_m}{dT} \tag{2.19}$$

Equation 2.19 also represents the latent heat contribution to total effective specific heat capacity, $c_{p,eff}$, for a slurry, which is found by summing the sensible and latent heat (Equation 2.20):

$$c_{p,eff} = \phi_m c_{p,ice} + (1-\phi_m)c_{p,brine} + h_{s,f}\frac{d\phi_m}{dT} \tag{2.20}$$

Kumano et al. (2007) observed a drop in latent heat recorded as NaCl concentration in the liquid phase increased. This is a result of the energy from dilution, often assumed small enough to exclude when compared with the large latent heat of fusion.

However, changing NaCl concentration has a smaller effect on the recorded latent heat than ethanol and propylene aqueous solutions (Kumano et al. (2007)).

### Thermal conductivity

As with many other properties of a multi-phase fluid, thermal conductivity is also a combination of physical properties of ice and water thermal conductivity. Kauffeld et al. (2005) outlined an approach originally by Maxwell (1873), where ice particles are modelled as spheres in a matrix (liquid). Using the volume fraction (not mass fraction) and the conductivity for each part an approximation of the total thermal conductivity can be found for low fractions slurries. At higher fractions Jeffrey and Acrivos (1976) take better account of the actual behaviour, including sphere interaction. Both methods still only provide an approximation because they assume no phase change is taking place and rely on knowledge of the liquid phase NaCl concentration.

### Heat transfer

No universal rule relating ice fraction and local heat transfer between solid pipe and slurry exists; variations in the measurement techniques, slurry particle size, ice fraction and pipe geometry make it difficult to compare results. All current work applies heat using electrical heaters or condensing refrigerant, to the outside of a pipe containing slurry. Surface temperatures, slurry temperature and solid fraction changes along the heated section are recorded. Nusselt numbers for different $\phi_m$ slurries and single-phase carrier fluid are calculated and compared. Christensen and Kauffeld (1997) and Bellas et al. (2002) observed an increase in heat transfer when using slurries above $\phi_m = 5\%$ and no change from carrier fluid below this.

However, Knodel et al. (2000) observed a reduction in heat transfer with mass fraction increase for small ice fractions ($\phi_m < 10\%$). This difference is likely because Knodel et al. (2000) used turbulent high Reynolds number (Re) flows which can begin to re-laminate when ice particles are present. Generally, authors have noted a significant increase for heat transfer with slurries over that of water or carrier fluid (Bedecarrats et al. (2003), Jensen et al. (2001) and Christensen and Kauffeld (1997)).

Further work on heat transfer of ice slurries conducted by Castelain et al. (2001) and Mokrani et al. (1998), determined that stratification of the ice particles in the slurry affects the heat transfer. The heat transfer was increased by using 90° bends or coiled pipes, thereby creating Dean-roll-cells (secondary flows) in the pipe to aid mixing. This was found to be especially effective for low Reynold number flows.

All current work in this area relates to heat being added to slurry, no authors have investigated cooling the slurry, which is the main area investigated in this thesis. The main difference being that $\phi_m$ will be increasing rather than decreasing, especially around the area of the pipe wall. Previous authors work indicates that increasing $\phi_m$ in a laminar flow will lead to increases in heat transfer.

### 2.3.7 Pressure Drop

A significant amount of work has been conducted in this area by a wide range of authors with different experimental results and empirical relationships presented. Ayel et al. (2003), Kauffeld et al. (2005) and Monteiro and Bansal (2010) all reviewed current work and attempted to find the best empirical relationship or rheological model to represent ice slurry behaviour.

Meewisse and Infante Ferreira (2001) used similar fraction slurries made from seven different FPD solutions. Methanol, sodium chloride and potassium formate were found to produce the lowest pressure drop, due to their lower viscosity and weaker FPD concentration needed to achieve the ice slurry, compared with other FPD such as ethylene glycol.

Most of the research conducted has focused on horizontal pipes, though different sizes, $\phi_m$, particle sizes and flow rates ($\dot{m}$), have been used. Many authors observed larger $\Delta P/L$ (pressure drop per unit length) for slurries than water, though this difference was smaller at higher flow rates, though always increased with $\phi_m$ and $\dot{m}$ (Grandum et al. (1997), Snoek et al. (1995) and Inaba (2000)). also noticed a greater dependence of $\Delta P/L$ on $\dot{m}$ at low $\phi_m$ below 10%. Above $\phi_m = 15\%$, $\Delta P/L$ increased with $\phi_m$. Y. Liu et al. (1997) and Knodel et al. (2000) observed a decrease in $\Delta P/L$ with ice fraction, contrary to most other work in this area; Knodel et al. (2000) attributed this to re-lamination, a decrease in the flows turbulence as a result of interactions between the fluid and particles. Niezgoda-Zelasko and Zelasko (2007) found that horizontal rectangular tubes produced a larger $\Delta P/L$ than horizontal circular tubes, there was also an increase in $\Delta P/L$ for thinner rectangular cross sections (height $\ll$ width).

Very few authors have attempted to link this with different types of flow patterns, such as those discussed in §2.3.5. The flow rate and preceding pipe geometry will influence whether the flow is a dispersed flow or a column flow which will subsequently affect the pressures drop recorded. This may explain some of the discrepancies in the results.

The latent heat and higher heat capacity of slurries make them useful as a heat

transfer fluid in a heat exchanger. As heat is transferred from the slurry, solid phase drops significantly but not temperature. Bellas et al. (2002), Norgaard et al. (2005) and Shire et al. (2009) all investigated pressure drops inside plate heat exchangers and observed higher $\Delta P/L$ for slurry than water, which increased with $\dot{m}$ and $\phi_m$. Pressure drop was also larger with larger crystals relative to the plate heat exchanger's hydraulic diameter. Norgaard et al. (2005) found similar higher pressure losses than water when pumping slurry through different geometry pipes, constriction, 90° bend and expansions.

It is difficult to compare results from authors as many exclude details which could have an effect. For example ice crystal size is often not mentioned, but is known to have some effect on the pressure loss and flow of a slurry. A standardised experimental method using similar equipment for measurements and ice generation could help improve this field of study.

### 2.3.8 Slurry Behaviour in Helical Coils

Haruki and Horibe (2013) conducted experiments melting ice slurry in vertical-axis[1] helical coiled heat exchangers; heat transfer, flow patterns and pressure drop were investigated for different diameter coils and pipes. Visual images of the flow indicated that solid particles tended to move to the outside wall of the coiled pipes due to secondary circulation (Dean roll curves) above 1 m $s^{-1}$ flow speed, but moved towards the top under buoyancy forces if the speed dropped to 0.7 m $s^{-1}$.

For a laminar flow, heat transfer was higher than horizontal pipes, though lower for turbulent flow due to the re-lamination of the flow. Higher pressure drops were observed over horizontal pipes with similar flows. No known relationship has been found relating $\Delta P/L$ to wall temperature in a helical coiled pipe.

[1]In this thesis both vertical- and horizontal-axis helical coiled heat exchanges are referred to, the terms refer to the central axis of the coil and its orientation.

## 2.4 Solid Content Determination

Measuring the solid content of an ice slurry mixture presents a challenge. Prolonged storage of the slurry can lead to changes in crystal homogeneity, crystal size or melting of the solid phase. Some methods used are reviewed briefly in this section.

### 2.4.1 Calorimetry

Calorimetry involves measuring the temperature (enthalpy) changes as a known mass of slurry is melted. The phase change of ice to water requires a known quantity of energy (latent heat) which can be used to estimate ice fraction. Calorimeters, consisting of an electrically heated chamber to control heating of a sample, can be used. Power consumption, test duration, and sample temperature are used to find an accurate ice fraction measurement.

Faster but coarser measurements of ice fraction can be achieved without a calorimeter by melting ice slurry in hot water. Cold brine and melting ice cause enthalpy changes observed by a reduction in the hot water temperature. The masses and temperatures of the slurry ($m_{slurry}$, $T_{slurry}$) and hot water ($m_{hot}$, $T_{hot}$) need to be measured before mixing. New measurements of mass and temperature ($m_{end}$, $T_{end}$) are taken after mixing slurry and hot water. Mixing and storage of fluids needs to occur in insulated containers to prevent heating from the environment; preferably $T_{hot}$ and $T_{end}$ should be close to room temperature, for the same reason. The enthalpy changes are balanced and used to calculate the heat energy used for latent heating. This and the known latent heat required to melt ice are used to estimate the ice fraction content. See § 3.3.5 for more details on these calculations. Energy of dilution is not included because it is small compared to the latent heat of fusion (Evans (2007)).

### 2.4.2 Liquid Phase Concentration

As discussed in § 2.3.1 a relationship between FPD concentration and ice fraction exists. For this method to work effectively the solute concentration in liquid phase of the slurry needs to be homogeneous. Two methods of measuring liquid phase concentration are outlined below.

**Conductivity** - With NaCl aqueous solutions, NaCl molecules nearly completely dissociate when dissolved, this greatly improves the conductivity of the fluid. The new conductivity has been measured for many different concentrations, temperatures and pressures (Quist and Marshall (1968)). A conductivity probe can be used to monitor the NaCl content in the carrier fluid. Direct in line readings can be difficult because of ice build-up on a conductivity probe, which acts as an electric insulator, distorting the results. Often these probes are used where only the fluid component is found, such as during a re-circulation phase in the ice generation process (Hales (2015)). This method only works with certain FPD which change the conductivity by a measurable amount (such as NaCl).

**Temperature** - As discussed previously in § 2.3.1, temperature can be related to ice fraction. Assuming the relationship between FPD concentration and freezing point reduction are known, a graph such as Figure 2.6 can be created. However, accuracy relies on precise temperature measures and sample thermal equilibrium (e.g. no melting or freezing taking place).

### 2.4.3 Phase Separation

Separating the phases of a slurry is done at industrial scale to retain the ice component and increase ice fraction, though it can also be used to measure ice fraction.

The cafetiere method developed at the University of Bristol has been used to gauge quick approximate ice fractions. Force (300-400N) is applied to a cafetiere plunger, which has sufficiently small holes to block most of the ice crystals. Ice becomes compacted in the lower section with most liquid at the top, though liquid is also still trapped in the compacted ice. Figure 2.9 displays a diagram of the process, the height of compacted ice ($L_1$) and the whole sample ($L_2$) are used to find cafetiere ice fraction ($\phi_{caf}$).

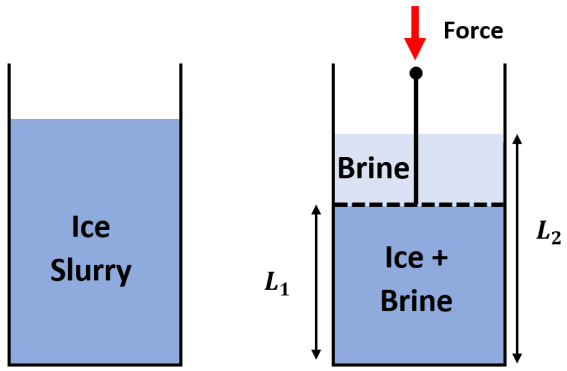


Figure 2.9: Diagram of steps to measure cafetiere ice fraction.

$$\phi_{caf} = \frac{L_1}{L_2} \tag{2.21}$$

$\phi_{caf}$ is not a true ice fraction reading due to the trapped liquid in the packed ice. Conversions factors exist to convert $\phi_{caf}$ to ice mass fraction ($\phi_m$) , 0.61 is valid for $75\% < \phi_{caf} < 85\%$ and 0.57 is used for$45\% < \phi_{caf} < 75\%$ (Evans (2007) and Deans (2006)).

The main variation in results comes from the force applied to the plunger. As this is user operated it is difficult to produce repeatable force applied over the same period. Results have still been found to be repeatable to within 3% (Shire (2006)).

### 2.4.4 Microwaves

Electromagnetic (EM) waves can be absorbed in water molecules but not ice, this means EM waves can be used to measure ice fraction. Hales et al. (2014) designed and tested a successful in-line method of measuring ice fraction in ice slurry made from 5 wt.% sodium chloride solution, using EM waves from 2.3-2.7 GHz. The method monitors signals absorbed and transmitted though the sample to estimate ice fraction, the method is accurate to ±1.2%, though it does require specific pipe geometry to obtain accurate results (Hales et al. (2014)).

## 2.5 Current Ice Slurry Generation Methods

### 2.5.1 Introduction

Many different ice slurry generation methods exist, utilising different methods of cooling fluid and collecting ice formed. In this section these methods are explained and evaluated to highlight any benefits or drawbacks. Depending on the use of the slurry different methods offer different benefits, such as smaller ice crystals, faster production or greater energy efficiency.

### 2.5.2 Bulk Ice Production

Most slurries are made from a feedstock material, usually a FPD with water. However, ice can be made from water and combined with a FPD aqueous solution later. Ice made by this method is often made in bulk and hence called bulk ice production. Ice is usually produced from pure water with no FPD to lower the freezing point. Therefore, it is produced consistently at warmer refrigeration temperatures rather than from a solution with a low freezing point. This increases the thermal efficiency and Coefficient of Performance (COP) of the method (A. Leiper (2012)).

Solid ice sheets or blocks formed need to be broken down (comminution) to the smaller particles needed for slurries. This can be energy intensive, reducing the overall energy efficiency of the method. A FPD aqueous solution is added to form a slurry; the amount added can be used to control the slurry ice fraction. A. Leiper (2012) investigated the method extensively and reported less energy was used in total compared with scraped surface generators. Some of the most popular bulk production methods include:

- **Block ice cubes**

  This method was a scaled up version of an ice cube tray' with water frozen in containers. Ice growth slows as the ice formed insulates the remaining water and impedes further ice growth.

- **Contact melting**

  Ice is formed on a cooled surface (often a vertical tube or plate) and removed by heating the surface. Switching between heating and cooling reduces the method's efficiency. Previous work has focused on optimising the process to find the ideal layer thickness and heating time to maximise production rate or efficiency (Vargas and Bejan (1995)).

- **Scraped surface**

  Ice formed on a cooled surface is scrapped off, see § 2.5.3 for more details on this method.

Many of these methods can also be used to freeze FPD aqueous solutions directly as well as pure water, though the refrigeration fluid must be at a lower temperature.

### 2.5.3 Scraped Surface Generators

Scraped surface ice makers are the most widely used slurry generation method. A liquid solution is cooled, and heterogeneous nucleation initiated on the cooling surface. Scrapping blades, rods, helical screws or brushes are then used to remove the ice from the surface and expel it. Figure 2.10 displays a diagram of a helical screw mechanism which is commonly used. Cooling fluid runs around the outer surface of a cylinder containing the feedstock solution. With a helical screw, only solid ice is carried up to the top of the Auger and out the generator. Feedstock solution is replaced using a header tank.

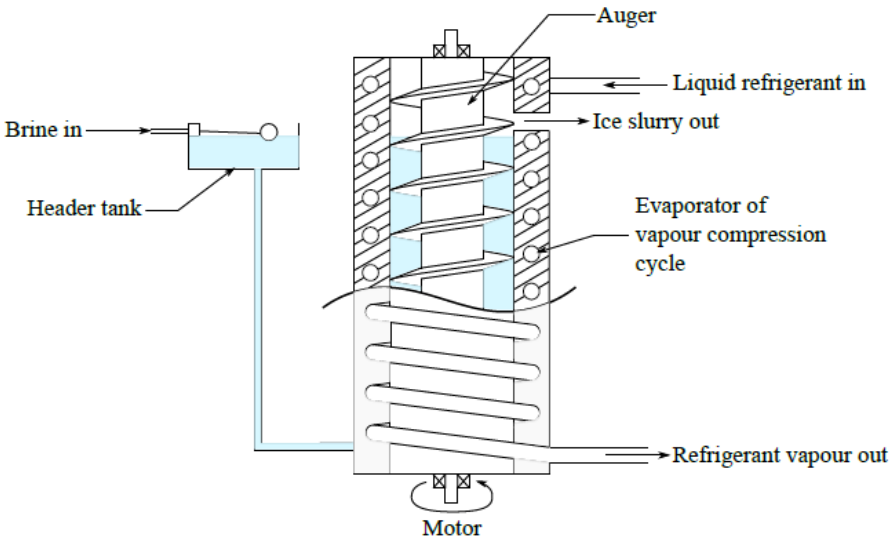


Figure 2.10: Diagram of a scraped surface generator using a helical scraper to remove ice from a cooled cylinder, taken from A. Leiper (2012).

Work by researchers such as Lakhdar et al. (2005), to optimise the blade clearance distance, and Vargas and Bejan (1995), to find the optimum ice layer height before removal, have helped to optimise the process. An insulating ice layer slows heat transfer and work need for mechanical scraping adds to the total energy consumption. Yang and S. Liu (2015) improved the efficiency of a scraped surface generator

by up to 43%, by adding a pre-cooling (of feedstock solution) cycle to the basic refrigeration cycle. It is is unclear from their work if this efficiency improvement could be applicable to other scraped surface generators or just the type tested.

### 2.5.4 Fluidised Bed Generators

Fluidised bed generators use small solid particles added to a flow of feedstock solution, cooled below freezing in a shell and tube type heat exchanger (see Figure 2.11).

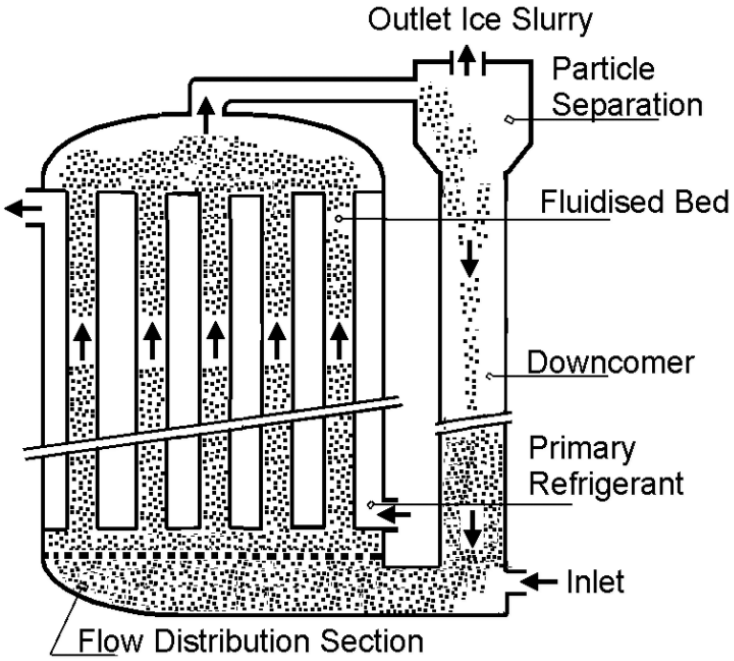


Figure 2.11: Diagram of a fluidised bed ice generator made from a shell and tube heat exchanger, taken from Pronk et al. (2001).

Ice which forms on the heat exchanger walls is removed by attrition form the solid particles allowing for continuous high heat transfer to the fluid. Mechanical work is supplied by the flow of solution as it moves the particles around the heat exchange; the initial work was presented by Meewisse and Infante Ferreira (2000) who constructed a working prototype which was able to produce ice slurry from a range of aqueous solutions. The constant attrition of the ice crystals by solid particles meant

that the crystal size was limited to 0.18 -0.20mm (Van der Gun et al. (2001)).

Further work by Stamatiou et al. (2005) evaluated a fluidised bed crystalliser and two popular scraped surface ice slurry generators. It was found that the scraped surface generators tended to be more reliable and offer a more versatile range of operating conditions while the fluidised bed crystalliser was found to only be stable in a certain range of concentrations and temperatures. However, fluidised bed generators operate at warmer refrigeration temperatures and have improved COPs over scraped surface generators.

### 2.5.5 Direct Injection/Contact

Direct injection involves adding cold refrigeration fluid directly into the aqueous solution to be frozen, no mechanical work to remove ice is required because often the refrigeration fluid evaporates or separates from the slurry due to different densities. Wijeysundera et al. (2004) conducted the initial successful research. They came up with the concept and modelled the problem, proving that significantly higher heat transfer coefficients could be achieved without a surface between the refrigerant and the fluid. Vuarnoz et al. (2015) focused on making an improved prototype by optimising the evaporation section where the refrigerant is injected. Vuarnoz et al. (2015) also changed the nozzle to try and induce turbulence in the injected flow, though this was found to be ineffective. A final version of Vuarnoz's improved direct injection generator prototype was made using a smaller compressor. Importantly the research found that all the prototypes and the original design had a better COP than a traditional scraped surface ice maker, almost 50% better in some cases. The problem with the method is that refrigerant which does not evaporate or separate is often found in the ice slurries produced. Further work on refrigeration fluid selection could prevent this (Vuarnoz et al. (2015)).

### 2.5.6 Yun et al. (2016) method

Yun et al. (2016) found a similar method to direct injection, except a bath of high concentration NaCl brine was used as a non-toxic refrigerant to prevent contamination. Water at 0°C was added at the bottom of a high concentration brine environment (up to 22 wt.%) at low temperatures (-12 to -18 °C), see Figure 2.12(a). As water entered and rose through the bath the heat transfer proves faster than mass transfer, solidifying up to 70 % of the water to ice before it mixes with the brine. See Figure 2.12 (b) for a picture of ice being made. Some water remained and diluted the brine-refrigerant reducing the effectiveness of the method. To produce ice consistently the excess water left in the refrigeration bath needs to be removed. This method is discussed further in Chapter 8.

(a) Cooled bath of brine (b) Ice produced in cooled bath

Figure 2.12: Pictures of Yun et al. (2016) ice slurry generation method; (a) shows a cooled bath high concentration brine; (b) shows ice being produced from water introduced through the pink tube.

### 2.5.7 Supercooling Pure Water

Aqueous solutions can be supercooled below their freezing point and freezing initiated to create ice. Many authors have investigated supercooling water; differences in their work are related to how nucleation is initiated and controlled. Often they are based on the same basic procedure (see Figure 2.13); water is supercooled, nucleation

occurs and ice is created before the ice and water are separated. The water phase is heated to 0.5 °C to remove any remaining ice crystals, before being supercooled again (Kauffeld et al. (2005)).

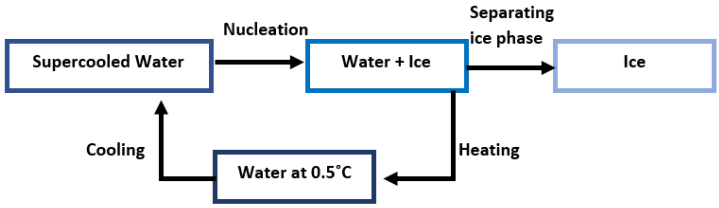


Figure 2.13: Ice slurry production process using supercooled water.

Bedecarrats et al. (2000) created a flow of supercooled water in which nucleation was initiated by the impact of water falling into the storage tank at 0 °C. It was concluded that ice fractions of 1.25%/°C of supercooling could be achieved. Castaing-Lasvignottes et al. (2006) and H. Wang et al. (2016) also conducted similar work using heat exchangers to cool fluid. They noted the need for precise temperature control of the fluid to avoid blockages. Tanino (2000) cooled water to -2°C and ice growth was initiated using seeding or ultrasonic waves in a 'releaser' section after the cooling section. Continuous ice production for up to 6 hours was demonstrated.

Mito et al. (2002) noted that production through Tanino's method could lead to blockages as ice nucleation could propagate back along the fluid flow into the cooling section. A jet of water (see Figure 2.14) at 0.5°C was used to prevent ice propagation up the tube, increasing the operation time up to 12-hours. Bedecarrats et al. (2010) supercooled water in pipes and ice nucleation was initiated using a small ice crystal. The authors found that with less than 1.2 °C supercooling no blockages were observed and 2 °C or more of supercooling led to frequent blockages in the pipe.

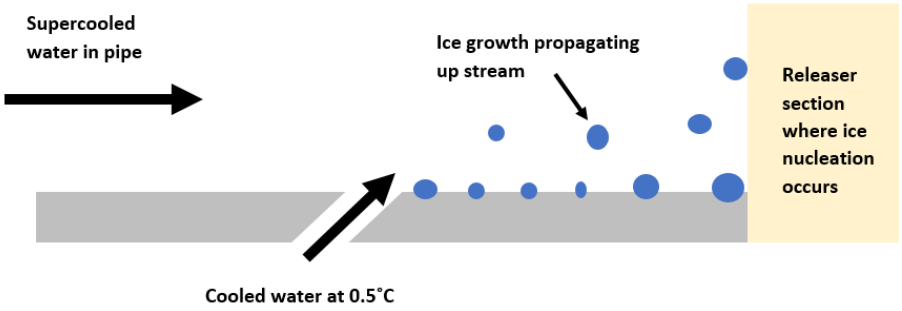


Figure 2.14: Diagram of jet of water used to prevent ice propagation, replicated from figures in Mito et al. (2002).

Thomason (1987) investigated the freezing of turbulent water in cooled pipes; experiments were conducted using a metal shell and tube heat exchanger with water at Reynolds numbers 4,500-10,000 and a range of temperatures below 0 °C. A key observation made in this work was that there are three different possible outcomes when attempting to freeze the water.

1. The pipe blocked from excessive water freezing.
2. No ice formed.
3. There was a certain range of temperatures and flow rates where the water appeared to oscillate from blocked to unblocked.

For outcome three ice and water mixtures were expelled from the pipe. Usually, outcome number 3 would end with the pipe blocked or no ice production. Graphs demonstrating the different outcomes and production region were plotted.

The main problem with supercooling water experiments is blockages in the cooling pipe. Too much cooling, either from refrigeration temperature or flow rate change leads to blockages of the supercooled flow. Pure water can also only be cooled by 1-2 °C below 0°C before nucleation begins to occur, meaning ice production rates are low.

### 2.5.8 Supercooling Aqueous Solutions

**Spray jet on a cooled surface** - Mouneer et al. (2010) tested an ice slurry generator that used spray nozzles of supercooled water which was directed at a cooled tube surface. Supercooled liquid froze to the surface and was removed by the jet of unfrozen fluid, thereby generating an ice slurry. To work effectively, the supercooled fluid needed to be sprayed fast towards the cooled walls of the tube (meaning high Reynolds number flows). Using a jet of supercooled water was found to use 10-20% less energy than a similar scraped surface generator, though the ice fraction of the slurry produced was lower.

**Hydro-Scraped ice slurry generator** - Barth and Leprieur (2002) investigated using a variable flow rate inside a heat exchanger to control ice slurry production. A flow of water and ethylene glycol was cooled until ice formed on the cooled heat exchanger surface. The growth of ice was measured as a pressure loss and temperature change through the cooled section. In response to ice formation, a control system increases the flow rate to promote turbulence and detach ice crystals from the cooled walls. The increased flow rate changed the heat transfer to the fluid and combined with a controller initiated decrease in refrigeration capacity, resulted in more ice crystals being removed. Not many details of this exact design have been reported but a brief overview has been presented in Barth and Leprieur (2002) and Kauffeld et al. (2005).

**Heat exchanger with bubbles** - Zhang et al. (2008) created ice slurry in a vertical shell and tube heat exchanger from ethylene glycol solution. Ice formed on the walls of the heat exchanger but was removed by the addition of air bubbles at the bottom of the exchanger. The bubbles were observed to help remove ice from the

exchanger walls, which were already coated in hydrophobic coatings. Unfortunately, the authors only measured the total mass of ice produced not the mass produced on every pass though the heat exchanger, through the method did prove effective. It is unclear from the work presented if the bubbles cause a shear force on the ice helping to dislodge it. Alternatively, it could be that the bubbles become trapped between ice and surface as it forms, lowering the adhesion strength.

Supercooling solutions with a FPD enables them to be cooled much further below freezing than pure water and increases the experiments possible. No data has been presented by authors mentioned here about the operational range of these methods. The authors are vague about the conditions their generators will and will not operate under and how efficient they are.

### 2.5.9 Peristaltic Ice Slurry Generation

Ash (2012) successfully trialled a peristaltic based ice slurry generator intended to producte hygienic ice slurry to clean catheter tubes. Feedstock fluid was circulated through pipes using a peristaltic pump, see Figure 2.15. Ice formed was removed by rollers massaging the tube; ice production rate was poor and low refrigeration temperatures of -27°C were required. The design was effective at producing hygienic ice slurry up to 35% mass fraction, without any contamination.

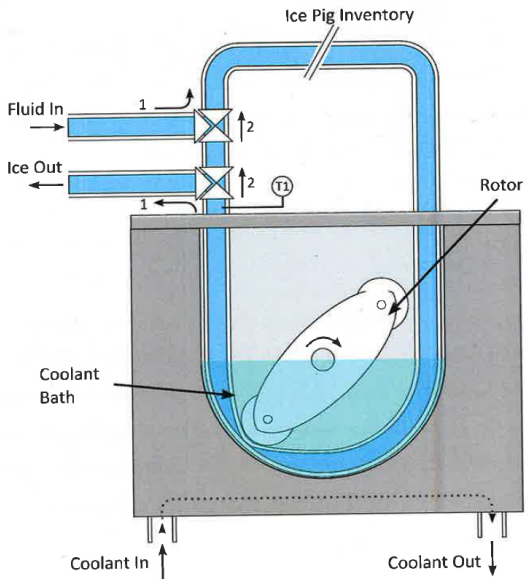


Figure 2.15: Schematic of peristaltic pump ice generator. Valve position 1 is when the fluid is pulled in or exits, 2 is when the fluid is re-circulated to form ice slurry. Figure taken from Ash (2012).

This method was not explored further than a few experiments. It is not known what the effect of using warmer refrigeration temperature or changing pump speed has on ice production. It could hold great potential, especially if the cooled area of the pipe where ice forms could be expanded.

## 2.6 Ice-Solid Adhesion

Ice adhesion (and heterogeneous nucleation) has been the subject of significant work, though no unifying theory of ice nucleation and adhesion to different surfaces has been found (Schmelzer and Hellmuth (2013)). The basic mechanics of ice adhesion and factors known to affect it have been outlined here. Reducing ice adhesion to a surface is key to reducing the energy needed to remove it.

### 2.6.1 Mechanics of Ice Adhesion

Ice adhesion to a surface is known to depend largely on the interfacial energies ($\gamma$) between water (or ice), the surface and the surrounding fluid (gas or liquid). Figure 2.16 displays a drop of water on a flat surface with corresponding surface energies for the surface-vapour (s,v), water-vapour (w,v) and surface-water (w,s) interfaces. This produces the following rule:

$$\gamma_{w,s} + \gamma_{w,v} cos\theta = \gamma_{s,v} \tag{2.22}$$

The same theory can be applied to ice formation on a surface, though water (w) is exchanged for ice (i) and vapour (v) is exchanged for water (w).

$$\gamma_{i,s} + \gamma_{i,w} cos\theta = \gamma_{s,w} \tag{2.23}$$

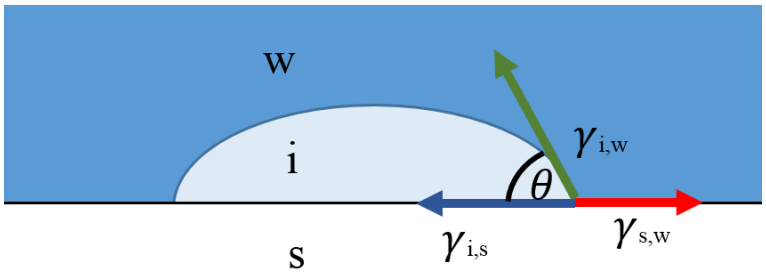


Figure 2.16: Diagram illustrating wetting (contact) angle and interfacial energies for water or ice on a surface.

Interfacial energies for ice are generally unknown or difficult to find between ice/surface and ice/water. As discussed in §2.2.2, $\theta$ for ice and water formation are assumed to be the same. Similarly, interfacial energies for ice and water are often approximated as the same (Schmelzer and Hellmuth (2013)). An equation for the approximate work of adhesion holding the surfaces together ($W_a$ $[Jm^{-2}]$) can be found (Makkonen (2012)).

$$W_a \approx \gamma_{i,w}(1 + cos\theta) \tag{2.24}$$

Where $\theta$ is the wetting angle or water contact angle as discussed in § 2.2.1. Using Equation 2.24 it is apparent that for low $\theta$ values, $W_a$ will be higher, while at high $\theta$ values such as with hydrophobic materials ($\geq 90°$), $W_a$ is significantly lower. In reality, it is far more complex as $W_a$ is not the only factor contributing towards overall ice adhesion.

Most experimental methods to test adhesion strength involve a flat plate of material with ice attached. A force is either applied perpendicular (normal to the plate) or more commonly parallel to the plate. A fracture can occur within the ice, a 'cohesive break', or at the interface itself, an 'adhesive break'. Cohesive breaks are often seen when ice is removed from metal surfaces, while adhesive breaks are often seen with hydrophobic materials (Petrenko and Whitworth (2002)). Water drops are also often used, though this is not representative of ice adhesion inside pipes or other submerged cooled surfaces.

### 2.6.2 Factors Affecting Ice Adhesion

Many experiments have attempted to find accurate adhesion strengths. Experimental measurements recorded often differ due to the difficulty of replicating conditions and the different experimental methods tried. Many factors have been found to affect adhesion strength, the key ones are discussed in this section.

**Water contact angle (surface energy)** - As discussed in the previous section, $\theta$ has an effect on adhesion ($\theta$ is largely dependent on the material being tested). Many experiments on ice adhesion have focused on this property and proved that

adhesion strength increased as $\theta$ increases as long as average surface roughness is kept the same (Fillion et al. (2017), Bascom et al. (1969), and Zou et al. (2011)). Though, this correlation is not as strong as the basic theory outlined previously suggests (Petrenko and Whitworth (2002)). Hydrophobic material (such as PTFE) is consistently proven to have lower ice adhesion, but not superhydrophobic materials (Bharathidasan et al. (2014)).

**Surface Roughness** -A large amount of work on ice adhesion strength has focused on investigating surface roughness. All the work agrees that increasing average surface roughness of a material increases adhesion strength (Fillion et al. (2017), Bharathidasan et al. (2014), Zou et al. (2011), Saeki et al. (2011), and Hassan et al. (2010)). This is due to the increase in contact area created by a rougher surface. Exact values of adhesion strength recorded vary between studies because it is impossible to replicate the same surface topography for a new experiment. Saito et al. (1991) concluded that below 20 $\mu$m surface roughness, ice adhesion strength was related to surface energy, however above 20 $\mu$m surface roughness had a significant effect (H. Murase and Fujibayashi (1997)).

**Temperature** - As water freezes on a surface a thin liquid film becomes trapped between the ice and the material surface. The ice and surface keep the film trapped at a higher pressure keeping it liquid below 0 °C. A thicker liquid film results in a lower ice adhesion strength to the surface (Makkonen (2012)). Jellinek (1959) observed this effect with stainless steel and ice. Adhesion strength increased as temperature was reduced from 0 to -13 °C, as more of the film solidified at lower temperatures. Above -13 °C an adhesive break was observed, however below -13 °C the temperature no longer had a significant effect because the ice fractured through a cohesive break first. Landy and Freiberger (1967) noted a similar effect with plastic

materials, though the rate of adhesion strength increases as temperature fell differed between materials. Teflon barely increased while adhesion to PVDF (Polyvinylidene fluoride) nearly doubled from -5 to -20 °C.

The coefficient of thermal expansion is also different for ice and metals or plastics. This difference can result in a weakening of the bond between materials if a rapid temperature change occurs; usually cooling is slow enough that the creep of ice and liquid film can accommodate the stresses created (Petrenko and Whitworth (2002)).

**Water salinity** - As discussed in §2.3.1, freezing a NaCl solution results in a higher concentration NaCl liquid phase. The fluid becomes trapped throughout the ice, including at the surface interface. Reducing the effective contact area and adding to the interface film thickness and reducing the ice adhesion. The brine pockets in the ice also weaken its structure making it vulnerable to cohesive breaks under stress. Makkonen (2012) reviewed much of the current work on this subject and noted that ice adhesion strength decreased with increasing salinity especially for lower concentrations up to 5wt.%. Temperature reductions result in an increase in brine expulsion to the small remaining liquid phase, making it harder to freeze. Therefore, the temperature is observed to have a smaller effect on ice adhesion in FPD solutions than with pure water (Makkonen (2012)). Hong et al. (2004) also noted reductions in adhesion strength with increasing FPD (glycol) added.

**Electrostatic forces** - Ryzhkin and Petrenko (1997) demonstrated that electrostatic forces had a significant effect on ice adhesion in metal-ice interfaces due to the presence of a small charges on the ice surface. Adhesion energies were calculated as higher for ice-metal interfaces than ice-plastic due to the presence of surface charges.

**Air entrapment** - Air can become trapped in small gaps in and between materials which reduces the effective contact area, reducing adhesion strength. The same is also true of any impurities or loose particles (such as dirt) found on the surface (Petrenko and Whitworth (2002)).

### 2.6.3 Methods for Preventing Ice Adhesion

Preventing a build-up of ice or snow has been the subject of a significant number of investigations because of the substantial damage (and extra cost) it can cause. Some of the more effective methods of preventing ice adhesion or removing ice are mentioned here.

#### Mechanical Methods

*Scraping or hitting a surface* - This can be difficult and hazardous for workers and almost impossible in some situations. As discussed previously fluidised bed ice slurry generators use solid particles to knock ice off the wall of the pipes and prevent blockages. For more information see §2.5.4.

*Pneumatic de-icers* - These have been employed on some ships, aircraft wings or large flat surfaces. Tubes on the surface, or built into a 'boot' structure, are inflated to dislodge ice formed on the surfaces (Petrenko and Whitworth (2002)), see Figure 2.17. The difficulty is that the boot does not work if it becomes damaged or is not attached to the surface.

*Flexible cover* - A cheaper method which is used often is to add a flexible cover to a surface, with the idea being that the wind will move the cover and prevent ice building up on the surface. Too much ice can stiffen the cover and prevent this from working (Petrenko and Whitworth (2002)).

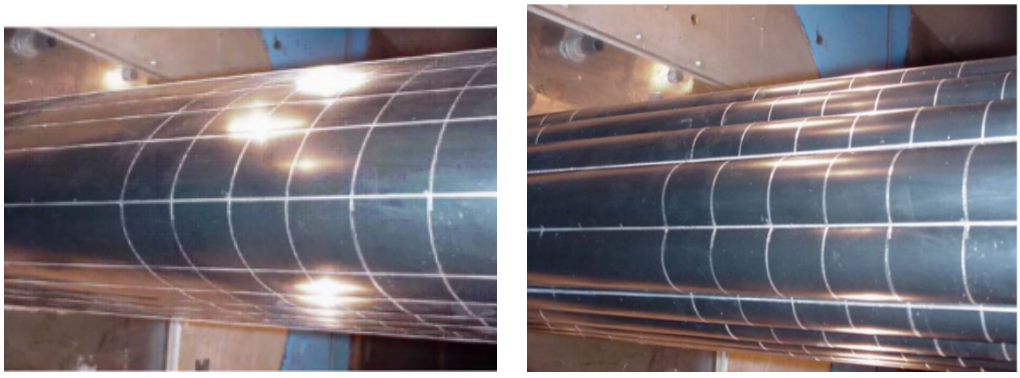

(a) Boot on aircraft wing (b) Inflated boot on aircraft wing

Figure 2.17: Pictures of a boot used on an aircraft wing, taken from Aviation Research and Development (2006)

### Paints or coatings

Many different types of hydrophobic coatings exist, Bascom et al. (1969) tested polymer based hydrophobic coatings on steel sheets and found they reduced adhesion strength by 70-80%. Grease-based coatings are also commonly used to coat surfaces because they are cheap, though not durable. H. Wang et al. (2014) added a hydrophobic coating to the copper tube in a heat exchanger generating ice slurry. This extended the useful time for which the heat exchanger could be used to produce ice slurries without blocking. Hydrophobic coating never prevents complete ice adhesion and often needs to be combined with another prevention method for best results.

More recently coatings which prevent water from even nucleating have been considered as a more effective way of protecting surfaces (such as aircraft wings) from droplets of supercooled water (Maitra et al. (2014)).

### Thermal methods - heating

One of the simplest methods for preventing ice adhesion or removing ice is to use heat, either applied to the outer surface of the material or by heating up the material

itself. This method is similar to contact melting discussed in § 2.5.2 and works best with high conductivity materials such as metals. However, the large energy cost, due to the high latent heat of ice, makes this method expensive (Petrenko and Whitworth (2002)).

## 2.7 Chapter Summary

From reviewing previous work, a number of key conclusions can be made.

- To freeze aqueous solutions they need to be supercooled below $T_f$. Initial fast dendritic ice forms often impeding flow (if present), followed by slower layer growth on the surface from which heat is being extracted.
- Nucleation can be encouraged, though only a few methods are known to do this reliably. Spontaneous heterogeneous nucleation will usually occur first at warmer temperatures than homogeneous nucleation which requires much colder temperatures.
- Conveying ice slurry through pipes results in higher pressure losses than pumping its pure liquid phase. No governing rule has been agreed on and no known work exists for pressure loss from cooling slurry as it is pumped.
- Pumping ice slurry through curved or coiled pipes can increase heat transfer and mixing in the pipe but does result in an increased pressure loss over a horizontal straight pipe.
- Ice formed in pipes from supercooled aqueous solutions can block the pipe; having a freezing point depressant can delay blocking. Two patents exist for ice slurry generators freezing alcohol-water solutions in pipes. However, no known data on the efficiency or work to optimise them has been published.

- Ice adhesion is lower on low surface roughness and energy materials. This indicates that smooth plastic surfaces might provide a favourable surface for ice production with less energy needed to scrape the ice away.

- Pneumatic devices which could flex a surface may remove ice build-up, similar to a boot outlined in the previous section. This has never been utilised to generate ice, only to remove unwanted build up on surfaces.

# Chapter 3

# General Experimental Method

## 3.1 Introduction

This chapter outlines the basic experimental methods and equipment used in most of the experiments in this thesis. Future chapters often refer to methods and measurement techniques outlined in this chapter.

## 3.2 Experimental Equipment

The set-up outlined here was used for most experiments. Some changes made to the material, coil orientation and length are outlined in more detail in later chapters. A coil of Brewmaster 2 nylon pipe was submerged in a bath of cooled refrigeration fluid, in the structure displayed in Figure 3.1. Each feature is detailed in the corresponding section below, as labelled on Figure 3.1.

An insulated inlet tank (*Item A*) held a supply of brine at a constant temperature, between 18-20 ° C for each experiment. Figure 3.2 displays a picture of the inlet tank used. A lid was added to prevent particulates from falling into the fluid and creating extra sites for ice to nucleate on.

A peristaltic pump (*Item B*)(series 200 unit manufactured by Williamson Manufacturing) was used to provide flow to a maximum differential pressure of 100 kPa.

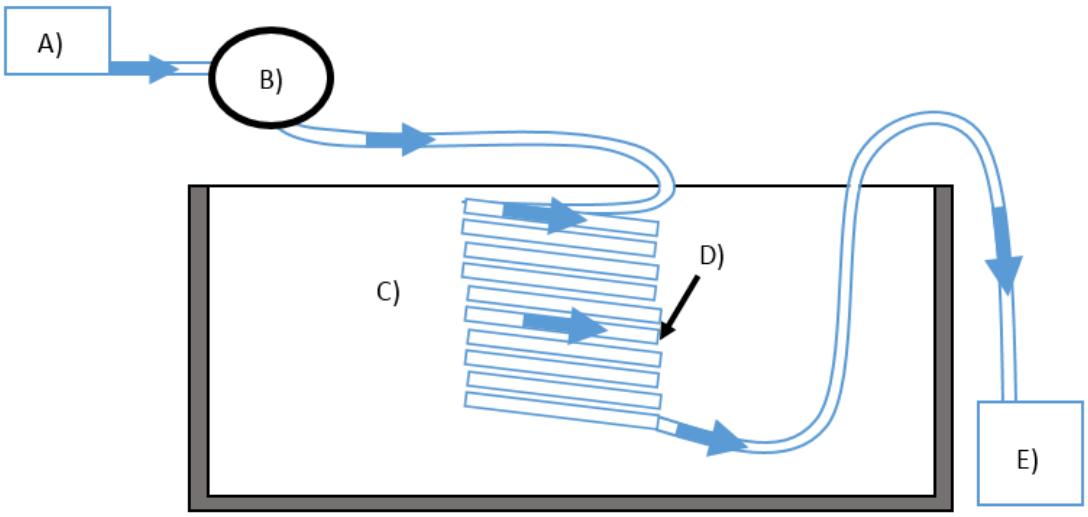


(a) Diagram of experiment Set up.

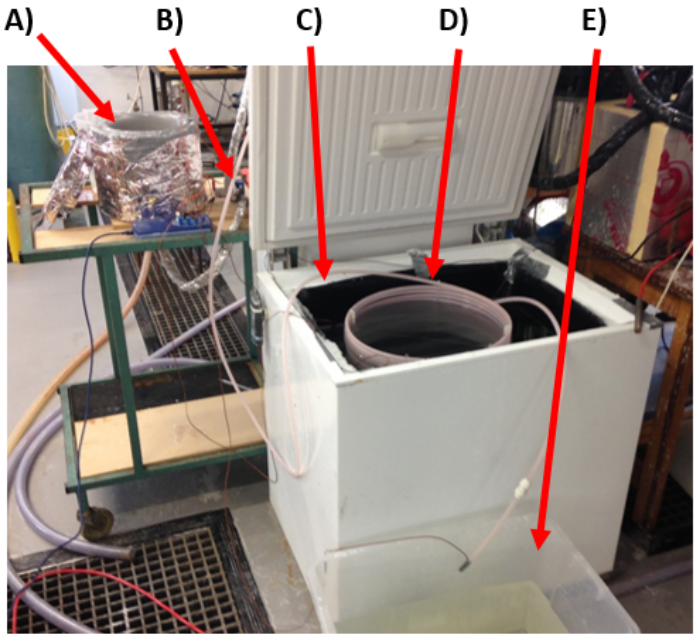


(b) Picture of final experiment set up.

Figure 3.1: Diagram (a) and picture (b) of basic experimental set up are shown. A) inlet water tank; B) peristaltic pump used to move fluid; C) refrigeration fluid; D) coil of nylon pipes; E) outlet water tank.

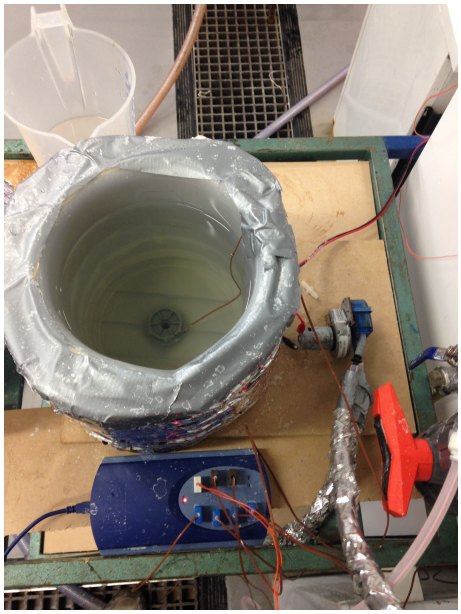

Figure 3.2: Inlet fluid storage tank, insulated with Celotex insulation board to maintain constant inlet temperature.

A more detailed analysis of pump pressure and flow rate characteristics is shown in §3.3.4. The pump flow is started before the pipe (*Item D*) is submerged in the refrigeration bath (*Item C*).

The refrigeration fluid (*Item C*) used was 20 wt.% NaCl brine. The high NaCl concentration meant it could be cooled to -16.5°C without freezing. 115 litres were cooled and stored in a 150 litre chest freezer (see Figure 3.1 (b)). The cold brine acted as a cold source sink for experiments. Often ice would form in the freezer when it was too cold, this was melted before any experiments were conducted. The fluid was also mixed and left to settle before each experiment to try and ensure a uniform starting temperature.

Nylon coils (*Item D*) of 0.0067m internal diameter and 0.0095m outer diameter were used in all experiments except those detailed in Chapter 6 and 7.3.

Valpar Brewmaster nylon pipe was chosen for several reasons:

1. Specimens tested on a profilometer were found to have a surface roughness of 1.5 $\mu$m $\pm$0.5 $\mu$m, ideal to reduce ice adhesion.

2. It has a low surface energy compared to metal, which has been identified as crucial in the previous chapter.

3. The material used is translucent which means blockages can be observed.

4. The pipe can be easily obtained, cheap, and in sizes which can be easily interfaced with pumps and sensors used.

The roughness is sufficiently small that ice adhesion is controlled by surface energy rather than physical topography of the surface (Saito et al. (1991)), as the surface energy of nylon is low (Owens and Wendt (1969a)), the inner tube wall will have a low propensity for ice to bond to it.

To maximise heat transfer area nylon coils were separated (by 0.003m) and held in place by a thin Perspex frame (see Figure 3.3). The coils were less dense than the refrigeration fluid and therefore supports between the frame and the freezer lid were used to keep the coil submerged when the lid was closed.

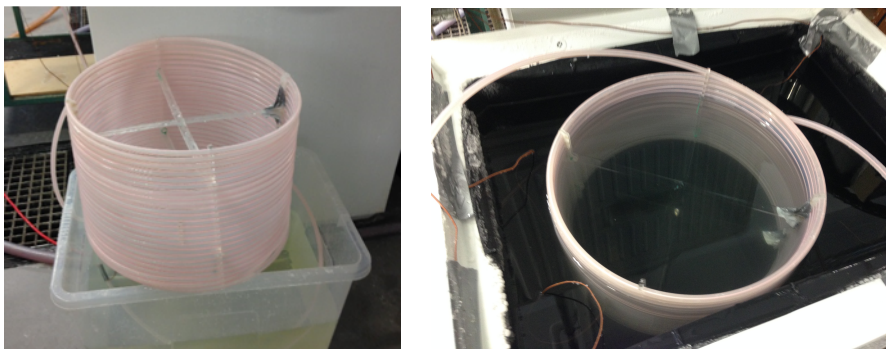

(a) (b)

Figure 3.3: (a)Picture of the coil and the thin plastic support structure used to separate coils. (b) Coil of pipe inside brine refrigeration bath.

A collection tank (*Item E*) was placed at the end of the coil to collect the brine or ice slurry from the output. The outlet fluid was filtered to remove any dust or particulates before the concentration was checked using a density meter for use in future experiments.

## 3.3 Measurements and Sensors

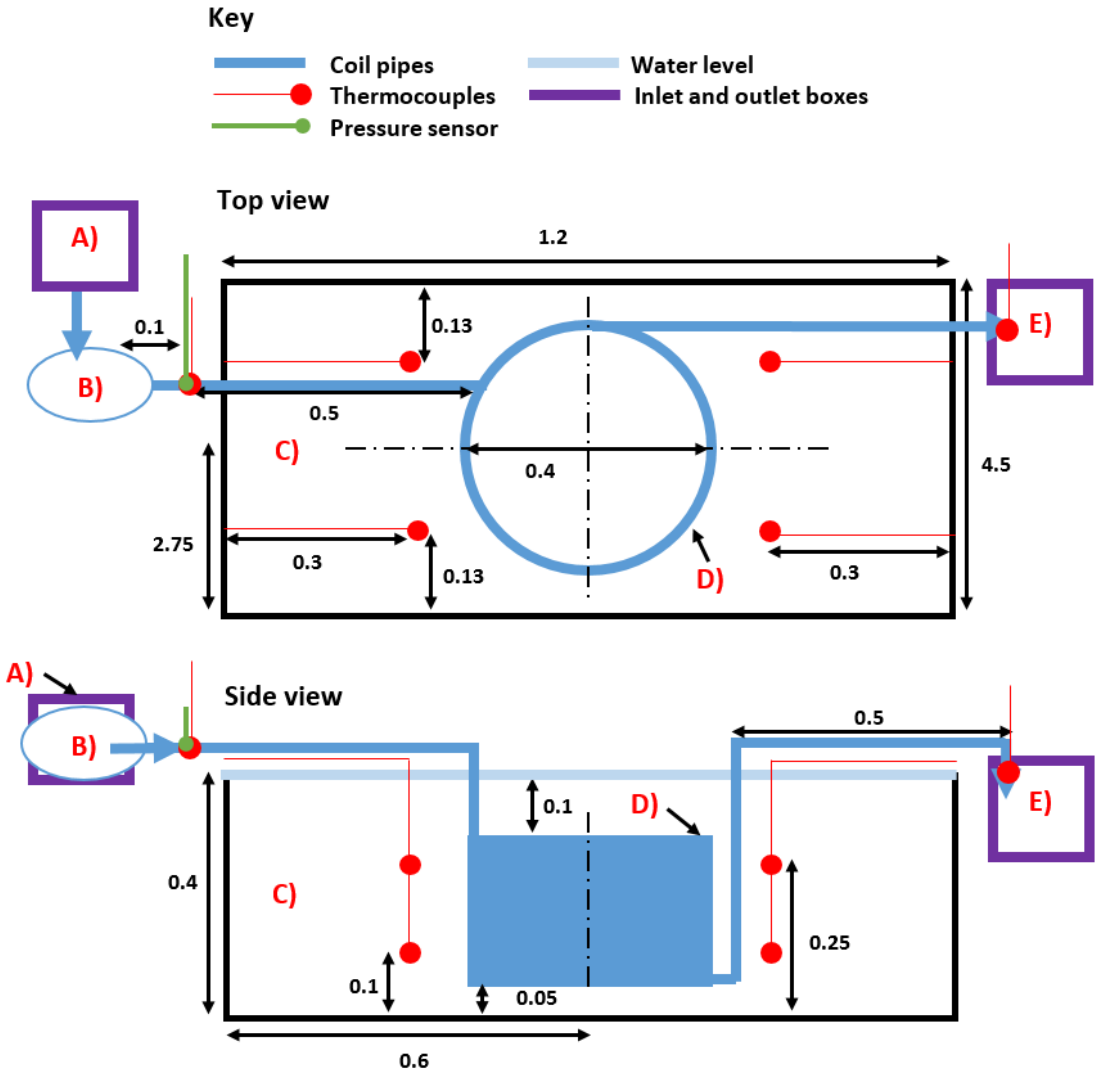


Figure 3.4: Experimental set up, thermocouple locations are in red, four are placed in the bath and one at inlet and outlet. The green line indicates where pressure reading were taken from.

This section reviews the sensors and other data collection methods used. Each measurement, the method used, calibration conducted and associated errors are outlined. Figure 3.4 illustrates the location of the sensors used to monitor temperature and pressure during experiments.

### 3.3.1 Temperature Measurements

Four T-type thermocouples measured bath temperatures and an average was taken. One thermocouple was used at the outlet and one at the inlet pipe. To calibrate the thermocouples, they were tested in an ice and water bath (at 0 °C) to identify ones that were corroded, damaged and produce large deviations in recordings. Two PT100 probes were also used to monitor the temperature as the ice melted and the water warmed up; these readings were compared to the thermocouples at the same location. Any thermocouples deviating by >0.5 °C from the PT100 probe or with large fluctuations in recordings were removed. The average of the final thermocouples used was within +/-0.2 °C of the PT100 probe.

All readings from thermocouples were taken using a TC-08 Pico data logger equipped with filters to help eliminate noise in the readings. Two PT100 probes were also kept in the bath with the four thermocouples throughout experiments to help identify if a thermocouple wire became corroded/damaged and needed replacing.

The accuracy of the temperature measurements is taken as +/- 0.2 °C. The PT100 probes can only be considered +/- 0.1 °C accurate, therefore the total error in recorded temperature was taken as +/- 0.22 °C. It is acknowledged that thermocouples can normally only be considered accurate to +/-1 °C, though extra steps have been taken here to reduce that error.

### 3.3.2 Pressure Measurements

Pressure measurements were taken using a Honeywell 24PC/26PC Series Low-Pressure Sensor. The sensor was attached at the end of an empty tube at right angles to the main flow. A pocket of air was left between sensor and fluid to act as a damper, removing oscillation in the flow rate which may occur due to the use of a peristaltic pump.

Readings from the sensor were calibrated using hydrostatic pressure. A container of water was raised to a range of heights from 0-5 m and measurements of voltage taken from the sensor, the process was repeated a total of three times. Data was also recorded with the TC-08 Pico data logger.

Due to noise in the sensor signal, repeated experiments were found to vary by up to 0.5kPa, therefore, the error in the result was taken as +/- 0.5kPa.

### 3.3.3 Brine Preparation

Brine was employed as the refrigeration fluid outside the pipe and the working fluid inside. Concentration was monitored using an Anton Paar density meter (Model DMA 4500 M) and data on densities of NaCl brine from CRC Handbook of Chemistry and Physics. Between experiments, brine was stored in sealed fermenting containers which were checked for temperature and concentration before each experiment.

Using the density meter to measure Brine concentration proved accurate. Initially, when water or stronger brine was added, it was found that a density gradient could occur in the brine due to insufficient mixing. This gradient could lead to deviation

in results of +/- 0.1 wt.%, though with sufficient mixing for >3 minutes the gradient was removed, and deviations fell to +/- 0.01wt.%.

### 3.3.4 Flow Rate Measurements

Flow rate measurements were taken using two key methods. Initially, in the experiments outlined in Chapter 5 and 4, they were taken using a measuring cylinder and a stopwatch at the start of each experiment. A pump speed was set using the voltage from the power supply to the pump. The volume of outlet flow in 2 minutes was then recorded at room temperature, volume, density and time were used to calculate the flow rate in kg $s^{-1}$. Similar measurements were taken throughout the experiments. For experiments in Chapter 7 and 6 an in-line mechanical flow rate monitor (a Parker Variable Area Flow Meter) was employed to allow continuous flow rate monitoring throughout the experiments.

The errors for the first measurement method depended on the resolution possible with the measuring cylinder which was $\pm 0.015$ L, giving a possible error of 0.3 g $s^{-1}$. For the mechanical flow rate monitor the scale was recorded in L $min^{-1}$ resolution was 0.167 L $min^{-1}$, giving a possible error of 0.3 g $s^{-1}$.

A pump curve was created using water at 20 °C for the pump used in all the experiments because no curve currently existed. A set pressure loss was applied to a flow using hydrostatic pressure and the change in flow rate was recorded using a Parker Variable Area Flow Meter, these results are shown in Figure 3.5. The graph and values would change with the temperature of the fluid as the measurements are taken in volume flow rates. As pure water approaches 4 °C the density is at a maximum; therefore, a higher volume flow rate would be recorded than above or below this temperature.

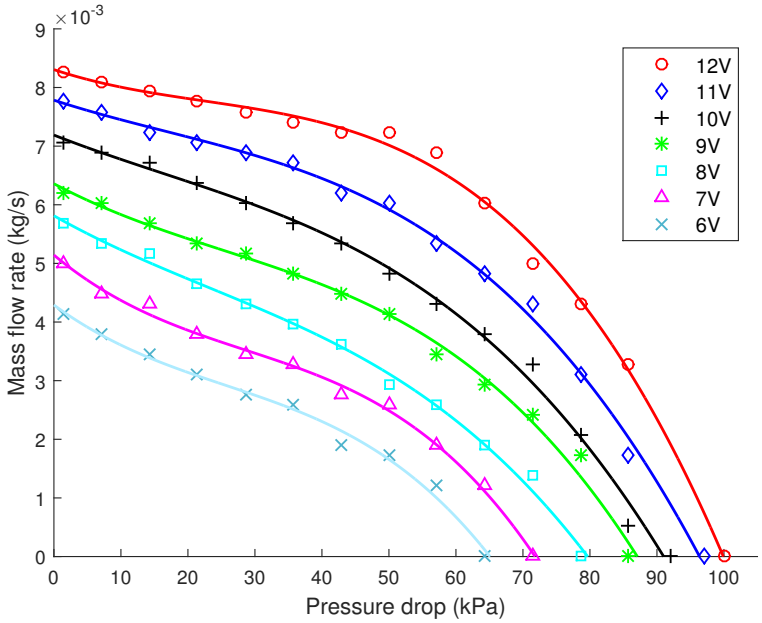


Figure 3.5: Pump curve for 12V series 200 peristaltic pump (Williamson Manufacturing Ltd) at different input voltages.

The errors in the recorded values from the creation of the pump curve are the same as outlined previously: pressure = +/- 0.5 kPa: flow rate = 0.3 g $s^{-1}$.

### 3.3.5 Ice Fraction Measurements

Many methods of recording ice fraction exist, which are discussed in §2.4. Calorimetry was chosen because it offered the best accuracy at low ice fractions and could be integrated with the current set up without creating possible nucleation sites.

Slurry produced during 40 seconds of operation was added to an insulated container holding a measured mass ($\approx$ 0.75 kg) of 35 +/-1 °C water. The cold brine and melting ice caused enthalpy changes, recorded as a reduction in the hot water temperature. Enthalpy changes are found using masses ($m_{hot}$, $m_{slurry}$, $m_{end}$) and temperatures ($T_{hot}$, $T_{slurry}$, $T_{end}$) for the hot water, ice slurry and final combined mixture. Mass of brine can be calculated as the difference between mass of slurry

and ice $m_{brine} = m_{slurry} - m_{ice}$.

$$\begin{aligned} \text{Enthalpy loss from hot water} = {} & \text{Enthalpy to melt ice} \\ & + \text{Enthalpy to heat ice to } 0^{\circ}C \\ & + \text{Enthalpy to heat melted ice} \\ & + \text{Enthalpy to heat brine phase} \end{aligned} \tag{3.1}$$

Equation 3.2 is the derived energy change balance, which is rearranged to make Equation 3.3. Terms $c_{p,ice}$, $c_{p,w}$ and $c_{p,slurry}$ correspond to the specific heat capacity of ice, water and ice slurry brine.

$$\begin{aligned} c_{p,w} m_{hot}(T_{hot} - T_{end}) = {} & m_{ice} h_{s,f} + \\ & 0.5 m_{ice} c(0 - T_{slurry}) + \\ & m_{ice} c_{p,w}(T_{end} - 0) + \\ & (m_{slurry} - m_{ice}) c_{p,slurry}(T_{end} - T_{slurry}) \end{aligned} \tag{3.2}$$

The energy required to heat the ice from slurry temperature ($T_{slurry}$) to ice melting temperature (0°C) was approximated by assuming the temperature of the whole ice increased at the same rate until 0°C. Ice is assumed to melt linearly with T as the ice is heated from $T_{slurry}$ to 0°C. On rearrangement:

$$m_{ice} = \frac{c_{p,w} m_{hot}(T_{hot} - T_{end}) - m_{slurry} c_{p,slurry}(T_{end} - T_{slurry})}{0.5(c_{p,ice} + c_{p,w})(0 - T_{slurry}) + h_{s,f} + c_{p,w}(T_{end} - 0) + c_{p,slurry}(T_{end} - T_{slurry})} \tag{3.3}$$

$$\text{Ice Fraction} = \phi_m = \frac{m_{ice}}{m_{slurry}} \tag{3.4}$$

Average $c_p$ values were used because the value changed little over this range of tem-

peratures. All mass measurements were taken with an Ohause TS4000 precision balance, with 0.01 g resolution, though they can only be considered accurate to the nearest 0.001kg, due to small water drops falling on the balance causing variation in measurements. Temperature readings were taken using a PT100 probe, accurate to 0.1 °C.

Some of the ice data is also presented as mass of ice produced per second. Ice production rate was found using Equation 3.5, where $\dot{m}$ was the flow rate through the pipe and $\tau$ was the time over which the ice slurry measure was collected ($\tau$ =40 seconds).

$$\dot{m}_{\phi_m} = \frac{\int_{\tau}^{0} \phi_m dt}{\tau} \tag{3.5}$$

This equation assumes that ice is shed from the wall and conveyed out at a continuous rate. There are two possible measurements with contributing errors to errors in ice fraction measurements, mass and temperature, 0.001 kg and 0.1 °C. Specific heat capacity, $c_{p,w}$, also changes with the temperature of the water and can be considered another source of error. In the range of measurements taken $c_{p,w}$ could change by +/-20 $\text{Jkg}^{-1}\text{K}^{-1}$. Using this and both the maximum and minimum possible values for all temperatures ($T_{hot}, T_{slurry}, T_{end}$)and masses ($m_{hot}, m_{slurry}$) an average uncertainty in measurement was found to be $\approx$ 1.5%.

Ice production rate ($\dot{m}_{\phi_m}$) is a multiple of flow rate and ice fraction, therefore the errors are also multiplied. The flow rate is a relatively small error compared with ice fraction, therefore the ice fraction error is the only one considered to affect the production rate readings, giving an error of 0.015 x $\dot{m}$.

### 3.3.6 Ice Crystal Measurements

Ice crystal measurements were taken using images of slurry crystals, collected with Zeiss microscope and AxioCam 5 camera with 10x magnification (see Figure 3.6). All images were taken within 10 minutes of ice production to avoid ripening of crystals in the sample. Images produced contained 120 to 160 ice crystals; crystal sizes were broken down into ranges of 50$\mu$m (e.g. 0 - 50$\mu$m)and the number of each counted. All size measurements were taken as the longest visible length of the ice crystal. The mean size is taken as the mean of all these measured values.

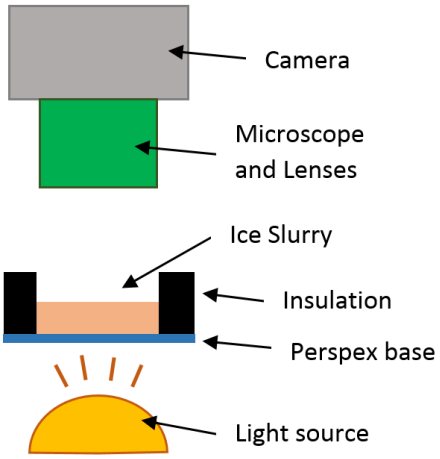


Figure 3.6: Diagram of microscope and set up used to take pictures of ice crystal in slurry.

Pictures were taken at random points close to the centre of a sample and do not necessarily represent the whole sample. Ten pictures of each slurry were taken at different points; only two are used for measurements but they were compared to other pictures to ensure they are representative and not at an area where ice might be melting and therefore have smaller crystals. Another source of error is human mistake, small crystals may be missed. It is estimated that up to +/- 2 crystals were missed or added for each size under 100$\mu$m.

### 3.3.7 Expected Error

A summary of the errors is shown in Table 3.1.

Table 3.1: Table of sources of error in all experimental measurements.

| Source of Uncertainty | Justification | Error (Absolute) |
|---|---|---|
| Mass | Observed repeatability | 1x10$^{-4}$ kg |
| $c_{p,w}$ | Changes with temperature | 20 J kg$^{-1}$K$^{-1}$ |
| Temperature (PT100) | Sensor accuracy | 0.1 °C |
| Temperature (Thermocouple) | Sensor accuracy | 1 °C |
| Ice Fraction | from temp. measurements | 1.5% |
| Brine concentration | Density gradients | 0.01 wt.% |
| Flow rate (measuring cylinder) | Sensor resolution | 3x10$^{-4}$ kg s$^{-1}$ |
| Flow rate (mechanical monitor) | Sensor resolution | 3x10$^{-4}$ kg s$^{-1}$ |
| Pressure | Sensor noise | 0.5 kPa |
| Crystal size distribution | Human error | +/- 2 crystals |

## 3.4 Chapter Summary

Initially, in this chapter, measurement methods have been outlined and reviewed and any sources of error discussed. Ice fraction and production rate calculation using calorimetry was described. This chapter is a useful guide for the following

chapters which refer to the methods outlined here.

# Chapter 4

# Initial Helical Coiled Heat Exchanger Experiments

## 4.1 Introduction

This section outlines initial experimental work conducted to test the HCHX set-up from §3.2. Initially, the theoretical heat transfer through the nylon coil was calculated, thermal resistances from conduction, forced convection and natural convection were compared. Three experimental sets with different concentration of FPD (NaCl) were conducted. Results of each experimental set are presented, including temperature distributions, operation graphs and ice production measurements. Lastly, results are compared to see if production stability or rate changes with concentration of FPD.

## 4.2 Initial Experimental Set-up

As mentioned previously, the work conducted focused around producing ice from a fluid flowing in a pipe immersed in a cold environment. The aim was to eliminate the scraping which is traditionally used by ice slurry generators by slowing down heat transfer and trying to encourage ice to form within the middle of the pipe as much as possible.

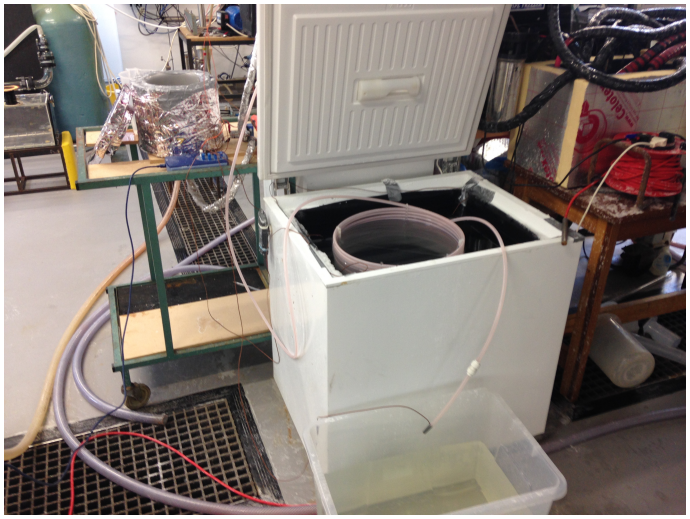

Figure 4.1: Picture of experimental set up used in initial experiments with varying NaCl concentration.

Nylon pipe was used in the setup outlined in §3.2 and Figure 3.1. A picture of the set up taken during an experiment is shown in Figure 4.1. Brine flow through the nylon pipe in initiated before the coils are immersed in the cooling fluid.

## 4.3 Heat Transfer Theory

Equation 4.1 is the basic theoretical equation governing the transfer of heat from the fluid in a pipe to the cold bath it is submerged in (Bergman et al. (2011)). Terms $T_{in}$ and $T_{out}$ are the inlet and outlet temperature from the pipe. Bath temperature, $T_{Bath}$, is assumed to change slowly and therefore be constant for this analysis.

$$\frac{T_{Bath} - T_{out}}{T_{Bath} - T_{in}} = \mathrm{e}^{-\frac{\bar{U}A_s}{\dot{m}c_p}} \tag{4.1}$$

For a circular pipe, with fluid on both sides, the $A_s\bar{U}$ can be found using Equation 4.2. $A_s$ is the surface area of the pipe, it must be combined with $\bar{U}$ as the inner and outer surface area cannot be separated from the term $A_s\bar{U}$. Term $\bar{U}$ represents the overall average heat transfer coefficient.

$$\frac{1}{\bar{U}A_s} = R_{total} = \frac{1}{2\pi L}\left(\frac{2}{D_i\bar{h}_i} + \frac{1}{k_{Pipe}}ln\left(\frac{D_o}{D_i}\right) + \frac{2}{D_o\bar{h}_o}\right) \tag{4.2}$$

The difficult term to find is the local heat transfer coefficients at the boundary between the inner pipe and fluid ($h_i$), and outer pipe and fluid ($h_o$). In reality, the local heat transfer coefficients would change along the length of the coil as fluid temperature changed. Average Nusselt number and average local heat transfer coefficients ($\bar{h}$ and $\bar{Nu}$) are related using Equation 4.3 (Rogers and Mayhew (1980)).

$$\bar{Nu}_D = \frac{\bar{h}D}{k} \tag{4.3}$$

$$\bar{Nu}_D = f(Re, Pr, Ra, De) \tag{4.4}$$

### 4.3.1 Internal Flow

The local heat transfer coefficient for internal flow is dependent on the Reynolds number (Re) of the flow, values of which fall between 300-800 for work in this thesis. For straight pipes, transition from laminar to turbulent flow occurs at $Re_D > 2300$ and $Re_D < 10,000$ (Bergman et al. (2011)), however the pipes used are coiled, which changes the transition Re. Jayakumar et al. (2010) presented correlations for transitional Re number in different coils. For a coil of $D_{coil} = 0.4m$ and $D_i = 0.0067m$ used in this work, the fluid transitions at approximately Re = 4500, showing fluid flow is laminar.

Equation 4.5 is used to calculate Dean number (De) which takes account of the curvature of the pipe. De is 39 to 122 for flow and coil used.

$$De_{D_i} = Re_{D_i}\left(\frac{D_i}{D_{coil}}\right)^{0.5} \tag{4.5}$$

Naphon and Wongwises (2006) present a range of correlations for $Nu$ for internal flow in HCHX; Equation 4.6, presented by Dravid et al. (1971), was found to be the most appropriate for the range of De and Pr (Prandtl number) used.

$$Nu_{D_i} = \left(0.76 + 0.65\sqrt{De_{D_i}}\right) Pr_{D_i}^{0.175} \tag{4.6}$$

This is valid for $5 < De < 2000$ and $5 < Pr < 175$

An approximation for the hydrodynamic and thermal entry lengths ($x_{fd,h}$ and $x_{fd,t}$) was calculated using Equation 4.7 and 4.8.

$$x_{fd,h} \approx 0.05 Re_{D_i} D_i \tag{4.7}$$

$$x_{fd,t} \approx 0.05 Re_{D_i} Pr_{D_i} \tag{4.8}$$

$x_{fd,h}$ ranges from 0.13 to 0.32m, while $x_{fd,t}$ ranges from 1.65 to 4.06m. This entry length is a relatively small section of the 27.4m coil, inside this entry length the heat transfer coefficient and Nusselt number varies with distance from the entrance. For simplicity, it was assumed that $Nu$ in thermal entry length follows the same rule as outside (Equation 4.6). Average $Nu$ ($\bar{Nu}_{D_i}$)) and $\bar{h_i}$ are calculated and shown in Table 4.1.

### 4.3.2 Outer Natural Convection

There is no forced movement of the fluid in the bath, meaning that buoyancy force (natural convection) is the only force moving the fluid away from the outside of the tube. $Nu$ is now a function of the Rayleigh Number (Ra) which is calculated using

Equation 4.9. For a cylinder in fluid, $N\bar{u}_{D_o}$ is found using Equation 4.10.

$$Ra_{D_o} = \frac{g\beta(T_s - T_{Bath})D_o^3}{(\mu/\rho)^2} Pr_{D_o} \tag{4.9}$$

$$N\bar{u}_{D_o} = \left(0.6 + \frac{0.387Ra_{D_o}^{1/6}}{(1 + (0.559/Pr)^{9/16})^{8/27}}\right)^2 \tag{4.10}$$

Valid when $Ra_{D_o} \leq 10^{12}$

The temperature $T_s$ is taken as the average film temperature between the pipe and the bath fluid. The heat transfer coefficient depends only on the fluid properties and is therefore constant, $N\bar{u}_{D_o} = 6.7$. Equation 4.10 is for unobstructed buoyancy convection, in reality, heat conveyed from one pipe in the coil could interfere with heat transfer from another because pipes are close and placed above each other.

### 4.3.3 Thermal Resistance

Equation 4.2 can be split into three different thermal resistances as demonstrated by Equation 4.11.

$$R_{total} = \frac{1}{\pi D_i h_i L} + \frac{1}{2\pi L k_{Pipe}} ln\left(\frac{D_o}{D_i}\right) + \frac{1}{\pi D_o h_o L} \tag{4.11}$$

$$R_{total} = R_{in} + R_{pipe} + R_{out}$$

Table 4.1 shown the values of $R_{total}$ and $R_{in}$ for the range of $Re$ values used, while $R_{out}$ and $R_{pipe}$ stay constant at 0.082 and 0.154. The results demonstrate that $R_{total}$ changes little with $Re_{D_i}$, the dominating resistance to heat transfer is the pipe wall which accounts for 50-54% of thermal resistance.

Table 4.1: Table of theoretical heat transfer coefficients and thermal resistances as Re changes during the experiments.

| $Re_{D_i}$ | $N\bar{u}_{D_i}$ | $\bar{h}_i$ (W m$^{-2}$K) | $R_{in}$ (K/W) | $R_{total}$ (K/W) | $U\bar{A}_s$ (W/K) |
|---|---|---|---|---|---|
| **805** | 11.5 | 994 | 0.048 | 0.284 | 3.53 |
| **735** | 11.0 | 954 | 0.05 | 0.286 | 3.50 |
| **655** | 10.5 | 906 | 0.052 | 0.288 | 3.47 |
| **580** | 9.9 | 859 | 0.055 | 0.291 | 3.43 |
| **510** | 9.4 | 812 | 0.059 | 0.294 | 3.4 |
| **380** | 8.3 | 715 | 0.067 | 0.302 | 3.31 |
| **310** | 7.6 | 656 | 0.073 | 0.308 | 3.24 |

## 4.4 Results and Discussion

### 4.4.1 Experiment Settings

Table 4.2: Table outlining variable used in each experiment set (a), (b) and (c).

| Variable | Experiment set (a) | Experiment set (b) | Experiment set (c) |
|---|---|---|---|
| Inlet NaCl concentration | 3.5 wt.% | 5 wt.% | 8 wt.% |
| Freezing temperatures ($T_f$) | -2.1 °C | -3.05 °C | -5.08 °C |
| Bath Temperature range | -15 to -5 °C | -16 to -6 °C | -17 to -7 °C |
| Number of experiments | 58 | 55 | 60 |
| Flow velocities (m s$^{-1}$) | 0.21, 0.19, 0.17, 0.15, 0.13, 0.12, 0.1, 0.08 | | |
| Residence time (s) | 130, 144, 161, 183, 211, 228, 274, 322 | | |
| Bath NaCl concentration | 20 wt.% | | |
| Pipe material | Nylon | | |
| Pipe length | 27.4 m | | |
| Pipe diameters | 0.0067 m Inner, 0.0095 m Outer | | |
| Experiment length | 1000 seconds | | |
| Bath brine volume | 115 litres | | |
| Equipment | Outlined in §3.2 | | |

Weaker brine solution at constant room temperature (20°C) was pumped through the submerged coil at a prescribed flow rate for 1000 seconds. This was repeated with eight different flow rates, keeping all other variables constant. Table 4.2 details

the variables kept the same and those changed during experiments.

### 4.4.2 Outcomes Observed

For each concentration, 55-60 experiments were conducted, and three categories of experimental outcome observed. Outcomes included:

1. **Pipe blockage** - Ice slurry was produced but the pipe blocked; the experiment was stopped (Figure 4.2 (a)).

2. **Ice slurry production** - Ice slurry was produced, the experiment continued for 1000 seconds and three ice fraction measurements taken at 300, 600 and 900 seconds (Figure 4.2 (b)). The degree of supercooling was between 4 to 6 °C, similar to that observed by previous authors working with tap water (Gilpin (1977) and Zeng et al. (2015)). When ice formed, the outlet temperature rose to just below the freezing temperature ($T_f$). It should be acknowledged that this indicates that fluid was nucleating on particulates in the tap water not on the wall.

3. **No ice formed** - Often the fluid was supercooled below its freezing point, though no formation of ice was observed. Experiments were stopped after 500 seconds; from tests it was observed that no ice would form after the first 500 seconds, due to increasing bath temperature (Figure 4.2 (c)).

These three outcomes are similar to those outlined in Thomason (1987), though ice production was stable and did not oscillate from blocked to unblocked as noted in their work with metal pipes. It is unclear if ice nucleates on the surface of the pipe or particulates in the tap water. Appendix B discusses the mechanics of possible layer growth further.

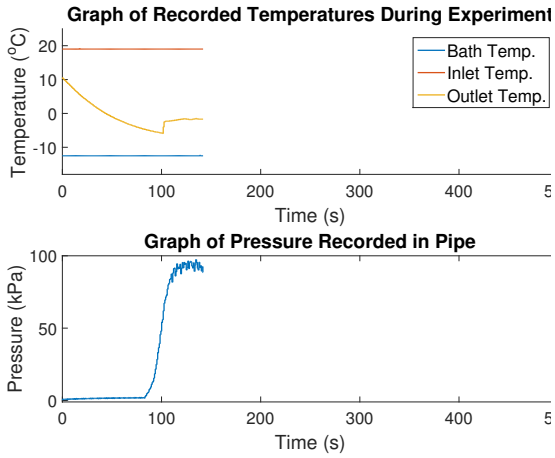


(a) Pipe blocked

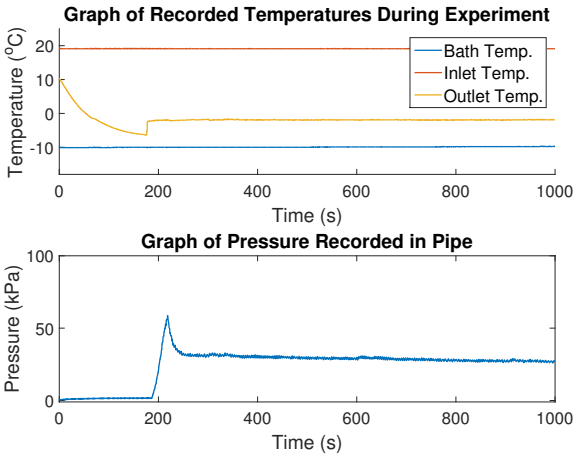


(b) Ice slurry produced

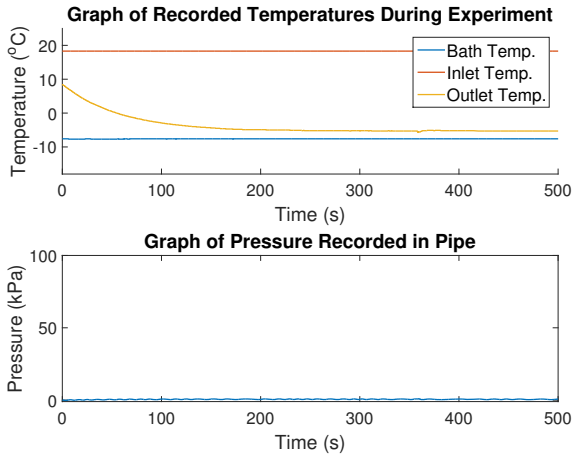


(c) No ice slurry produced

Figure 4.2: Graphs displaying readings from three experiment outcomes with 5wt.% NaCl brine pumped at 0.0056kg $s^{-1}$ (0.15m $s^{-1}$, 183 seconds residence time). Figure (a) displays an experiment where the pipe became blocked; (b) shows one where ice was produced; (c) no ice is being produced.

A spike in outlet temperature and inlet pressure is observed when ice begins to form, similar to experiments in pipes with static cooled fluid (see §6.5). The temperature and pressure spike are observed close together, either at or just after the residence time. Pressure and temperatures observed for each outcome in Figure 4.2 are discussed below:

**Pipe blockage** - With low flow rates, allowing inlet brine to spend longer in the coil, and/or a high driving temperature difference, ice forms quickly. Two different types of blockages were noted:

- Type 1: the pipe blocked within 10 seconds of ice nucleation occurring. This is likely caused by dendrite ice crystals forming quickly across the tube (discussed further in §4.4.5), bonding to the surface and leading to a high-pressure spike, as seen in Figure 4.2 (a).

- Type 2: a drop in flow rate above $3x10^{-4}$ kg $s^{-1}$ was observed. Fluid is cooled for longer, thereby further increasing fluid ice fraction and force needed to convey it. Blockages occur when this force is above that which can be supplied by the pump.

**Ice slurry production** - Brine suffers sufficient enthalpy loss to form ice from the solution. However, the rate of ice formation is insufficient to stop the flow or ice does not bond effectively to the tube wall. This leads to ice being conveyed away by the remaining fluid flow. A sharp pressure rise is observed, (when the supercooled fluid initially nucleates) which drops quickly when slurry is conveyed out of the outlet. Outlet temperature rises to just below the freezing temperature of the brine, leading to an increased temperature difference driving further nucleation which can lead to a delayed blockage. A drop in flow rate was observed; this drop was less than the error in flow rate measurements mentioned previously of $3x10^{-4}$ kg $s^{-1}$ so is difficult to analyse. Stable ice production continues when ice slurry formation and expulsion rates are similar. Falling pressure after the initial spike indicates that ice fraction could be decreasing slightly throughout the experiment due to the increasing bath temperature.

**No ice formed**- The brine is supercooled and the pipe walls are cold, but there is

not sufficient supercooling to drive crystallisation, though fluid is still supercooled. The addition of ice particles could lead to nucleation of the supercooled brine and low ice fraction slurry (<6 % from previous authors). Many other researchers have used different techniques to initiate nucleation of a supercooled flow of aqueous solution to make ice slurry (Bedecarrats et al., 2000; Castaing-Lasvignottes et al., 2006; Tanino, 2000).

### 4.4.3 Operation Region

For each FPD concentration an operation graph was created of the supercooling temperature ($T_{Bath} - T_f$) against Reynolds Number (Re), displayed in Figure 4.3. Properties such as dynamic viscosity would change with temperature and ice formation, therefore Re presented is for the inlet fluid at room temperature.
Reynolds number:

$$Re_{D_i} = \frac{4\dot{m}}{\pi D_i \mu} \tag{4.12}$$

Freezing temperature ($T_f$), varies with concentration, $T_{Bath}$ changes with each measurement. The final graphs are displayed on Figure 4.3 (a), (b) and (c).

Figure 4.4 displays a diagram of the three regions created by the different operation outcomes and where they are found on the operation graphs in Figure 4.3.

The operation graphs created, and displayed, in Figure 4.3, demonstrate that ice slurry can be created by supercooling NaCl aqueous solutions in nylon pipes, without blockages becoming evident. The three different conditions observed were similar to those observed by Thomason (1987), except the process appeared to be stable and did not lead to consistent blocking.

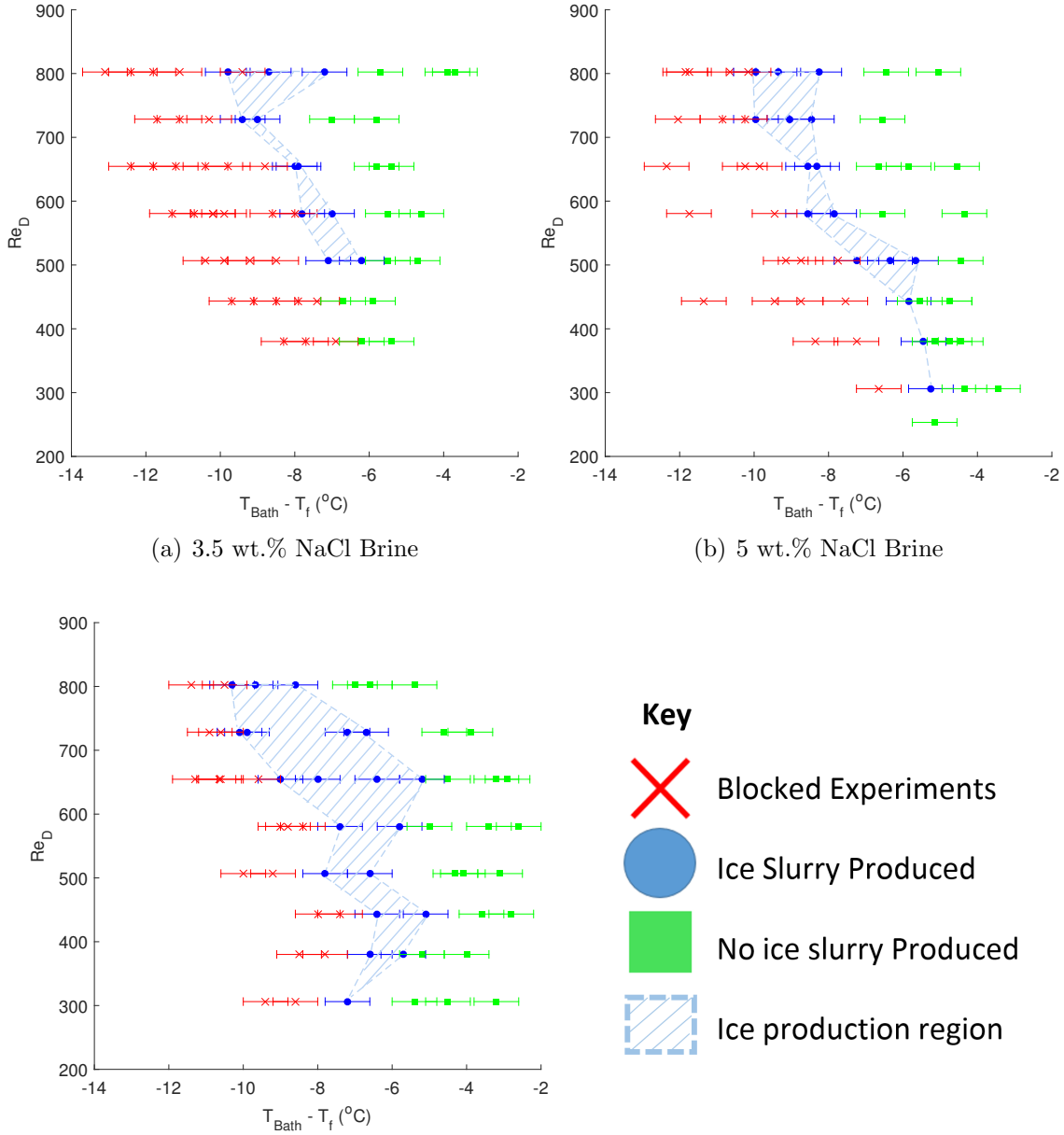


(a) 3.5 wt.% NaCl Brine

(b) 5 wt.% NaCl Brine

(c) 8 wt.% NaCl Brine

Figure 4.3: Operation graph for three brine concentrations, with Reynolds number (Re) against $T_{Bath} - T_f$. The concentration for each can be seen below the graph for (a), (b) and (C).

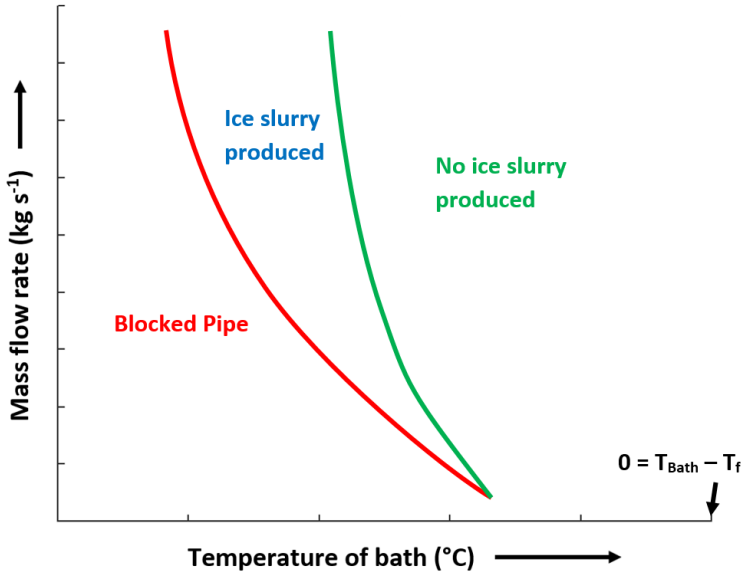


Figure 4.4: Graph demonstrating the three different conditions produced and how they vary with bath temperature and flow rate

All operation regions show a similar pattern, initially, they start out at their widest at high flow rates and appear to get narrower as the flow rate gets slower. At lower flow rates the pump had a lower cut off pressure, as shown by the pump curve on Figure 3.5, this is the likely reason for the narrowing of the production region. This narrowing effect was smaller with higher NaCl concentrations, probably due to the added FPD slowing down ice growth and reducing adhesion strength.

Increasing the NaCl concentration of the fluid decreases the freezing point and reduces ice growth rate for a set bath temperature, as discussed in §2.4. This makes the process easier to control and prevents blockages, which is demonstrated by the larger ice production region on 4.3 (c) and smaller region on 4.3 (a). However, increasing the NaCl concentrations means lower bath temperatures, $T_{Bath}$, are required. Demonstrated by the similar range of $T_{Bath} - T_f$ for all NaCl concentrations and a $T_f$ that decreases with increasing concentration. More cooling is required to reach the same $T_{Bath} - T_f$ for higher concentration FPD fluid. A user would have to

balance between efficiency and a wider operation range when selecting the starting FPD concentration.

Another factor which needs to be considered is the contact angle. Zeng et al., 2015 demonstrated that with changing NaCl concentration can increase $\theta$ from a minimum at 3-4wt.% to a maximum at around 10wt.%. The material used in this study was porous cement and very different from the nylon used here but it could explain the different operation region widths especially at low Re.

The fluid phase FPD concentration in the slurry produced will increase with ice production; the fluid phase could be recirculated through the nylon coil to generate more ice. The stability of the method may be increased in each recirculation of the fluid due to the higher FPD concentration. This has been explored further in Chapter 8.

### 4.4.4 Ice Fraction

The calorimetry process outlined in §3.3.5 was used to calculate ice fraction, $\phi_m$, and ice production rate, $\dot{m}_{\phi_m}$. Ice fraction (Figure 4.5 (a)) and production rates (Figure 4.5 (b)) were plotted against $T_{Bath} - T_f$. The $\phi_m$ values are the average of the three recordings taken during each experiment.

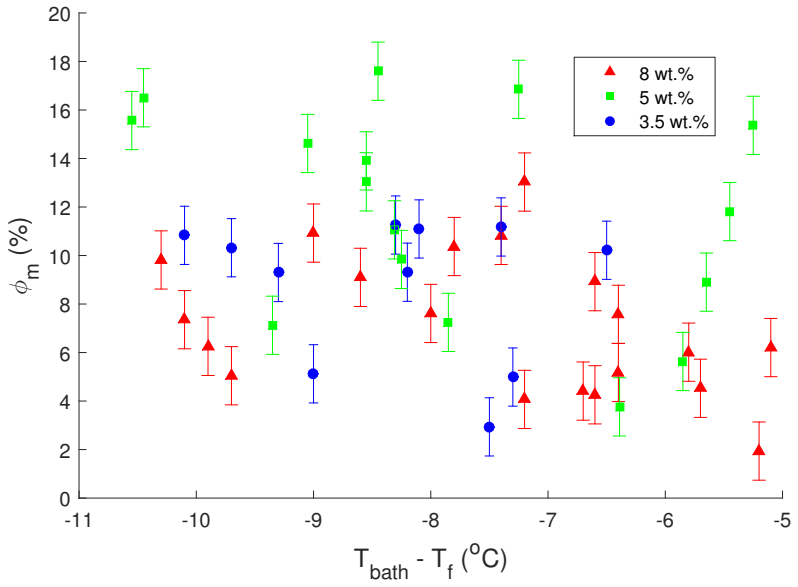


(a) Ice fraction ($\phi_m$)

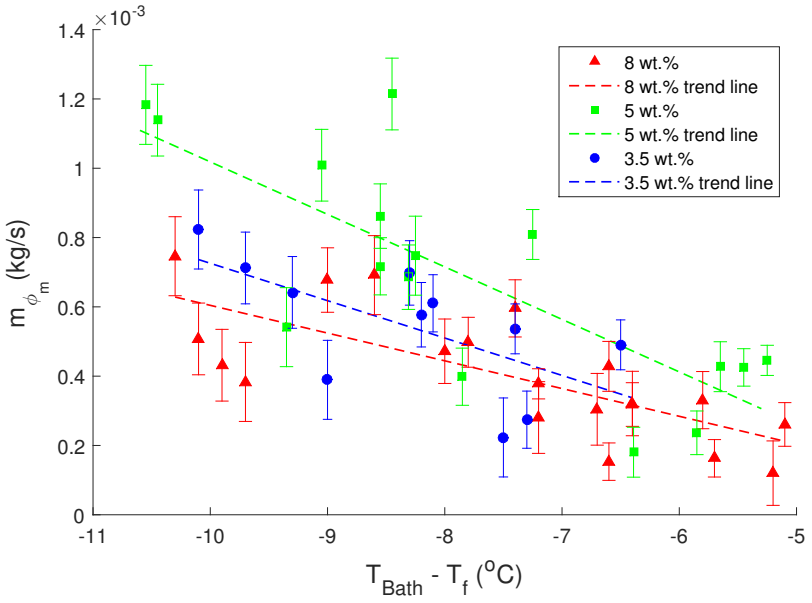


(b) Ice production rates ($\dot{m}_{\phi_m}$)

Figure 4.5: Graphs of average ice fraction (a) and average ice production rates (b) against $T_{Bath} - T_f$ for initial experiments with varying brine concentration.

The highest ice fractions were achieved at low flow rates and low temperatures; in reality, this is unsustainable as this region lies in the area where blockages occur. Figure 4.5 (a) and (b) display average $\phi_m$ and $\dot{m}_{\phi_m}$ for all the concentrations tested

versus $T_{Bath} - T_f$. The optimum region for both graphs is the top right, where high ice fractions and production regions are achieved at warmer temperatures. The highest ice fractions were measured with 5 wt.% brine across all $T_{Bath} - T_f$ values, see Figure 4.5 (a). Regression lines have been plotted on Figure 4.5 (b) to show the average ice production rate at different temperatures. Ice production rate for all FPD concentrations increases with decreasing temperatures ($T_{Bath} - T_f$). A higher line corresponds to the higher average ice production rate, 5wt.% has the highest $\dot{m}_{\phi_m}$ for similar $T_{Bath} - T_f$ out of the three concentrations tested, followed by 3.5wt.% and then 8 wt.%.

The highest ice production rates and ice fractions were observed with 5wt.% brine. At the higher NaCl concentration, 8wt.%, ice growth is slowed by the added NaCl (FPD) in the fluid, leading to lower ice fraction and production rates. The highest ice fractions should therefore have been achieved with 3.5wt.% brine. However, the lower brine concentrations result in fast ice growth, leading to high ice fraction slurry produced quickly, which blocks the pipe and/or slows the flow rate. A higher maximum pump pressure to move higher ice fractions could lead to the higher $\dot{m}_{\phi_m}$ and $\phi_m$ with 3.5wt% brine instead of 5wt.%. Makkonen (2012) noted that ice adhesion strength decreased with increasing salinity especially for lower concentrations up to 5wt.%. This could be a contributing factor for why the highest ice production is seen at 5wt.% brine.

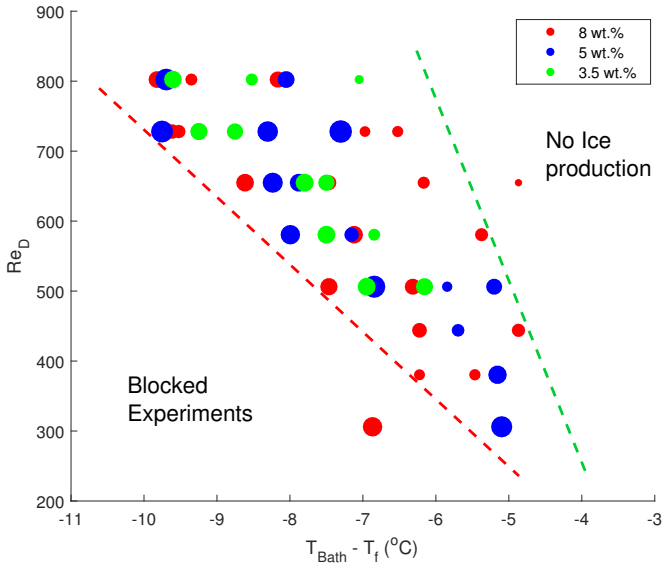


Figure 4.6: Graph of ice fraction production regions for 3.5, 5 and 8wt.% brine, point size indicates ice fraction recorded. The red dotted line is the limiting point before blockages occur and the green shows the limitings point before no ice production.

In Figure 4.6 points are plotted for all concentrations showing where ice was produced, ice fraction is represented by the size of the point (larger points represent larger ice fractions). It is apparent that the larger ice fractions form towards low flow rates and $T_{Bath} - T_f$ values. A dotted line has been added to Figure 4.6 to show a possible limiting section, beyond which blockages are known to occur. Staying close to this line is likely to produce the maximum possible ice fraction and has been explored further in §5.3. The graph also highlights the differences in production regions discussed previously.

### 4.4.5 Pressure Readings

As ice forms, high pressure spikes occur with a simultaneous rise in the outlet temperature. Equation 4.15 is derived to approximate the starting ice fraction ($\phi_{m,start}$) created from the supercooled fluid. Phase change is assumed to happen instantaneously, with no additional heat transfer to the fluid. Term $T_n$ represents the

outlet temperature when nucleation occurs. Specific heat capacities for brine and ice ($c_{p,brine}$ and $c_{p,ice}$) are taken at $T_f$ and assumed constant.

$$\begin{aligned}\text{Enthalpy to heat fluid to } T_f = \text{Enthalpy to create ice} \\ + \text{Enthalpy to heat ice to } T_f\end{aligned} \tag{4.13}$$

$$c_{p,brine}\dot{m}_{brine}(T_f - T_n) = \dot{m}_{ice}h_{s,f} + \dot{m}_{ice}c_{p,ice}(T_f - T_n) \tag{4.14}$$

$$\phi_{m,start} = \frac{\dot{m}_{ice}}{\dot{m}_{brine}} = \frac{c_{p,brine}(T_f - T_n)}{h_{s,f} + c_{p,ice}(T_f - T_n)} \tag{4.15}$$

Outlet temperature at the time of nucleation ($T_{out}$) and the temperature of nucleation ($T_n$) are not the same. The value of $T_n$ would be lower and at an unknown (and unmeasured) nucleation point within the coil. For simplicity, $T_n$ has been assumed to be $T_{out}$ at nucleation as this would be the coldest point in the coil. Brine of 5 wt.% concentration was supercooled by an average of 4.8 °C before nucleation, theoretical supercooling by this amount would lead to an initial ice fraction of 5.6%. This is too low to be the cause of the high pressure spike seen in experiments. Even supercooling by 7°C ($T_f - T_n = 7°C$) would only produce an ice fraction of 8.1%.

The peak of the pressure spike was not found to correlate to the temperature of the bath or the ice fraction. Previously in §2.3.7 it was identified that ice fractions needed to reach above 15% to have a noticeable increase in pressure loss. However, Gilpin (1977) conducted experiments at similar supercooling temperatures and identified that a dendritic growth of 5-6% ice fraction produced a pressure drop of 10-30Kpa $m^{-1}$. Assuming a similar effect is seen in experiments presented in this section, the pump flow could be stopped if there is 3 m of supercooled fluid nucleating in the pipe. The pipe used in the experiments in this section is also smaller

than that used by many authors discussed in §2.3.7, assuming ice crystal sizes are similar this could affect the pressure drop observed. For example, 1mm ice crystals could cause a larger pressure loss in a smaller 6.7mm pipe than a large 25mm pipe.

Pressure loss recorded after the initial high pressure spike was plotted against ice fraction produced for all concentrations tested (Figure 4.7).

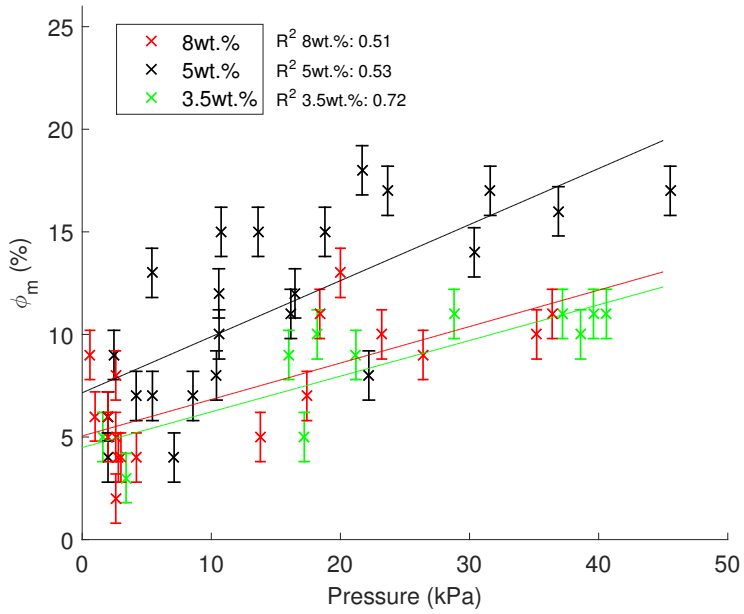


Figure 4.7: Average pressure reading after initial pressure spike against ice fraction produced for different concentrations.

There is a correlation between pressure reading and the ice fraction produced, though it is weak due to variance in the data. Previous work on pressure drop from pumping ice slurry uses constant temperature environments or heats the slurry during experiments. There is some variation in measurements, though not as significant as variance seen in these results. The increase in variance could be because of a relationship with flow rate and temperature which is not taken account of, or sensor error.

### 4.4.6 Ice Crystal Size

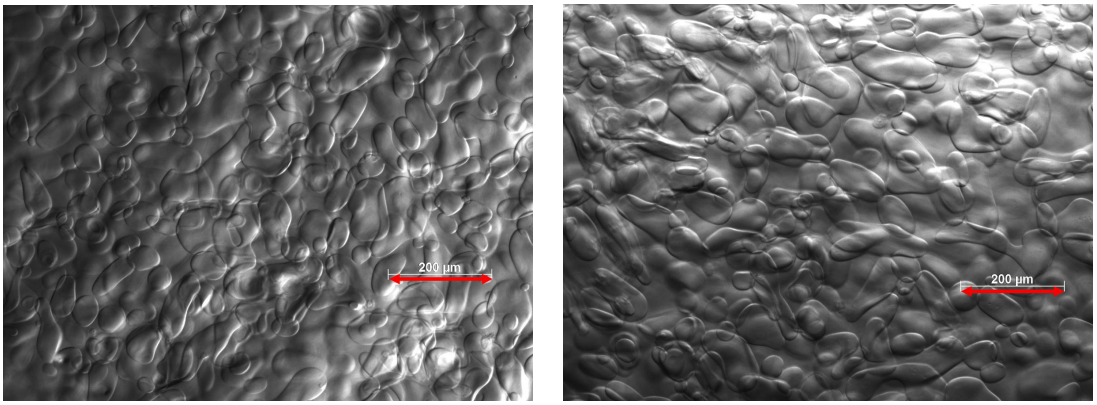


(a) Nylon HCHX (b) Scraped Surface

Figure 4.8: Pictures taken with 10X magnification of ice slurry produced with nylon HCHX generator, (a), scraped surface generator, (b). Each photo is 1.1mm wide and 0.77mm high, red arrows show a 200$\mu$m scale.

Measurements of ice crystal size were taken for ice produced using nylon HCHX and a scraped surface generator (Ziegra 70kg ice machine) using the method outlined in §3.3.6. Inlet brine of 5wt.% was used and all measurements taken within 15 minutes of ice generation. Example of pictures of ice slurry taken and used for measurement can be seen in Figure 4.8. Nylon HCHX has the lower mean and max size crystal found but only slightly lower than the scraped surface generator. Figure 4.9 shows the distribution of crystal sizes, both have the larger quantities of crystals at smaller crystal sizes. Scraped surface has the larger number of crystals above 100$\mu$m while nylon has the largest number below 100$\mu$m. The data shows that the nylon HCHX produces smaller crystals than the scraped surface generator tested, even when the maximum predicted error in counting crystal size is taken into account. Both generators produced crystal sizes below those generated in fluidized bed generators, which produced crystals up to 180-200$\mu$m (Van der Gun et al. (2001)).

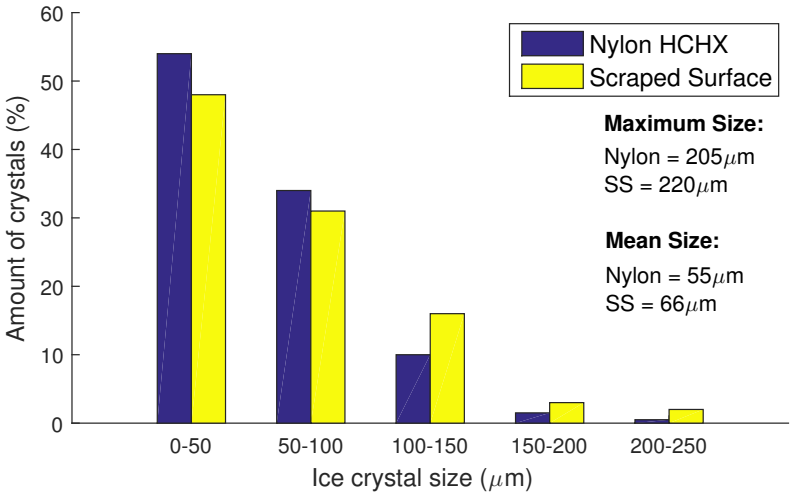


Figure 4.9: Histogram of crystal sizes measured from ice slurry from a nylon HCHX and a scraped surface generators.

### 4.4.7 Efficiency Comparison

Previous experiments conducted by A.N. Leiper et al. (2013) compared scraped surface generators to bulk ice production methods as discussed in §2.5.2. Total energy savings of up to 20% were found due to the increase in evaporation temperature from -30°C in scraped surface generators to -10°C for bulk production.

The evaporation temperature of a scraped surface generator was tested. The surface temperature of the inlet evaporation coil was measured using thermocouples and was found to be -21 +/-1°C. The actual evaporation fluid temperature would be lower, but this provides a good approximation.

As in A.N. Leiper et al. (2013), Carnot Coefficient of System Performance ($COP_{Carnot}$) was used as an initial indication of efficiency as it represents the theoretical highest amount of cooling possible per unit work, based on the $T_L$ and $T_H$ being the hot (condenser) and cold (evaporator) temperatures of the refrigeration fluid.

$$COP_{Carnot} = \frac{T_L}{T_H - T_L} \tag{4.16}$$

In this work the $T_H$ was taken as the ambient air temp +10°C ( 30°C) and $T_L$ as the evaporator fluid temperature ($T_{Bath}$ in nylon HCHX). $COP_{Carnot}$ for scraped surface and fluidised bed (value taken from Meewisse and Infante Ferreira (2002)) are shown in Table 4.3.

Table 4.3: Table comparing $COP_{Carnot}$ for two different ice slurry generators. All values have been rounded to nearest K.

| Method | $T_L$ (K) | $T_H$ (K) | $COP_{Carnot}$ |
|---|---|---|---|
| Scraped surface (SS) | 252 | 303 | 4.9 |
| Fluidised bed | 263 | 303 | 6.8 |

If 5wt.% ($C_{Bulk} = 0.05$) brine is used for the initial inlet fluid then Equation 2.13 can be rearranged.

$$C(T) = \frac{0.05}{1 - \phi_m} \tag{4.17}$$

Equation 4.17 shows the remaining brine concentration as ice forms. This can be converted to a fluid temperature ($T_{out}$) using Equation 2.14. The results showed that $T_{Bath} - T_f$ appears to be independent of the FPD concentration, ice slurry can be formed between $T_{Bath} - T_f = -10$ and -6 °C. Assuming this holds true for higher FPD concentrations then the $T_{Bath}$ (or $T_L$) can be found for any ice concentration. This value has been calculated for ice fraction up to 70% made from 5wt.% brine feedstock solution (see Table 4.4). The value of $T_{Bath}$ was taken as $T_{out}$ - 8 °C. Carnot COPs are also calculated for the HCHX when different ice fractions are produced.

Table 4.4: Predicted outlet temperatures for different slurry ice fractions and required bath temperatures needed for Nylon HCHX with 5wt.% feedstock solution.

| $\phi_m$ (%) | **C(T) (wt.%)** | $T_f$ (°C) | $T_{Bath}$ (°C) | $COP_{Carnot}$ |
|---|---|---|---|---|
| 10 | 5.6 | -3.4 | -11.4 | 6.3 |
| 20 | 6.3 | -3.9 | -11.9 | 6.2 |
| 30 | 7.1 | -4.5 | -12.5 | 6.1 |
| 40 | 8.3 | -5.3 | -13.3 | 6 |
| 50 | 10 | -6.6 | -14.6 | 5.8 |
| 60 | 12.5 | -8.6 | -16.6 | 5.5 |
| 70 | 16.7 | -12.7 | -20.7 | 5.0 |

If the bath fluid was replaced by primary refrigeration fluid, then this method could be more efficient than scraped surface generators for low fraction slurry production. It should also be noted temperatures as high as -10°C were recorded by some authors for scraped surface generators (Stamatiou et al. (2005)). Fluidised bed generators also produced similar ice fractions with warmer refrigeration temperatures. However, neither of these methods would prove suitable for hygienic ice slurry production which would require new sterile parts for each use.

It should be noted that the COP is only a theoretical efficiency and does not take account of extra work such as for pumping. The COP is also a maximum theoretical possible value for the whole system, in practice, it would be much lower. It is likely that implementing this method in a HCHX generator could require lower $T_L$ in the evaporator than those used in experiment refigeration bath.

Only the energy from refrigeration has been considered here. It should be noted that approximately 5% (400-600W in some studies X. Liu et al., 2019) of the energy use in SS generators goes to scraping power, while the pumps used here are only small 5W pumps.

## 4.5 Conclusion

The primary aim of this work was to investigate the viability of using nylon pipe in a HCHX arrangement to generate ice slurry from supercooling. A range of different temperatures, flow rates and FPD concentrations have been tested. It is unclear if initial ice nucleation occurs on the pipe wall or particulates found in the tap water. Operation regions were successfully identified for temperatures and flow rates with different concentrations. The regions indicated that higher brine with higher FPD concentration produced wider operation regions but required lower $T_{Bath}$ with lower COP.

The results from this work have indicated that ice will block conduits if the heat removed (heat flux) at the cold surface is sufficiently large. Blockages are prevented in this method by careful control of bath temperature and flow rate to ensure the right amount of heat transfer occurs. Too much heat transfer can cause ice to grow quickly and block the pipe, too little and no ice is produced. The careful control required could impede the reliability of this method.

Previous work has proved that using low surface energy and roughness pipe material produces a less favourable surface for ice to form on or adhere to. Nylon has proved effective, especially compared to metal used in previous work by Thomason (1987) and H. Wang et al. (2014). One challenge to overcome is the low ice fraction that can be produced, this can be maximised by running the generator at the slowest speeds or lowest temperatures in the operation region. However, a further separation and recirculation of the remaining fluid component would be required for ice fractions above 20%. Recirculating the fluid phase would increase the stability of the method as the operation regions became wider as FPD concentration increased. However,

the maximum ice fraction is reduced at higher FPD concentrations. A pump with a higher operating or maximum pressure head could also increase the operation region and ice fraction possible.

Theoretically energy savings could be possible with this method over SS generators tested here, due to the warmer evaporation temperatures, though only at low ice fractions. More efficient modern SS generators using warmer refrigeration temperatures could be more efficient. To validate if energy savings are possible a prototype generator using refrigeration fluid and a refrigeration cycle would be required (instead of cooled brine as a refrigerant).

Pipes used throughout this work are cheap and could be easily replaced for different fluids to avoid the need for thorough cleaning between uses.

## 4.6 Chapter Summary

- Ice slurry was successfully produced using a nylon HCHX in a range of temperatures and flow rates. Ice formed by heterogeneous nucleation but it is unclear if it is formed on particulates in the flow or on the cold inner wall.
- Three outcomes were observed during experiments: the pipe blocked with excessive ice growth, ice was produced, or no nucleation occurred and the fluid was only supercooled.
- Operation graphs were created showing conditions in which ice could successfully be produced. The widest operation ranges were achieved with higher concentration inlet brine (8 wt.%), although lower $T_{Bath}$ temperatures were required for these FPD concentrations.

- The highest ice fractions and production rates were achieved with 5 wt.% inlet brine.
- Higher $COP_{Carnot}$ and hygienic ice slurry production could be achieved with this method over scraped surface generators, though at this stage of development not with the same reliability.

# Chapter 5

# Increasing Ice Fraction

A series of experiments was designed to increase the ice fraction produced in the experiments outlined in Chapter 4. Methods including, reversing flow direction, changing coil orientation and flow rate control were explored.

## 5.1 Reversed Flow

### 5.1.1 Introduction

It is apparent, that submerging a warm coil in a cold refrigerant bath leads to a temperature distribution within the bath. Buoyancy forces cause the heated refrigerant to rise, creating a temperature stratification. Currently during experiments, warmer fluid enters at the top and colder fluid exits at the bottom, leading to a large temperature difference between top and bottom. Reversing the flow will likely reduce the size of this difference, leading to a more uniform temperature increase throughout the refrigerant. These experiments aim to investigate if reversing the flow direction improves ice slurry fraction (or production rate).

### 5.1.2 Experimental Set-up

An identical set up was used to that outlined in §3.2 with the flow reversed to bottom moving up (BMU) rather than the original top moving down (TMD) direction. See Figure 5.1 for diagrams and pictures of both TMD and BMU set up.

Thermocouples were placed at different depths (0.09m apart) within the bath to obtain the temperature distribution throughout the experiment.

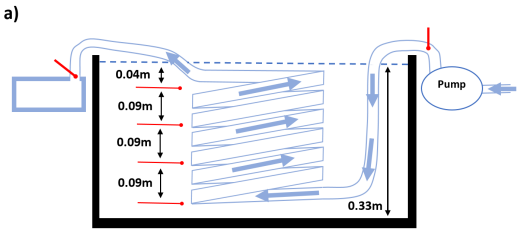


(a) Diagram of BMU

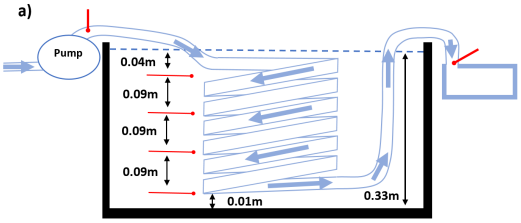


(b) Diagram of TMD

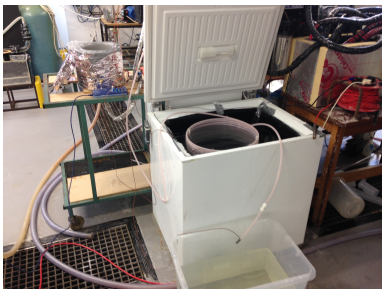

(c) Diagram of TMD

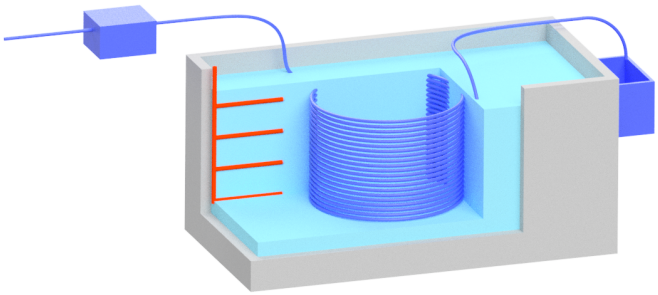

(d) CAD model

Figure 5.1: (a) Diagrams of BMU, (b) diagram of TMD, (c) picture and (d) a CAD model of the experiments. Coil of nylon pipe is submerged vertically in a bath of cold brine. Thermocouple locations are shown in red on (a),(b) and (d).

### 5.1.3 Results and Discussion

Experiments were conducted for a range of different flow rates and temperatures (similar to the ones used in Chapter 4) each for 1000 seconds. Brine of 5 wt.% NaCl was the inlet fluid, because it was identified as the optimum one in the previous chapter. The same three outcomes were observed: ice slurry production with pipe blocking, ice slurry produced without blocking, and no slurry production. Where

ice slurry was produced, ice fraction measurements were taken using calorimetry.

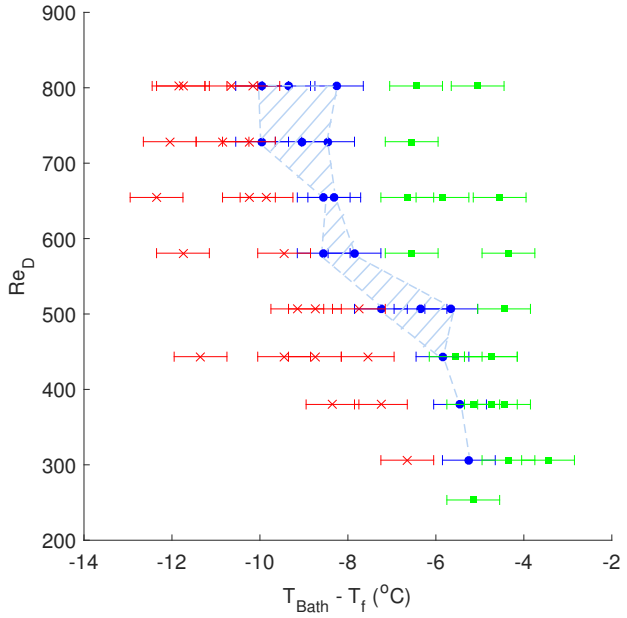


(a) TMD

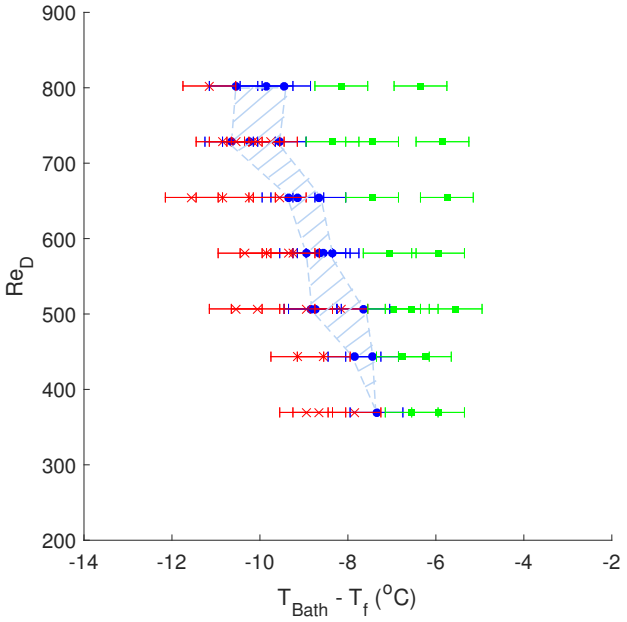


(b) BMU

Figure 5.2: Operation graph of Re number against $T_{Bath} - T_f$ for original TMD flow (a) and the new BMU flow (b) in vertical coiled nylon pipe with 5 wt.% NaCl brine. Blockages are represented by red x, ice production by blue circles, and no ice formation by green squares.

The operation region created for the reversed BMU flow is shown in Figure 5.2 (a), with the original TMD in (b). The TMD data is from the original experiments conducted in §4.4.

The operation regions produced are very similar, both show a narrow band of temperatures where ice is produced without blocking. With the BMU flow (Figure 5.2 (b)) the range appears smaller. Around Re = 700 for BMU, blockages occur between experiments where ice was produced, showing it is harder to find clear separation between the two regions. The original TMD flow appears to have a wider operation region but this is likely to be because the original points were taken slightly further apart. Future experiments could be improved by taking measurements at the same $T_{Bath}$ values to make differences clearer. Both regions also fall in similar temperature ranges for ice production, though ice slurry was produced with TMD at warmer bath temperatures above -6 °C = $T_{Bath} - T_f$ which was not possible with BMU.

Ice fraction measurements taken were plotted on Figure 5.3 (a) and the average $\dot{m}_{\phi_m}$ in Figure 5.3 (b), versus $T_{Bath} - T_f$.
For the graphs in Figure 5.3 (a) and (b) the optimum conditions are high ice production and ice fractions at warmer temperatures (top right corner of the graph). The highest ice fraction was achieved with BMU, though similar fractions were achieved at warmer $T_{Bath} - T_f$ values with TMD. Similarly, with $\dot{m}_{\phi_m}$ in Figure 5.3 (b), comparable readings are observed at warmer $T_{Bath} - T_f$ values with TMD. This indicates that TMD is the better of the two flow directions for producing ice efficiently.

For each experiment the temperature inside the bath was measured at different depths, as shown in Figure 5.1. Two graphs of the temperature profiles are shown in Figure 5.4 for TMD and BMU.

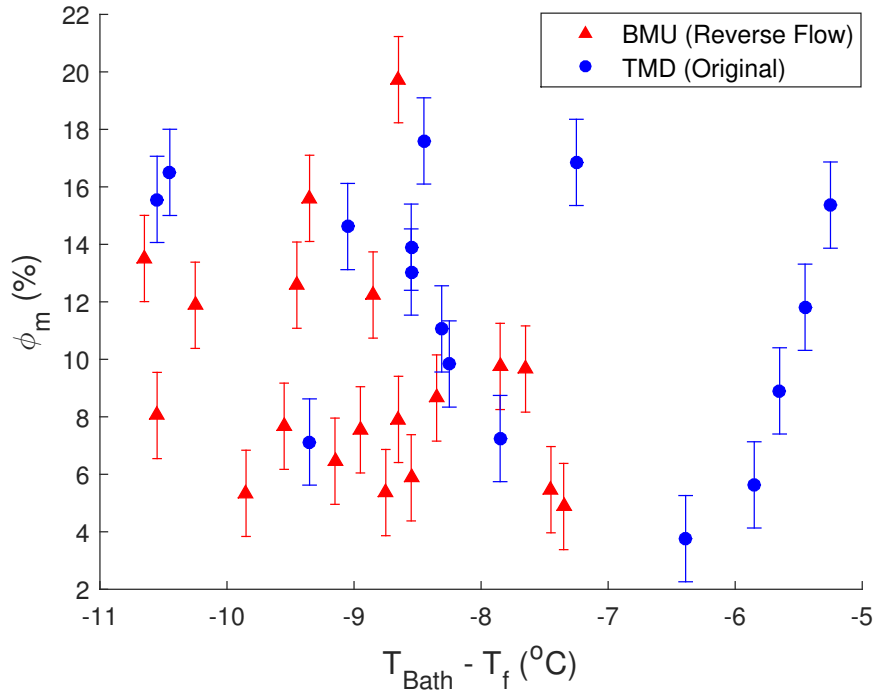


(a) Ice fractions produced ($\phi_m$)

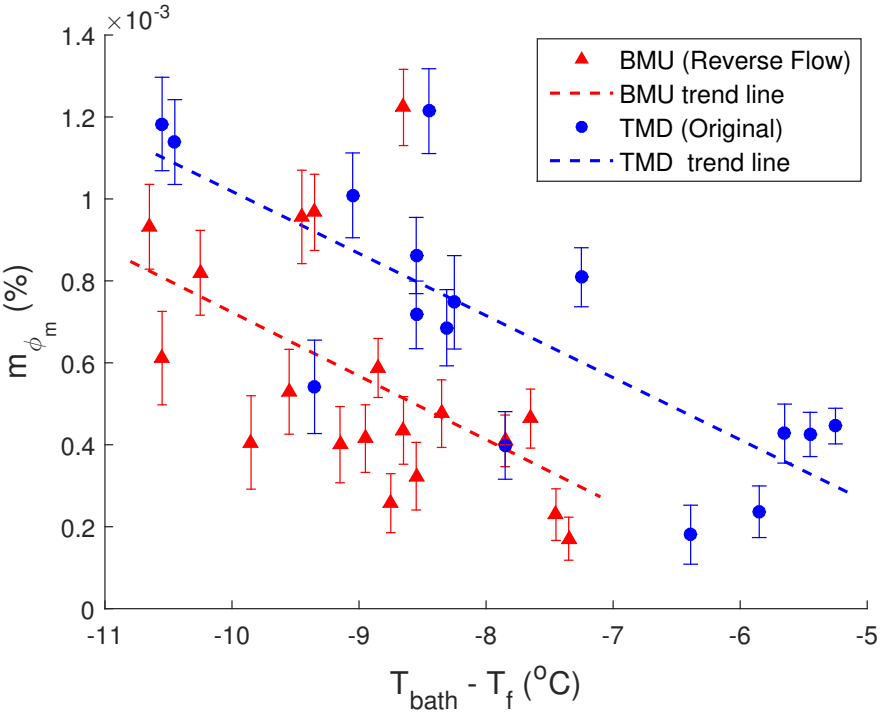


(b) Ice production rate ($\dot{m}_{\phi_m}$)

Figure 5.3: Graphs of ice fraction, (a), and ice production rate, (b), against $T_{Bath} - T_f$, for all TMD and BMU experiments.

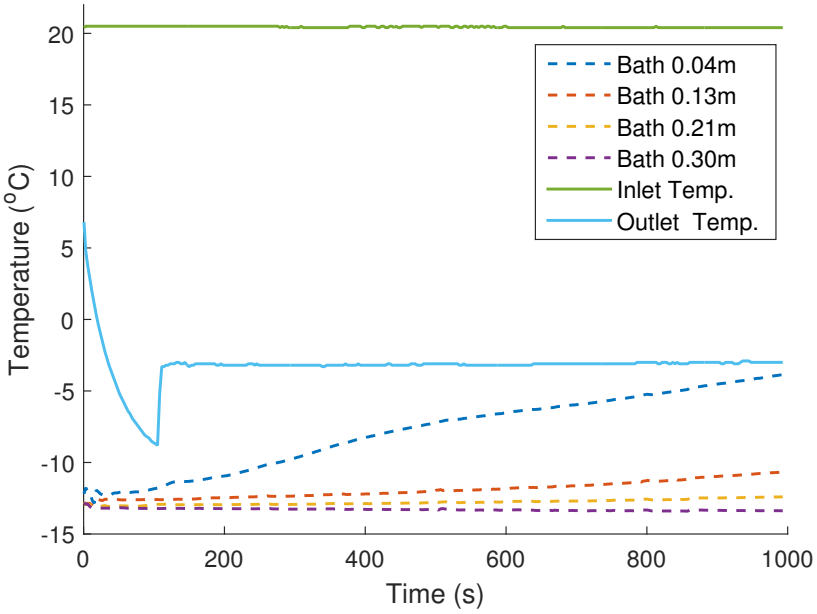


(a) TMD temperatures

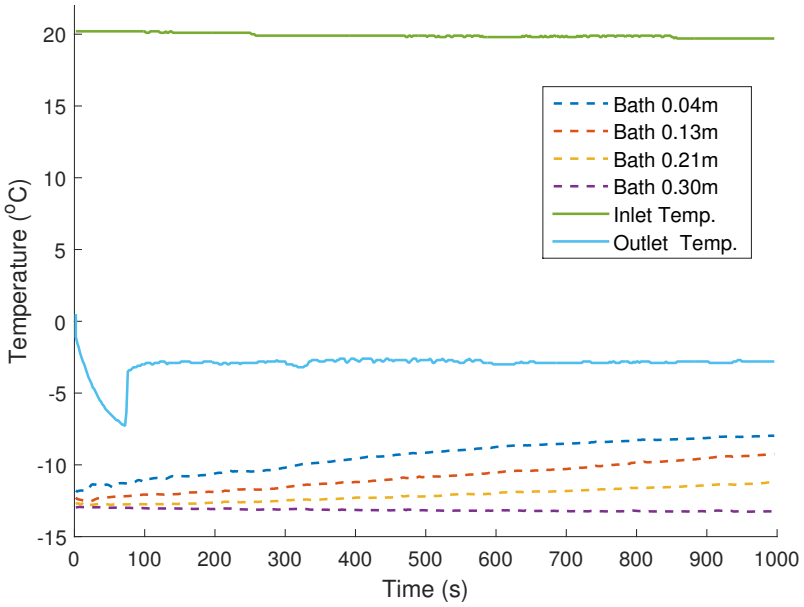


(b) BMU temperatures

Figure 5.4: Graph of temperature distribution in bath, (a) is the original TMD flow, (b) is the reversed BMU flow. Flow rate of 0.0076 kg $s^{-1}$ and starting temperature of -13°C for both.

All bath thermocouple started recording the same temperature, except for the thermocouple closest to the top which has a slightly warmer bath temperature due to the heat loss to the atmosphere. For TMD and BMU the largest temperature rise was seen at shallower depths, due to buoyancy-driven convection caused by heat transferred from the pipes. With TMD the warmer fluid entering the top caused a larger rise in temperature here and a small increase at the bottom three depths. With BMU the temperature rise was spread more evenly across all positions (except the bottom); the internal fluid sees the coldest part first at the bottom followed by the warmer fluid as it moves up the coil.

The temperature distribution the pipe passed through in a TMD experiment was similar to a counter-current heat exchanger. BMU temperature distributions were similar to a co-current heat exchanger.

### 5.1.4 Conclusion

The flow was reversed (to bottom moving up) in a submerged HCHX to explore the effect on ice slurry production. Heat transfer area, flow rates and pipe material, were kept the same for all experiments. The aim was to generate a more even temperature distribution in the bath. This was achieved, though it had no beneficial effects on ice slurry production. However, similar operation regions and ice fractions were produced. The original flow direction (top moving down) was more effective, as a result of similar ice fraction at warmer bath temperatures. It was noted that the flow experienced a similar temperature distribution to that of a counter-current and co-current heat exchanger.

## 5.2 Pipe Orientation

### 5.2.1 Introduction

As shown in the previous section, a submerged coil heats up the bath fluid and creates a temperature distribution of warmer fluid at the top and colder at the bottom. Contact melting, and cycling between hot and cold to dislodge ice on a surface, has been discussed previously as a form of ice slurry production (see §2.5.2). A similar process was proposed, though the fluid would pass hot and cold surfaces rather than on the same surface heated and cooled. The coil axis was rotated to a horizontal orientation rather than the original vertical axis. Fluid pumped through one coil turn will move from lab temperature at 20 °C, to warmer bath fluid and lastly to the coldest bath fluid at the bottom 180 degrees; then the same in reverse as it moves back up 180 degrees through a coil turn (see Figure 5.6). The aim is to see if the movement from hot to cold can help prevent ice adhesion to the walls and increase $\dot{m}_{\phi_m}$ or $\phi_m$. A horizontal coil will also experience higher rates of natural convective heat transfer as the coils convection currents will not flow over other coils, as shown in Figure 5.5.

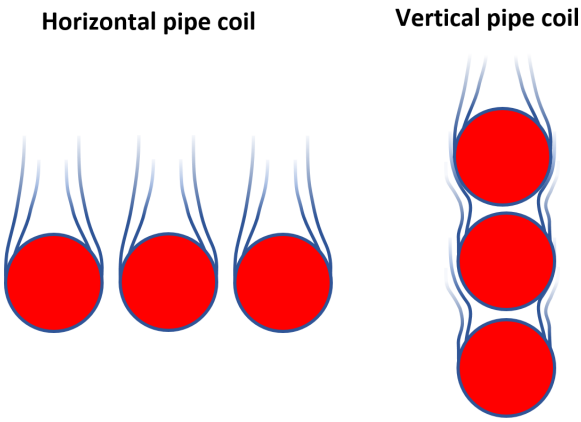


Figure 5.5: Diagram showing heated fluid (blue) moving away from warm pipe (red). As the fluid warms it rises, when pipes are stacked vertically it flows over other warmer pipes as shown.

### 5.2.2 Experimental Set-up

The experimental set up is outlined in Figure 5.6. A 0.4m diameter coil was submerged by 0.32m in the bath of brine refrigeration fluid, leaving 0.08m height of coil exposed (0.37m of pipe length exposed). To adjust for this exposed surface area the number of coils was increased from 21 to 30, increasing the total length from 27.4m to 39.1m, while ensuring the submerged surface area was the same as the original vertical experiment. The experimental procedure and other equipment used was the same as outlined in §3.2.

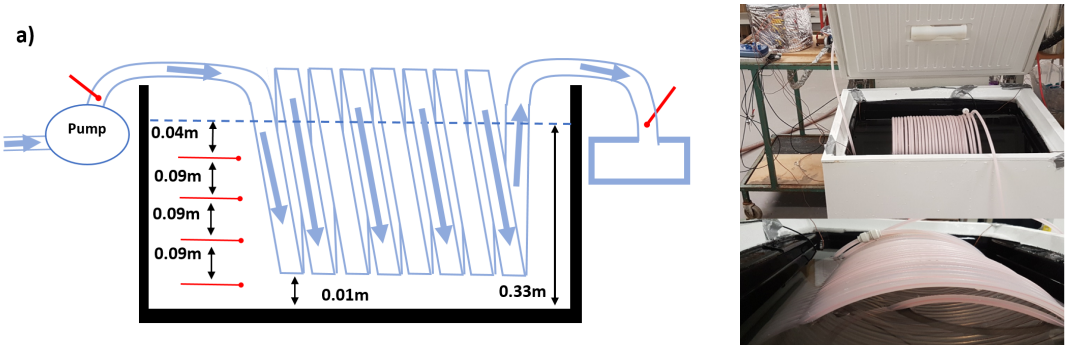


(a) Diagram (b) Picture

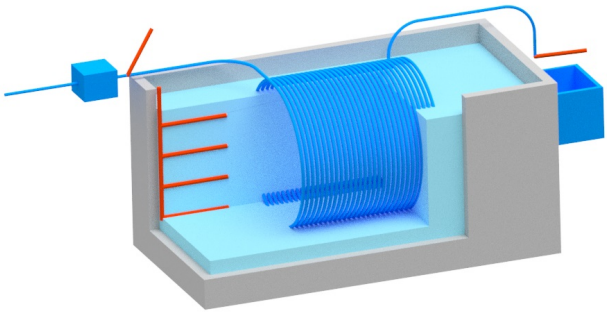

(c) CAD model

Figure 5.6: (a) A diagram, (b) a picture and (c) a CAD model of experimental set up. A horizontal axis coil of nylon pipe is partially submerged in a bath of cold brine. The red lines show positions of thermocouples in the bath, outlet and inlet.

### 5.2.3 Results and Discussion

A total of 56 experiments were conducted each for 1000 seconds each, with a range of different flow rates and temperatures (similar to the ones used in §4.4). NaCl brine (5 wt.%) was used as the internal fluid, with the same three outcomes observed as previously in §4.4.2. When ice slurry was produced, ice fraction measurements were taken using calorimetry.

An operation region was plotted with the new data (Figure 5.7 (b)) along with the original one for 5wt.% from §4.4 (Figure 5.7 (a)).

The operation graphs produced are similar, both regions are a similar size at high flow rates. However, no ice was produced at the lower flow rates with the horizontal coil. This is likely due to the increased pipe length which increases the pressure loss from pumping in the pipe. At lower flow rates, where the cut off pressure for the pump is lower, there is insufficiency force left to pump ice slurry through the extended length. Haruki and Horibe (2013) noted that solid particles tended to move towards the top of the coil under buoyancy forces at low laminar speeds. Ice could be building up at the top of the coil where the pipe is not submerged and blocking the pipe. This could also explain why no ice production region is found at low speeds. However, this was not observed during the experiment in the visible section of the coil.

Regions of $T_{Bath} - T_f$ where ice was produced are similar or lower, indicating no energy saving is achieved with this method.

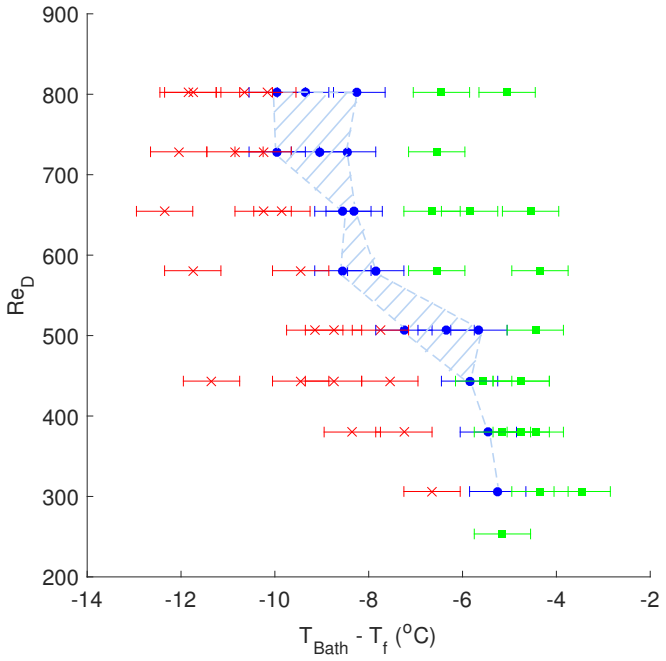


(a) Vertical axis coil (original)

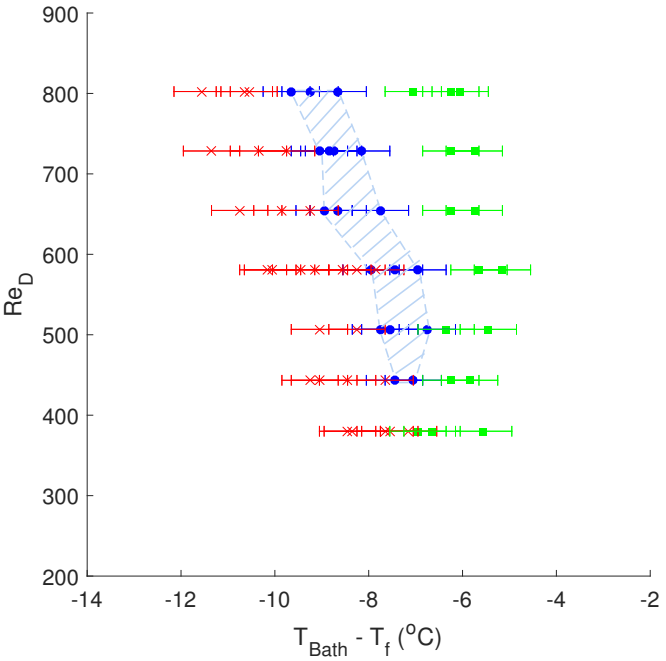


(b) Horizontal axis coil

Figure 5.7: Operation graphs of Re number against $T_{Bath} - T_f$ for (a) vertical axis orientation, and (b) the new horizontal axis orientation in a coiled nylon pipe with 5 wt.% NaCl brine. Blockages are represented by red x, ice production by blue circles, and no ice formation by green squares.

Ice fraction ($\phi_m$) measurements taken were plotted on Figure 5.8 (a) and $\dot{m}_{\phi_m}$ in Figure 5.8 (b). Trend lines were plotted on (b) to show the reduction in average ice production rate as the bath temperature gets warmer.

The original vertical arrangement appears to offer the best $\phi_m$ and $\dot{m}_{\phi_m}$, with comparable values produced at lower $T_{Bath} - T_f$. There is more variation in the vertical coil axis results than the horizontal coil axis. This is not a bad characteristic but indicates more consistent but lower ice fractions with the horizontal coil axis.

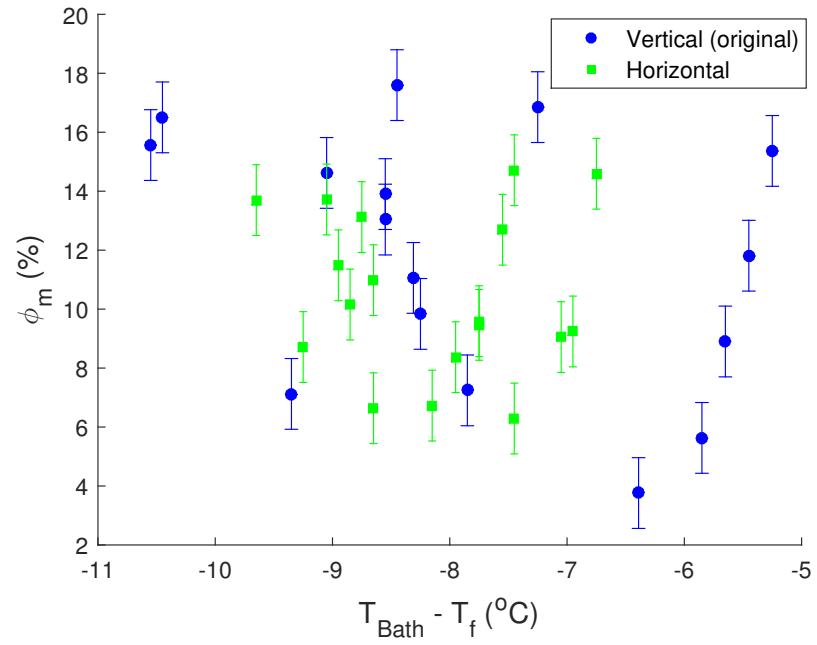


(a) Ice fractions ($\phi_m$)

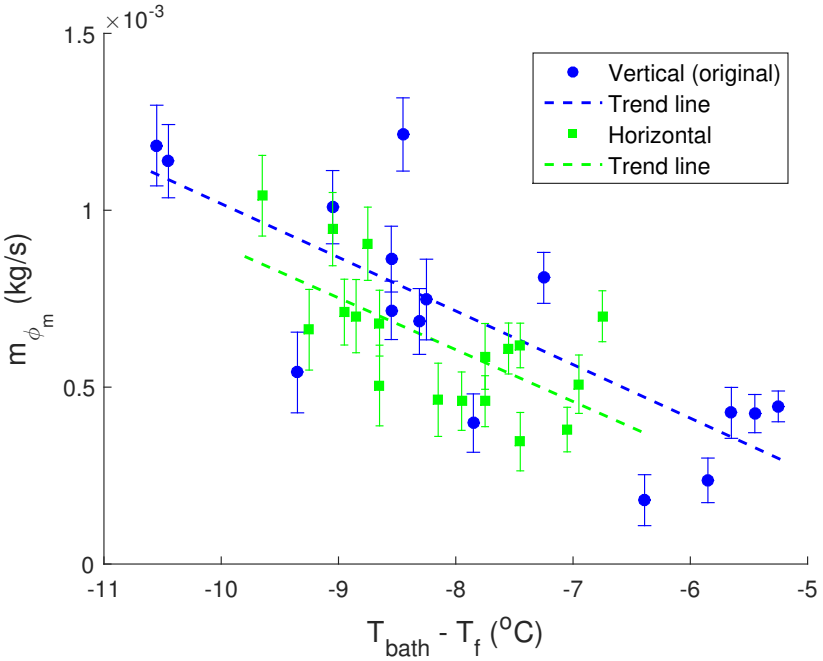


(b) Ice production rate ($\dot{m}_{\phi_m}$)

Figure 5.8: Graphs of (a) ice fraction, and (b) ice production rate against $T_{Bath} - T_f$, for vertical and horizontal axis HCHX arrangements.

### Temperature distributions

Examples of temperature distributions measured for experiments with the horizontal coil axis are plotted in Figure 5.9 (b), with the original vertical coil axis in (a).

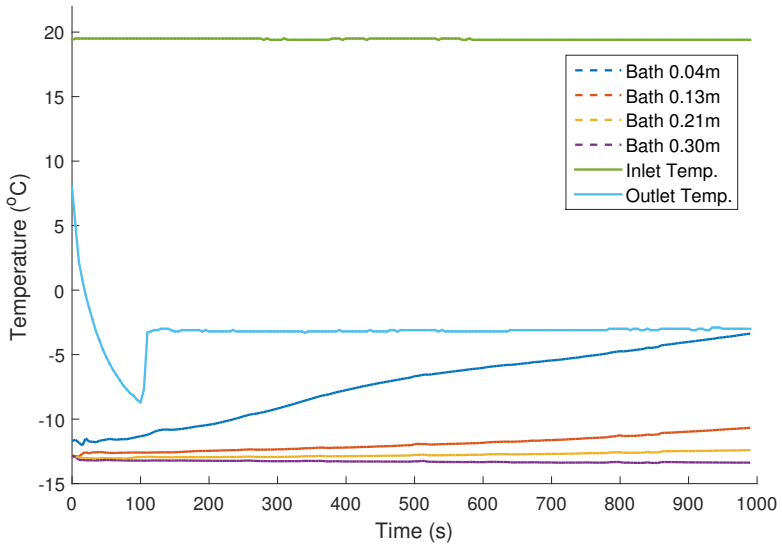


(a) Vertical axis coil

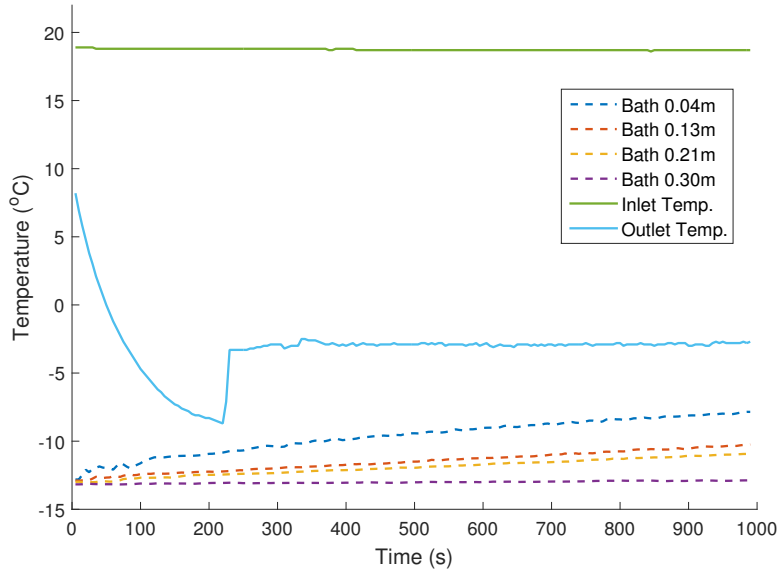


(b) Horizontal axis coil

Figure 5.9: Temperatures taken during an experiment, (a) shows the vertical axis coil orientation, and (b) the horizontal axis coil orientation. A 0.0076kg $s^{-1}$ flow rate and -13°C bath temperature were used for both experiments.

As outlined previously, the vertical axis coil leads to a large temperature distribution with a significantly larger rise in temperature observed at the top. A more even spread of temperatures is observed for the horizontal axis coil, similar to BMU flow in §5.1.3. This is demonstrated by the two middle thermocouples (0.13 and 0.21m) which appear to rise at the same rate; In the vertical coil experiment the 0.13m temperature reading always rose faster than 0.21m.

One noticeable difference with the horizontal axis coil is the increase in time taken to supercool the brine; it took about 105 seconds with a vertical axis coil while it took nearly 220 seconds with the horizontal axis coil. This was observed throughout the experimental process, where the horizontal pipe regularly took 1.5 - 2 times longer to reach nucleation temperatures. This large increase in time could be as a result of the extra horizontal pipe length. However, the length was only increased by a factor of 1.17 but the time increases by more than double.

### 5.2.4 Conclusion

Two different coil orientations (vertical and horizontal axis) were tested to examine the effect on ice slurry production. The aim was to utilise the temperature distribution in the bath to create alternating hot and cold surface for ice formation. The heat transfer area, flow rates and pipe material, were kept the same for experiments. Similar operation regions and ice fractions were produced. Ice production occurred at a wider range of flow rates with the vertical axis coil. The vertical axis coil also had ice fraction and production rates at the warmer, and therefore more efficient, $T_{Bath}$ temperatures. The original vertical axis coil set up proved more effective for high ice slurry production at low bath temperatures.

## 5.3 Control System Experiments

From the original experiments outlined in Chapter 4 it is apparent that the maximum ice fraction is achieved at low bath temperatures and low flow rates. Therefore, an optimum line for ice slurry production exists, shown by the dotted line on Figure 5.10. A control system could manage the flow rate to maximise ice production by staying in this region based on $T_{Bath}$ readings.

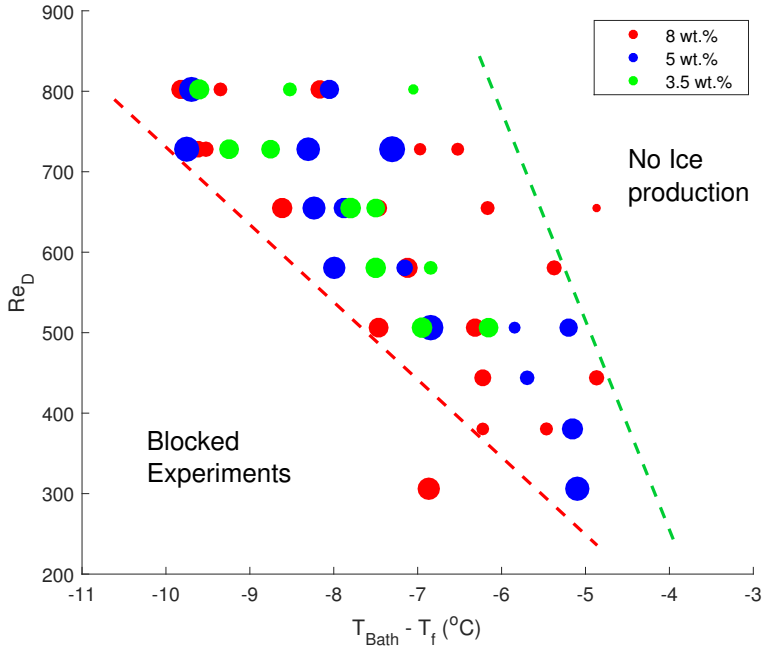


Figure 5.10: Graph of ice fraction production regions for 3.5, 5 and 8wt.% brine, point size indicates ice fraction recorded. The red dotted line is the limiting point before blockages occur and green shows where no ice is produced. Same as Figure 4.6 from chapter 4.

### 5.3.1 Introduction

Current ice slurry generators are controlled using three key methods: 1) control of the primary refrigeration fluid loop by monitoring the outlet slurry temperature;

2) control of primary refrigeration fluid loop by monitoring slurry collection tank temperature; 3) inlet flow rate and primary refrigeration loop control based on inlet and outlet temperatures (Kauffeld et al. (2005)). Controlling $\phi_m$ in an ice slurry generator using temperature measurements proves difficult. Especially at warmer temperatures, low $\phi_m$ and low NaCl concentration solutions, where small changes in temperature can change the production rate. This is especially true for the HCHX design used in this thesis. If higher FPD concentration solutions (above 5wt.%) and therefore lower bath temperatures were used, using temperature could be a viable method. The method explored in this section was similar to the third method outlined. However, both temperature and pressure readings were taken as inputs to increase the controllability at lower ice fractions.

**Objective**

The aim of the work was to create a versatile Control System (CS) to initiate and maintain a higher $\phi_m$ above 10% for longer than 1000 seconds. Careful flow rate control based on temperature and pressure readings was utilised. This automated the method and reduced the need for operator intervention to prevent blockages, while also optimising the ice fraction produced.

### 5.3.2 Experimental Set-up

The set up used was identical to the one outlined in §3.2, though pump voltage is not set by the user. Pressure and temperature data recorded by the Pico logger was utilised in a MATLAB program to set an output signal. The signal was linked to an Arduino and transistor circuit, which regulated voltage reaching the pump motor; thereby controlling the flow rate. Figure 5.11 displays a diagram of the complete arrangement used to regulate the pump voltage. Ice fraction ($\phi_m$) measurements were taken using calorimetry, as outlined in §3.3.5 ($\phi_m$).

Two different control systems were tested which are outlined in the following sections.

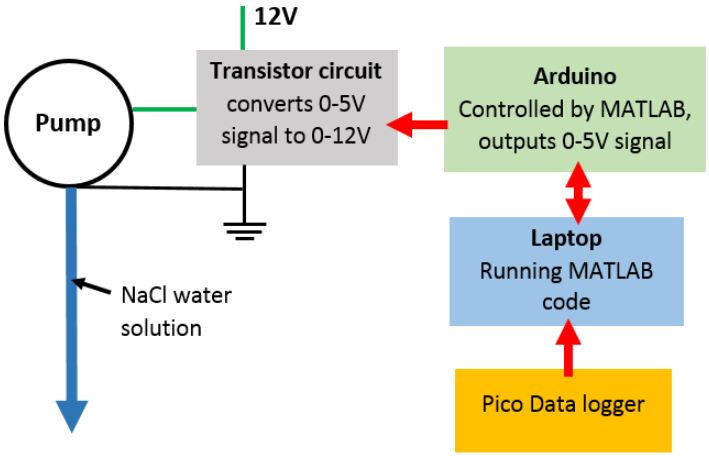


Figure 5.11: Diagram of control set-up used, an Arduino and MATLAB program control the voltage signal which controls pump voltage.

### 5.3.3 Basic Control System (BCS)

#### Control system

Increases and decreases in gauge pressure readings were taken every second and used as indicators of ice fraction rising or falling. The BCS had the following steps (also shown in Figure 5.12):

- Initially, a minimum safe flow rate was set to help prevent sudden unstoppable blockages occurring when supercooled brine nucleates. This is determined using the red dotted line on Figure 4.6.

- Every second a safety check was used to make sure pressure had not risen above a maximum value of 60kPa. Above this pressure, the flow rate was increased to its maximum (0.0076kg $s^{-1}$) by increasing the pump supply voltage to maximum. Previously nearly all experiments where pressure remained above

60kPa (with no added flow rate) resulted in a blockage which is why this value was used here.

- Pressure readings were stored and evaluated, if a pressure change (dP/dt) of 5kPa $s^{-1}$ was observed between readings then the signal setting the supply voltage to the pump was increased to maximum (increasing flow rate to a maximum) as a preventative measure against blockages.

- An extra check also monitored the outlet temperature. After 300 seconds if the fluid is insufficiently cooled (no nucleation of ice but still supercooled), $T_{out} < T_f - 0.5$, then the flow rate could be dropped further to encourage further cooling and ice nucleation.

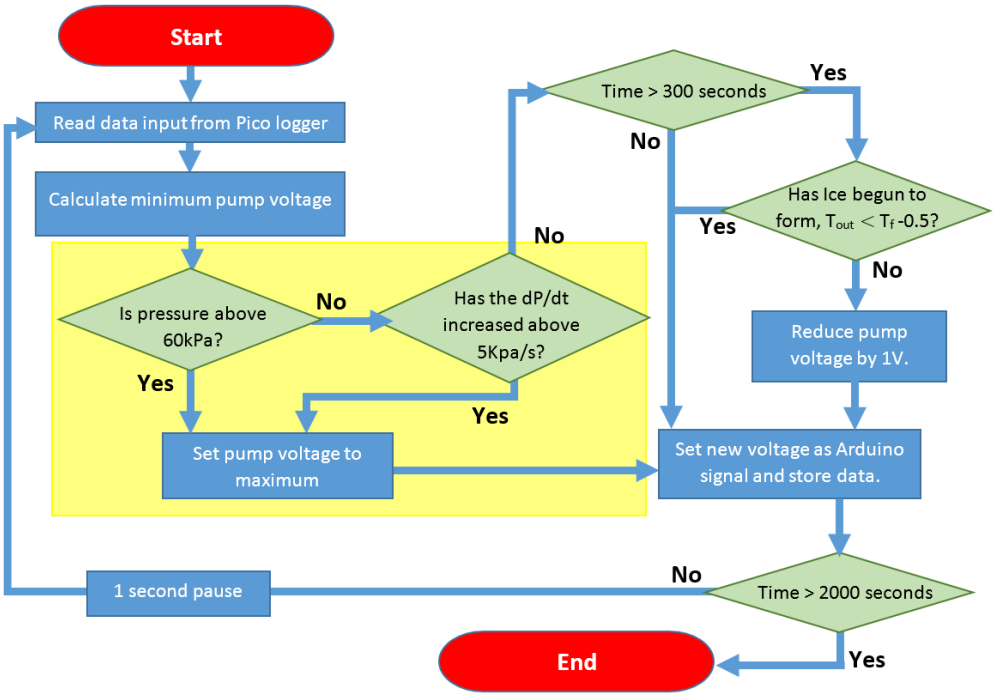


Figure 5.12: Flow chart of BCS designed to manage flow rate and maximise ice production.

### Initial results

Three experiments with bath starting temperatures of -10 °C, -11.5 °C and -13 °C were conducted. Temperatures and pressures were recorded and plotted in Figure 5.13 (a), (b) and (c). Experiments ran for 2000 seconds and five measurements of $\phi_m$ were taken. Ice fraction ($\phi_m$) and ice produced rate ($\dot{m}_{\phi_m}$) were plotted against time, Figure 5.14 (a) and (b). Equation 3.5 in section §3.3.5 was used to find $\dot{m}_{\phi_m}$.

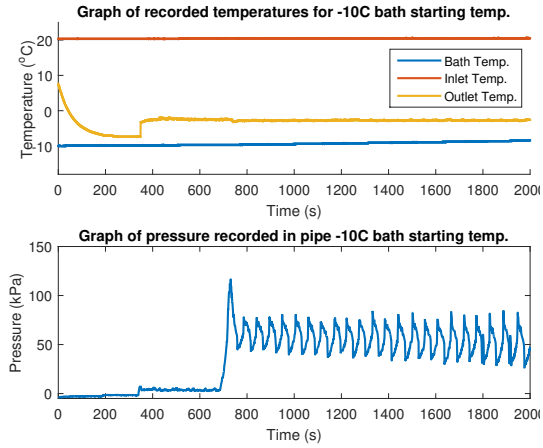


(a) -10°C = $T_{Bath}$

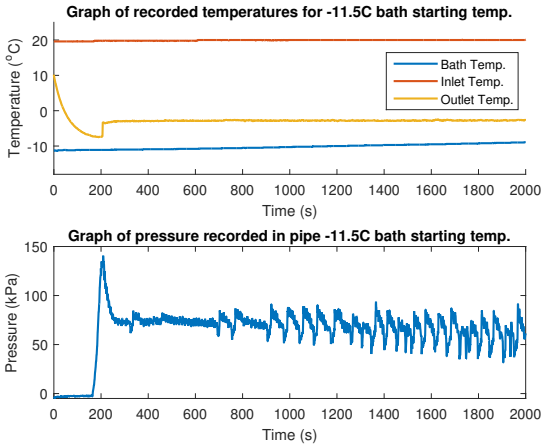


(b) -11.5°C = $T_{Bath}$

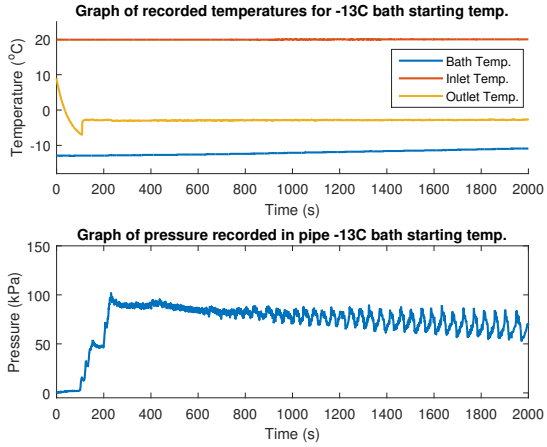


(c) -13°C = $T_{Bath}$

Figure 5.13: Top, temperature recordings, bottom, pressure readings, for tests with the BCS. (a) is -10°C, (b) is -11.5°C and (c) is -13°C starting bath temperature.

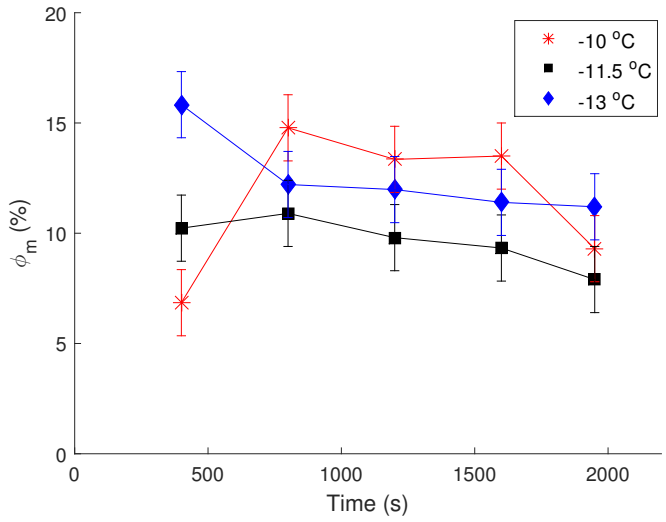


(a) Ice fraction ($\phi_m$)

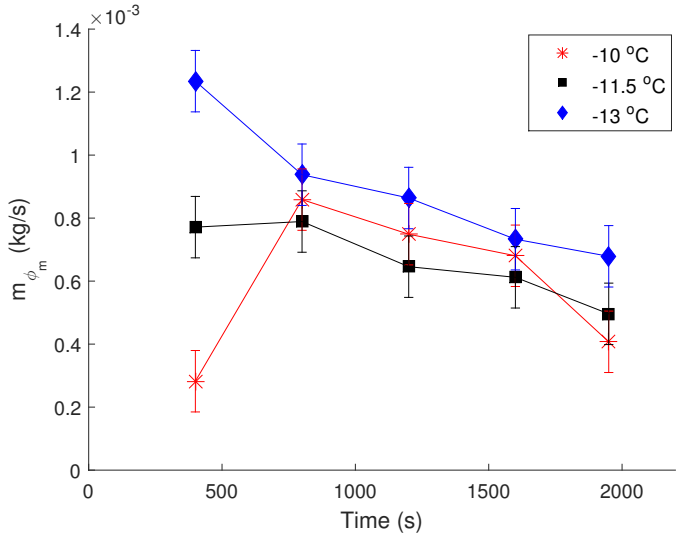


(b) Average ice production rates ($\dot{m}_{\phi_m}$)

Figure 5.14: Graph representing (a) ice fraction and, (b) average mass production rate, with the BCS and bath starting temperatures at -10°C, -11.5°C and -13°C

Ice nucleation from supercooled liquid to ice slurry is indicated on Figure 5.13 for BCS by the sharp rise in outlet temperature and pressure. The rise in pressure is lowest with -10 °C bath temperature (Figure 5.13 (c)), though a larger rise is observed at 700 seconds. The $\phi_m$ and $\dot{m}_{\phi_m}$ follow a similar pattern from low (7% or 0.3 x10$^{-3}$kg s$^{-1}$ at 400 seconds) but rising quickly (above 14% or 0.8 x10$^{-3}$kg s$^{-1}$

at 800 seconds), see Figure 5.14. This indicates that the second rise in pressure corresponds with a rise in ice fraction and production rate. For all BCS experiments, average pressure, $\phi_m$ and $\dot{m}_{\phi_m}$ fell after 800 seconds. Oscillations in pressure appeared to grow during experiments, as the pump speed jumped from the set minimum to the safe maximum. The fall in ice fraction and growth of oscillations in flow rate and pressure led to the creation of the improved control system (ICS).

### 5.3.4 Improved Control System (ICS)

The pressure oscillated significantly when using the BCS; these oscillations grew in amplitude over time. To reduce these oscillations a simpler alternative CS was designed, using a gradual proportional based flow rate increase.

#### Control system

ICS steps (also shown in Figure 5.15):

- Initially, a minimum safe flow rate is set using an operation region of flow rates and temperatures found in previous work.
- Using the pressure readings, a proportional increase was added above 20kPa to the output signal to increase the flow rate proportionally up to the max flow rate 0.0074kg $s^{-1}$. The aim was to reduce sharp increases in pressure and flow rate.
- As mentioned previously, an end check was also added to check if ice had formed and decrease the flow rate to encourage further cooling if needed.

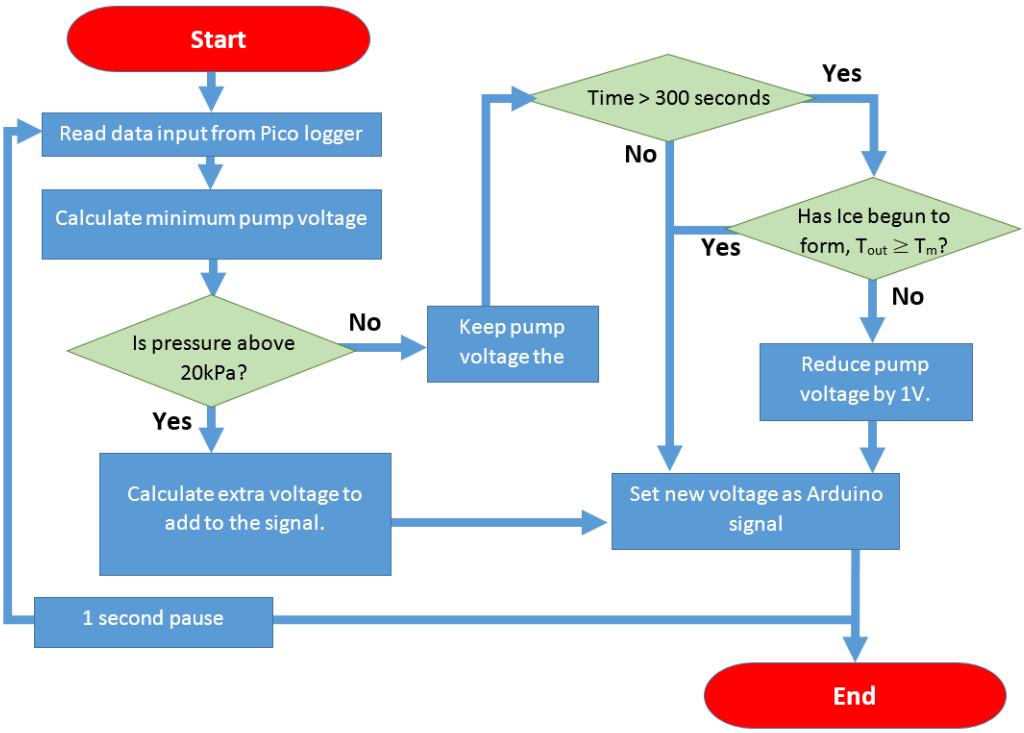


Figure 5.15: Flow chart of BCS designed to manage flow rate and maximise ice production.

### Control system - improved results

To test the ICS three similar experiments with bath starting temperatures of -10 °C, -11.5 °C and -13 °C were conducted. Temperatures and pressures were recorded and plotted in Figure 5.16 (a), (b) and (c). Experiments also ran for 2000 seconds and five measurements of $\phi_m$ (and $\dot{m}_{\phi_m}$) were taken and plotted against time, Figure 5.17 (a) and (b).

The pressure and temperature readings displayed on Figure 5.16 (a), (b) and (c) (for ICS) follow a similar pattern to the ones for BCS. Notably, there is a reduction in amplitude of pressure oscillations, due to the gradual proportional increase in flow rate. The ICS also reduced the large pressure spike when ice nucleation started, observed in Figure 5.13 (a), (b) and (c). This was achieved by the removal of the

dP/dt safety check which appeared to have no significant positive effect.

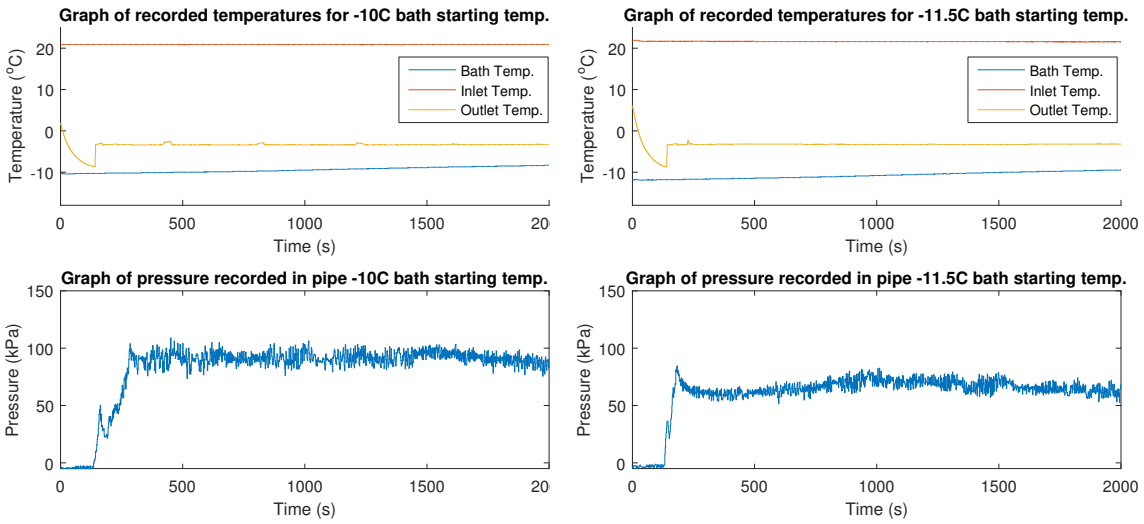


(a) -10°C = $T_{Bath}$ (b) -11.5°C = $T_{Bath}$

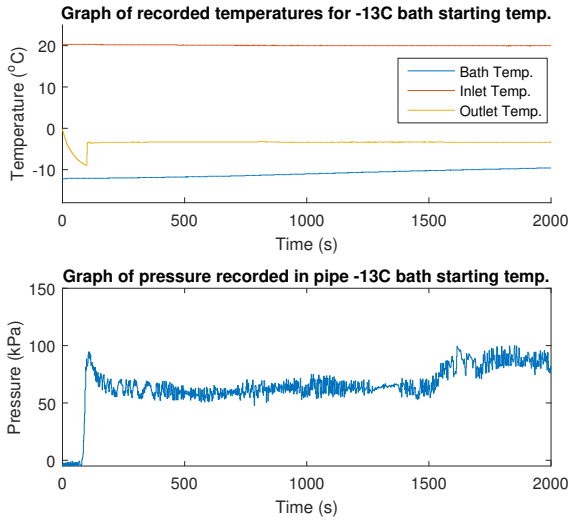


(c) -13°C = $T_{Bath}$

Figure 5.16: Top, temperature recordings, bottom, pressure readings, for tests with the ICS. (a) -10°C starting bath temperature, (b) -11.5°C starting bath temperature, (c) -13°C starting bath temperature.

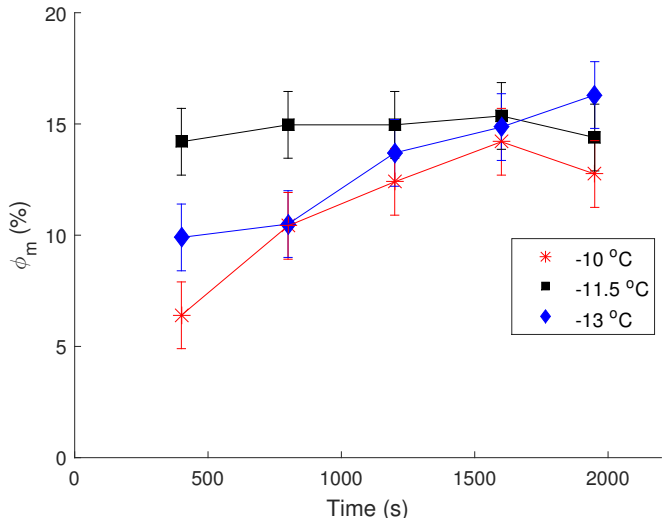


(a) Ice fraction ($\phi_m$)

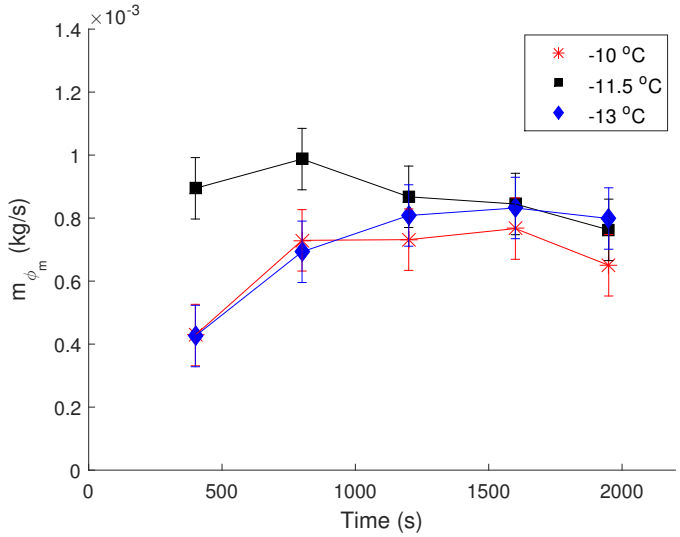


(b) Ice production rates ($\dot{m}_{\phi_m}$)

Figure 5.17: Graph representing (a) ice fraction and, (b) average mass production rate, over each 2000 second test with the ICS. With bath starting temperatures at -10°C, -11.5°C and -13°C

When comparing the results from each control system some key differences were noted. Lower $\phi_m$ (and $\dot{m}_{\phi_m}$) were observed initially for $T_{Bath}$ = -10 or -13°C (not 11.5°C) when using the ICS instead of BCS, though only until 1200 seconds. Crucially, $\phi_m$ increased, or remained level, during most of the ICS operation, dropping

only slightly at the end. A longer test beyond 2000 seconds would be needed to determine if the decrease would continue. Comparison of $\dot{m}_{\phi_m}$ results (Figure 5.14 (b) and 5.17 (b)) shows ice $\dot{m}_{\phi_m}$ falls over time for both control systems, though this fall is larger with the BCS. For experiments with -10 °C starting $T_{Bath}$, between 800 and 1600 seconds a higher ice fraction slurry was produced using the BCS rather than ICS. A drop of nearly 4% was observed between the last two readings using the BCS, while only a 1.5% drop was seen at the end of the ICS experiments.

### 5.3.5 Discussion

As discussed previously, Kauffeld et al. (2005) outlined three known control methods used for ice slurry production. The control system here builds on the third one, controlling inlet flow rate based on inlet and outlet temperatures. Barth and Leprieur (2002) utilised a similar method to the one used in this work where pressure and temperature inside a heat exchanger were used to indicate ice formation. When ice formed, the flow rate and evaporation temperature were increased. This work successfully produced a similar method of ice production without the need to change the temperature in the evaporator. Little information exists about Barth and Leprieur (2002) and unfortunately no comparison of results can be made.

Currently, these experiments only monitor ice production as the bath (refrigeration fluid) temperature falls. During operation, the bath fluid temperature would rise and fall as it was replaced with new colder fluid or cooled. The control system should be able to cope with the rise provided it remains within the tested temperature range of -13°C to -10°C. Further work is needed to test this and improve the control system further. Other control methods such as PID (proportional integral and difference) control could improve the results, though a known target pressure would be needed for this method.

### 5.3.6 Conclusion

Two control systems were designed to measure pressure and pipe inlet and outlet temperatures. The flow rate of internal fluid in a HCHX was set based on the measurements. The aim was to maintain $\phi_m$ above 10%; both control systems achieved this for the majority of the 2000 second tests. The ICS did this more successfully because it did not create growing pressure oscillations (caused by the BCS safety check). Produced $\phi_m$ and ($\dot{m}_{\phi_m}$) were also increased and stayed higher for longer periods of time. The large oscillations in pressure with the BCS may not be detrimental to ice production but the growth in amplitude should be controlled to avoid potential damage to equipment.

## 5.4 Chapter Summary

The key points from the three different methods of optimisation investigated are:

- Reversing the flow direction for a vertical coiled pipe in a HCHX reduced the size of the operation region, the ice fraction and production rates. The same three outcomes were observed in each experimental set as those in the previous chapter.

- Temperature profiles of the bath created in the reversed flow experiments were analysed. They indicated that top moving down flow direction acts to maintain stratification of bath refrigerant, creating a more efficient counter-current temperature profile.

- A partially submerged horizontal axis HCHX was found to be ineffective at increasing ice slurry production or operation region size over the original vertical HCHX arrangement.

- Using a control system to boost ice slurry production was effective; ice fraction was maintained above 10% despite the warming refrigerant bath.
- A control system using a proportional increase in flow rate in response to pressure increase proved more effective.

# Chapter 6

# Pipe Material Investigations

## 6.1 Introduction

Nylon pipe used previously in the HCHX has proven successful, though other materials could produce even better results. In this chapter, alternative materials are investigated to see if they could be more effective. Metal pipe has also been tested to reinforce the findings from the literature review that metal will lead to blockages because of ice adhesion and high heat transfer.

The aim of this work is to see if ice slurry production can be correlated to material properties. Materials will be evaluated for:

- Improved ice production - this is observed by monitoring ice fraction and production rates during the experiments.
- Reduce energy cost - if ice production can be improved or maintained with a higher refrigeration temperature this indicates greater efficiency.
- Improved reliability - Observed by an increase in size of the stable production region.

In §6.3 the materials are compared to the original nylon pipe to see if they offer any of these benefits.

## 6.2 Experimental Design

The experimental set up used is identical to the one outlined in §4.2, though pipe material and length have been changed for each material depending on its properties.

### 6.2.1 Material Selection

The three extra materials chosen for tests and the reason for their selection are:

- **PTFE** - A material with a high contact angle with water (hydrophobic), this should reduce ice adhesion (as discussed in §2.6) increasing maximum ice fraction which can be produced.
- **Silicone rubber** - Has a contact angle between nylon and PTFE and lower thermal conductivity than both. A flexible pipe was also chosen as previous authors (Work and Lian (2018)) have noted that material deformation or strain has a big impact on ice adhesion. A pipe which can flex and expand could help dislodge ice adhered to the side. It is also utilised in the final technical chapter of this thesis.
- **Aluminium** - A metal pipe was needed to confirm the previous work showing that ice produced will block the pipe. Aluminium also does not rust significantly in NaCl water and can be bent easily into a coil shape.

Pictures of each material in the coil used are displayed in Figure 6.1. A different supporting structure was designed for each plastic pipe, including one to allow silicone rubber pipes to expand and contract freely.

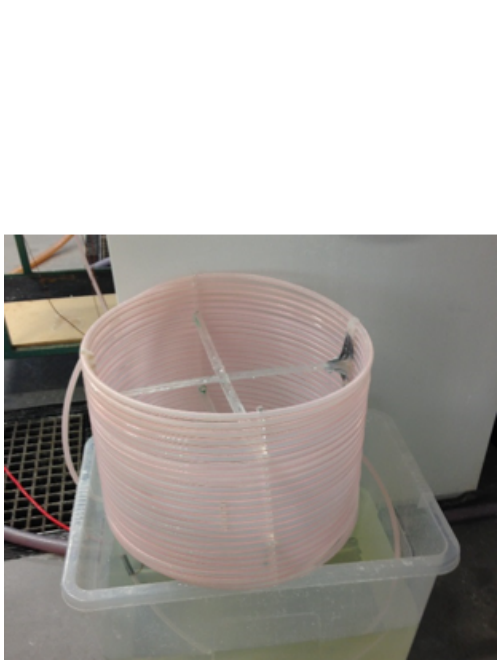

(a) Nylon coil

(b) PTFE coil

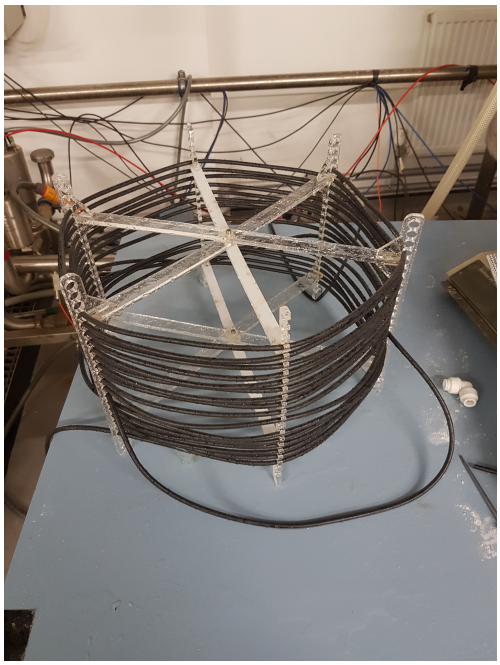

(c) Silicone rubber coil

(d) Aluminium coil

Figure 6.1: Pictures of material coils used, (a) nylon, (b) PTFE, (c) silicone rubber, and (d) aluminium.

Table 6.1: Table for different properties of material used, nylon, PTFE, silicone rubber and aluminium.

| **Material** | **Nylon** | **PTFE** | **Silicone** | **Aluminium** |
|---|---|---|---|---|
| **Thermal conductivity (W m$^{-1}$K$^{-1}$)** | 0.36 [i] | 0.25[ii] | 0.2 [iii] | 205 [ii] |
| **Contact angle with water (°)** | 70[iv] | 109.2[iv] | 85[v] | 85[vi] |
| **Inner Diameter (m)** | 0.0067 | 0.0064 | 0.005 | 0.007 |
| **Outer Diameter (m)** | 0.0095 | 0.0079 | 0.006 | 0.0095 |
| **Thermal Resistance per m (K m/W)** | 0.154 | 0.134 | 0.145 | 0.00018 |
| **Length (m)** | 27.4 | 23.6 | 26 | 2.5 |
| **Thermal resistance (K/W)** $10^{-3}$ | 5.63 | 5.68 | 5.6 | 0.07 |
| **Surface Roughness ($\mu$m)** | 1.5 | 4.9 | 5.7 | 6.7 |
| **Cost (£/total coil)** | 20.6 | 70.80 | 12.10 | 29.90 |

The properties of each pipe and material are outlined in Table 6.1.

The surface roughness of the internal pipe was measured using a Taylor Hobson Talysurf profilometer. The surface profile over a 10mm length was measured from

[i] Quoted from Manufacturer (Valper)
[ii] From Bergman et al. (2011)
[iii] Quoted from Manufacturer (Silex)
[iv] From Owens and Wendt (1969b)
[v] From Aziz et al. (2003)
[vi] From Majeed (2014)

five samples of each pipe. The maximum profile height was taken as the highest to the lowest point. The average of these maximum values are shown in Table 6.1.

The contact angles were taken from a range of sources. They are the contact angles for a water drop on the surface in atmospheric conditions (water-surface-air). As discussed in §2.2.2, these values do not accurately represent the contact angle for an ice nucleus forming on the submerged surface. However, they can give an indication of which material should produce a lower contact angle between ice and the surface (ice-surface-water contact angle).

Values for thermal conductivity ($k$) were either quoted by the manufacturers or found from literature. To account for the differences in $k$ of each material, pipe wall thickness and length were varied to get similar thermal resistances ($R_{pipe}$).

$$R_{pipe} = \frac{\ln D_i/D_o}{2\pi Lk} \tag{6.1}$$

A change in $k$, is offset by changing $D_i/D_o$ and/or Pipe length (L), as done with PTFE and silicone rubber. Aluminium has a significantly higher thermal conductivity than plastic; a length of just 0.032m is required to provide the same resistance. In reality, this is impracticable and does not provide sufficient length to cool the fluid. Therefore, a length of 2.5m was used, to allow some length for the thermal boundary layer to form. The internal radius was kept close to the value of nylon for all materials, to maintain the same range of Re values for pipe flow.

Costs for the total price for the tubing of one coil and per metre, are shown in Table 6.2. For all plastic coils, 50m of the pipe was purchased, only 4m of aluminium pipe was purchased because it was the most expensive material and only a small

quantity was required. The results in the table give an indication of which pipes are most cost-effective. This is an important factor if the pipes need regular changing or replacing. Silicone and then nylon offer the most cost-effective coils. PTFE is the most expensive, with it cosign more than double per coil than any other coil. These cost estimations do not take account of the operational life of the coils; for example, the high cost of PTFE may be justifiable if it has a long operational life.

Table 6.2: Table of material cost for, nylon, PTFE, silicone rubber and aluminium. All prices taken during 2018.

| **Material** | **Nylon** | **PTFE** | **Silicone** | **Aluminium** |
|---|---|---|---|---|
| **Length purchased** | 50 | 50 | 50 | 4 |
| **Cost (£)** | 38.00 | 197.40 | 29.00 | 29.58 |
| **Cost (£m$^{-1}$)** | 0.76 | 3.95 | 0.58 | 7.40 |
| **Cost per coil (£)** | 20.6 | 70.80 | 12.10 | 29.90 |
| **Purchased from** | Valpar | Polyflon | Silex | Viper Performance |

## 6.3 Results

Ice slurry was successfully produced with all materials except aluminium. This and other results collected are outlined further in this section. Nylon was repeated as PT100 probes were used to measure $T_{Bath}$, improving the accuracy.

### 6.3.1 Observed Outcomes

The same three outcomes seen with nylon HCHX previously, blocking, ice production and no nucleation, were observed with silicone and PTFE pipes. Only blocking and no ice nucleation were observed with aluminium. Figure 6.2 shows graphs of temperature and pressure recorded during ice production experiments.

For aluminium, no consistent ice production was found so a graph of ice production and subsequent blocking is shown (Figure 6.2 (c)).

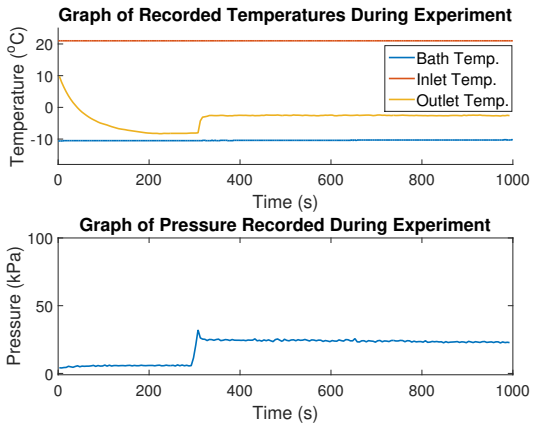


(a) Nylon, $T_{Bath} - T_f = -7.6°\text{C}$

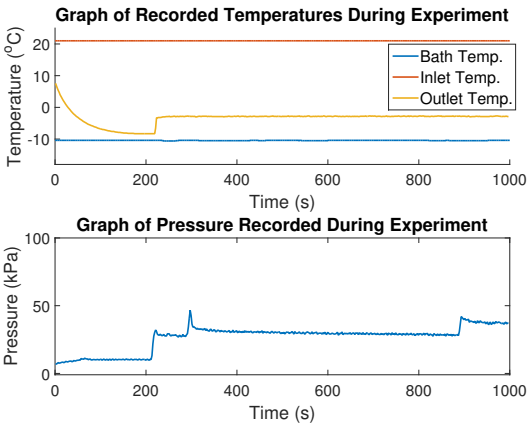


(b) PTFE, $T_{Bath} - T_f = -7.3°\text{C}$

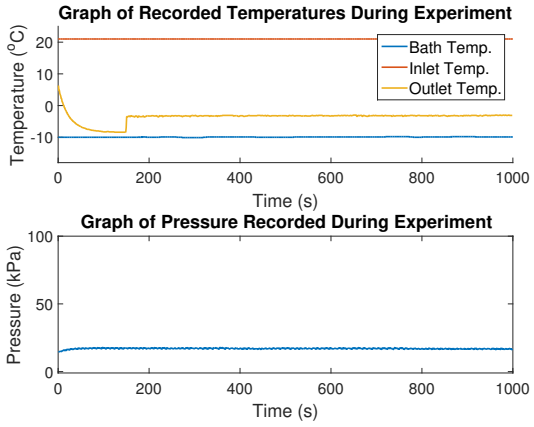


(c) Silicone rubber, $T_{Bath} - T_f = -7.4°\text{C}$

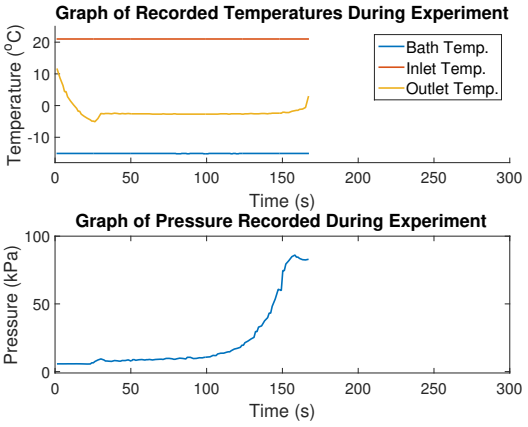


(d) Aluminium, $T_{Bath} - T_f = -12.2°\text{C}$

Figure 6.2: Top: temperature readings, bottom: pressure readings for (a) nylon, (b) PTFE, (c) silicone rubber, and (d) aluminium pipe. $T_{Bath} - T_f$ is detailed below each graph and flow rate is 0.0047kg $s^{-1}$. Experiments lasted 1000 seconds except with aluminium.

### Nylon, PTFE and silicone rubber

The $T_{Bath} - T_f$ values and flow rate for the experiments shown were kept as close as possible to ensure a comparison could be made between Figure 6.2 (a), (b) and (c). For measurements shown in the graphs, the origin (time = 0s) was when the

outlet temperature had cooled to 10°C. The three graphs show a similar pattern. Initially fluid is supercooled, then nucleation occurs, raising the outlet temperature to $T_f$ for the remainder of the experiment. A key difference between the graphs is the time of nucleation. With silicone pipes the fluid appears to nucleate earliest at about 170 seconds, followed by PTFE at 220 and nylon at 300. However, nucleation happened at similar outlet temperatures around -8 to -8.2°C. Silicone pipe appears to transfer heat fastest followed by PTFE, indicating that silicone rubber thermal resistivity is probably lower than indicated by the manufacturers. This is explored further later in this section.

For nylon and PTFE, a rise in pressure is observed when ice nucleates, though not for silicone. This may be because of a higher $\phi_m$ of 8.6% and 8.3% for nylon and PTFE, while silicone is only 7.3%. A high pressure loss from pumping fluid in the silicone pipes (up to 20kPa) was also observed, this could be for to two reasons. Firstly, the smaller pipe diameter leads to increased friction factor and pressure loss. Secondly, the flexibility of the pipe leads to sagging and pinch points in the pipe coil. These have been minimised but cannot be eliminated completely. Pressure spikes were only observed with ice formation in silicone pipes above 8% $=\phi_m$. Pressure spikes above 40kPa always lead to blockages in silicone pipes. This is lower than the other pipes because an increase in pressure in silicone pipes causes them to expand. Flow velocity is reduced, and the fluid spends longer in the pipe; leading to increased ice production and blockages in the pipe.

### Aluminium

With the aluminium pipe, the fluid was cooled quickly, nucleating in under 30 seconds. Nucleation occurred at a much higher temperature, around -5.2°C. Ice was produced and observed in the outlet, though the ice content of the outlet fell over

the following 100 seconds. Eventually, only fluid just below $T_f$ was observed at the outlet, indicating that ice was still present in the tube. A layer growth of ice had formed and bonded to the cold pipe walls faster than it could be removed. This is similar to what was observed by Jain et al. (2019), who cooled pipes to create ice to block flow in small pipes.

### 6.3.2 Operation Regions

Similar operation regions were created to conditions in which ice could be produced, see Figure 6.3 for all four materials. Experiments with nylon were repeated for these experiments because PT100 probes were now used for bath temperature measurements instead of thermocouples, increasing the accuracy of measurements.

The operation regions show distinct differences for each material, they are discussed further below. The same three outcomes were observed as outlined previously in §4.4.2, for nylon, PTFE and silicone; however, not with aluminium which is discussed further below.

*Nylon* - The region created (Figure 6.3 (a)) is similar to the one created previously (see Figure 4.3 (b)). The range of temperatures at which ice is produced gets smaller as the pump flow rate is reduced. This is probably due to the fall in cut off pressure as the voltage to the pump was reduced, as identified previously.

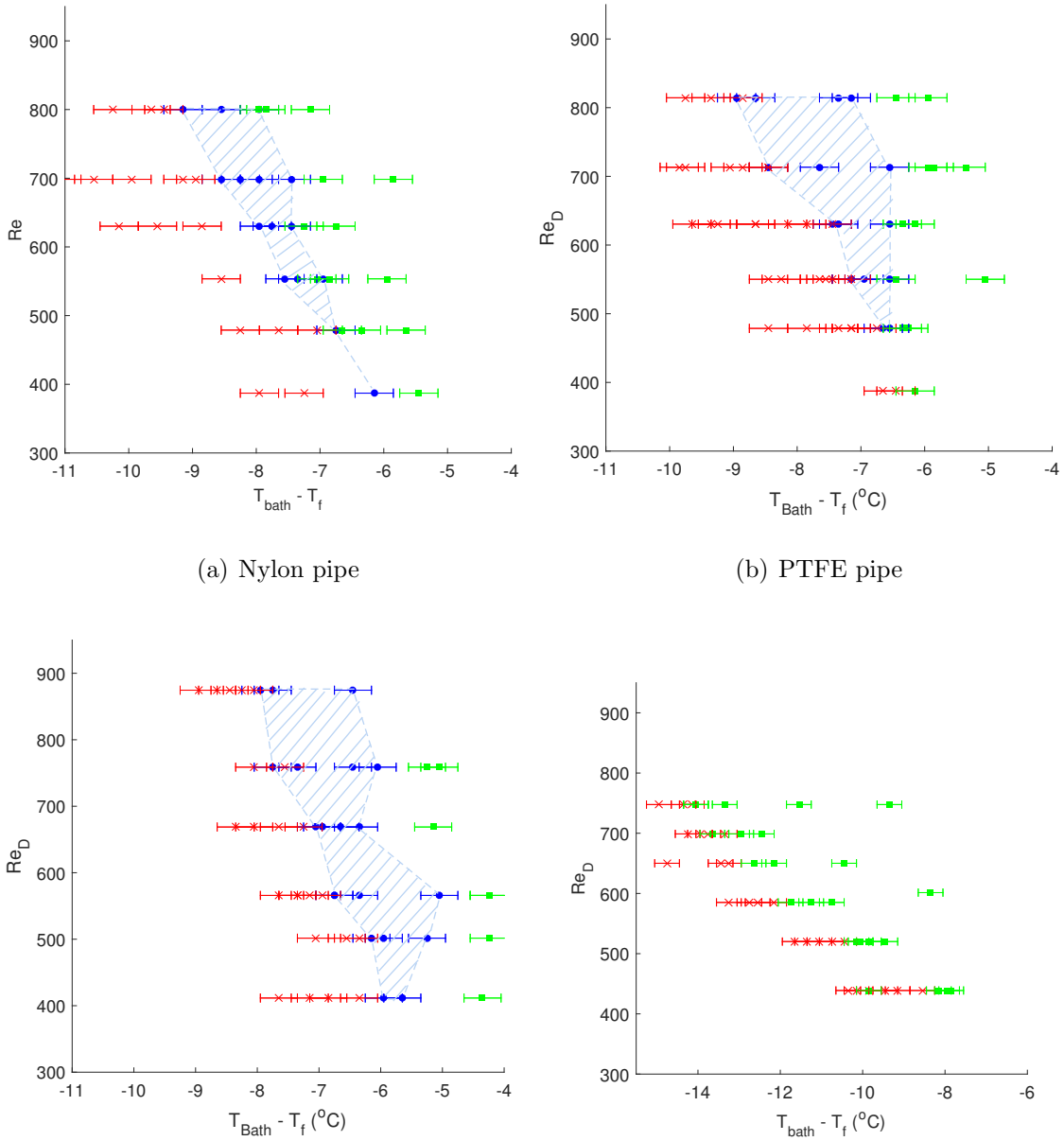


(a) Nylon pipe

(b) PTFE pipe

(c) Silicone rubber pipe

(d) Aluminium pipe

Figure 6.3: Operation graph of Re number against $T_{Bath} - T_f$ for coiled pipes, (a) shows nylon, (b) PTFE, (c) silicone rubber, and (d) aluminium. Blockages are represented by red x, ice production by blue circles, and no ice formation by green squares.

*PTFE* - PTFE (see Figure 6.3 (b)) has a very wide operation region at higher Re readings, with 2 °C between the highest and lowest ice production temperature. However, at lower Re values, this range shrinks until no ice can be produced for

the lowest Re value (lowest flow rate). The operation region also occurs at lower $T_{Bath} - T_f$ than nylon, likely due to the reduced thermal resistance per metre of pipe.

*Silicone rubber* - Silicone rubber (see Figure 6.3 (c)) has a wider operation region at the top than nylon but not as wide as PTFE. However, this wide region is maintained across all flow rates (Re values), unlike nylon and PTFE. The ice production region also has a lower $T_{Bath} - T_f$ than nylon and PTFE. Again, this result indicates the resistance should be much lower, possibly due to a higher thermal conductivity than that quoted.

*Aluminium* - Initially ice slurry would be produced quickly within a few 100 seconds of the experiment starting. All aluminium experiments where ice slurry was produced resulted in a blockage (See Figure 6.3 (d)).

### 6.3.3 Ice Measurements

Ice measurements were taken three times during each experiment using calorimetry, an average was taken and plotted against $T_{Bath} - T_f$, see Figure 6.4. The highest ice fraction is achieved with PTFE and nylon pipe though PTFE appears to produce the same ice fractions at a warmer $T_{Bath} - T_f$. Silicone has the lowest ice fractions, but ice production was possible at warm $T_{Bath} - T_f$ close to -4.5°C. Lower ice production with silicone could be because of the increased pressure loss from pumping the slurry similar to the increase seen from pumping feedstock fluid. Also, the flexible silicone rubber pipe can expand under large internal pressures, slowing fluid velocity further and increasing the ice fraction further.

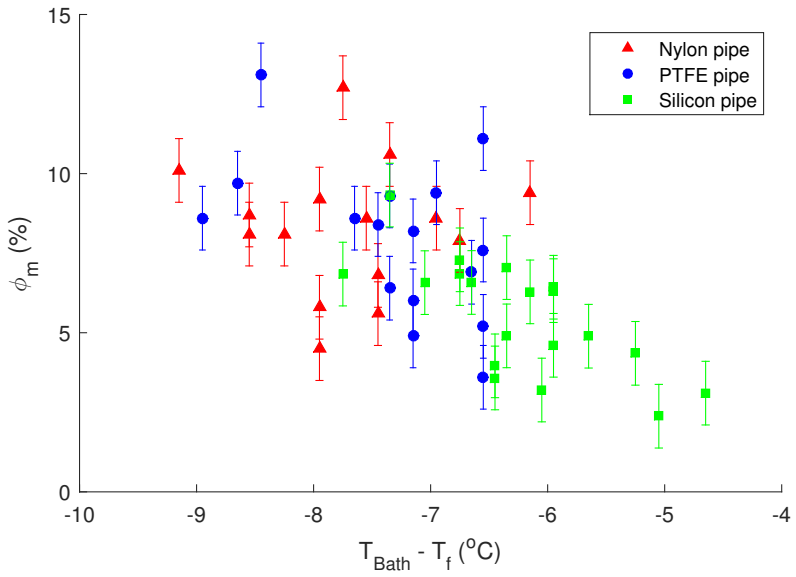


Figure 6.4: Graphs of ice fraction against $T_{Bath} - T_f$, for experiments with four different material coils. Inlet brine was kept at 20°C.

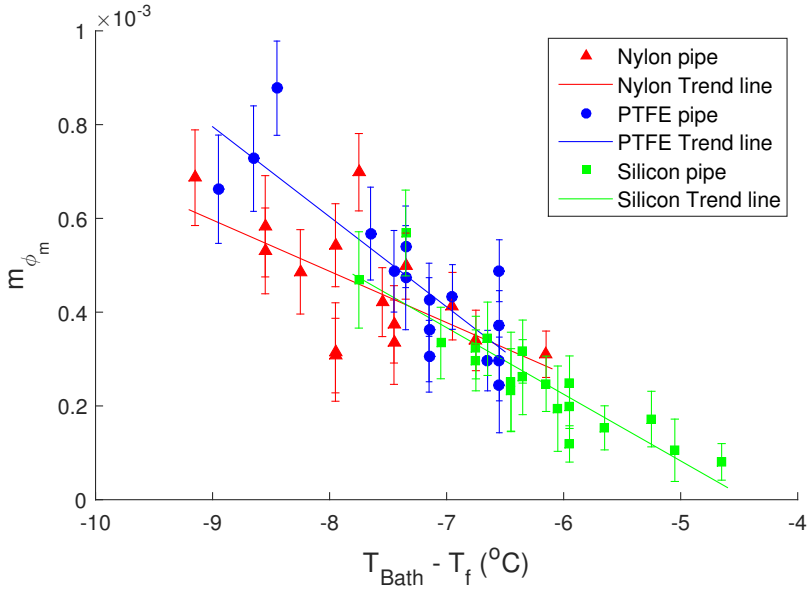


Figure 6.5: Graphs of ice production rate against $T_{Bath} - T_f$, for experiments with four different material coils. Inlet brine was kept at 20°C.

The ice fraction was combined with the experiment flow rates to plot ice production rate against $T_{Bath} - T_f$ in Figure 6.5. Ice production rates also appear to be similar for nylon and PTFE, though PTFE still occurs at warmer temperatures. This

indicates that ice contact angle (surface energy) of the material could have impact on ice production and appears to enable higher ice production and fractions to be produced. However, the results the silicon rubber pipe contradict this theory. Further investigation with a wider range of surface properties would be required to confirm this relationship.

### 6.3.4 Ice Crystal Size

Ice crystal results were collected using the procedure outlined in §3.3.6. Examples of the pictures taken for nylon, PTFE and silicone rubber pipes can be seen in Figure 6.7. Figure 6.6 shows a histogram of the recorded measurements. The data shows very similar crystal sizes for the three materials, it is difficult to conclusively prove one is better. PTFE has the lowest max size measured but silicone has the lowest mean, though only by 1$\mu$m. Nylon has the highest mean and max size reading and appears to produce bigger crystals. Overall, changing the plastic material appears to have little effect on crystal size especially when compared to scraped surface generator results.

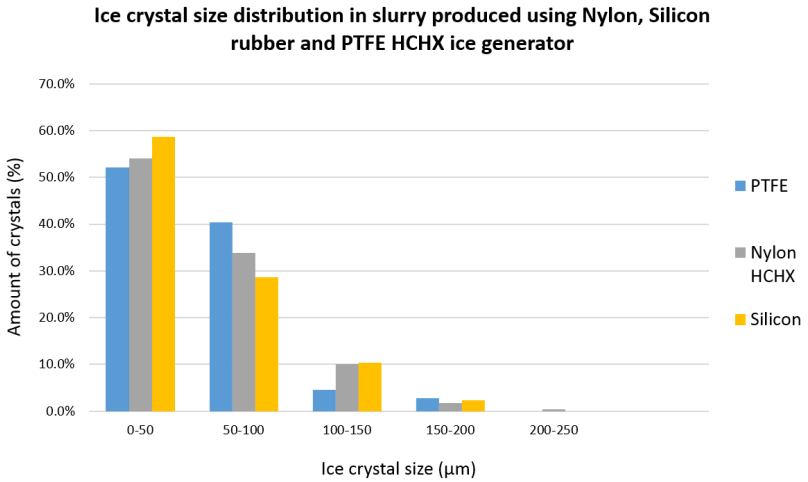


Figure 6.6: Histogram of crystal sizes measured from ice slurry from a nylon, silicone and PTFE HCHX.

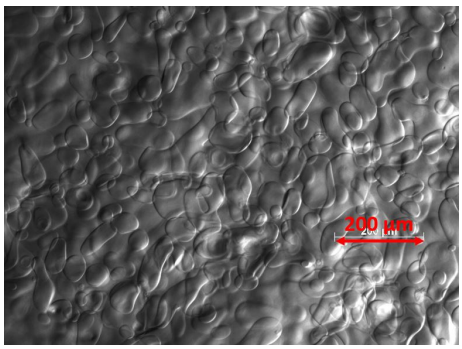


(a) Nylon HCHX

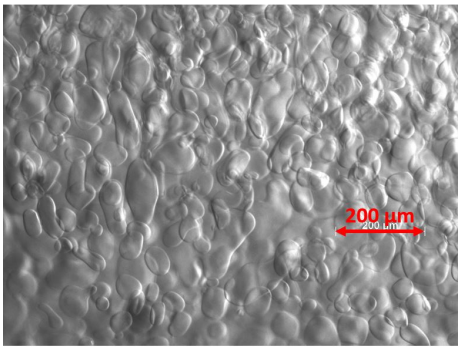


(b) PTFE HCHX

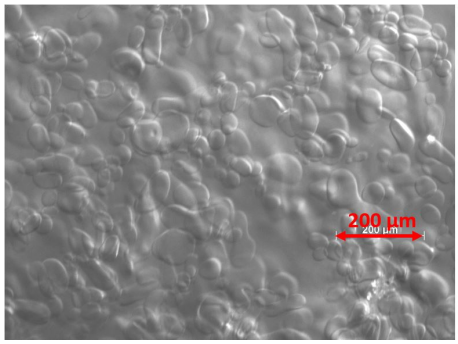


(c) silicone rubber HCHX

Figure 6.7: Pictures taken with 10X magnification of ice slurry produced with nylon, (a), PTFE, (b), silicone rubber pipe, (c). Each photo is 1.1mm wide and 0.77mm high.

## 6.4 Discussion

Using PTFE instead of nylon resulted in an increase in ice production. This could be because of the reduced ice adhesion strength with increased contact angle of PTFE, as noted by authors such as Zou et al. (2011). Work and Lian (2018) evaluated much of the work on ice adhesion strength, concluding that temperature and roughness (even below 20$\mu$m) had an effect. The reduction in adhesion strength from the high contact angle PTFE pipe may have been counteracted by its increased surface roughness over nylon. Similarly, warmer temperatures may have led to lower ice adhesion with PTFE. However, changes in surface roughness and temperature are

comparatively small and would probably have a smaller effect on adhesion than a large contact angle change. None of the work cited previously has used brine, which is known to affect adhesion strength (Makkonen (2012)).

Silicone has a contact angle between the PTFE and nylon, but lower ice fractions were produced. This could be as a result of a higher pressure loss from pumping fluid and slurry through the flexible pipe.

Aluminium pipes blocked as ice created adhered to the wall. Previous authors have shown that ice adhesion strengths are higher for metals with similar surface properties (Raraty and Tabor (1958), Petrenko and Whitworth (2002)). As noted previously, lower temperatures and higher surface roughness could also contribute to greater ice adhesion (Work and Lian (2018)). However, it is most likely that the metal pipe had a high conductivity which failed to slow ice growth down sufficiently allowing too much ice to grow until the pipe blocked.

### 6.4.1 Section Conclusion

Assessing results form the different HCHXs against the original objectives, the following conclusions can be made:

*Improved ice production* - Nylon and PTFE offered the highest production rates and ice fractions, though PTFE was slightly better than nylon. Silicone consistently produced lower ice fractions and production rates.
*Reduce energy cost* - Silicone rubber allowed the warmest refrigeration temperatures and therefore could be the most energy efficient of the materials tested. PTFE allowed slightly warmer refrigeration temperatures than nylon. This indicates that reducing the thermal resistance of the pipe reduces the energy cost.

*Improved reliability* - As expected the high conductivity of the aluminium pipe made it impossible to slow and control ice production rate. Ice formed in the pipe appeared to adhere to the sides and block the pipe over time offering no stable production region. Silicone had the largest stable production region of the remaining three materials, with a wide operating temperature range, even at low Re flows. PTFE was better than nylon but only at higher Re values.

## 6.5 Residence Time Experiments

### 6.5.1 Introduction

Obtaining an operation graph for a coil every time a new material or size pipe is used can be time consuming. An experiment was designed to try and predict where the stable ice production region might be.

The longer a fluid spends in the cooled pipes the more heat that is transferred. The proposed experiments were designed to investigate if the time until nucleation can be quantified to estimate when nucleation and blocking occur.

### 6.5.2 Experimental Method

Samples of each coil material, 0.25m long, were held in a fixed position in the refrigeration bath. Each pipe was given 0.1m clearance either side, at least 10 times its $D_o$. A diagram of the experimental apparatus can be seen in Figure 6.8. A picture of the frame and samples is displayed in Figure 6.9. Valves were opened to let new 5wt.% brine in and closed before submerging the coils. This prevented heat transfer axially outside of the cooled section. Thermocouples ran from the valve to the middle of the pipe; small rubber rings held the thermocouple at least 2 mm from

the inner surface. Data was processed using the same method as discussed in §3.2.

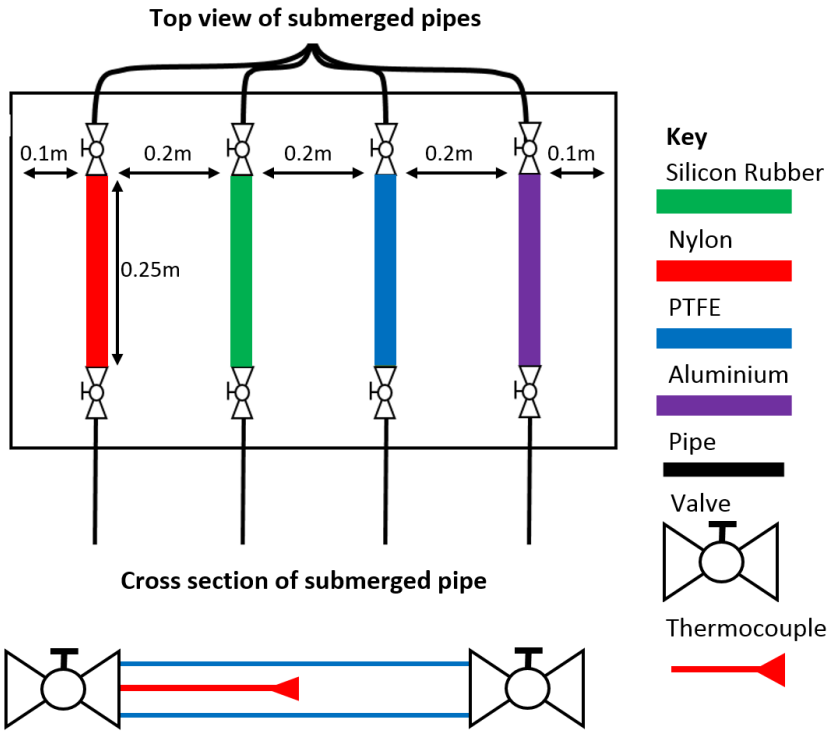


Figure 6.8: Diagram of experimental set up for residence time experiments, including positions of pipes and thermocouple.

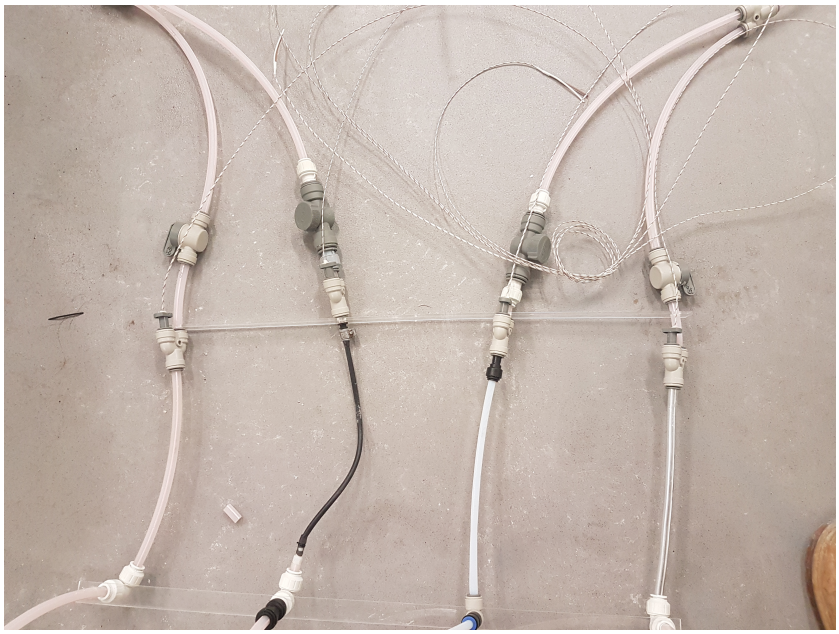

Figure 6.9: Picture of coils and valves, with perspex frame used to hold them in place.

### 6.5.3 Results and Discussion

For each pipe material at least 35 experiments were conducted with valid results collected. Invalid results occur when there was no nucleation in the pipe within 500 seconds. Beyond this point the bath starts to heat up and no ice nucleation was observed in the coil during the experiments in §4.4.

The time of ice nucleation was determined by examining temperature measurements from inside the pipes. Fluid nucleation is observed as a sharp rise in temperature after the fluid has been supercooled. The time taken until this occurrs is the nucleation time, $t_{nuc}$.

As discussed in §2.3.1 temperature can be used to indicate ice fraction when a known quantity of FPD has been added. Using Equations 2.13 and 2.14 a temperature of $\approx -3.9$°C for $\phi_m = 20\%$ was found. The fluid will reach this temperature twice, once during supercooling and once after nucleation. Time taken to reach the second occurrence is the time to reach 20% ice fraction, $t_{20}$.

Temperatures recorded during one experiment are displayed in Figure 6.10. All pipes started at the same temperature (22°C) and were submerged at the same time. The basic heat conduction through a pipe, ignoring film coefficients on the walls, is governed by Equation 6.2.

$$q' = q/L = \frac{2\pi k(T_{in} - T_{Bath})}{ln\left(\frac{D_i}{D_o}\right)} \tag{6.2}$$

Thermal conductivity, k, and $ln(\frac{D_i}{D_o})$ are the determining factors which influence the rate of heat transfer through the pipe wall.

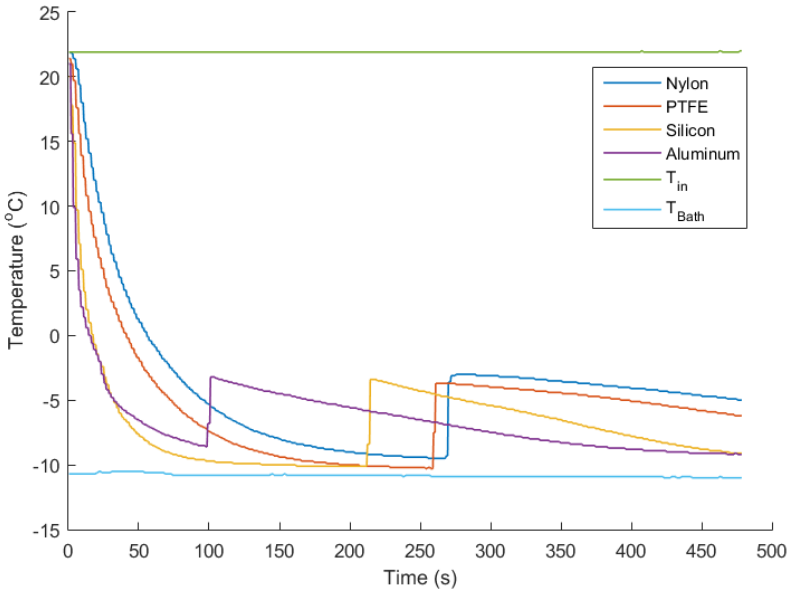


Figure 6.10: Temperature distributions for one residence time experiment with four different material samples, $T_{in} = 22°C$, $T_{Bath} = -10.5°C$. The internal fluid used was a 5wt.% NaCl brine solution at 22°C.

A lumped capacitance method was used to approximate the rate of heat loss from the pipes. The pipe and containing fluid are lumped together and considered as one part, with close to uniform temperature. Energy in and energy out are balanced assuming the $T_{Bath}$ changes little due to heat removed from the submerged samples and using U as the heat transfer coefficient.

$$\dot{Heat}_{out} = -\dot{Heat}_{in} \tag{6.3}$$

$$UAs(T - T_{Bath}) = mc_p \frac{dT}{dt} \tag{6.4}$$

Solving this differential equation produces Equation 6.5, where $T_{Start}$ is the temperature of the fluid (and pipe) before submerging in the bath.

$$T - T_{Bath} = (T_{Start} - T_{Bath})e^{\frac{-mc_p t}{UA_s}} \tag{6.5}$$

Temperature followed an exponential relationship with time as long as m, $c_p$, U and

$A_s$ are constant. In reality, $c_p$ and U would change with fluid phase change. Also, the conductivity of PTFE, nylon and silicone would be too low for a lumped capacitance model. Though, it is adequate to show that the temperature of the pipes fell exponentially at a rate based on their thermal conductivity.

As expected, aluminium cooled the fastest, though surprisingly silicone had a similar cooling rate. Brine inside the silicone pipe remained supercooled and reached steady state before nucleation was observed. With aluminium, nucleation occurred quickly, within 100 seconds, before steady state had been reached. PTFE and nylon had slower rates of cooling and appear to nearly reach steady state before nucleation occurred.

After nucleation, aluminium and silicone maintained similar slower cooling rates than previously observed at the same temperature. Nucleation causes an increase in the driving temperature difference as the fluid warmed from supercooled to $T_f$. However, the formation of ice layers inside the pipes increases the thermal resistance and slows heat transfer. The rate of temperature decrease slowed further over time as as the driving temperature difference dropped as a result of decreasing $T_f$.

The temperature at which nucleation ($T_{nuc}$) started was also recorded in the experiments and has been plotted in Figure 6.11. Aluminium $T_{nuc}$ was the warmest, as predicted by the theory. At low $T_{Bath}$ temperatures (below $T_{Bath} - T_f < -8\ ^\circ$) the recorded nucleation temperatures were very low with a lot of variation in the readings. The variation could be due to the frequency of data logging (every second) and the high rate of heat transfer. The exact temperature at the point of nucleation may have been missed.

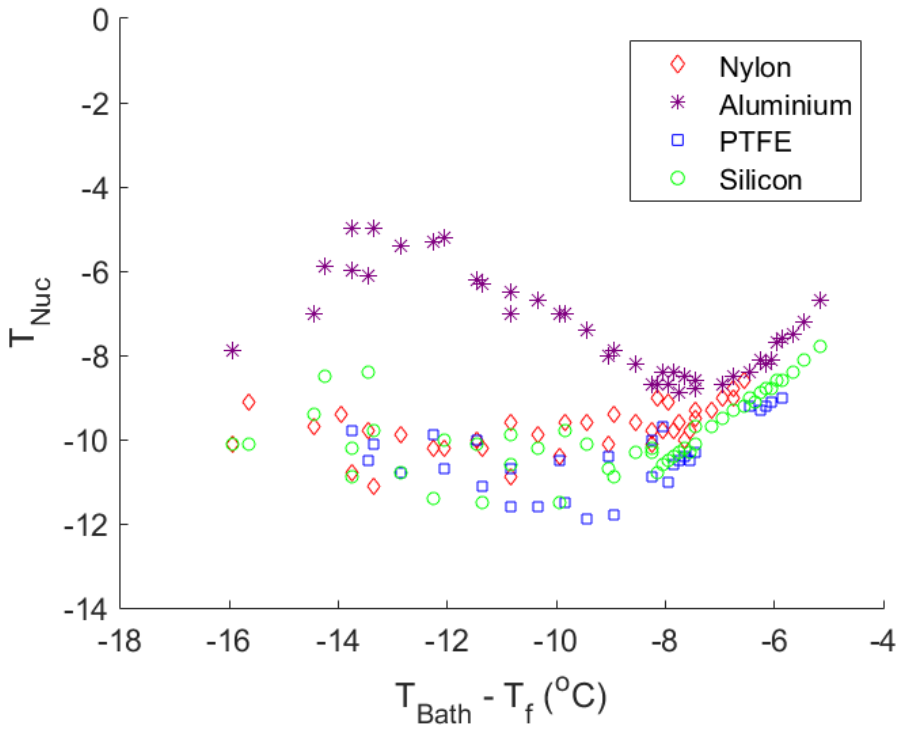


Figure 6.11: Graphs of nucleation temperatures (in °C) against $T_{Bath} - T_f$, for experiments with four different material samples. The internal fluid cooled was 5wt.% NaCl brine solution at 22°C.

Fluid temperatures at the point of ice nucleation, for nylon, silicone and PTFE were close together. Nylon appeared to have the warmest average $T_{nuc}$ followed by silicone then PTFE. This fits with the theory that contact angle (and surface energy) influence ice nucleation. However, aluminium does not fit this rule.

Above $T_{Bath} - T_f = -8$°C ($T_{Bath} = -11$°C) nucleation temperatures linearised and stayed just above the limiting cooling temperature of $T_{Bath}$, a small difference in nucleation temperature between materials is still observed. Therefore these results indicate that nucleation temperature is dependent on the material used, though also limited by $T_{Bath}$ when $T_{Bath} > -11$°C.

Graphs of results, with $t_{nuc}$ (time until nucleation occurs) against $T_{Bath} - T_f$, were

plotted and are shown in Figure 6.12 for all four materials. Exponential lines of best fit have been plotted along with the coefficient of determination, $R^2$. An exponential was chosen because Equation 6.5 shows that the nucleation time and temperature are related by an exponential when cooling or heating.

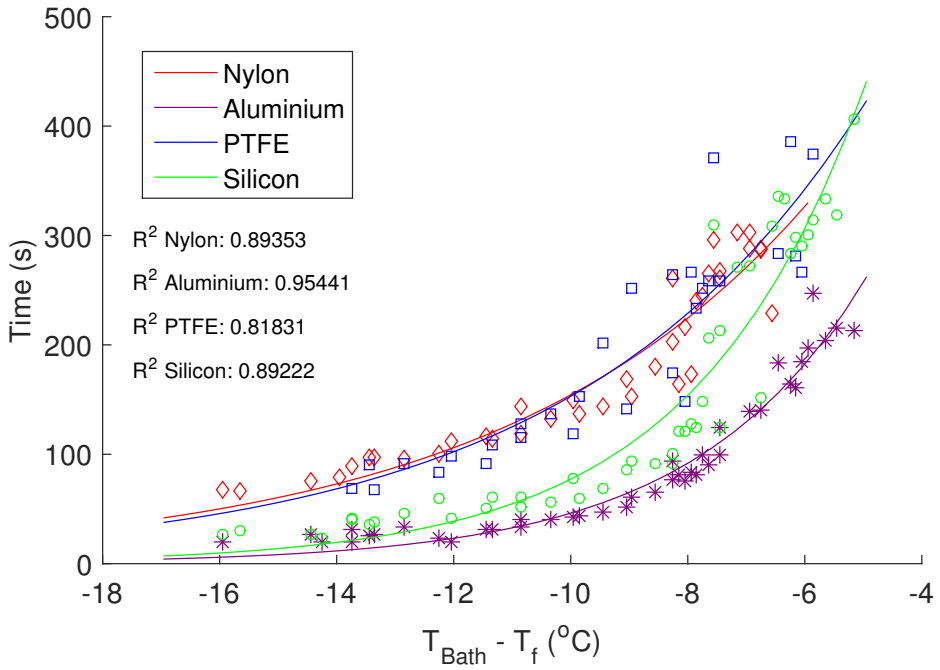


Figure 6.12: Graphs of time until nucleation occurred for different $T_{Bath} - T_f$, for experiments with four different material samples.

All materials showed an increase in $t_{nuc}$ as the temperature difference ($T_{Bath} - T_f$) got warmer, though the rate of increase for silicone was much higher than other materials. Initially, silicone has $t_{nuc}$ values comparable with aluminium, though they rise to similar values to PTFE and nylon at warmer temperatures. It is apparent that for nylon and PTFE $t_{nuc}$ values were similar, though at colder $T_{Bath} - T_f$ nylon took slightly longer than PTFE to nucleate and the reverse at warmer $T_{Bath} - T_f$ values. As expected, due to its high conductivity, aluminium consistently had the shortest nucleation times.

At warmer $T_{Bath}$ values there is more scatter and deviation between experimental

results. The displayed $R^2$ values show that the most accurate fitted curve is for aluminium, and the least for PTFE, which had the largest variation in results. There were also experiments at $T_{Bath} - T_f$ values (-9 to -5°C) where no nucleation was observed with PTFE. This is likely due to the low contact angle and the hydrophobic surface which makes it unfavourable for ice nucleation.

The times until 20% ice fraction has been achieved ($t_{20}$) were plotted against $T_{Bath} - T_f$. The data in Figure 6.13 follows an almost identical pattern to the one is Figure 6.12 except the values are higher. At lower $T_{Bath} - T_f$ values, $t_{20}$ is close to $t_{nuc}$, as $T_{Bath} - T_f$ gets warmer $t_{20}$ and $t_{nuc}$ get wider apart and higher due to a lower temperature difference driving heat transfer. PTFE and nylon no longer follow the same trend. Nylon's $t_{20}$ times increase more than PTFE, showing that they will have a higher predicted operation region.

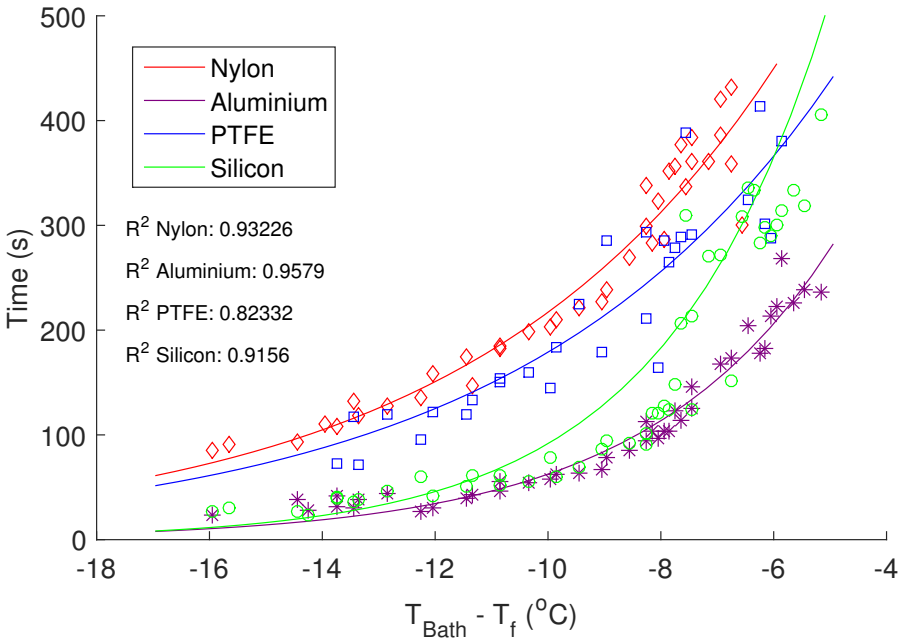


Figure 6.13: Graphs of time $\phi_m = 20\%$ was reached, for different $T_{Bath} - T_f$, for experiments with four different material samples.

### 6.5.4 Plotted on to Operation Graphs

The data and lines of best fit from Figure 6.12 and 6.13 can be used to find a relationship for the times ($t_{20}$ or $t_{nuc}$) based on $T_{Bath}$ ($t_{nuc}(T_{Bath})$ and $t_{20}(T_{Bath})$). The times found can be converted into an equivalent flow rate and therefore Re, using Equation 6.6.

$$\dot{m}_{pre} = \frac{(\pi(D_i/2)^2 L\rho)}{(t_{nuc}(T_{Bath}))} \tag{6.6}$$

Figure 6.14 shows the new lines predicting operation regions for the four materials and the actual operation region found. Red represents the line created using $t_{20}$ and green represents $t_{nuc}$.

For all materials, the predicted operation regions plotted is at lower $T_{Bath}$ temperatures than those found during experiments. This is likely because of two factors:

- Firstly, heat transfer within the pipe only occurs by natural convection, whereas steady flow forced convection increases the heat transfer rate and encourages mixing in the pipes.
- Secondly, Equation 6.6 assumes the fluid all travels at a constant average speed through the pipe. In reality, it would travel at a slower speed and spend longer in the pipe.

The gap between the two lines is the predicted operation region, assuming blockages occur at $20\% = \phi_m$; in reality blockages occur at lower ice fractions. For nylon the predicted region is a similar width to the experimental region, indicating it could be reasonably accurate. However, PTFE and silicone both have wide experimental regions but thin predicted ones. The area is dependent on the time between $t_{nuc}$ to $t_{20}$ which is short for PTFE and silicone. This could be an error with the regres-

sion lines plotted in Figure 6.13 and 6.12. At warmer $T_{Bath}$ (warmer $T_{Bath} - T_f$) values there is more scatter in the time recorded. For example two $t_{20}$ readings at $T_{Bath} = -11.8°C$ were 278 and 390, over 100 seconds difference. This scatter is likely because the chance of ice nucleation is dependent on the temperature driving the phase change. Natural statistical variance is known to occur with nucleation and can lead to scattered results, such as seen here.

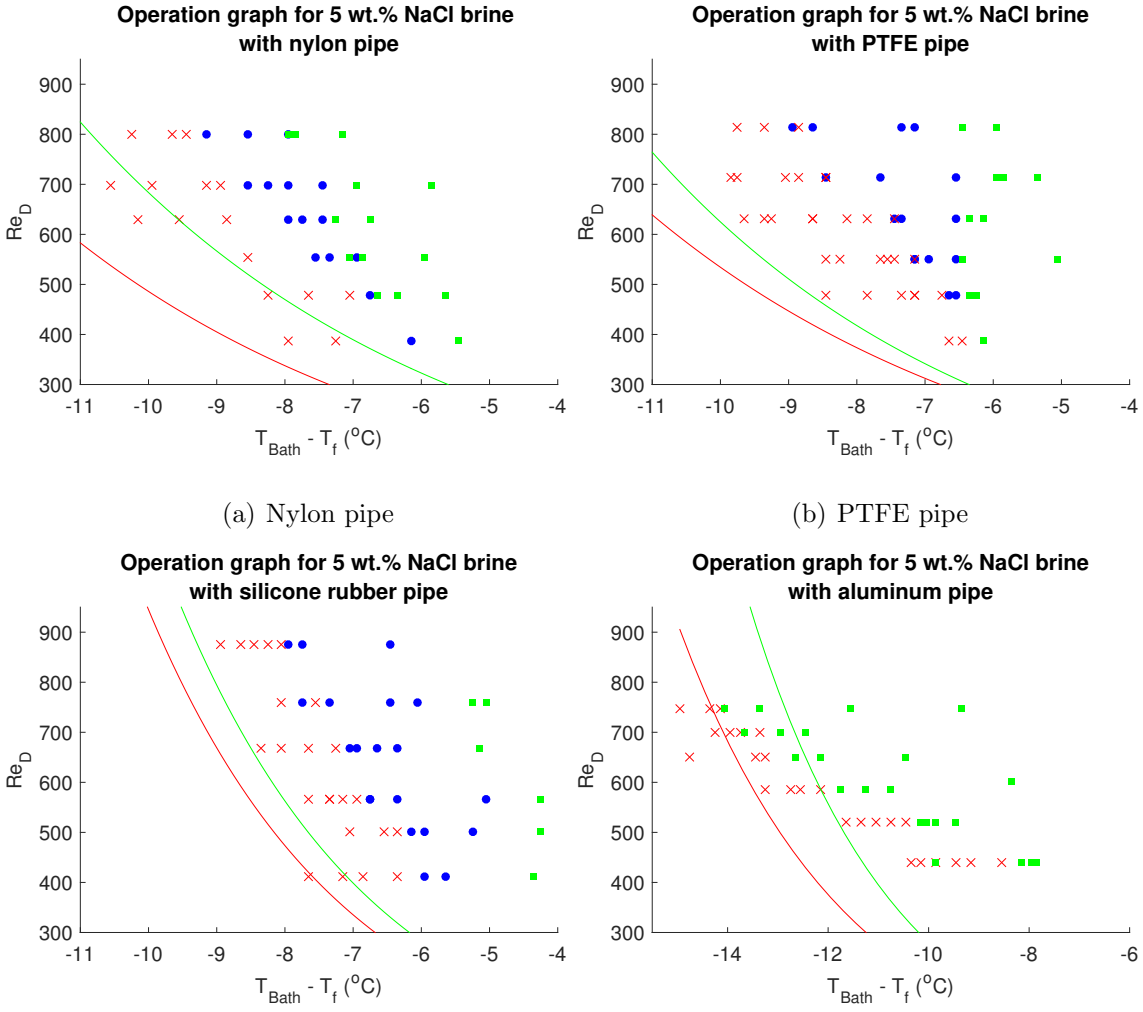


(a) Nylon pipe

(b) PTFE pipe

(c) Silicone rubber pipe

(d) Aluminium pipe

Figure 6.14: Operation graph of Re number against $T_{Bath} - T_f$ for coiled pipes of (a) nylon, (b) PTFE, (c) silicone rubber, (d) aluminium. Inlet fluid is 5 wt.% NaCl brine. Red line: predicted blockage point (20% ice fraction). Green line: predicted nucleation point.

The amount of supercooling at the point of nucleation has also not been accounted for in this work. The nucleation of ice from the cooled fluid can lead to ice fraction close to 10% already meaning little cooling is needed to reach 20% = $\phi_m$ condition.

For aluminium it is difficult to draw a significant conclusion as there is no stable ice production region, though both lines fall in the same area as the cross over point between blocking and no ice production. This demonstrates that the method still indicates close to the correct temperature region.

### 6.5.5 Adjusted for Flow Speed

As mentioned previously, particles in the flow do not travel at the average velocity for the whole length. The graphs were replotted with an adjustment factor assuming the fluid is moving at 2/3rds the average speed. The factor of 2/3 is from the CFD simulation outlined in Appendix C. From these simulations, a graph of axial velocity for the coiled pipe used was created. It is plotted alongside the analytical solution for flow in a straight pipe (see Figure 6.15). Fluid found within 1mm of the inner bend internal wall moves at half the speed of the average velocity.

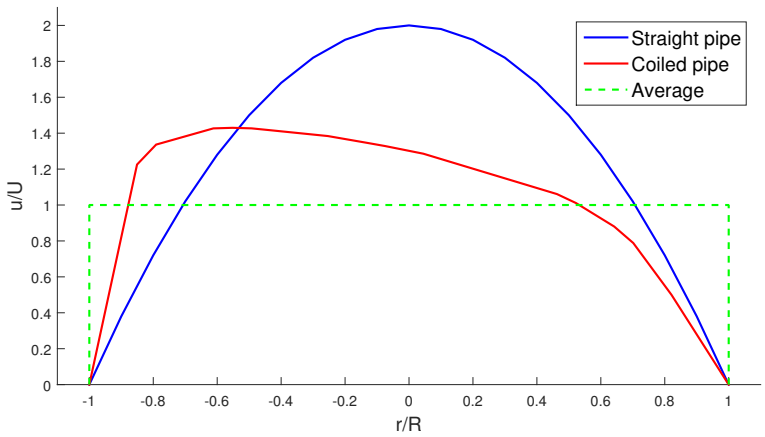


Figure 6.15: Graph of normalised horizontal flow velocity profiles for straight pipe (analytical solution) and coiled pipe (found from the CFD simulation). Outer side: left. Inner side: right.

The adjustment (plotted on Figure 6.16) factor appears to help move the lines closer to the experimental regions. Nylon still shows the best approximation, with the adjustment the nucleation region is close to experimental results. Silicone and PTFE are still away from their regions. The blocking lines are close, but the nucleation still occurred at much lower temperatures in experiments than the line predicts. The motion of the flow could be causing nucleation earlier than with static fluid.

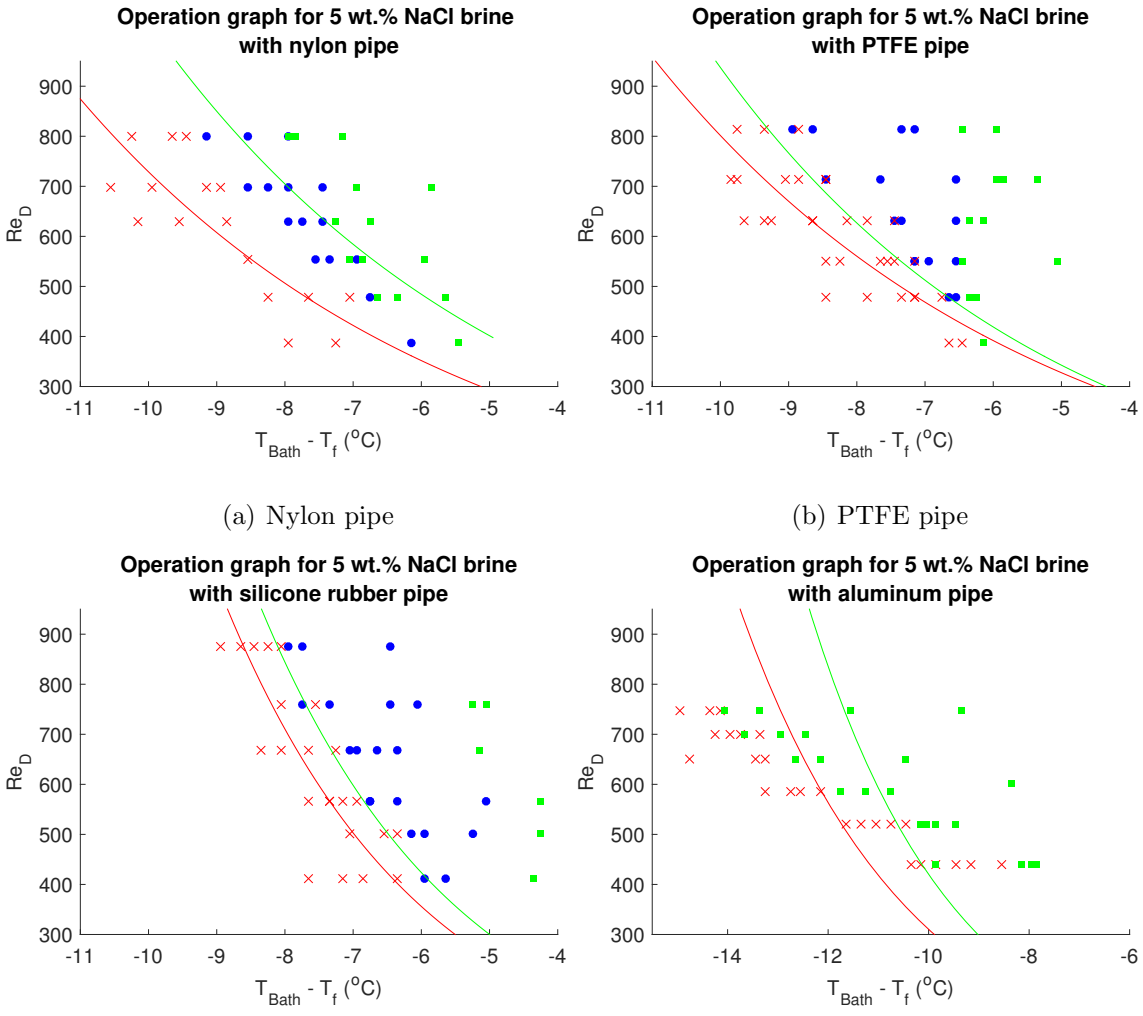


(a) Nylon pipe

(b) PTFE pipe

(c) Silicone rubber pipe

(d) Aluminium pipe

Figure 6.16: Operation graph of Re number against $T_{Bath} - T_f$ with predicted blocking and nucleation lines, same as Figure 6.14. Flow is assumed to move at 2/3rds the average speed.

### 6.5.6 Conclusion

Four samples of material pipe, containing 5wt.% NaCl brine, were submerged in a cold refrigeration bath. Temperature of the brine was monitored over time. Time of nucleation and time to reach 20% = $\phi_m$ were recorded and plotted against bath temperature. Exponential lines of best fit were fitted and used to predict time of nucleation and blocking for flow in different material HCHX.

The predicted regions created provide a good initial approximation of the operation region, though, they fail to adequately take account of the pump characteristics and the effect of forced convection on the flow. With the adjustments to the flow rate the prediction is improved, though regions for PTFE and silicone pipe are still too narrow. This method could still be useful when plotting the operation region as it gives a good indication of where it will fall.

There are indications that nucleation temperature seems to correlate to material contact angle with water for plastic pipes, though this relationship is hard to prove conclusively from these results. However, this conclusion does fit with current literature and theory outlined in §2.2.2.

The results also appear to indicate that the thermal conductivity on the silicone rubber or thickness of the pipe deviates from those quoted in Table 6.1.

## 6.6 Chapter Summary

- Silicone, nylon, PTFE and aluminium HCHX were all created and tested. Thermal resistance was initially matched though was found to vary in experiments. Results were compared to see if changing the material could improve ice production, increase efficiency or reliability.

- Silicone rubber pipes appeared to offer a wider operation region than other materials, especially at low flow rates. Ice production rates and fraction were consistently lower due mainly to the extra force required to convey fluid.

- No stable ice production region was created with aluminium pipe. PTFE and nylon had the best production rates and ice fractions, these were achieved at warmer temperatures with PTFE than nylon.

- Times taken for stationary fluid to nucleate and reach $\phi_m = 20\%$ were recorded in a separate experiment (residence time experiments). Predictions of ice production regions for each material were created from the data. The predictions did not take account of forced convection and predicted regions at lower temperatures than those from experimental result.

- When fluid flow was assumed to be 2/3rds the average speed the predicted stable operation regions lined up more closely. However, the width of the regions did not match those found in experiments with silicone and PTFE.

# Chapter 7

# Utilisation of Pulsations

## 7.1 Introduction

This chapter explores the effect of adding pressure pulsation to the internal flow pulsations to increase ice production. A pulsing internal flow rate is used to try and create large waves of pressure and flow which can dislodge ice forming. Later in this chapter pressure fluctuations are applied to the outer surface of a flexible pipe during ice formation within the pipe. These methods are compared to the initial experimental method to see if the ice fraction or production rate is increased.

## 7.2 Pulsating Internal Flow

### 7.2.1 Introduction and Background

The effect of internal pulsating flow has been extensively studied in physiology, though, little work has been done with ice slurry generation. However, Gillham et al. (2000) utilised pulsating flow to increase cleaning rates inside HX pipes fouled by whey. A bellows and piston applied a pulse to a uniform inlet flow. High amplitude pulses and big changes in velocity of the pulse increased the shear force at the wall and fouling material removed. Similar results can be obtained with faster steady flow, but this requires more pumping power. Augustin et al. (2010) noted similar results and found pulsing created high periodic acceleration at the wall

which aids fouling removal. Increasing the frequency of pulses decreased cleaning time. Similarly, Weidemann et al. (2014) used pulsatile flow to clean filters. The best improvements in fouling removal were observed at lower velocity flows. Both these papers provide little information on adhesion strengths or shear stress increase.

Womersley number ($Wo$) is often used in physiology and engineering to characterise pulsating flows in pipes. It is calculated using Equation 7.1 where $\omega$ is the angular frequency of the pulsating flow.

$$Wo = D_i\left(\frac{\omega\rho}{\mu}\right)^{\frac{1}{2}} \tag{7.1}$$

Kumar and Narayanan (2010) showed that increasing Womersley number (frequency of oscillation) increased shear stress at the wall over steady flow for all $Wo > 4$. All $Wo$ have been kept above this value in the following work.

Mehta and Khandekar (2015) demonstrated that for single-phase laminar flow, increases in heat transfer (Nu) could be achieved at higher $Wo$. Values of $Wo < 1$ produced much lower heat transfer rates.

The aim of this work was to utilise this fouling removal method and use it to remove ice adhered to the pipe walls. It was theorised, that removing ice from the wall could increase heat transfer from the fluid and increase ice fraction produced.

### 7.2.2 Experimental Method

An experiment was devised using the original set up detailed in §3.2, with the addition of an automated value after the pump and the pressure sensor tube, as shown in Figure 7.1. Closing the valve increased pressure in the air pocket and created a

build up of fluid, which was released by opening the valve.

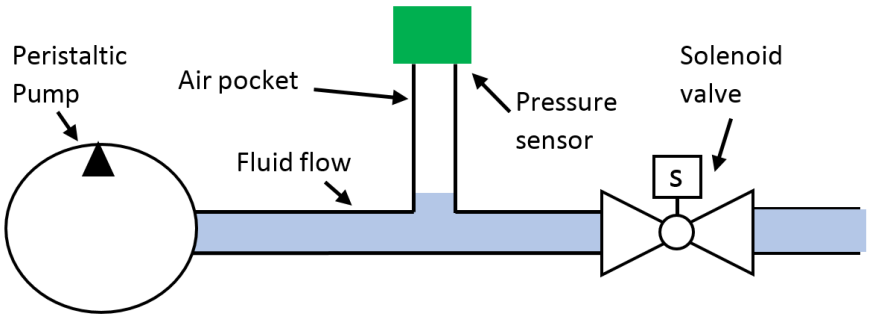


Figure 7.1: Diagram of experimental set up used to generate oscillation in the flow rate.

Five different experimental conditions, with different frequencies, were created by altering the time for which the valve was open and closed. The ratio of open to closed (mark-to-space ratio) was kept the same in each experiment. Table 7.1 shows the experimental settings and pressure build up created. Temperatures and pressure were recorded using the same methods outlined in previous chapters.

Table 7.1: Table of the experimental settings used for pulsating internal flow experiments. Including time flow is on for and the frequency of valve position change.

| **Experiment Figure** | **(a)** | **(b)** | **(c)** | **(d)** | **(e)** |
|---|---|---|---|---|---|
| **Bath Temperature (°C)** | 10.5 | 10.5 | 10.5 | 10.5 | 10.5 |
| **Inlet Temperature (°C)** | 21 | 21 | 21 | 21 | 21 |
| **Pump voltage (V)** | 10 | 10 | 10 | 10 | 10 |
| **Time valve closed (s)** | 1.5 | 2.0 | 2.5 | 3.0 | 3.5 |
| **Time valve open (s)** | 1.5 | 2.0 | 2.5 | 3.0 | 3.5 |
| **Frequency (Hz)** | 1/3 | 1/4 | 1/5 | 1/6 | 1/7 |
| **Womersley number** | 7.23 | 6.26 | 5.60 | 5.11 | 4.73 |
| **Pressure build up (kPa)** | 34 | 51 | 75 | 90 | 90 |
| **Number of Successful experiments** | 3 | 4 | 3 | 3 | 3 |

Figure 7.2 displays a sketch of the pressure and flow rate wave produced using this method of cycling the valve on and off for a set time ($t_{on}$ and $t_{off}$). The exact profile would change depending on the time allowed for pressure and fluid to build in the air

pocket. Unfortunately, the flow rate profile cannot be confirmed as no continuous reading was taken. However, the sketch was similar to what was observed on the Parker Variable Area Flow Meter during experiments.

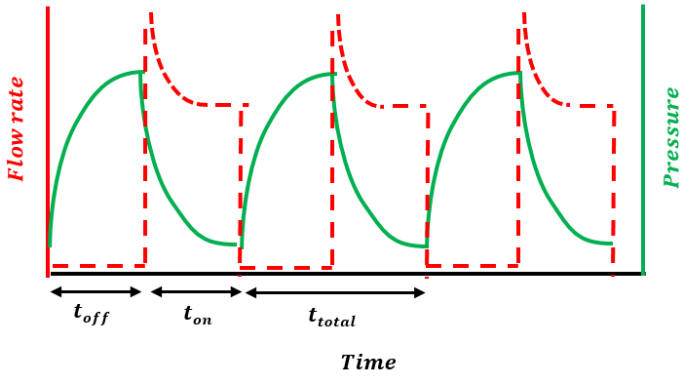


Figure 7.2: Profiles of pressure before and flow rate after the valve is switched on and off.

### 7.2.3 Results

The number of experiments at each frequency is shown in Table 7.1. The range of $Wo$ numbers used was limited by the range where ice slurry could be produced. Outside of these frequencies the pipe blocked. For $Wo > 7.23$ no ice slurry was produced and for $Wo < 4.73$ the pipe blocked. Settings for (a), (b), (c), (d) and (e) from Table 7.1 correspond to the graphs in Figures 7.4 and 7.3.

The solenoid valve used in this experiment had a fast response time of 0.1 seconds, allowing quick changes. Graphs of the pressure readings recorded during each experiment are displayed in Figure 7.3.

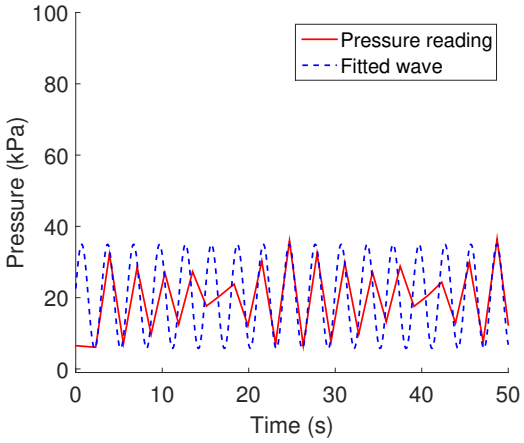


(a) 1/3 Hz

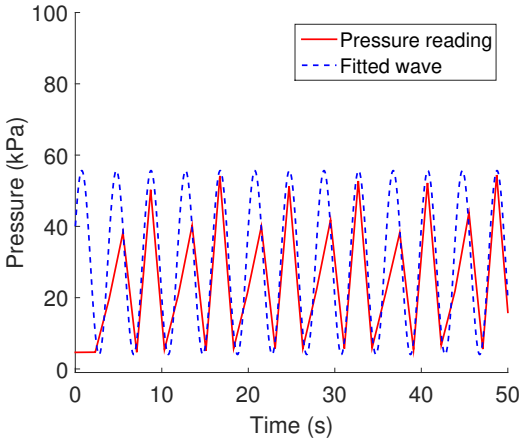


(b) 1/4 Hz

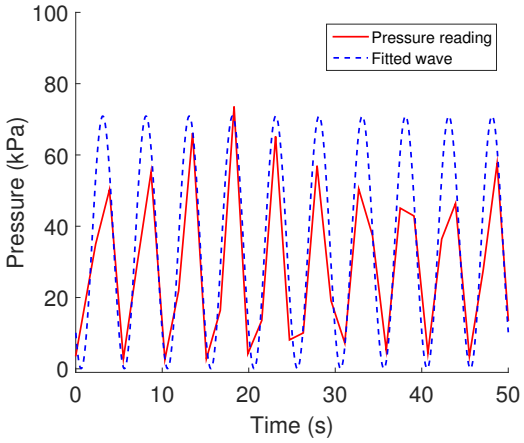


(c) 1/5 Hz

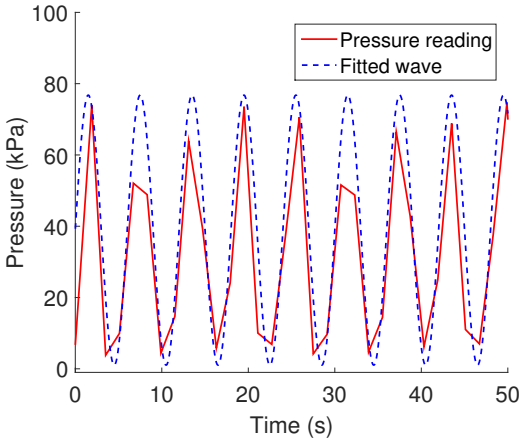


(d) 1/6 Hz

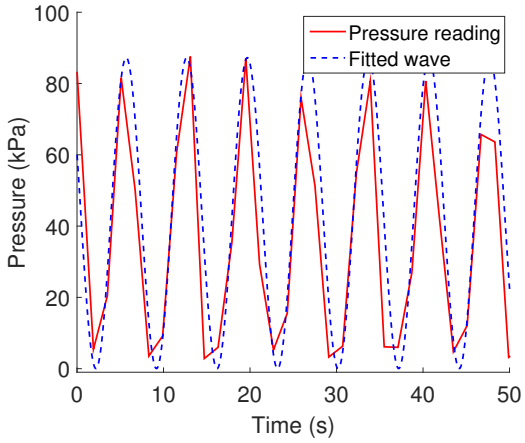


(e) 1/7 Hz

Figure 7.3: Pressure reading for 0-50 seconds of each experiment with a fitted sine wave.

The data logger only sampled data every 1.5 seconds during this experiment due to the large number of channels in use ($f_{sampling} = 1/1.5$). Unfortunately, this was close to the flow pulsation frequency, $f$. The minimal Nyquist sampling criterion of $f/2 \leq f_{sampling}$ was still met for all the experiments. Aliasing was still observed in the data recorded, which appears to have another wave superimposed on it. Therefore, a sine wave matching the frequency of pressure oscillation has been added to Figure 7.3. The frequency of the original data was checked using a fast Fourier transform, to ensure the sine wave fitted was the correct frequency. In reality, a sine wave would not adequately represent the profile, but it has been used here as a reasonable approximation.

As the frequency and $Wo$ decreased, the valve was closed for longer and a larger amplitude of pressure produced. Until 1/6Hz, at which point it reaches the maximum cut off pressure for the pump.

Figure 7.4 shows the pressure and temperatures during experiments with different frequencies. The temperatures followed a similar profile to that shown in previous chapters with a spike in outlet corresponding to ice nucleation. Oscillating flow leads to small oscillations in temperature at the outlet as the fluid here stops and starts. All inlet and $T_{Bath}$ values are kept constant to allow an accurate comparison. Nucleation occurred between 280 and 400 seconds and -7.9 to -8.6°C for all experiments, no correlation with pulsation frequency was observed. Nucleation took between 50 - 100 seconds longer to occur than the same conditions with no pulsating flow.

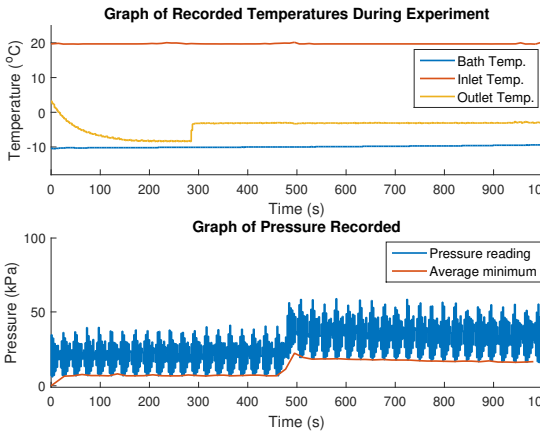


(a) 1/3 Hz, 6.2% $=\phi_m$

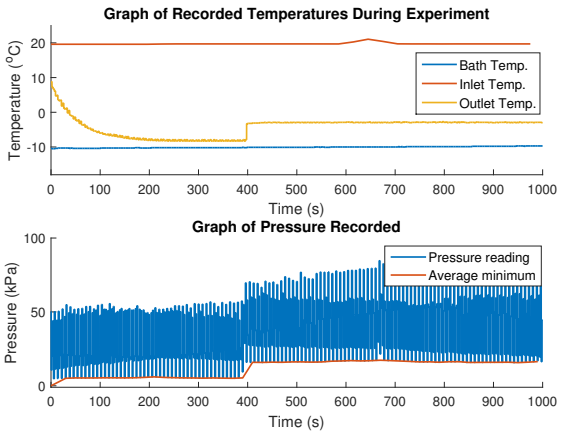


(b) 1/4 Hz, 7.5% $=\phi_m$

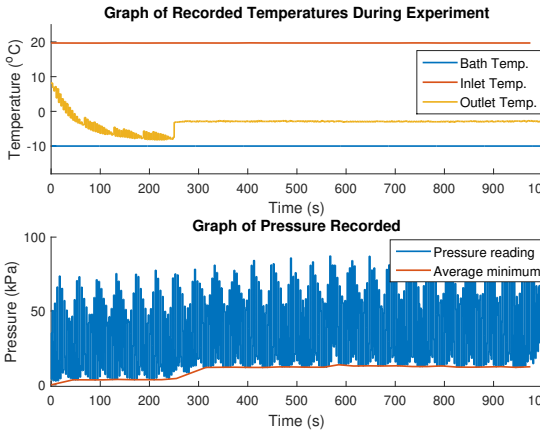


(c) 1/5 Hz, 8.7% $=\phi_m$

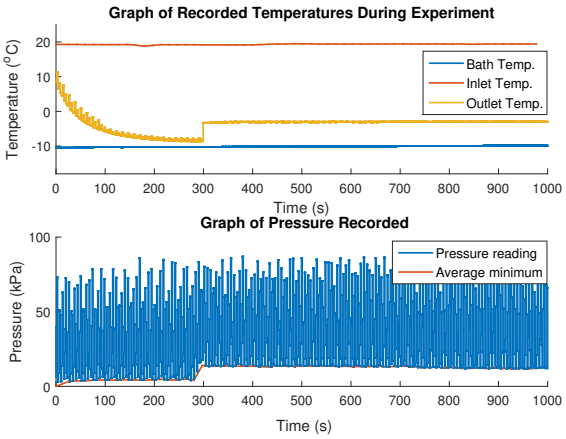


(d) 1/6 Hz, 11% $=\phi_m$

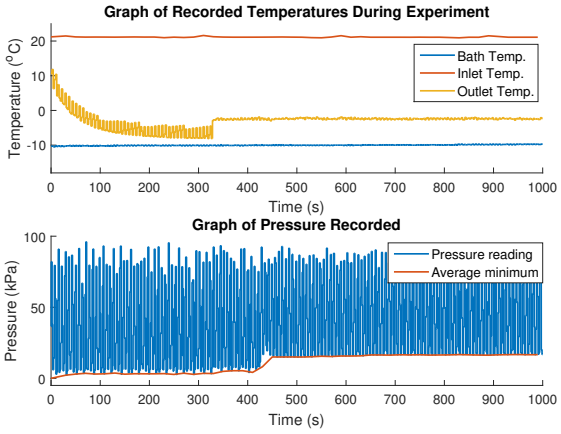


(e) 1/7 Hz, 11.2% $=\phi_m$

Figure 7.4: Graph for different oscillation frequencies, top shows the temperature readings, and bottom, the pressure readings taken. The minimum pressure reading has been averaged to show the pressure drop needed to move ice slurry inside the pipe.

Pressure readings fluctuated with valve frequency, as discussed previously. The minimum pressure recorded increased and stayed high after nucleation occurred. The change has been highlighted by plotting the minimum pressure values at set time steps, see red lines on bottom graphs in Figure 7.4. As with previous experiments, a peak is seen on the red line showing when ice nucleates.

Ice fractions produced were plotted against $Wo$, see Figure 7.5. Measurements were taken using calorimetry from three samples taken throughout an experiment. There is significant scatter in the data with experiments at the same frequency oscillations producing up 4.5% difference in ice fractions. There is a correlation between the data, decreasing $Wo$ from 7.5 to 4.5 increases the ice fraction produced, though the correlation is weak as shown by the low coefficient of determinant ($R^2$).

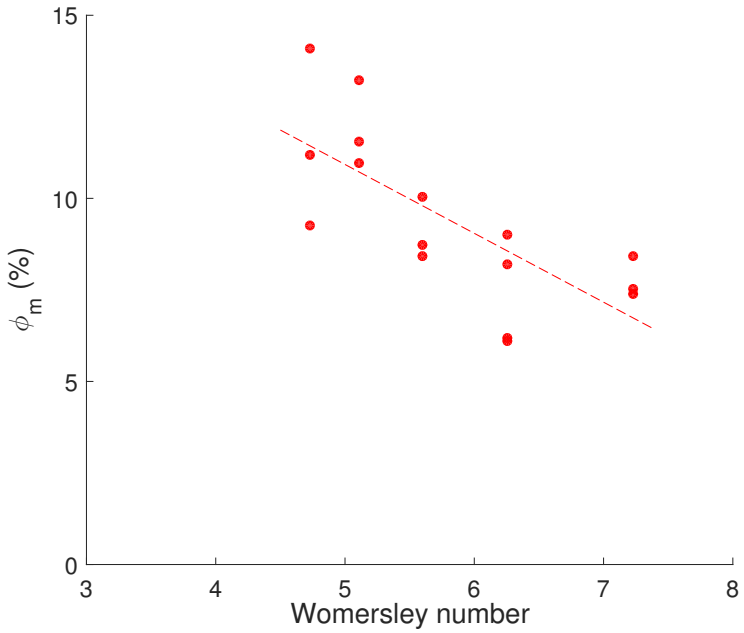


Figure 7.5: Graphs of Womsley number against $\phi_m$ for flow at $T_{Bath} = -10.5°C$ and same pump settings. $R^2 = 0.53$

It was noted that with decreasing $Wo$ there was a decrease in flow rate which could

be causing the increased ice fraction. Experiments without oscillations at the same mass flow rates as those recorded with oscillations were conducted. The results are shown in Figure 7.6. The two sets of data match very closely, showing mass flow rate change was the driving factor for ice fraction increase rather than oscillation.

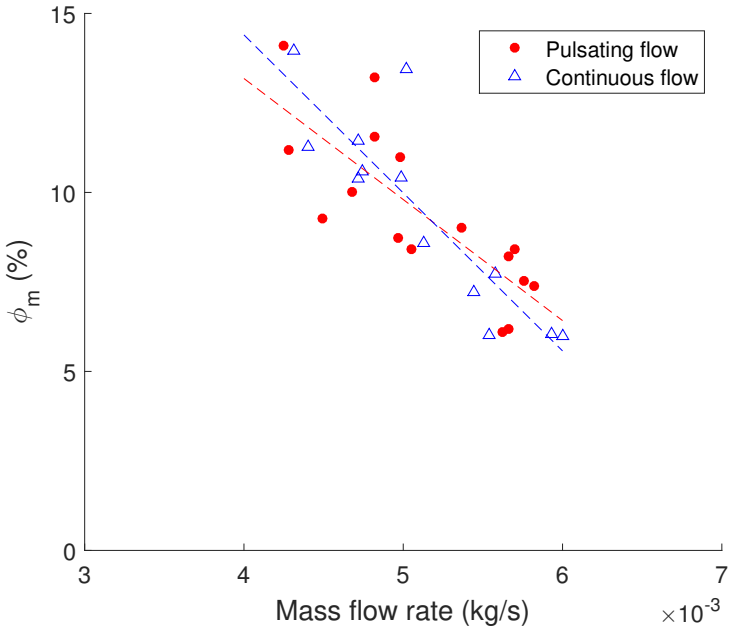


Figure 7.6: Graphs of flow rate through the pipe against $\phi_m$ produced for flow with oscillation and without, $T_{Bath} = -10.5°C$

### 7.2.4 Discussion

Oscillating the flow led to no increase in ice fraction production. Unlike Gillham et al. (2000) and Weidemann et al. (2014) fouling removal appeared not to improve with the addition of a pulsating flow. This may be due to the large distance between the ice generation pipe section and the pulsation source. Hemida et al. (2002) demonstrated an analytical solution for pulsating flow. As the distance from the pulse source increased the flow approached steady flow conditions. Any increase in shear force at the wall, due to velocity pulsation, will be greatly reduced at the end of the coil where ice nucleates. Chattopadhyay et al. (2006) also noted higher

*Nu* values in the entrance region close to the pulse source which fell to steady flow values later in the pipe. Increases in internal heat transfer are unlikely to improve heat transfer to the internal fluid significantly, as the pipe thermal resistance is still high and the limiting factor in heat transfer between fluids.

### 7.2.5 Section Conclusion

Fluctuations in flow rate were created by switching a value on and off, flow speed entering the coil changed from stationary to full speed. Five different frequency pulsations were tested. Pump setting and $T_{Bath}$ were kept constant along with all other parameters in the experiments. Initially, the ice fraction appeared to increase with decreasing frequency flow fluctuations. Closer analysis showed that the flow oscillations reduced the average flow rate through the pipe. Fluid spent longer in the pipe resulting in higher ice fractions. There is no indication that fluctuating the flow caused increases in shear stress where ice was formed.

Further work on this method could aim to place the valve further along the pipe closer to ice nucleation region. A second improvement could be to use a bellow pump or piston to create a large backflow, as utilised by Gillham et al. (2000).

## 7.3 Compression of the Outer Pipe

### 7.3.1 Introduction

A review of ice adhesion conducted by Work and Lian (2018) noted that wall strain has an impact on ice adhesion. If a surface strain differs from that of attached ice an adhesive break is likely to occur at the interface. This process is observed with pneumatic de-icers outlined in §2.6.3 (Petrenko and Whitworth (2002)) which are used to remove ice build-up on plane wings.

Two different experimental designs are proposed in this section for how this could be achieved; one was successfully tested. An oscillating pressure is applied to the outer surface of a silicone rubber pipe to cause it to deform. The aim was to deform the pipe enough to break up ice formed on the pipe walls and force it out the pipe.

### 7.3.2 Background

Silicone rubber pipe used previously in Chapter 6 was used in these experiments, with a pressure applied to the outside. Shapiro (1977) and Kozlovsky et al. (2014) provide an outline of the governing 'tube law' for pressure applied to a flexible pipe. The dimensionless transmural pressure ($\Pi$) shown in Equation 7.5, is varied to force the pipe into different cross sections, as shown by Figure 7.7.

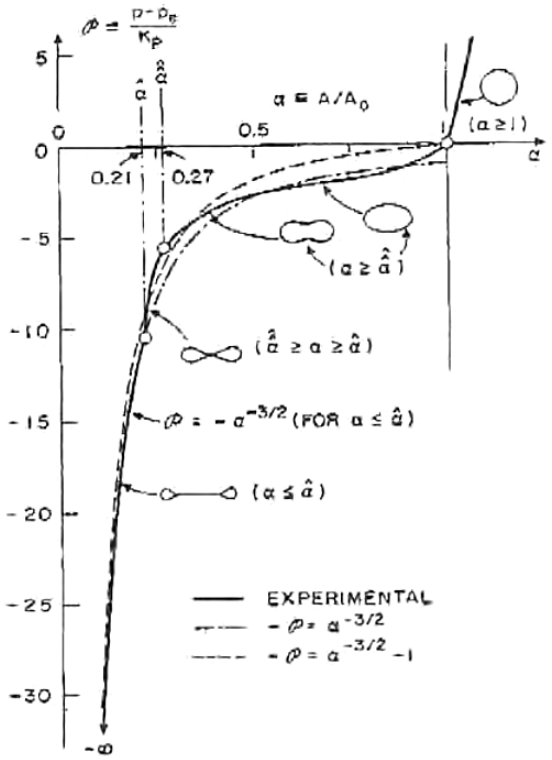


Figure 7.7: Graph taken from Shapiro (1977) of non-dimensionalised cross section, $\alpha$, against transmural pressure $\Pi$ (represented by $\varphi$ on the graph).

Young modulus, E, Poisson's ratio, $\nu$ and thickness ratio, $\lambda$, are used to find flexural rigidity of the tube ($K_p$). Term $\alpha$, is found from original cross-sectional area ($A_{c,0}$) and current pipe cross sectional area ($A_c$). Internal and external pipe pressure are represented by $P_{int}$ and $P_e$.

$$\lambda = \frac{(D_o - D_i)/2}{D_i} = 0.1 \tag{7.2}$$

$$K_p = \frac{E}{12(1-\nu^2)}(ln(1+\lambda))^3 = 469Pa \tag{7.3}$$

$$P_{tm} = P_{int} - P_e \tag{7.4}$$

$$\Pi = \frac{P_{tm}}{K_p} \tag{7.5}$$

$$\alpha = \frac{A_c}{A_{c,0}} \tag{7.6}$$

As $P_{tm}$ approaches $-20K_p$, the pipe's open cross-sectional area is reduced to 20% of its original. For silicone rubber Young's modulus values can be as high as 50 MPa which leads to a value of $-20K_p \approx 100kPa$. This will constrict the pipe to the almost flat profile shown in Figure 7.7 and prevent flow if the pump pressure is insufficient to push the fluid through the constriction.

### 7.3.3 Initial Experimental Design

The original experimental design utilised a large glass 40 litre fermenting vessel, see Figure 7.8 and 7.9. Air was pumped into the silicone rubber coil held inside the glass container. The container was sealed using four threaded rods holding metal struts in place. As the bolts were tightened the rubber seal around the lid compressed to make an air tight seal. The whole container was then lowered into the large bath, see Figure 7.9 (c) and cooled there. Glass was used to enable visualisation of pipe compression. Initially cold brine was pumped into the glass

vessel, though the geometry made it difficult to distribute the brine throughout the container sufficiently.

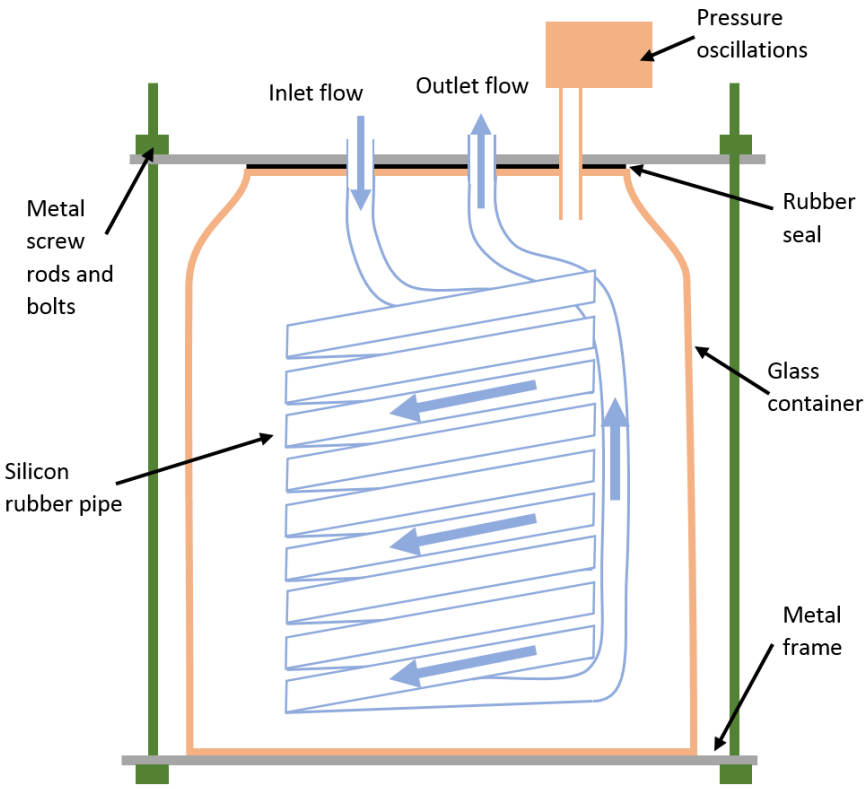


Figure 7.8: Diagram of the glass vessel used with coils inside.

Only 10m of coil could fit inside the glass vessel. During an experiment brine was pumped into the coil to replace the air inside and cooled to try and initiate ice growth. Outer pressure oscillations were provided by a syringe with a pneumatic oscillating press (Figure 7.9 (d)). This method was unsuccessful for the following reasons:

- *Insufficient cooling* - The volume of fluid in the vessel provided an insufficient thermal sink to supercool the fluid low enough for ice nucleation; even when all 40 litres were cooled to the lowest refrigeration temperature of -20°C. When submerged in the larger cold bath, internal heat could not be removed quickly enough through the glass. Adding cooling coils cooled the fluid down in a

localised area and meant further holes in the vessel where leaks could occur were required.

- *Insufficient volume displaced* - The oscillating syringe held a volume of 150ml ($0.00015m^3$), which was insufficient to replace the fluid pushed out as the pipe compresses. Total volume taken up by the pipe is 2.87 x$10^{-4}m^3$ and maximum volume added by the syringe is 1.5x$10^{-4}m^3$ meaning a maximum $\alpha = 0.48$. Ideally, a wider range of $\alpha$ values would be possible.

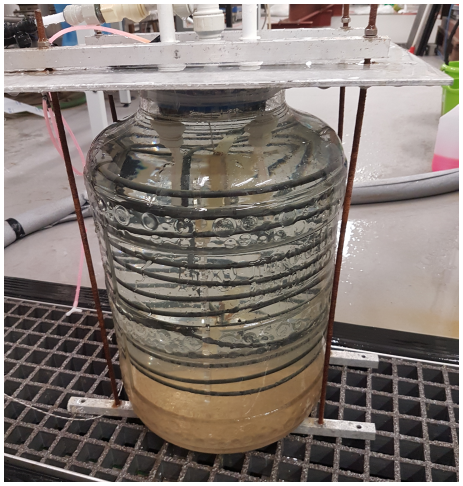

(a) Glass compression vessel

(b) Close up view

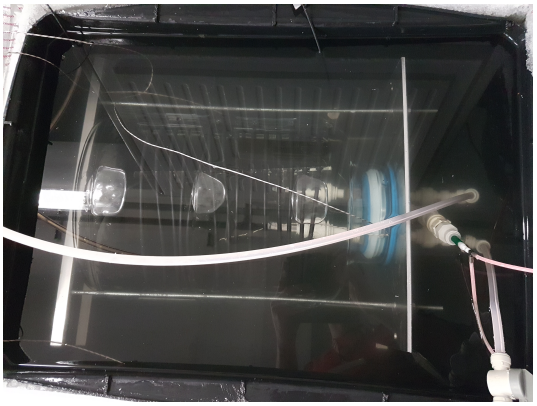

(c) Vessel submerged in bath

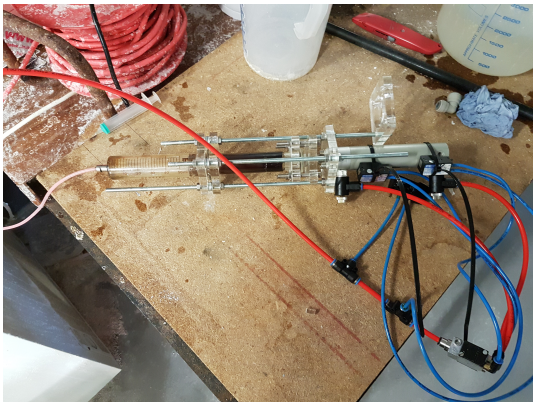

(d) Pneumatic syringe

Figure 7.9: Pictures of (a) glass compression vessel, (b) close up view of coil, (c) vessel submerged in cold brine, and (d) pneumatic controlled syringe to increase and decrease pressure.

- *Trapped air* - Air stored in the pipe between experiments was difficult to remove, it becomes trapped in sections of the pipe. When compressed these air pockets shrunk and expanded effecting the compression and pumping force applied to the pipe.

Blockages and problems with this equipment were also difficult to repair, as correct assembly and disassembly could take a whole day.

### 7.3.4 Tube-in-Tube Experimental Design

Due to the problems outlined in the previous section a simpler design was conceived using a tube-in-tube heat exchanger (HX), see Figure 7.10. A counter-current design was used as it had previously been identified as potentially the better method for ice generation in coiled pipe experiments in §5.1. The same peristaltic pump as used previously (series 200 unit, by Williamson Manufacturing) was used for the inner fluid flow. Voltage was kept constant at 11V with a check valve preventing back flow towards the pump.

A diaphragm pump with a maximum pressure of 6.7 bar and 3.0L $\text{min}^{-1}$ flow rate was used for the refrigeration fluid. A solenoid valve was used at the outlet of the refrigeration fluid flow to oscillate pressure in the pipe. Closing the valve increased pressure in the outer fluid of the HX, the fluid used to compress the pipe is replaced quickly with refrigeration fluid from the diaphragm pump. Two pressure readings were taken, one differential ($\Delta P = P_{internal} - P_{external}$) and one gauge ($P_{external}$). The outer pipe was made of PVC insulated to prevent heat loss to the environment. Refrigeration fluid (20wt.% brine) was taken from a tank of constant temperature fluid (-14 to -20°C). Warm brine was stored in the outer pipe between experiments to prevent ice formation between experiments.

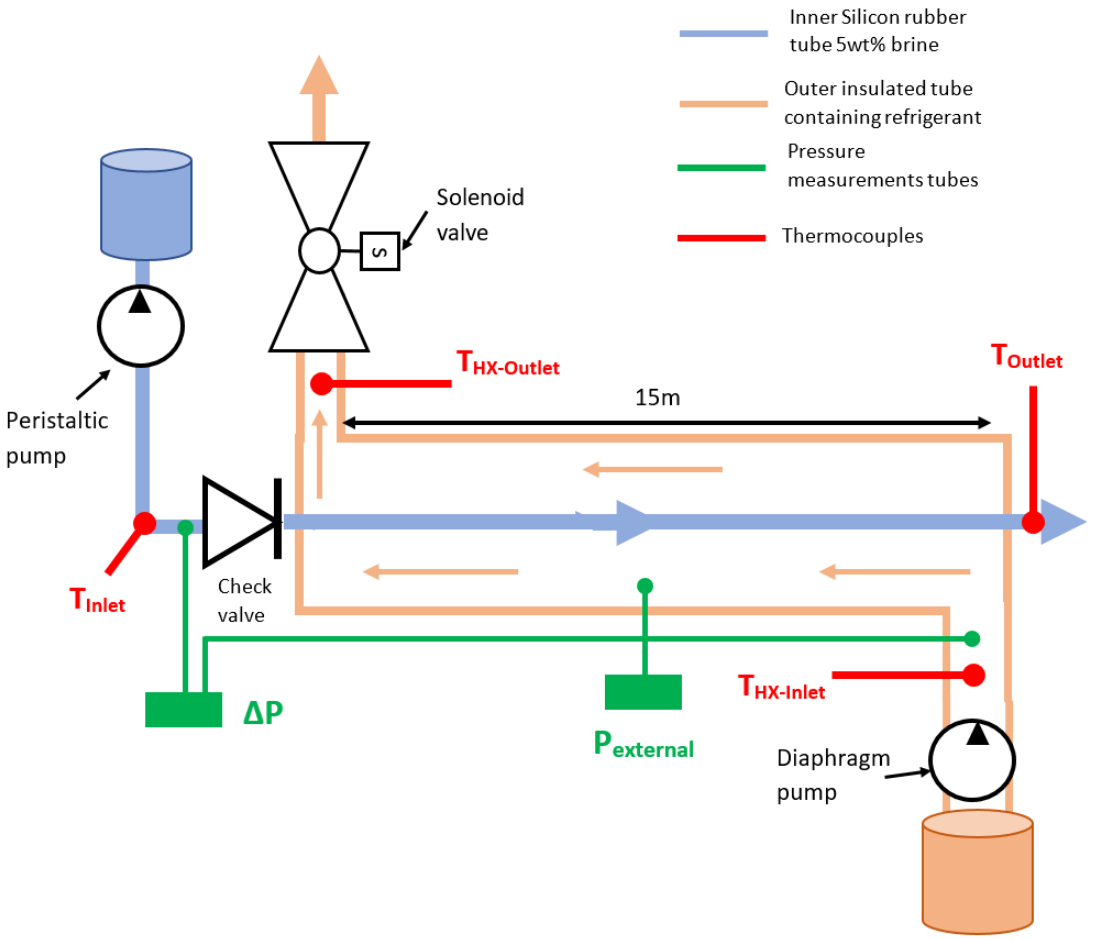


Figure 7.10: Diagram of tube-in-tube heat exchanger design, a check valve is used to prevent back flow and a solenoid valve to increase pressure in the outer fluid. The pressure and temperature measurement points are also shown.

Figure 7.11: Picture of transition point between soft silicone rubber pipe and solid stiff/hard pipe.

Creating an effective seal around the silicone pipe proved difficult, an interface part was used. A barbed connection was used to hold the silicone pipe to a small section of nylon pipe which could be made airtight, see Figure 7.11.

### 7.3.5 Results

Experiments were carried out with and without outer pressure oscillations for 1000 seconds. When nucleation occurred after 700 seconds an experiment was extended by 200 seconds to check blockages did not occur. The 500 seconds after nucleation gave time for fluid to pass at least three times through the heat exchanger. The experimental setting used are detailed in Table 7.2.

Table 7.2: Table of experimental settings for tube-in-tube HX experiments, with and without oscillations.

| **On off ratio** | **1:1** | **2:1** | **3:1** | **No oscillations** |
|---|---|---|---|---|
| **Closed valve signal (s)** | 5 | 5 | 5 | N/A |
| **Open valve signal (s)** | 5 | 10 | 15 | N/A |
| **# Experiments conducted** | 12 | 15 | 8 | 30 |
| **Inlet concentration (wt.%)** | 5 wt.% | | | |
| **Inlet Temperature (°C)** | 20 | | | |
| **Inner Pipe diameters** | 0.005 m Inner, 0.006 m Outer | | | |
| **Outer pipe diameters** | 0.025 m Inner, 0.030 m Outer | | | |
| **Length of pipe** | 15m | | | |
| **Heat transfer area** | 0.283 $m^2$ | | | |
| **Pump voltage** | 11 V | | | |
| $T_{Bath} - T_f$ **range** | -15 to -10°C | | | |

### Pressure and temperature recordings

The same three outcomes seen previously in §4.4.2 were observed. Figure 7.13 shows these three outcomes without oscillations while Figure 7.14 shows it with oscillations. Temperatures are taken at the inlet and outlet of the inner pipe ($T_{Inlet}$ and $T_{Outlet}$), as well as the outlet and inlet of the outer pipe ($T_{HX-Inlet}$ and $T_{HX-Outlet}$). Pressure readings shown are $\Delta P$ and $P_{external}$.

$P_{external}$ was recorded using a 0-700kPa gauge pressure sensor. $\Delta P$ was recorded using a 0-115kPa differential sensor. The internal pressure was taken as $P_{internal} = \Delta P + P_{external}$. All three pressures are plotted together for each ratio tested, see Figure 7.12. $\Delta P$ was the pressure force pushing the fluid through the inner pipe. When it dropped to 0 the flow stopped because the outer pressure has constricted the pipe preventing fluid being pumped. This occurred when $P_{external} > max(P_{pump})$, where $max(P_{pump})$ was 100kPa for the inner flow peristaltic pump. As $P_{external}$ continued to increase above this point the $P_{internal}$ increases with it at the same pressure.

The solonoid valve had a four second response time between fully open and closed. Pressure increased steadily throughout this time and faster once the valve was fully closed. Five seconds after the signal closing the valve, the external pressure had reached 400 to 500 kPa. More than enough to compress pipe and push out the internal fluid. This signal mark-space-ratio was varied during the experiments. The valve was closed for five seconds ($t_{off}$) and time between closures ($t_{on}$) was changed. The ratio (mark-space-ratio) $t_{on}$:$t_{off}$ is used to show this, with $t_{on}$=5 (1:1 ratio), $t_{on}$=10 (2:1 ratio) and $t_{on}$=15 (3:1 ratio) seconds used.

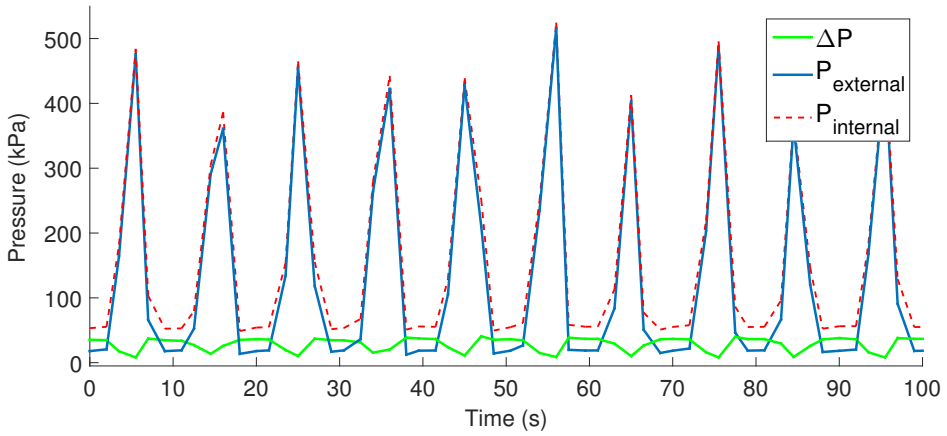


(a) 1:1 ratio

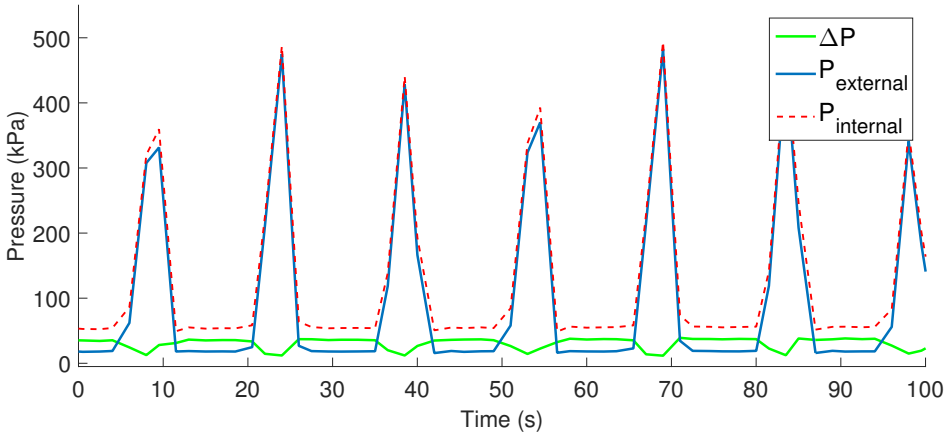


(b) 2:1 ratio

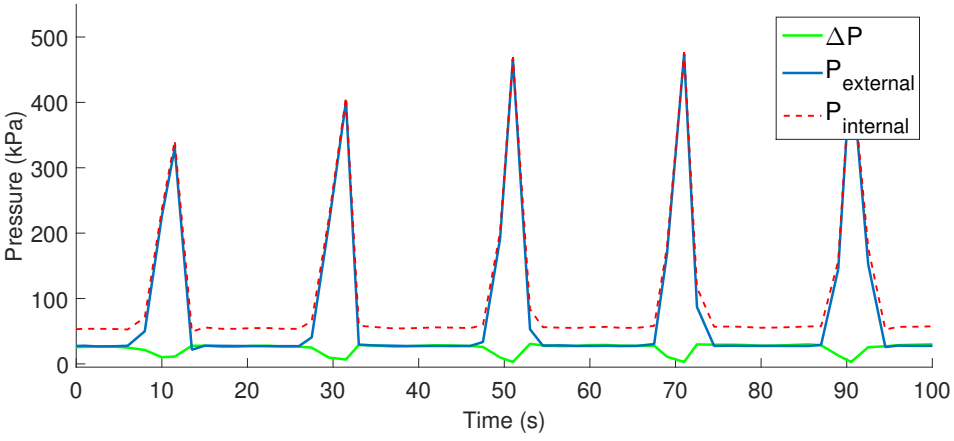


(c) 3:1 ratio

Figure 7.12: Effect on pressure recorded in inner and outer pipes and difference between them for different valve oscillation ratios ($t_{on}$:$t_{off}$) used.

The temperature profiles created are similar to those produced in §4.4. The $T_{Outlet}$ is supercooled slowly until ice nucleates. The cooling takes longer than previous experiments with a submerged coil, due to the time needed to replace the warm brine in the outer pipe with fresh cold brine. Approximately 150 -200 seconds into the experiment, $T_{HX-Outlet}$ starts to drop from room temperature, reaching steady state in an additional 250-350 seconds. The inner fluid cools immediately but much more slowly and reaches steady state at close to the same time as the $T_{HX-Outlet}$. Problems occur (with and without oscillations) when ice nucleates before $T_{HX-Outlet}$ has reached steady state, as shown in Figures 7.13 (a) and Figures 7.14 (a). $T_{Outlet}$ and $T_{Outlet}$ fluid cool further until the pipe blocks. A control system such as the one in §5.3 would help prevent blockages by increasing the flow rate to account for the reducing temperature. Stable production occurred when ice nucleation occurred after outlet temperatures had reached steady state.

For all experiments, there was a constant value of $\Delta P$ when fluid was flowing through the internal pipe. With pressure pulses, $\Delta P$ fluctuated with $P_{external}$, falling to 0 when $P_{external}$ was increased above 100kPa. When no pulses were used, a consistent pressure loss of 20kPa was observed from pumping fluid in the outer pipe. When ice nucleated a rise in $\Delta P$ was seen, as shown by Figure 7.13 (a) and Figure 7.14 (a) and (b). Figure 7.13 (b) only shows a very small rise which is difficult to observe on the graph. Pressure readings, such as $P_{external}$, also suffer from aliasing and the peak pressure seems to vary sinusoidally due to the sampling frequency as seen in the previous section. The addition of outer pressure pulsation appeared to reduce the time until nucleation was seen. This was observed in most of the experiments .

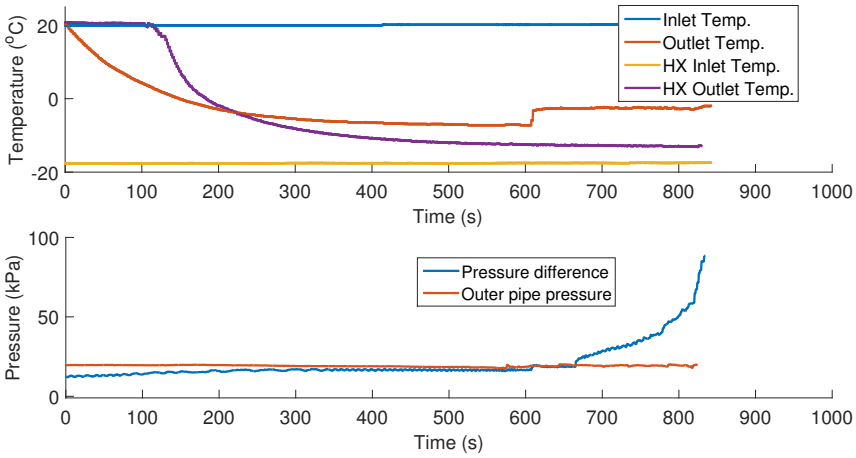


(a) Blocked, no oscillation

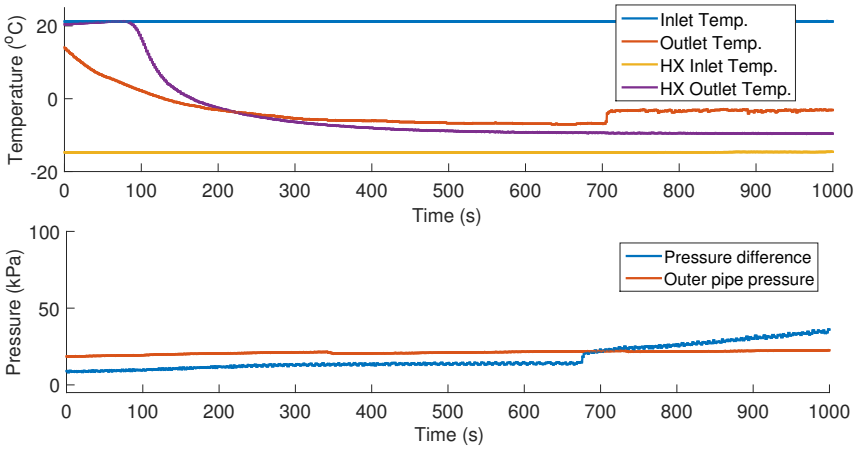


(b) Ice produced, no oscillation

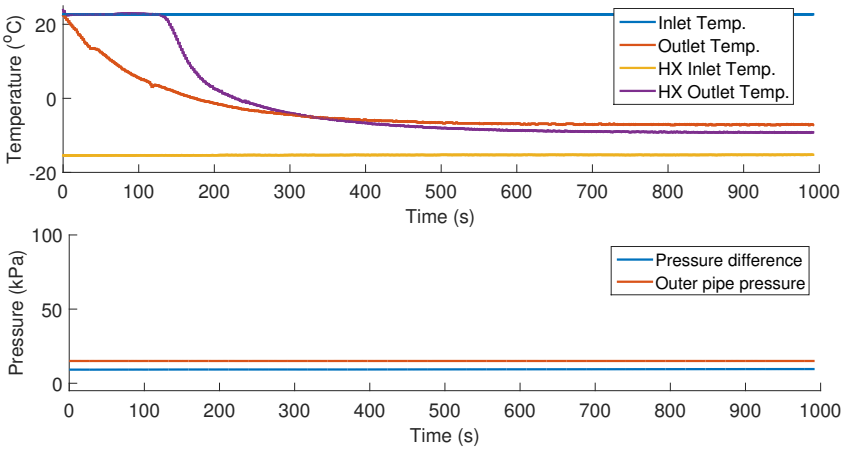


(c) No ice, no oscillation

Figure 7.13: Graphs of the three outcomes observed for silicone rubber tube-in-tube heat exchanger without pressure oscillations. Top: temperature. Bottom: pressure readings. (a) show blockages, (c) show ice production and (b) no ice produced.

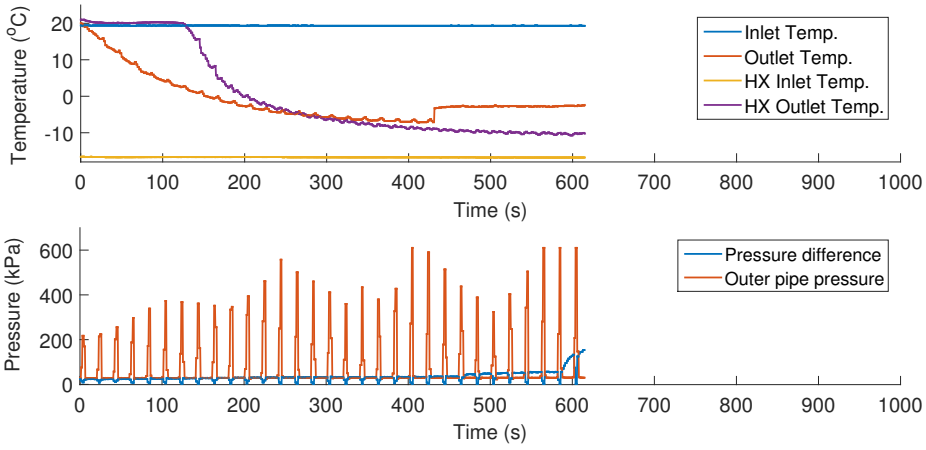


(a) Blocked, with oscillation

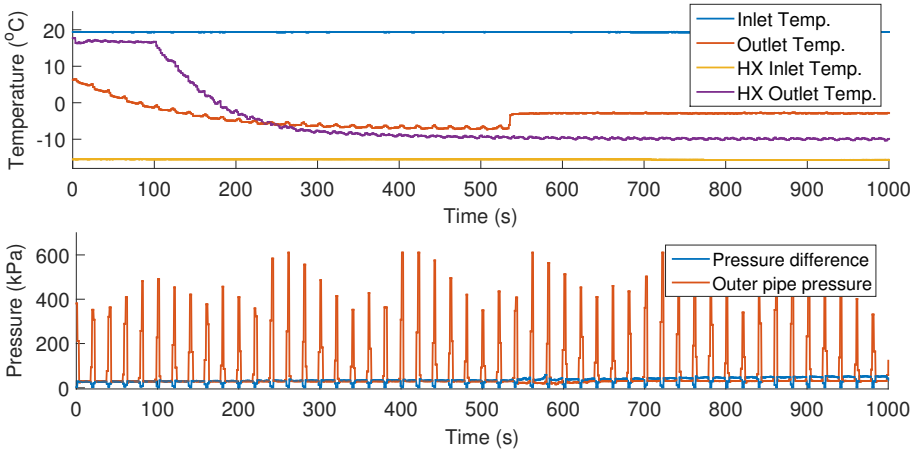


(b) Ice produced, with oscillation

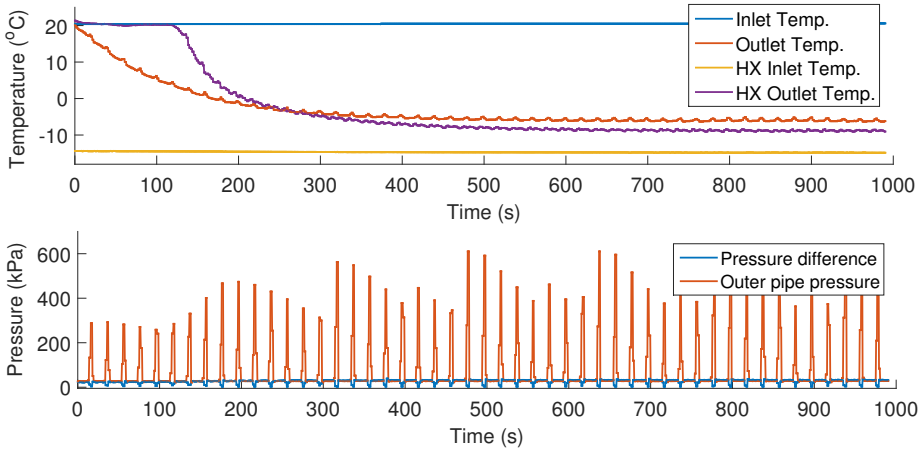


(c) No ice, with oscillation

Figure 7.14: Graphs of the three outcomes observed for silicone rubber tube-in-tube heat exchanger with pressure oscillations. Top: temperature. Bottom: pressure readings. (a) show blockages, (c) show ice production and (b) no ice produced.

### Operation regions

Operation regions were plotted for both sets of experiments, one with outer pulsation and one without. Re for the internal flow was plotted against $T_{Bath} - T_f$, with $T_{Bath}$ taken as $T_{HX-Inlet}$. Experiments were conducted in a similar range of temperatures and flow rates. To account for the intermittent flow rate caused by the outer pressure pulsation, flow rates were taken as the average outlet flow rate over three minutes. All experiments with pressure pulsation used an 11V pump voltage. Flow rate, and therefore Re, varied with the mark-space-ratio used.

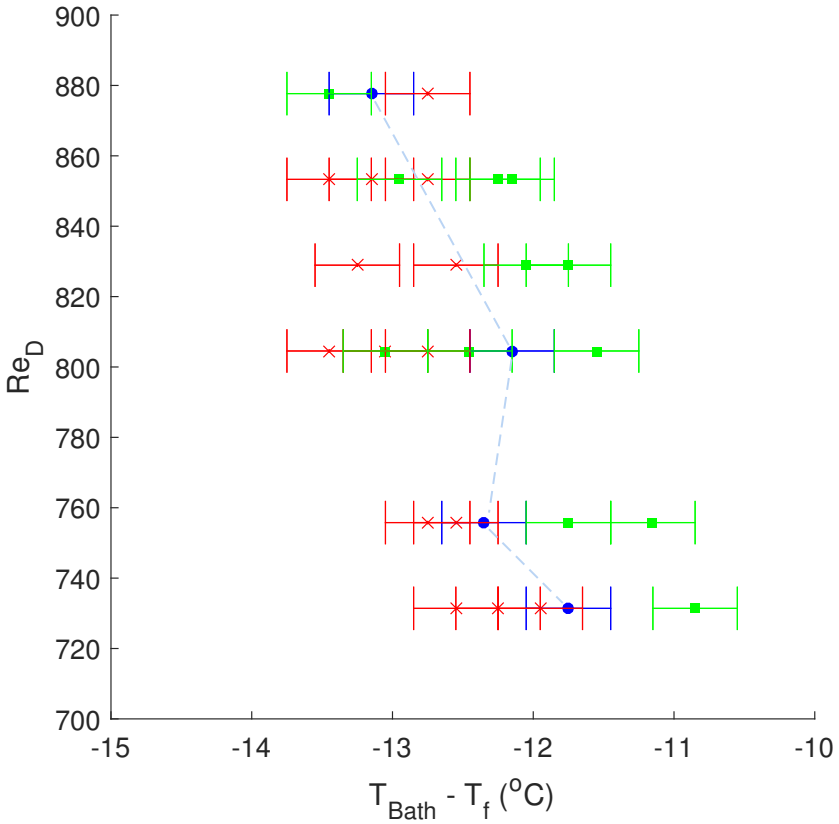


Figure 7.15: Operation region created for tube-in-tube experiments without oscillations. Red: blocked pipe, green: no ice produced, blue: ice slurry production.

The initial operation region without oscillations (Figure 7.15) is very narrow, only four points were successfully found where ice nucleated. This is probably because nu-

cleation occurred before the HX has reached steady state. Lower voltages, between 10-8V, were also used to generate the operation region without pressure oscillations, leading to lower cut off pressures. Lots of cross over between experiments with blockages and no ice produced is shown in Figure 7.15. This makes it difficult to see a clear usable operation region. Higher slurry temperatures resulted with these operation regions than the ones produced in §6.3.2 because of a shorter length of pipe used and therefore reduced surface area.

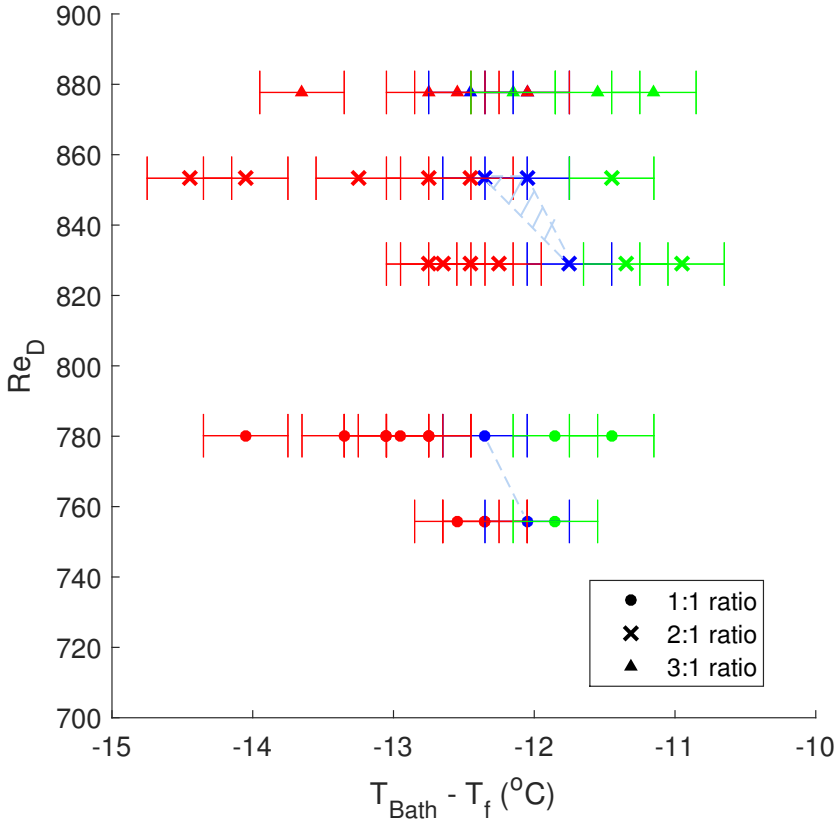


Figure 7.16: Operation region created for tube-in-tube experiments with oscillations. Red: blocked pipe, green: no ice produced, blue: ice slurry production. Ratios used are $t_{on}$: $t_{off}$.

The operation region produced with pressure oscillations (Figure 7.16) is slightly bigger. This indicates that pressure oscillations could have a stabilising effect on ice production. As the mark-space-ratio increases so did the flow rate, though the

temperatures ($T_{Bath} - T_f$) are close to the same value, or even warmer than mark-space-ratio 1:1 to 2:1. A ratio of 2:1 seems to show the best results as ice was successfully made three times at this oscillation ratio.

### Lost surface area

The surface area of the HX was previously shown as 0.283m$^2$. This assumes the pipe stays in the middle of the outer pipe, which it would not. The effective surface area can be estimated by analysing the system as a cylinder within a cylinder shown in Appendix D. Using this theory, material properties for the pipes, and changing the applied pressure to the cylinder, an estimation for surface area lost due to pipe on pipe contact is found. Figure 7.17 shows how it changes with applied pressure, this theory assumes it is pushed against the side of the pipe along the whole 15m length.

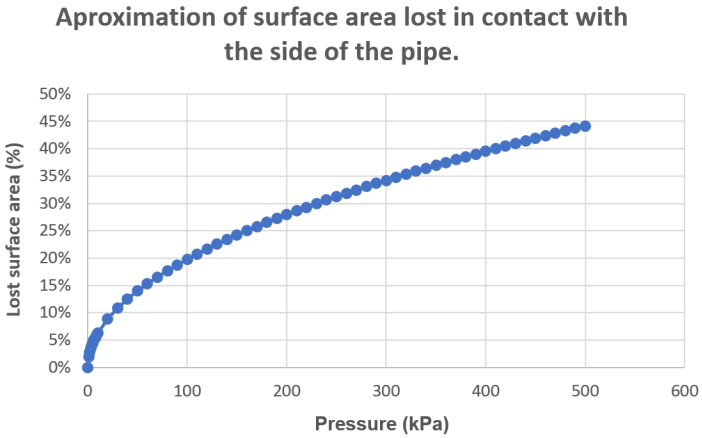


Figure 7.17: Estimated percentage of surface area lost due to pressure pushing the pipe against the wall of the pipe.

From 100 to 500kPa external pressure, 20-45% of the heat transfer surface area wasted. If this surface area was available, it could increase the efficiency of the tube-in-tube HX. It is also likely to be a reason for the colder refrigeration temperatures required in this experiment than those used previously.

### Ice measurements

Ice fraction and production rates were recorded three times during each experiment using calorimetry. The average of the three readings is plotted against $T_{Bath} - T_f$. Ice fraction is shown in Figure 7.18 and ice production rate in Figure 7.19. The experiments with oscillations offer better efficiency, producing higher fractions and production rates at the same $T_{Bath} - T_f$ for all experiments except one. However, it is unclear from this data if one oscillation ratio is better for ice production. More data points would be required to draw an accurate conclusion.

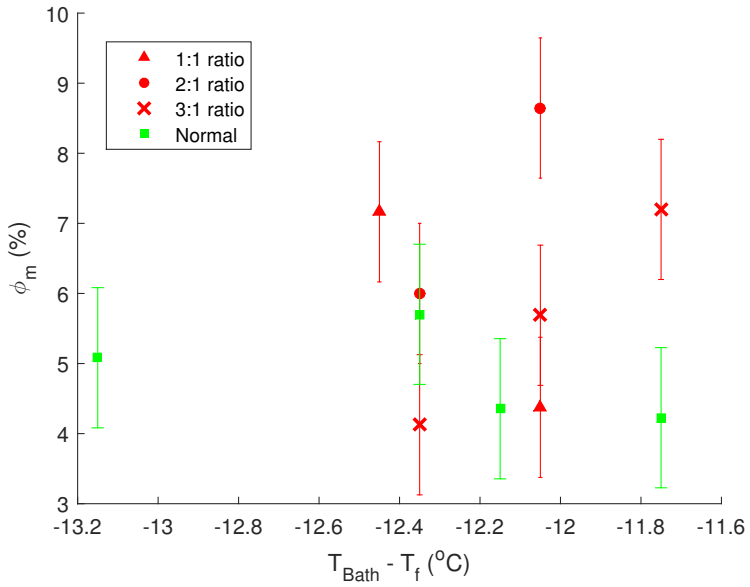


Figure 7.18: Ice fractions produced for tube-in-tube experiment with and without outer oscillation. Ratios are time valve open to time valve closed.

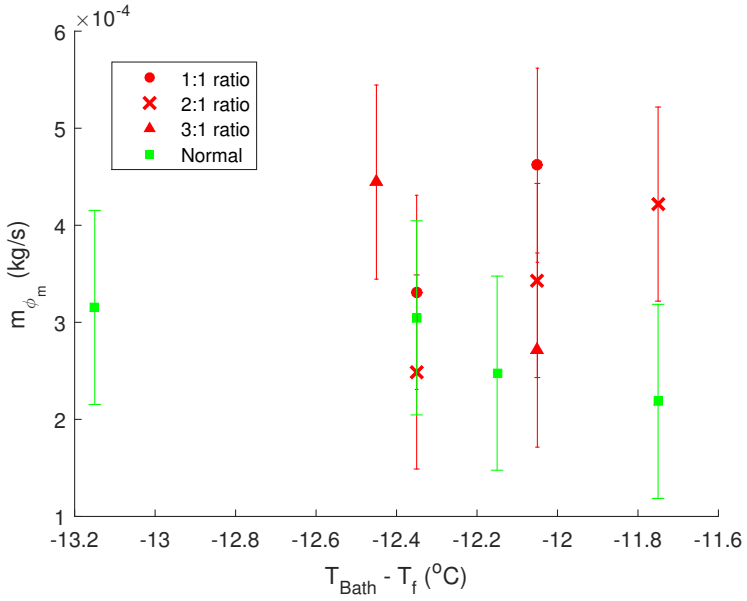


Figure 7.19: Ice production rates for tube-in-tube experiment with and without outer oscillation. Ratios are time valve open to time valve closed.

### 7.3.6 Discussion

Previous work pumping ice slurry in heat exchangers has been conducted by a range of authors as discussed in §2.3.7. However, most of the work focuses on heat added to the slurries and not heat being removed. Some authors have created ice slurry in a heat exchanger. Zhang et al. (2008) used a vertical shell and tube heat exchanger with bubbles to dislodge ice formed on the walls. H. Wang et al. (2014) used hydrophobic coatings in a heat exchange to reduce blockages. All these methods used rigid surfaces, not flexible compressed tube, as used here.

Ash (2012) successfully trialled a peristaltic pump based ice slurry generator for hygienic ice slurry production. The rollers flattened the pipe to break up and dislodge ice formed in the pipe. The fluid phase was recirculated through the cooling section and pump until enough ice had been produced. This is similar to the silicone rubber HX used here, except fluid is re-circulated through a small cooled section rather

than one pass in a long cold pipe. The pipe is also compressed using a mechanical force rather than increased external pressure. Refrigeration temperatures down to -27°C were used, colder than ones used here, indicating that the silicone rubber HX method used might be more efficient. Ice fractions produced were higher, up to 35%. This result is difficult to compare to the current work presented here as the fluid phase was recirculated extensively to achieve this fraction. Similar ice fractions may be achieved by recirculating the fluid phase from the silicone rubber pipe.

### 7.3.7 Section Conclusion

A tube-in-tube HX was successfully designed and used to make ice slurry. Refrigeration fluid was pumped through the outer pipe enclosing a smaller silicone rubber pipe with 5wt.% brine. The same three outcomes seen in previous sections were observed, blocked pipe, stable ice production and no nucleation of ice. The operation region produced was smaller than with the submerged HCHX, used previously. This could indicate that this method is less stable for ice production. External pressure was oscillated by opening and closing the exit valve for the outer fluid. Different mark-space-ratios (ratio of time value is open and closed for) were tested. Using oscillating external pressure led to slight improvements in operation region stability and ice production. Ice fractions (under 10% $=\phi_m$) and production rates were still smaller than those found with submerged nylon and PTFE helical coiled heat exchangers.

Further work should focus on changing the frequency of the oscillation as well as the mark-space-ratio (duty cycle). The operation region could also needs to be expanded to improve the reliability. This could be done with a thicker silicone rubber pipe, which would slow down the rate of cooling to the internal pipe fluid, allowing external fluid to reach steady state before ice nucleates.

## 7.4 Chapter Summary

- The flow rate inside the pipe was stopped, allowing a pressure wave to build up and a flow pulse subsequently generated. The hope was to dislodge ice formed on the walls by increasing wall shear stress by pulsating the flow rate.
- Pulsating the flow rate, slowed down the average flow rate, which led to higher ice fractions being produced. The increase in ice fraction was the same as that produced by reducing flow rate of a steady flow. This showed that the flow pulsation had no positive effect on ice fraction produced.
- A flexible silicone rubber pipe was used in a tube-in-tube heat exchanger. External pressure on the tube was changed to compress the silicone rubber pipe. The aim was to break up ice formed in the pipe and increase ice fraction that could be produced.
- Adding external fluctuations increased the operation region where ice was produced. It also allowed slight increases in ice fraction, indicating that this method could be beneficial for ice production. Current fractions are still lower than those produced previously with nylon and PTFE HCHX.

# Chapter 8

# Final Generator Design Proposals

## 8.1 Introduction

This chapter aims to bring together improvements found from previous chapters and discusses the feasibility of a helically coiled heat exchanger (HCHX) ice generator. Experimental work with extended experiments running beyond 2000 seconds is presented. Implementation of HCHX methods with work done previously by Yun et al. (2016) is discussed, including a proposed design. Designs for a unique plastic HCHX are also discussed and evaluated in the final section of this chapter.

## 8.2 Extended Operation Experiments

### 8.2.1 Introduction

From the work in the previous chapters several improvements were found over the original nylon HCHX, including:

1. In chapter 4, 5wt.% brine concentration was found to offer a wide operation region and warm $T_{Bath}$; crucially, it was the concentration with the highest ice fractions produced.

2. In chapter 5, a control system was shown to maintain high ice production despite changing temperature.

3. In chapter 6, different material coils were tested. PTFE was found to offer higher ice production and ice fraction at warmer bath temperatures than nylon or silicone rubber.

4. In chapter 7, applying outer pressure oscillations resulted in improvements in ice fraction and production for silicone rubber pipe in a tube-in-tube HX.

Improvement number four is difficult to implement with the other improvements because it relies on a different operational set-up than the previous three. The first three, however, were implemented in one method outlined in this section.

### 8.2.2 Experimental Method

The experimental equipment used is outlined in Figure 8.1. It is similar to that detailed in §3.2 except fewer coils are submerged in the bath and the output feeds into the input tank, creating a recirculation of brine (fluid phase). Less coils were used to see if the generator could be compacted into a smaller space. Both nylon and PTFE pipes were utilised in the experiments as they both produced high ice fractions. The control system used previously was used to set the flow rate based on $T_{Bath}$ and pressure readings. It was adapted for PTFE to fit the operation graph created previously.

Inlet fluid temperature will fall during the operation of this design, the length of pipe submerged is, therefore, an important consideration constant refrigeration temperatures will be used. Ideally, the pipe should be of sufficient length that when $T_{in} = T_f$ (-3.05°C) or warmer the outlet temperature is 6°C of supercooling, as this is when ice is observed to nucleate in previous experiments. For the initial concentration of 5wt.% the outlet needs to be close to -9°C. If the pipe is too long nucleation can occur early in the pipe, leaving a long length of pipe filled with slurry and a large

pressure drop. This was observed with an identical experiment with 27.4m of coil, where nucleation occurred half way along and blocked the pipe before it could be conveyed out. If the pipe is too short the inlet fluid and the fluid in the whole pipe will be supercooled. Upon nucleation a large amount of dendritic ice will form inside the whole pipe length, causing it to block. Again, this has been observed when a shorter pipe of 3m was initially tested.

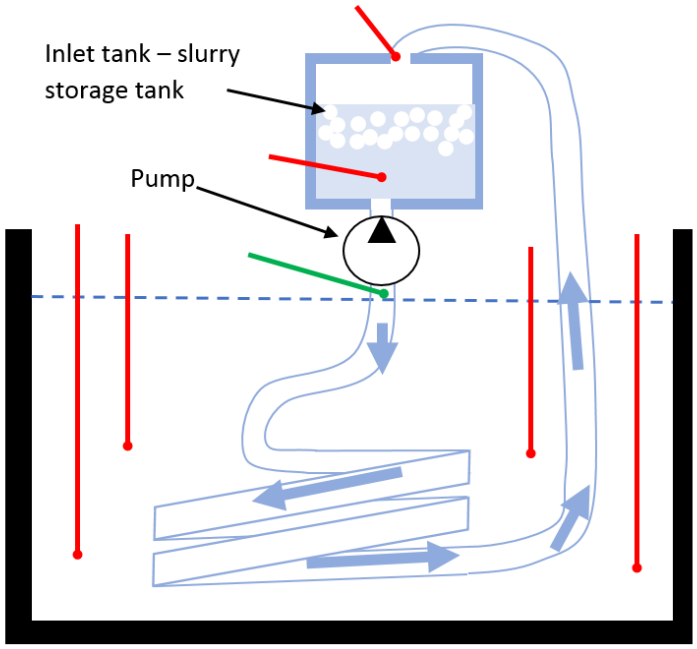


Figure 8.1: Diagram of extended experiment set up designed to generate ice slurry.

Equation 4.1 from §4.3, can be rearranged to make surface area ($A_s$) the subject. L (Length) is unknown so $A_s/L = A_{s,L}$ is used instead, where $A_{s,L}$ is the perimeter of the pipe. Equation 8.1 is used to find the lengths shown in Table 8.1.

$$-\ln\left(\frac{T_{Bath}-T_{out}}{T_{Bath}-T_{in}}\right)\frac{\dot{m}c_p}{\bar{U}A_{s,L}} = L \tag{8.1}$$

$$\frac{1}{\bar{U}A_{s,L}} = \frac{1}{2\pi}\left(\frac{2}{D_i\bar{h}_i} + \frac{1}{k_{Pipe}}ln\left(\frac{D_o}{D_i}\right) + \frac{2}{D_o\bar{h}_o}\right)$$

Once a length has been calculated it needs to be checked. To do this the quantity of ice added to brine when it enters the coil with ice crystals present, was calculated. Equating energy to cool the fluid and conduction through the pipe leads to Equation 8.2, assuming temperature change of the fluid is small.

$$-\bar{U}A_{s,L}L(T_{Bath} - T_f) = \dot{m}\phi_m h_{s,f} \tag{8.2}$$

Table 8.1: Table of values used to calculate new pipe length needed.

| **Material** | **Nylon** | **PTFE** |
|---|---|---|
| $\dot{m}$ **(kg s$^{-1}$)** | 0.0076 | 0.0076 |
| $\bar{U}A_{s,L}$ **(W m$^{-1}$K$^{-1}$)** | 3.53 | 3.79 |
| $T_{in} = T_f(5wt.\%)$ **(°C)** | -3 | -3 |
| $T_{out}$ **(°C)** | -9 | -9 |
| $T_{Bath}$ **(°C)** | -12.5 | -12.5 |
| **L (m)** | 8.6 | 8 |
| **Number of coils (nearest 0.5)** | 6.5 | 6 |
| $\dot{m}_i$ **(kg s$^{-1}$)** | 0.00084 | 0.00083 |
| $\phi_m$ **(%)** | 11 | 11 |

The ice fraction added to fluid passing through the coil was calculated and shown in Table 8.1. Ice fractions of 11% produced for both are towards the maximum produced using nylon and PTFE HCHX. Above 15% the pipes could block as noted in previous experiments, though a shorter length was used than previously so the pipe may not block so readily.

### 8.2.3 Results and Discussion

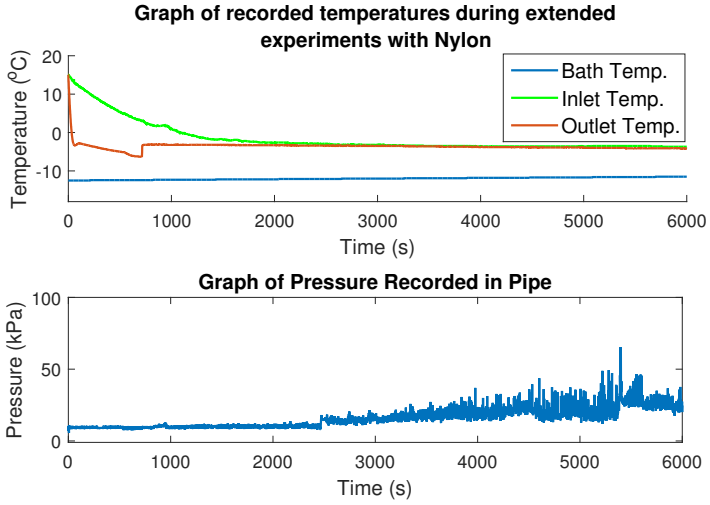


(a) Nylon HCHX

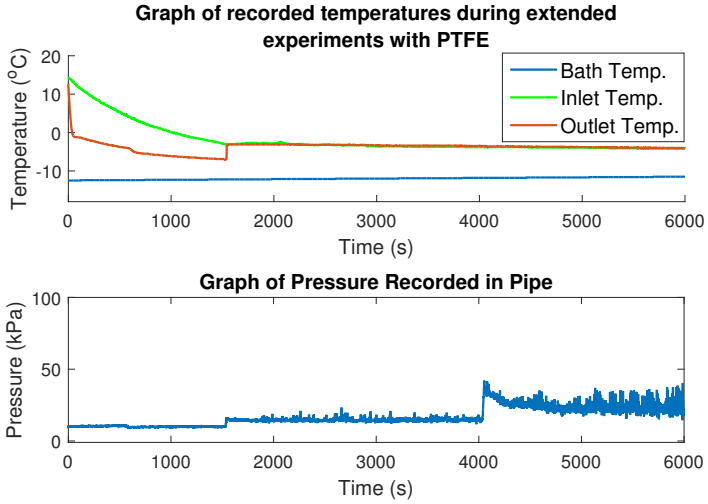


(b) PTFE HCHX

Figure 8.2: Graphs of temperature and pressure taken during extended time experiments with shorter coils, flow rate control and recirculation tank. Nylon, (a), PTFE, (b).

As outlined in the Table 8.1, 6.5 coils were used with the nylon pipe and 6 with PTFE. Experiments ran for 6000 seconds, three times longer than any previous one, with 4 litres of 5wt.% brine initially held in the inlet tank. Temperature and

pressure readings were taken every second and are plotted in Figure 8.2. The inlet temperature was the storage tank temperature, from which fluid was extracted.

Temperature initially fell quickly, as the fluid cooled from the first pass through the coils. Inlet temperature also began to fall lowering the outlet temperature further but at a slow rate. Fluid in the nylon pipe nucleated quickly while fluid in the PTFE pipe took longer and nucleated at a lower temperature due to the hydrophobic surface. After nucleation the inlet and outlet temperatures were very similar, though the outlet is often slightly lower as the brine concentration has increased in the fluid component depressing the freezing point.

After 6000 seconds the fluid was mixed using a whisk to achieve a close to homogeneous mixture, see Figure 8.3. Temperature readings of the slurry in the tank ($T_{Tank}$) and three calorimetry ice fraction measurements ($\phi_m$) were taken and averaged. $T_{Tank}$ was used with Equation 8.4 and 8.3 from §2.3.1 to find a temperature based ice fraction reading, $\phi_{m,temp}$. See Table 8.2 for the results. Total mass of ice produced is also estimated based on the final mass of fluid and average $\phi_m$ shown in the table.

$$\phi_m = 1 - \frac{C_{bulk}}{C(T)} \tag{8.3}$$

$$C(T) = a_3\hat{T}^3 + a_2\hat{T}^2 + a_1\hat{T} \tag{8.4}$$

$$\hat{T} = T - T_0$$

$$T_{eut} < T < T_0$$

Table 8.2: Table of calculated ice fractions and recorded inlet tank temperature.

| **Material** | $T_{Bath}$ (°C) | $T_{Tank}$ (°C) | $\phi_m$ | **Total Mass (Kg)** | $\phi_{m,temp}$ |
|---|---|---|---|---|---|
| **PTFE** | -12.5 | -4.3 | 24.3 % | 1.0 | 24.0 % |
| **Nylon** | -12.5 | -4.4 | 23.3 % | 0.96 | 25.6 % |

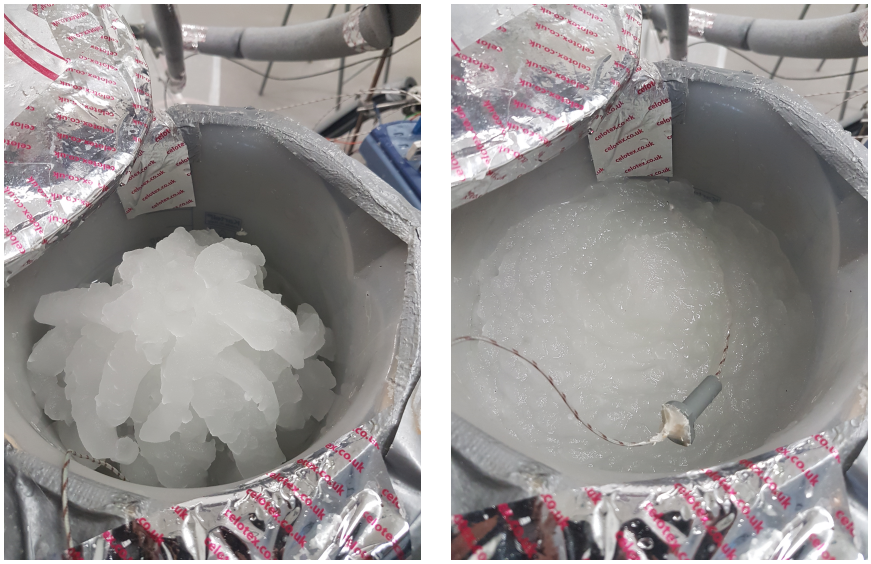

(a) Before mixing (b) After mixing

Figure 8.3: Pictures of ice produced at the end of the experiment before, (a), and, (b), after mixing.

For calorimetry ice fraction measurements there was a +/-1.5% error, as discussed previously. Ice fraction measurements using temperature can differ by at least +/-1.6% if the temperature sensor was accurate to 0.1°C, such as the PT100 probe used here. This error prediction does not take account of possible temperature gradients which could be present in the slurry. This is could explain the difference in measurements of $\phi_m$ and $\phi_{m,temp}$ shown in the results table. Both materials produced $\approx$ 1kg of ice in 100 minutes. Slightly more ice was produced with PTFE according to $\phi_m$ measurements taken. This production rate is still far from the 1ton/24 hours capacity of a small Ziegra or Snowkey ice generator.

## 8.3 Future Design Proposal

This section investigates two proposed designs for how a plastic HCHX could be implemented in an ice slurry generator. A combined method with Yun et al. (2016) and a refrigeration system with a HCHX are both proposed and evaluated. A comparison of the different designs and a scraped surface generator has been included, including cost estimates, production rate and possible used.

### 8.3.1 Design

The current design utilised for HCHX work so far in this thesis is inadequate for the final design. It uses a stationary bath of cool fluid, in reality a refrigeration loop would be required to maintain the cooling fluid temperature.

#### Design 1 - With secondary refrigeration loop

The first proposed design (see Figure 8.4) is similar to the one used in experiments, an initial refrigeration loop cools a secondary refrigeration fluid. This obviously adds an extra step and lowers the efficiency of the method, but also enables better control of heat transfer rate through the HCHX coil. The flow rate and temperature of the secondary refrigerant can be monitored and controlled much more easily than that in the primary refrigerant loop. If there is a fault with the primary refrigeration loop and evaporation temperatures fall quickly the secondary loop can be shut off to protect the HCHX from cooling too fast and blocking.

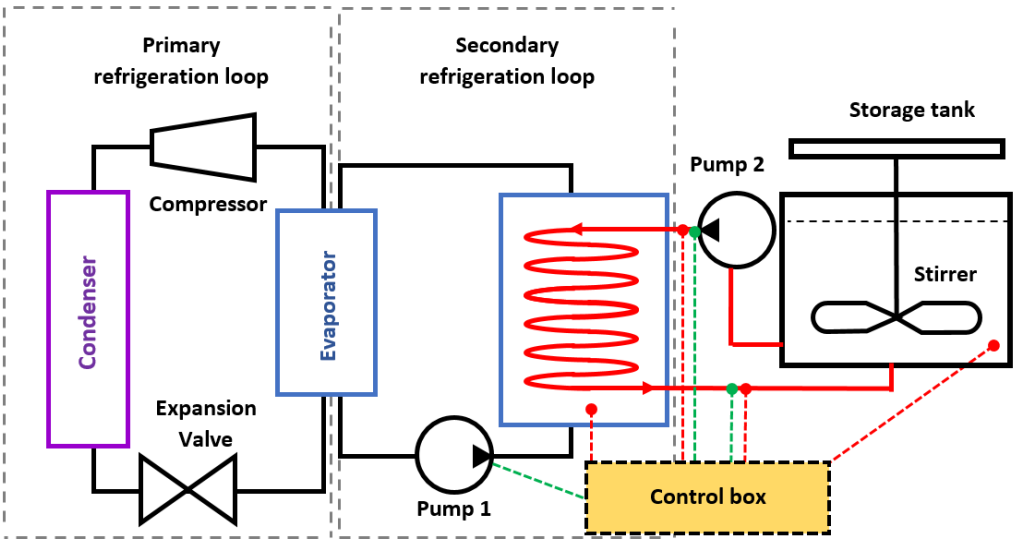


Figure 8.4: Design 1: Diagram of HCHX ice slurry generator design using secondary refrigerant to give improved control or refrigerant passing the coil.

A control box (in yellow on Figure 8.4) would monitor temperature and pressure readings. Processing the data to set flow rate through the HCHX. Fluid is extracted and returned to a storage tank, similar to the extended experiments.

### Design 2 - Single refrigeration loop

The second design is similar to the first though without a secondary refrigeration loop, an evaporating refrigerant is applied directly to the coil. Careful control of the refrigerant would be needed as +/-1°C outside of the operation range would stop ice production or block the pipe. If successfully implemented, it could greatly improve efficiency as evaporation temperatures close to -13°C could be used instead of -30°C as used by other generators.

This method offers the greatest potential to replace scraped surface generators.

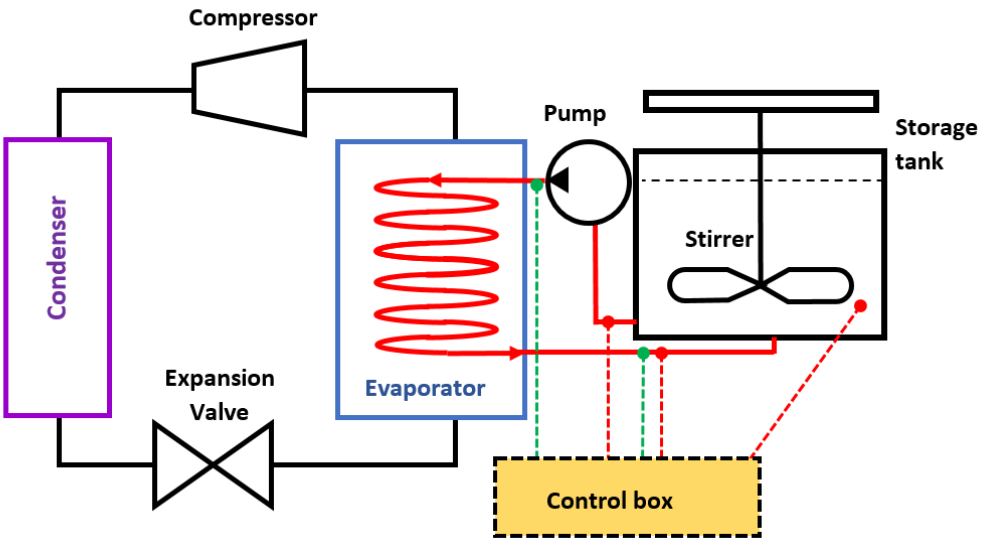


Figure 8.5: Design 2: Diagram of HCHX ice slurry generator with primary refrigerant used and evaporator in contact with the coil.

## 8.4 Combining With Yun et al. (2016)

Previously, in Yun et al. (2016) a method was presented for creating ice in a cooled bath of brine. However, not all water is converted to ice, around 30% dilutes the cold brine it is made in. For the method to be sustainable this excess water needs to be removed, a plastic HCHX could be used to do this. Figure 8.6 outlines a design proposed in Yun (2017) with some added details showing how HCHX could be utilised in the design.

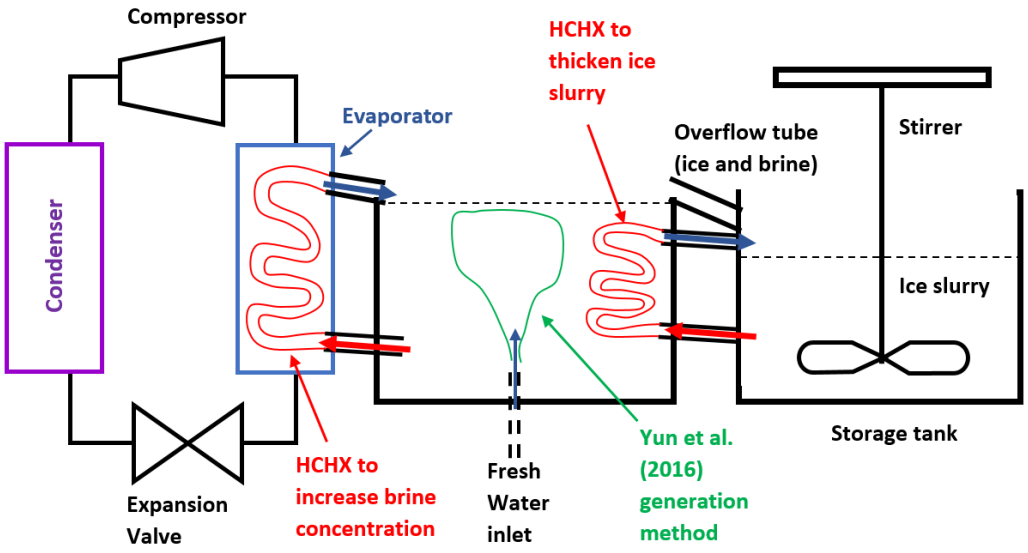


Figure 8.6: Diagram of ice generation set up proposed in Yun (2017), adapted to include plastic HCHX generation methods.

### 8.4.1 Process Steps

The design proposed is explained in more detail moving from left to right across the design.

*Refrigeration loop* - The first stage is a standard refrigeration loop, with a compressor, condenser, evaporator and expansion valve. This is where the greatest energy use would be, due to the low evaporation temperature required.

*First HCHX loop* - Brine circulated through the loop would be high concentration, close to 19-20wt.%., with a $T_f$ of -15 to -16°C. From previous work conducted it has been seen that a refrigerant temperature ($T_{Bath}$) of -10°C below $T_f$ is needed for nucleation and ice production. Therefore, evaporation temperatures in the refrigeration loop are likely to be -26 to 30°C. One advantage of a high concentration could be a wider operation region, as noted in Chapter 4 for higher concentration brine. Even if ice is not generated the coil will still serve to cool down the brine

environment and maintain it at the -16 to -18°C needed for high ice production with Yun et al. (2016) method.

Ice generated in the evaporator HCHX could enter either at the bottom or top of the cooled brine environment. At the top, the ice produced is close to the ice extraction and will be moved to the slurry tank quickly before it melts. However, if ice came in at the bottom where the fresh water enters, it could provide a nucleation site. Thermocouples and concentration probes would be utilised to monitor fluid properties in and out of the coil, with a pressure sensor to measure if blocking was occurring.

*Ice formation in supercooled brine* - This section involves a cooled brine environment, fresh water is added at the bottom of the tank, it rises and forms ice in the tank (Yun et al. (2016) method). At the top some form of extraction is needed to remove the ice from the bath without too much brine, this step is currently shown by an overflow tube, though it requires further design. Temperature and concentration of the bath should be monitored to ensure it is sufficient for ice formation.

*Storage tank* - Ice and brine extracted previously falls into the storage tank, a stirrer is used to keep the mixture moving and prevent amalgamation of ice crystals. Temperature and concentration readings need to monitor the ice fraction.

*Second HCHX loop* - The second HCHX is used to thicken ice slurry produced, in a similar method to the extended experiments conducted previously in this chapter. Liquid phase (possibly with ice crystals) is extracted from the bottom of the storage tank and is cooled in the previously cooled brine environment" tank next to it.

### 8.4.2 Evaluation

The high heat transfer area utilised by the Yun et al. (2016) method makes it a very effective ice generation method. However, it still requires a refrigeration loop with -30°C evaporation temperatures, similar to a scraped surface generator. It also contains a lot more steps and processes than a scraped generator, all of which need to be carefully controlled and potentially create extra energy losses. Further work creating a working 1ton/24-hour prototype, would be needed to confirm this, but the author predicts that the efficiency gain would be marginal if any.

## 8.5 Comparison of Designs

The three ice slurry generator designs outlined previously have been evaluated and compared in more detail in this section. Table 8.3 shows estimates of the initial capital cost, the production rates, energy costs, running costs and floor space used. Each row of the table is discussed in more detail and a summary, including proposed industrial uses, is given. The values are all based on a small capacity generator ($< 50$ kg day$^{-1}$) of similar size to the ones tested in this thesis. For a larger scale version of these generators ($> 50$ kg day$^{-1}$) the capital and running cost would be much higher.

Table 8.3: Table comparing estimated capital and running costs for different ice slurry generators.

| | **Yun + HCHX Design** | **Design 1** | **Design 2** |
|---|---|---|---|
| **Capital costs** | £9509 | £7305 | £6405 |
| $T_L$ (°C) | -30 | -20 | -15 |
| **COP** | 2 | 2.7 | 3 |
| **Production rates** | 1.2 kg hour$^{-1}$ | 0.6 kg hour$^{-1}$ | 0.6 kg hour$^{-1}$ |
| **Energy costs (per kg ice)** | 59.2 Wh | 43.8 Wh | 39.4 Wh |
| **Energy costs (per hour)** | 71 Wh | 26 Wh | 24 Wh |
| **Running cost (per hour)** | £1.05 | £0.39 | £0.35 |
| **Running cost (continuously for a year)** | £9161 | £3393 | £3054 |
| **Floor space** | 1.5 m$^2$ | 1.5 m$^2$ | 1 m$^2$ |

### 8.5.1 Categories

**Capital costs** - Estimates for all capital cost have been made by considering the parts and quantity required for each generator. Further details on the parts and capital cost calculation are shown in Appendix E. Values were estimated based on prices of lab equipment used and Yun (2017).

**Evaporation temperatures ($T_L$)** - Evaporation temperatures were taken as the lowest cooling temperature required for each generator. The Yun + HCHX design and design 1 both have multiple stages of cooling and therefore a colder evaporation temperature. However, for design 2 the refrigerant is in direct contact with the surface and is, therefore, warmer; temperature $T_L$ was taken as -15 °C because this

is the temperature of $T_{Bath}$ required to produce 50% $=\phi_m$ slurry, as detailed in §4.4.7.

**COP** - COPs are found using Figure 8.7 and the evaporation temperatures from the step above.

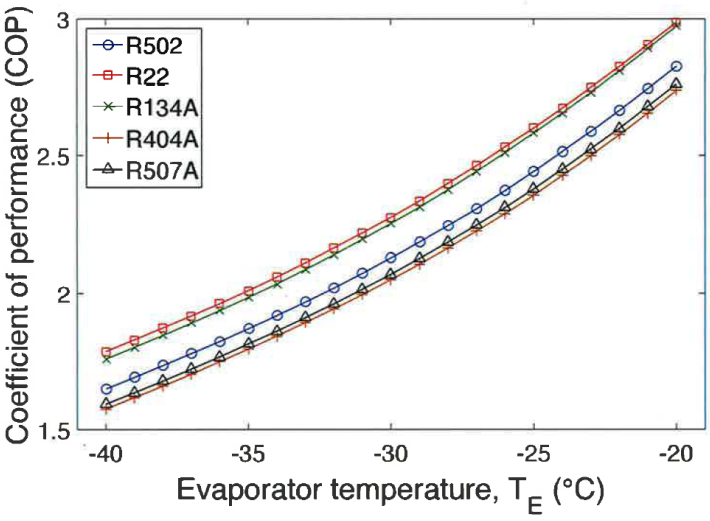


Figure 8.7: Change in COP for a refigeration system with different evaporation temperatures and refigerants; taken from Yun (2017)

**Production rates** - The production rates for design 1 and design 2 were taken from the extended experiments shown earlier in this chapter, where 0.6kg was the average production per hour. For the Yun + HCHX design, the production rate was assumed to be at least double because there are two HCHX and the cooled brine environment all working together to make ice slurry.

**Energy costs** - Approximately 334 kJ of heat needs to be removed to make 1 kg of ice. Assuming the ice is formed from 5 wt.% brine at 20 °C a further 92KJ would be needed to cool it down to its freezing point. Using Equation 8.5 for COP and the total cooling required (426 kJ = Q) an estimate for generator work (W) required can be found.

$$COP = \frac{Q}{W} \tag{8.5}$$

Results are shown in Wh in Table 8.3 as kWh is often used as the standard unit for quoting energy prices. Energy use per hour is found by multiplying energy to produce a kg by production rates.

**Running cost** - The current average price of a kWh of energy is £14.73, this value is used to estimate the financial cost to run the generator courteously for an hour and a year. It is important to consider this because if a generator is in use for 10 or 20 years the running costs will be much larger than the initial set up cost. The running cost for the Yun + HCHX design are much higher partly due to the high production rate.

**Floor space** - Floor space is calculated by assuming each tank and each refrigeration loop takes up 0.5 $m^2$. For example, design 1 uses two refrigeration loops and one slurry storage tank and therefore takes up 1.5 $m^2$.

### 8.5.2 Summary

*Design 2* offers the best efficiency with the lowest energy used per kg of ice made. It also offers cheaper ice production and the lowest capital cost of all three designs. However, as mentioned previously the design could be prone to blocking, making it inappropriate to uses in areas such as medicine, where reliability is important. This design could be used to clean drink dispensing pipes in bars and restaurants where keeping cost low is key. Reliability is not as important because cleaning pipes can

easily be halted for a few hours if the generator needs to be defrosted.

*Design 1* costs more to make the same quantity of ice slurry but it is still lower than the Yun + HCHX design. The secondary refrigeration loop makes it easier to prevent blockages and improves reliability. Design 1 could, therefore, be used in medical application such as surgery, where ice slurry is being trialled to preserve organs. The small increase in capital and production costs are unlikely to be an issue as only small amounts of ice are used at any time. Good hygiene control is also preserved just like design 1.

The *Yun and HCHX Design* does not have the same level of hygiene control as the other two designs due to the cooled brine environment. Ideally, the generator should also be running continuously/regularly because if the large volume brine environment is left to heat up it will take lots of energy to cool it back down. This reason and the higher volume of ice production make it attractive to industries where continuous cooling is required such as cooling data centres or vertical farms. The only issue is the higher running costs, though these would be comparable to scraped surface generators as they use similar refrigeration temperatures, as mentioned previously.

## 8.6 Chapter Summary

- The HCHX pipe is shortened and brine is re-circulated through it for 6000 seconds. The control system used previously manages the flow rate to maximise ice production. PTFE and nylon pipes are both used.
- Ice fractions above 23% were produced, with a total of 1kg of ice produced with PTFE and nylon pipes. Slightly higher ice fractions up to 24.3% was generated with PTFE pipe.

- Proposed designs for a HCHX ice slurry generator were outlined. One using a secondary refrigerant and one without.
- A proposed design adapted from Yun (2017) was proposed. It was concluded that it is unlikely to offer significant improvements in efficiency for ice slurry production over scraped surface generators.
- The three final proposed designs were evaluated and compared. Design 1, using a coil directly in the evaporation section, was estimated to have the lowest capital and production costs.

# Chapter 9

# Conclusion

## 9.1 Recap of findings

There is a clear need for new, more efficient, ice slurry generation because ice slurries are utilised in a range of industries. Currently, scraped surface generators dominate the ice slurry generation market, despite low efficiencies caused by scraping work and a growing ice layer. In this thesis an alternative method was investigated, one first proposed in patents by Kauffeld et al. (1995) and Winston et al. (2011).

Initial experiments (Chapter 4) used nylon tubes cooled in a helical coiled heat exchanger arrangement. Brine pumped through the tubes was cooled until ice nucleated. Ice nucleation was assumed to occur on the walls of the pipe. Although this was not observed directly in the experiments, it was demonstrated by two key results. Firstly, outlet temperatures of 4 to 6°C below freezing were observed (leading to an increase in Gibbs function) at the time of nucleation, close to temperatures observed in previous experiments with heterogeneous nucleation. Secondly, in later chapters (Chapter 6) a correlation between nucleation and material properties was observed. It should be acknowledged that this could also because the fluid was nucleating on particulates in the tap water used. If ice growth within the tube and output from the tube are matched, then stable ice production can be achieved, however, this was found to occur only in a precise range of temperatures and flow rates. Increasing brine concentration increased the stable production region where ice was generated.

Ice production peaked with/using brine of 5wt% NaCl concentration, with lower ice production above and below this concentration.

Further work to try and increase ice production rate (Chapter 5) involved three different improvements. Firstly, the flow through a vertical coil was reversed to move from the bottom up to the top (rather than the original top moving down) within the submerged coil. Fluid in the original experiments (Chapter 4) experienced temperature profiles similar to those in a counter-current heat exchanger, while reversing the flow led to temperature profiles similar to those seen in a co-current heat exchanger. The results indicated that cooling in a counter-current heat exchange arrangement was more effective for high ice production. Secondly, experiments utilising a horizontal coiled pipe, partially submerged in refrigerating fluid, were conducted; no benefit to ice production was observed. Lastly, two control systems used temperature and pressure readings to control flow rate and thereby ice production. Ice fractions above 10% were successfully maintained. A proportional based control system proved to be the more effective of the two control systems tested.

Different material pipes (Chapter 6) were tested in HCHX to investigate if the ice production rate, the production region or refrigeration temperatures could be increased. PTFE pipes produced the highest production rates and ice fractions. Aluminium was the least effective material, the high thermal conductivity led to fast ice growth and no stable ice slurry production. Silicone rubber had the widest production region, though consistently low ice fractions. Further experiments to quantify and predict when ice nucleation would occur, were conducted. The nucleation temperature appeared to change with material and contact angle, as suggested by previous work. Other factors such as thermal conductivity and surface roughness also had an impact, making it difficult to prove the correlation conclusively.

Fluctuating the flow in a nylon pipe and external pressure on the outside of a flexible silicone rubber pipe were investigated (Chapter 7). Turning the internal fluid flow on and off slowed the average flow rate and increased the ice fraction produced. Unfortunately, a similar effect was achieved much more easily by lowering the flow rate in the pipe. The application of external pressures to silicone rubber pipes was successfully employed using a tube-in-tube heat exchanger design. The external pressure fluctuations led to slight improvements in ice production and increased the stable production region.

Improvements from previous experiments were combined in one ice slurry generator (Chapter 8). Improvements included PTFE pipe (Chapter 6), a flow rate control system (Chapter 5) and brine of 5wt.% NaCl (Chapter 4). The generator was run for 6000 seconds with fluid phase recirculated; calorimetry ice fractions above 23% were achieved. Designs utilising a primary and secondary refrigerating loop to cool the pipes were discussed. A design for interfacing a HCHX generator with the method proposed by Yun (2017) was outlined. It was suggested that using a plastic HCHX on its own for ice slurry generation could produce better efficiency than combining it with Yun's method.

## 9.2 Conclusion

This work successfully investigated ice generation using plastic heat exchangers. Ice slurry formed either on the internal wall of a HCHX, or on the particulates in the water, and was conveyed away by the flow of fluid due to low ice adhesion to the plastic walls. Most of the work conducted focused on trying to boost ice fraction. Maximum ice fraction produced was difficult to increase, though changing the ma-

terial and using a flow rate control system has shown some success. Maximum ice fraction appeared to be limited by the pump is maximum pumping pressure and the bath temperatures.

No work was conducted to show improved hygiene by using plastic HCHX rather than scraped surface generators. However, the benefit is clear from the design of the generator used; plastic helical coiled pipes used can be easily replaced at low cost for each operation or change in working fluid to avoid contamination. The pipes are used as they come off the shelf. Pipes contain no scraping parts or metal particulates (such as fluidised beds), making it easy to exchange pipes when needed.

This new design could have multiple uses in industries where small amounts of ice slurry are required. One example use is for cleaning pipes in the drink dispensing industry. Alcoholic drinks (with a freezing point below 0°C) could be made into ice slurry using a plastic HCHX generator. Each pipe could be cleaned with a small amount of slurry made from the dispensed drink. Different pipes could be used for each drinks/fluids to avoid cross-contamination, while keeping the rest of the generator the same. Another possible use is in medicine; small amounts of ice slurry are required for cooling organs or tissue during surgery to preserve cells. Between surgeries, the pipes could be replaced with newly cleaned or treated pipes to avoid infections. Only one cheap part needs replacing/cleaning to ensure the generator still works hygienically rather than several parts which would need cleaning or replacing with a scraped surface generator.

## 9.3 Further Work

A number of areas have been identified which could be investigated further to improve ice production.

### 9.3.1 Initiating Nucleation

It was noted initially in Chapter 4 that in many experiments brine was cooled by 5°C below $T_f$ without nucleation. Nucleation of ice could be initiated in these cases to expand the operation region. Only low $\phi_m$ ice fraction slurries would be produced, requiring lots more re-circulation to achieve high ice fraction. Initiating nucleation could help prevent early nucleation which led to lots of blockages in Chapter 7, and could enable operation at warmer temperatures. Previous authors have utilised ice crystals and ultrasound waves successfully to initiate nucleation of ice crystals which could be implemented with plastic HCHX.

### 9.3.2 Higher Pumping Pressure

In a many experiments, the limiting factor was the cut off pressure of the pump. Using a higher pressure pump, such as a gear pump, would increase the available force to push ice formed on the wall of the pipes. There would be an added financial cost, as gear pumps are often more expensive than peristaltic pumps of similar size. A gear pump would also make it difficult to maintain high levels of hygiene which can be achieved with a peristaltic pump. However, a pump with cut off pressures up to 10 bar (which is often used in the pharmaceutical industry) would greatly expand the operation region and the ice fraction produced. To achieve higher ice fractions lower $T_{Bath}$ values would probably be required.

### 9.3.3 Optimise Pipe Geometry

The current pipe geometry was chosen because it was easy to interface with other equipment used, but it is unlikely to be the optimum for ice production. Modelling the heat transfer from the pipe and the fluid as it cools would be useful. Pipe thickness, conductivity, thermal diffusivity, thermal capacity, length, fluid properties and flow rate could be varied in the model. Changing each parameter will change the region of refrigeration temperatures where ice production occurs. Modelling the flow would be tricky because two-phase flow behaviour is difficult to predict and there is often a natural variance in nucleation times/temperatures. Any model also would need to be verified with experimental results. Finding the optimum pipe geometry to maximise ice production, while maintaining a wide production region, would be useful.

### 9.3.4 Alternative Pipe Geometry

Currently, a coil has been used of 0.4m diameter, to induce secondary circulation and mixing within the pipe. Previous studies (Jamshidi et al. (2013)) have shown varying the pitch and coil diameter can increase or decrease heat transfer through the coil. Using this information, alternative coil designs could be tested to try and increase ice production.

### 9.3.5 Scaling Up Design

The current design would need to be scaled up to make a generator capable of 1ton/24 hours production. This could be done by multiplying the number of pipes or increasing the diameter of pipes. Increasing the pipe diameter is likely to lead to lower refrigeration temperatures required. It may also prevent blockages from occurring frequently or reduce ice production. These are all unknowns which need

investigating for this method to be shown to be a viable technique.

### 9.3.6 Further Work on Pipe Oscillations

As identified in chapter Chapter 7, further work utilising pulsing pressure or flow rate is needed. Large amplitude pulsations could be created using a piston close to the nucleation sites to dislodge ice formed on the pipe walls. When applying external pressure to a silicone rubber pipe, a smaller length of pipe being cooled and compressed might be more effective and easier to monitor.

### 9.3.7 Efficiency Comparison

A prototype of a plastic HCHX generator is needed with primary refrigerant in contact with the plastic coil. This prototype could then be compared to a similar capacity scraped generator. Measuring ice produced and power consumed would indicate the efficiency of each and allow for a better comparison and an accurate conclusion on generator efficiency to be made.

### 9.3.8 Different types of pipe

Alternative types of pipes could be used to maximise heat transfer and ice production while still reducing ice adhesion. Convoluted pipes which can flex, expand and contract could be used to increase and decrease surface area as required; thereby enabling changes in heat transferred without changing the bath temperature or flow rate. Another type of pipe could be a combination of metal with a plastic inner layer, or just a very thin plastic layer on its own. The aim would be to have a higher thermal conductivity while still having a plastic surface to reduce ice adhesion.

### 9.3.9 FPD and crystal size

The initial work in §4.4 only investigated crystal size in one ice slurry made from one FPD concentration. The size of the crystals produced using the HCHXs is likely to be dependent on the FPD concentration used. Crystal size will have an effect on the pressure loss from pumping the slurry and when the pipe blocks. Work to relate all these factors could prove very useful and be vital for improving the HCHX method.

It has been noted in this work that crystal size could impact pressure loss form pumping.

# Appendix A

# Nucleation

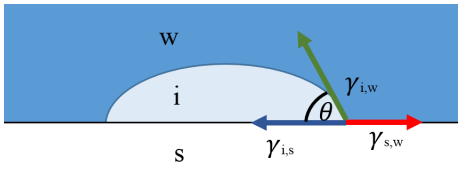


Figure A.1: *Figure of interfacial energies, $\gamma$, for an ice crystal embryo forming on a flat surface. $\theta$ is the wetting angle.*

Applying the same theory to heterogeneous nucleation of ice crystals on surfaces or particles within supercooled aqueous solutions a similar critical radius can be found. A curved shaped geometry is considered here because it offers the best volume to surface area ratio for a nucleus forming on a surface. The Gibbs free energy change ($\Delta G_{het}$) for nucleation on a surface or particle can be written as equation A.1, where V and A, represents volume and surface area, SL represents solid-liquid interface, SP represents solid-particle interface and PL, particle-liquid interface.

$$\Delta G_{het,r} = -V_s \Delta G_V + \gamma_{SL} A_{SL} + (\gamma_{SP} - \gamma_{PL}) A_{SP} \tag{A.1}$$

Equation A.2 is created by resolving $\gamma$, the interfacial energies between the different phases and a surface, displayed in Figure A.1.

$$\gamma_{SL} cos(\theta) = (\gamma_{SP} - \gamma_{PL}) \tag{A.2}$$

For a curved sphere like embryo on a flat surface (or pipe wall) the surface areas

and volumes can be calculated from the information in equation A.3.

$$A_{SL} = 2\pi r^2(1 - cos(\theta))$$

$$A_{SP} = \pi r^2 sin^2(\theta)$$

$$V_s = \frac{\pi r^3}{3}(2 + cos(\theta))(1 - cos(theta))^2 \tag{A.3}$$

When Equations A.1 and A.3 are combined the following derivation leads to a simplified equation for Gibbs free energy using the Gibbs free energy for homogeneous nucleation, $\Delta G_{hom}$.

$$\begin{aligned}\Delta G_{het,r} = &\left(-\frac{\pi r^3}{3}(2 + cos(\theta))(1 - cos(theta))^2\right) G_V + \\ &\gamma_{SL}(2\pi r^2(1 - cos(\theta))) + (\gamma_{SL} cos(\theta))(\pi r^2 sin^2(\theta))\end{aligned} \tag{A.4}$$

$$\begin{aligned}S(\theta) =& \frac{1}{4}(2 + cos(\theta))(1 - cos(\theta))^2) \\ \Delta G_{het,r} =& \left(-\frac{4\pi r^3}{3} S(\theta)\right) G_V + \\ &\gamma_{SL}(\pi r^2)(2(1 - cos(\theta)) + cos(\theta) sin^2(\theta)) \\ =& \left(-\frac{4\pi r^3}{3} S(\theta)\right) G_V + \\ &\gamma_{SL}(\pi r^2)(2 - 3cos(\theta) + cos^3(\theta)) \\ =& \left(-\frac{4\pi r^3}{3} S(\theta)\right) G_V + \\ &\gamma_{SL}(\pi r^2)(2 + cos(\theta))(1 - cos(\theta))^2) \\ =& \left(-\frac{4\pi r^3}{3}\right) S(\theta) G_V + \gamma_{SL}(4\pi r^2) S(\theta)\end{aligned} \tag{A.5}$$

This provides the final form of the equation displayed in the main text and below as Equation A.6.

$$\Delta G_{het,r} = \left( -\frac{4\pi r^3}{3} G_V + \gamma_{SL}(4\pi r^2) \right) S(\theta) \tag{A.6}$$

$$\Delta G_{het,r} = \Delta G_{hom,r} S(\theta)$$

# Appendix B

# Crystal Layer Growth

In previous chapters, it has been stated that ice nucleates on the wall (inner surface) of the pipes. This section explores further and tries to quantify this growth process. The diagram in Figure B.1 shows a 1-dimensional approximation of ice growth on the inner pipe wall.

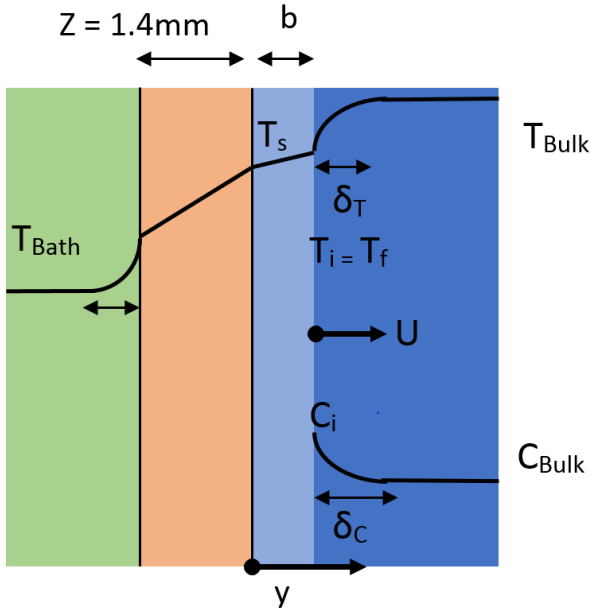


Figure B.1: A 1D diagram of heat conduction through a pipe wall to fluid forming ice. Layers from left to right: refrigeration fluid, pipe, ice layer and inner fluid.

The term $\bar{q}$ is the average heat flux through the pipe wall (units of W m$^{-2}$), calculated using the total heat to the fluid:

$$\bar{q''} = \frac{\dot{m}(\phi_m h_{s,f} + c_{p,brine}(T_{in} - T_f))}{\pi L D_i} \tag{B.1}$$

Values of $T_{in}$ (20°C), $T_{Bath}$ (-13°C), $T_f$ (-3.05°C), $\dot{m}$ (0.0069 kg s$^{-1}$) and $\phi_m$ (10%)

were taken from an experiment with nylon HCHX in §4.4. The value of $\bar{q''}$ (1517 W $m^{-2}$) was used to calculate an average surface temperature of the pipe, $T_s$, using Equation B.2 for heat conduction though the pipe. Heat transfer coefficients were not considered as this is only an approximation and the main source of thermal resistance is the pipe.

$$\bar{q''} = \frac{k_{Nylon}}{Z}(T_{Bath} - T_s) \tag{B.2}$$

The calculated surface temperature (-6.4°C ) was used to approximate the time taken to grow an ice crystal of size B on the pipe wall.

$$\rho_i h_{s,f} \frac{db}{dt} = \frac{k_i}{b}(T_s - T_f) \tag{B.3}$$

$$\int_B^0 b db = \frac{k_i}{\rho_i h_{s,f}}(T_s - T_f) \int_t^0 dt \tag{B.4}$$

$$t = \frac{B^2 \rho_i h_{s,f}}{2K_i(T_f - T_s)} \tag{B.5}$$

The size B is taken as the largest ice crystal observed from the crystal size measurements (200 $\nu m$), density and conductivity of ice were taken as 917 Kg $m^{-3}$ and 2.3 $Wm^{-1}K^{-1}$. This gave a time of 0.795 seconds, implying that ice crystals could be growing on the pipe wall for up to 0.795 seconds before being dislodged. Assuming the pipe surface temperature stayed the same with an increasing ice layer thickness, an estimate of time until the pipe blocked can be found. Using Equation B.5 and half the pipe diameter of 0.00335m as B gives a time of 223 Seconds, well within the length of one 1000 second experiment. However, in reality the growth rate would be lower because as ice forms NaCl is expelled and brine concentration increases at the freezing front. This slows ice layer growth by depressing the freezing point. Previous authors have shown that the growth rate is limited by the rate of

diffusion of the NaCl away from the freezing front and the size of the concentration boundary layer ($\delta_c$) (Smedsrud et al. (2003), Fujioka et al. (2013), Chellaiah and Viskanta (1987), and Wettlaufer et al. (1997)).

When ice production occurred in HCHX the fluid flow will helps to mix the fluid and remove the higher concentration brine layer.

# Appendix C

# CFD Simulation of Helical Coiled Pipe

## C.1 Introduction

Helical coiled heat exchangers (HCHX) aim to maximise the heat transfer surface area and minimise required space. As discussed in §2.3.8, fluid flow in a coil leads to an increase in pressure drop and heat transfer over horizontal pipes, with slurries and carrier fluid. Though, the benefits of heat transfer were deemed to outweigh the extra pressure loss.

In this section, an initial simulation was conducted. The aim was to investigate the flow speeds at different points within the coil. It is known that fluid speed will vary depending on the position in the coil. The fluid will also be cooled further when in the coil for longer. Therefore it is important to know where the fluid is moving slowest as this could be the point where nucleation occurs. The results of this simulation were utilised in §6.5. A simulation such as this could be used in the future to optimise the coil size and shape to maximise heat transfer and minimise space used. In this study, the size of the coil is limited by the bath size and shape which it has been designed to fit within.

## C.2 CFD Simulation

Previous CFD simulations have been published focused on HCHX modelling (Pawar and Sunnapwar (2014) and Jayakumar et al. (2010)). Heat transfer and *Nu*, have been found to be lowest on the inner curve of the coil, though flow velocity and temperature were also lower at this point (when cooling). None of this work matches the coil diameter ($D_{coil}$) of 0.4m and the inner diameter ($D_i$) of 0.0067m, therefore a basic CFD simulation was designed to find the flow profile in the pipe.

Figure C.1 shows pictures of the geometry and mesh created in Star CCM+. A longer base size in the axial direction would have greatly improved the speed of the computation and allowed a finer mesh in the radial direction. However, the software was unable to create these types of cells meaning 6.5 million cells were needed for 1 coil. Only one coil with no heat transfer was simulated to reduce the computational power. Simulation settings used are shown in Table **??**, including hydrodynamic entrance length ($\delta$), smallest residual and the number of iterations used. Properties of 5wt.% brine were used for the flowing fluid.

Table C.1: Table of settings used in the CFD simulation.

| | $D_i$ | **Length** | $\delta$ | **Base size** | **Max residual** | **Iteration** |
|---|---|---|---|---|---|---|
| **Value** | 6.7mm | 1.29m | 0.33m | 0.2mm | 1e-5 | 1000 |

The axial velocity magnitude across the pipe at different angles was plotted (Figure C.2). As expected, the fastest flow is on the outer side of the coil while the slowest is seen close to the wall and on the inner side. A more detailed representation of the flow across the pipe horizontal diameter, is shown in Figure C.3. Non-dimensionalised velocity profiles for the coil and a straight pipe are displayed. Peak velocity in a straight pipe is higher (2 times the average) and centred, while in a coil it is lower (1.4 times the average) and to the outer side. The shift in peak

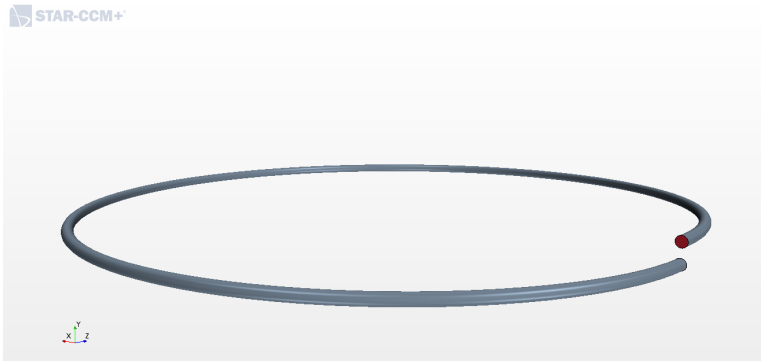

(a) Picture of geometry used

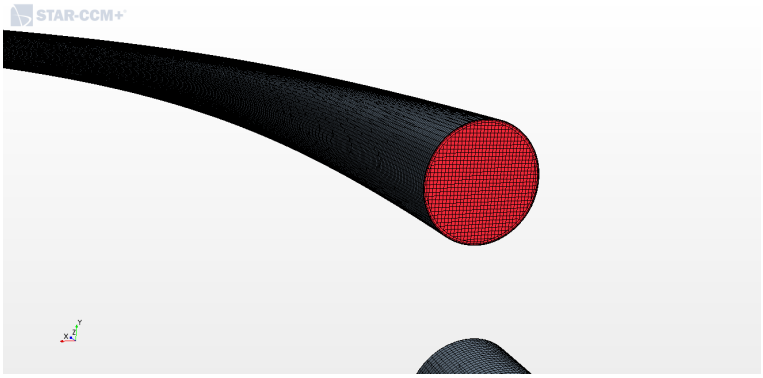

(b) Picture of final mesh used

Figure C.1: Pictures of the geometry, (a), and mesh used, (b), for a 1 coil simulation with 5 wt.% brine flow in a HCHX.

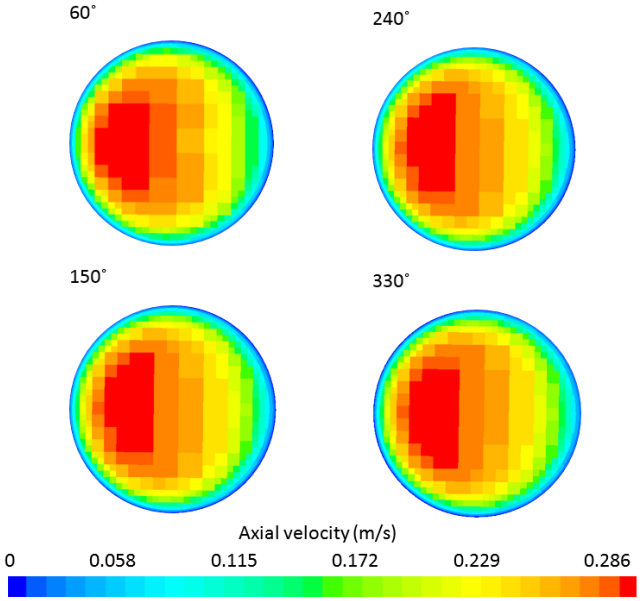


Figure C.2: Scalar velocity plots along coil, angles measured as rotation around the coil, inlet = 0°, outlet = 360°. The outer side of the coil is always left and inner right.

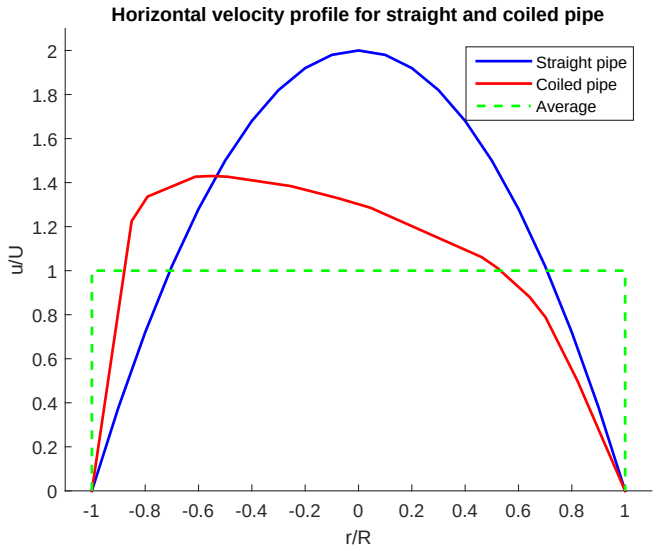


Figure C.3: Graph of normalised horizontal flow velocity profiles for straight pipe (analytical solution) and coiled pipe (found from the CFD simulation). Outer side: left. Inner side: right.

velocity is due to the centrifugal force of the fluid, which leads to the formation of secondary flows.

Flow is a coiled pipe is known to increases heat transfer through secondary circulation in the pipe. The coldest fluid in the pipe is found at the point where it is moving slowest, at the inside of the bend. This is the area were ice slurry is most likely to form in the tube. A CFD simulation was conducted to find the difference in velocity across the pipe. The maximum axial velocity was found to be only 1.4 times the average value for a coiled pipe and two times higher for a straight pipe. In a helical pipe, faster flow was found close to the outer wall compared to the centre in a straight pipe.

# Appendix D

# Pipe in Pipe Contact Area

Theory and equations presented here are taken from Brezeanu (2015) and applied to the tube-in-tube HX designed in Chapter 7. The inner pipe (pipe 1) is silicone rubber, with $E_1 = 5$ x$10^6$Pa and $\nu_1 = 0.48$, outer pipe (pipe 2) is PVC, with $E_2 = 15$ x$10^6$Pa and $\nu_2 = 0.38$. Length of both cylinders, L, is 15m.

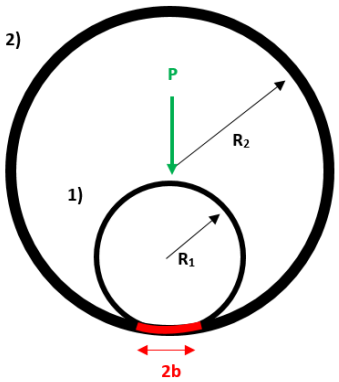


Figure D.1: Diagram of cylinder in cylinder geometry used for this contact area approximation.

Equation D.1 is used to calculate $b$, half the contact width. Results for different conditions during the experiment are shown in Table D.1.

$$b = 1.128\sqrt{\frac{P}{L}\frac{R_1 R_2}{R_2 - R_1}\left(\frac{1-\nu_1^2}{E_1} + \frac{1-\nu_2^2}{E_2}\right)} \tag{D.1}$$

Table D.1: Table of calculated values of pipe deformation under different pressures.

| **Condition** | **Pressure (Pa)** | **2b (mm)** | **Contact area ($m^2$)** |
|---|---|---|---|
| **Hydrostatic pressure** | 186 | 0.17 | 0.0026 |
| **Pumping fluid pressure** | 20000 | 1.8 | 0.027 |
| **Max oscillation pressure** | 500000 | 4.6 | 0.069 |

# Appendix E

# Cost estimates

This section details the process used to find a cost estimation for different ice slurry generator designs shown in Chapter 8. Parts used in the design have all been given a standard price, details on each component are given below. Final costs are shown in Table E.1.

- **Primary loop** - This is the primary refrigeration loop where the majority of the cooling comes from. It is also the highest cost and scales with cooling capacity as shown in Table E.1.
- **HCHX coil** - The coils used to cool brine and make a slurry. Nylon has been used for all estimations, though PTFE could also be used, though the cost would be slightly higher.
- **Controller (advanced and basic)** - For all generator designs a control system would be needed to regulate power, manage the refrigeration loop, and monitor temperatures and pressures. Some designs such as design 1 are simpler to implement and could use a less advanced (and cheaper) control system.
- **Pump** - Pumps are used to alter the flow rate through different sections of the generators. The Yun + HCHX design and design 1 both require two pumps as they have two loops of coolant being controlled while design 2 only requires one.
- **HCHX tank** - This is the tank where the HCHX is held and cooled, all

generators need one as they all use at least one HCHX.

- **Yun's tank** - This is the tank where the cooled brine environment is held for ice generation using Yun's method. Only the Yun + HCHX Design requires one of these.

- **Storage tank** - This is the tank where brine and ice slurry are stored after production, all generators require this.

- **Stirrer** - This is required to keep a homogeneous mixture of ice slurry and prevent the amalgamation of crystals in the slurry tank.

The cost of sensors, cabling, pipe and ducting has not been considered here because it is assumed the same for all designs other than the HCHX pipes. Assembly cost has also not been considered, these would scale with the number of parts and the complexity of the design.

Table E.1: Table of cost estimates calculated for different ice slurry generators using HCHX.

| | **Cost** | **Yun + HCHX Design** | **Design 1** | **Design 2** |
|---|---|---|---|---|
| **Primary loop (50kW)** | £7000 | 1 | 0 | 0 |
| **Primary loop (36kW)** | £5000 | 0 | 1 | 1 |
| **HCHX coil** | £5 | 2 | 1 | 1 |
| **Advanced controller** | £500 | 1 | 0 | 1 |
| **Basic Controller** | £300 | 0 | 1 | 0 |
| **Pump** | £300 | 3 | 2 | 1 |
| **HCHX tank** | £500 | 1 | 1 | 1 |
| **Yun's Tank** | £500 | 1 | 0 | 0 |
| **Storage tank** | £500 | 1 | 1 | 1 |
| **Stirrer** | £200 | 1 | 1 | 1 |
| Total | | £10110 | £7105 | £7005 |

# Bibliography


Archer, D.G. and R.W. Carter (2000). "Thermodynamic properties of the NaCl+ H2O system. 4. Heat capacities of H2O and NaCl (aq) in cold-stable and supercooled states". In: *The Journal of Physical Chemistry B* 104.35, pp. 8563–8584.

Ash, D. (2012). "Ice pigging in Narrow Bore Ducts". PhD thesis. University of Bristol, Queens School of Engineering.

Augustin, W., T. Fuchs, H. Foste, M. Scholer, J.P. Majschak, and S. Scholl (2010). "Pulsed flow for enhanced cleaning in food processing". In: *Food and Bioproducts Processing* 88.4, pp. 384–391.

Aviation Research, office of and Development (2006). "Investigations of Performance of Pneumatic Deicing Boots, Surface Ice Detectors, and Scaling of Intercycle Ice". In: *U.S. Department of Transportation*.

Ayel, V., O. Lottin, and H. Peerhossaini (2003). "Rheology, flow behaviour and heat transfer of ice slurries: a review of the state of the art". In: *International Journal of Refrigeration* 26.1, pp. 95–107.

Aziz, T., M. Waters, and R. Jagger (2003). "Surface modification of an experimental silicone rubber maxillofacial material to improve wettability". In: *Journal of dentistry* 31.3, pp. 213–216.

Barth, M. and M. Leprieur (2002). "Hydro-scraped ice slurry generator". In: *Proceedings of the 5th IIR Workshop on Ice Slurries, Stockholm*, pp. 175–178.

Bascom, W. D., R. L. Cottington, and C. R. Singleterry (1969). "Ice Adhesion to Hydrophilic and Hydrophobic Surfaces". In: *The Journal of Adhesion* 1.4, pp. 246–263.

Bedecarrats, J.P., T. David, and J. Castaing-Lasvignottes (2010). "Ice slurry production using supercooling phenomenon". In: *International Journal of Refrigeration* 33.1, pp. 196–204.

Bedecarrats, J.P., F. Strub, J.P. Dumas, and G. Roset (2000). "Supercooled ice slurry production, first results from a test plant". In: *Proc. 2nd IIR Workshop on Ice Slurries, Paris, France*, pp. 110–117.

Bedecarrats, J.P., F. Strub, C. Peuvrel, and J.P. Dumas (2003). "Heat transfer and pressure drop of ice slurries in a heat exchanger, ICR 0230". In: *Proceedings of the 21st IIR International Congress of Refrigeration, Washington*.

Bellas, I., I. Chaer, and S.A. Tassou (2002). "Heat transfer and pressure drop of ice slurries in plate heat exchangers". In: *Applied Thermal Engineering* 22.7, pp. 721–732.

Bellas, I. and S.A. Tassou (2005). "Present and future applications of ice slurries". In: *International Journal of Refrigeration* 28.1. Ice Slurries, pp. 115–121.

Bergman, T.L., A.S. Lavine, D.P. DeWitt, and F.P. Incropera (2011). "Fundamentals of heat and mass transfer". In:

Bharathidasan, T., S.V. Kumar, M.S. Bobji, R.P.S. Chakradhar, and B.J. Basu (2014). "Effect of wettability and surface roughness on ice-adhesion strength of hydrophilic, hydrophobic and superhydrophobic surfaces". In: *Applied Surface Science* 314, pp. 241–250.

Brezeanu, L.C. (2015). "Contact Stresses between Two Cylindrical Bodies: Cylinder and Cylindrical Cavity with Parallel Axes - Part I: Theory and FEA 3D Modeling". In: *Procedia Technology* 19. 8th International Conference Interdisciplinarity in Engineering, INTER-ENG 2014, 9-10 October 2014, Tirgu Mures, Romania, pp. 169–176.

Brout, R. (1963). "Theory of freezing". In: *Physica* 29.10, pp. 1041–1056. ISSN: 0031-8914.

Castaing-Lasvignottes, J., T. David, J.P. Bedecarrats, and F. Strub (2006). "Dynamic modelling and experimental study of an ice generator heat exchanger using supercooled water". In: *Energy Conversion and Management* 47.20, pp. 3644–3651.

Castelain, C., A. Mokrani, Y. Le Guer, and H. Peerhossaini (2001). "Experimental study of chaotic advection regime in a twisted duct flow". In: *European Journal of Fluid Mechanics* 20.2, pp. 205–232.

Chattopadhyay, H., F. Durst, and S. Ray (2006). "Analysis of heat transfer in simultaneously developing pulsating laminar flow in a pipe with constant wall temperature". In: *International Communications in Heat and Mass Transfer* 33.4, pp. 475–481.

Chellaiah, S. and R. Viskanta (1987). "Freezing of salt solutions on a vertical wall". In: *EXPERIMENTAL HEAT TRANSFER An International Journal* 1.3, pp. 181–195.

Chen, J.P., A. Hazra, and Z. Levin (2008). "Parameterizing ice nucleation rates using contact angle and activation energy derived from laboratory data". In: *Atmospheric Chemistry and Physics* 8.24, pp. 7431–7449.

Christensen, K.G. and M. Kauffeld (1997). "Heat transfer measurements with ice slurry, IIR". In: *IIF International Conference on Heat Transfer Issues on Natural Refrigerants*.

Clark, E., W. Colin, and D. Glew (1985). "Evaluation of the thermodynamic functions for aqueous sodium chloride from equilibrium and calorimetric measurements below 154 C." In: *Journal of Physical and Chemical Reference Data* 14.2, pp. 489–610.

Cocks, F.H. and W.E. Brower (1974). "Phase diagram relationships in cryobiology". In: *Cryobiology* 11.4, pp. 340–358.

Deans, T. (2006). "Determination of wall shear stree charateristics exhibited by high ice fraction pigging slurries". PhD thesis. University of Bristol, Queens School of Engineering.

Doron, P. and D. Barnea (1996). "Flow pattern maps for solid-liquid flow in pipes". In: *International Journal of Multiphase Flow* 22.2, pp. 273–283.

Dorsey, E. (1940). *Properties of ordinary water-substance*. Reinhold Publishing Corporation.; New York.

– (1948). "The Freezing of Supercooled Water". In: *Transactions of the American Philosophical Society* 38.3, pp. 247–328. ISSN: 00659746.

Dravid, A.N., K.A. Smith, E.W. Merrill, and P.L.T. Brian (1971). "Effect of secondary fluid motion on laminar flow heat transfer in helically coiled tubes". In: *AIChE Journal* 17.5, pp. 1114–1122.

Egolf, P.W. (2004). "Technical Note on Refrigerating technologies - Ice Slurry: a promising technology". In: *International Institute of Refigeration*.

Evans, T. S. (2007). "Technical Aspects of Pipeline Pigging with Flowing Ice Slurries". PhD thesis. University of Bristol, Queens School of Engineering.

Fikiin, K.A. and A.G. Fikiin (2000). "Individual quick freezing of foods by hydrofluidisation and pumpable ice slurries". In: *Science et technique du froid*, pp. 319–326.

Fillion, R.M., A. R. Riahi, and A. Edrisy (2017). "Design factors for reducing ice adhesion". In: *Journal of Adhesion Science and Technology* 31.21, pp. 2271–2284.

Fletcher, N.H. and J.B. Hasted (1971). "The Chemical Physics of Ice". In: *Physics Today* 24, p. 49.

Franks, F. (1982). *Water a Comprehensive Treatise: Volume 7: Water and Aqueous Solutions at Subzero Temperatures*. Plenum Publishing, New York.

Fujioka, R., L.P. Wang, G. Dodbiba, and T. Fujita (2013). "Application of progressive freeze-concentration for desalination". In: *Desalination* 319, pp. 33–37. ISSN: 0011-9164.

Gillham, C.R., P.J. Fryer, A.P.M. Hasting, and Wilson D.I. (2000). "Enhanced cleaning of whey protein soils using pulsed flows". In: *Journal of Food Engineering* 46.3, pp. 199–209.

Gilpin, R.R. (1977). "The effects of dendritic ice formation in water pipes". In: *International Journal of Heat and Mass Transfer* 20.6, pp. 693–699.

Gladis, S. (1997). "Ice slurry thermal energy storage for cheese process cooling". In: *ASHRAE Trans* 103, pp. 725–729.

Grandum, S., A. Yabe, M. Tanaka, F. Takemura, and K. Nakagomi (1997). "Characteristics of ice slurry containing antifreeze protein for ice storage applications". In: *Journal of Thermophysics and Heat Transfer* 11.3, pp. 461–466.

Hales, A. (2015). "Ice slurry diagnostics through electromagnetic wave attenuation and other techniques". PhD thesis. University of Bristol, Queens School of Engineering.

Hales, A., G. Quarini, G. Hilton, D. Ash, E. Lucas, D. McBryde, and X. Yun (2014). "Ice fraction measurement of ice slurries through electromagnetic attenuation". In: *International Journal of Refrigeration* 47, pp. 98–104.

Hansen, T.M., M. Kauffeld, K. Grosser, and R. Zimmermann (2000). "Viscosity of ice slurry". In: *Proceedings of the Second Workshop on Ice Slurries of the International Institute of Refrigeration, Paris, France*, pp. 38–45.

Hansen, T.M., M. Kauffeld, O. Sari, P.W. Egolf, and F. Pasche (2001). "Research, development and applications of ice slurry in Europe, from ancient Rome to modern technology". In: *Proceedings of the Fourth Workshop on Ice Slurries of the International Institute of Refrigeration, Osaka, Japan*. Vol. 12, p. 13.

Haruki, N. and A. Horibe (2013). "Flow and heat transfer characteristics of ice slurries in a helically-coiled pipe". In: *International Journal of Refrigeration* 36.4, pp. 1285–1293. ISSN: 0140-7007.

Hassan, M.F., H.P. Lee, and S.P. Lim (2010). "The variation of ice adhesion strength with substrate surface roughness". In: *Measurement Science and Technology* 21.7, p. 075701.

Hemida, H.N., M.N. Sabry, A. Abdel-Rahim, and H. Mansour (2002). "Theoretical analysis of heat transfer in laminar pulsating flow". In: *International Journal of Heat and Mass Transfer* 45.8, pp. 1767–1780.

Hong, Hiki, Jong Hyeon Peck, and Chaedong Kang (2004). "Ice adhesion of an aqueous solution including a surfactant with stirring on cooling wall: ethylene glycol a silane coupling agent aqueous solution". In: *International journal of refrigeration* 27.8, pp. 985–992.

Inaba, H. (2000). "New challenge in advanced thermal energy transportation using functionally thermal fluids". In: *International journal of thermal sciences* 39.9-11, pp. 991–1003.

Jain, A., A. Miglani, Y. Huang, J.A. Weibel, and S.V. Garimella (2019). "Ice formation modes during flow freezing in a small cylindrical channel". In: *International Journal of Heat and Mass Transfer* 128, pp. 836–848.

Jamshidi, N., M. Farhadi, D.D. Ganji, and K. Sedighi (2013). "Experimental analysis of heat transfer enhancement in shell and helical tube heat exchangers". In: *Applied Thermal Engineering* 51.1, pp. 644–652.

Jayakumar, J.S., S.M. Mahajani, J.C. Mandal, K.N. Iyer, and P.K. Vijayan (2010). "CFD analysis of single-phase flows inside helically coiled tubes". In: *Computers and chemical engineering* 34.4, pp. 430–446.

Jeffrey, D.J. and A. Acrivos (1976). "The rheological properties of suspensions of rigid particles". In: *AIChE Journal* 22.3, pp. 417–432.

Jellinek, H.H.G. (1959). "Adhesion properties of ice". In: *Journal of Colloid Science* 14.4-5, pp. 268–280.

Jensen, E.N., K.G. Christensen, T.M. Hassen, P. Schneider, and M. Kauffeld (2001). "Pressure drop and heat transfer with ice slurry". In: *Science et technique du froid*, pp. 572–580.

Kapembwa, M. and A.E. Rodriguez-Pascual M.and Lewis (2014). "Heat and Mass Transfer Effects on Ice Growth Mechanisms in Pure Water and Aqueous Solutions". In: *Crystal Growth and Design* 14.1, pp. 389–395.

Kauffeld, M., M. Kawaji, and P.W. Egolf (2005). *Handbook on ice slurries*. International Institute of Refrigeration.

Kauffeld, M., K. Rosenstedt, L. Moller, and F. Elefsen (1995). *Method and a refrigerating apparatus for making a slush ice*. US Patent.

Kauffeld, M., M.J. Wang, V. Goldstein, and K.E. Kasza (2010). "Ice slurry applications". In: *International Journal of Refrigeration* 33.8, pp. 1491–1505.

Knodel, B.D., D.M. France, U.S. Choi, and M.W. Wambsganss (2000). "Heat transfer and pressure drop in ice-water slurries". In: *Applied Thermal Engineering* 20.7, pp. 671–685.

Kong, W. and H. Liu (2015). "A theory on the icing evolution of supercooled water near solid substrate". In: *International Journal of Heat and Mass Transfer* 91, pp. 1217–1236. ISSN: 0017-9310.

– (2018). "Unified icing theory based on phase transition of supercooled water on a substrate". In: *International Journal of Heat and Mass Transfer* 123, pp. 896–910. ISSN: 0017-9310.

Koop, T., B. Luo, A. Tsias, and T. Peter (2000). "Water activity as the determinant for homogeneous ice nucleation in aqueous solutions". In: *Nature* 406.6796, p. 611.

Kozlovsky, P., U. Zaretsky, A.J. Jaffa, and D. Elad (2014). "General tube law for collapsible thin and thick-wall tubes". In: *Journal of Biomechanics* 47.10, pp. 2378–2384.

Kumano, H., T. Asaoka, A. Saito, and S. Okawa (2007). "Study on latent heat of fusion of ice in aqueous solutions". In: *International Journal of Refrigeration* 30.2, pp. 267–273.

Kumar, L. and S. Narayanan (2010). "Analysis of pulsatile flow and its role on particle removal from surfaces". In: *Chemical Engineering Science* 65.20, pp. 5582–5587.

Lakhdar, M.B., R. Cerecero, G. Alvarez, J. Guilpart, D. Flick, and A. Lallemand (2005). "Heat transfer with freezing in a scraped surface heat exchanger". In: *Applied Thermal Engineering* 25.1, pp. 45–60.

Landy, M. and A. Freiberger (1967). "Studies of ice adhesion: I. Adhesion of ice to plastics". In: *Journal of Colloid and Interface Science* 25.2, pp. 231–244.

Leiper, A. (2012). "Carnot cycle optimisation of ice slurry production through comminution of bulk ice". PhD thesis. University of Bristol, Queens School of Engineering.

Leiper, A.N., E.C. Hammond, D.G. Ash, D.J. McBryde, and G.L. Quarini (2013). "Energy conservation in ice slurry applications". In: *Applied Thermal Engineering* 51.1-2, pp. 1255–1262.

Leloux, M.S. (1999). "The Influence of Macromolecules on the Freezing of Water". In: *Journal of Macromolecular Science, Part C* 39.1, pp. 1–16.

Lindenmeyer, C. S. and B. Chalmers (1966). "Growth Rate of Ice Dendrites in Aqueous Solutions". In: *The Journal of Chemical Physics* 45.8, pp. 2807–2808.

Liu, X., Y. Li, K. Zhuang, R. Fu, S. Lin, and X. Li (2019). "Performance Study and Efficiency Improvement of Ice Slurry Production by Scraped-Surface Method". In: *Applied Sciences* 9.1, p. 74.

Liu, Y.H., E.Z. Zhang, J.M. Zhao, and P.L. Chen (1997). "Experiment study on friction loss characteristics of pipes with ice slurry". In: *Science et technique du froid*, pp. 490–494.

Maitra, T., M.K. Tiwari, C. Antonini, P. Schoch, S. Jung, P. Eberle, and D. Poulikakos (2014). "On the Nanoengineering of Superhydrophobic and Impalement Resistant Surface Textures below the Freezing Temperature". In: *Nano Letters* 14.1, pp. 172–182.

Majeed, M.H. (2014). "Static Contact Angle and Large Water Droplet Thickness Measurements with the Change of Water Temperature". In: *Nahrain University, College of Engineering Journal* 17.1, pp. 114–128.

Makkonen, L. (2012). "Ice adhesion theory, measurements and countermeasures". In: *Journal of Adhesion Science and Technology* 26.4-5, pp. 413–445.

Maxwell, J.C. (1873). *A treatise on electricity and magnetism, Clarendon Press.*

Meewisse, J.W. and C.A. Infante Ferreira (2000). "Ice slurry production with a fluidised bed heat exchanger". In: *Second IIR Workshop on Ice Slurries, Paris, IIF/IIR*, pp. 101–107.

Meewisse, J.W. and C.A. Infante Ferreira (2001). "Optimal properties of ice slurries in secondary cooling systems". In: *Science et technique du froid*, pp. 563–571.

– (2002). "Fluidized bed ice slurry generator: Operating range". In: *Fifth Workshop on Ice Slurries of the IIR*. Citeseer.

Mehta, B. and S. Khandekar (2015). "Local experimental heat transfer of single-phase pulsating laminar flow in a square mini-channel". In: *International Journal of Thermal Sciences* 91, pp. 157–166.

Melinder, A. (1997). *Thermophysical properties of liquid secondery refrigerents: Proprietes thermophysiques*. International Institute of Refrigeration.

Melinder, A. and E. Granryd (2005). "Using property values of aqueous solutions and ice to estimate ice concentrations and enthalpies of ice slurries". In: *International journal of refrigeration* 28.1, pp. 13–19.

Mito, D., Y. Mikami, M. Tanino, and Y. Kosawa (2002). "A New Ice-Slurry Generator Actively Thermal-Hydraulic Controlling Both Super-Cooling and Releasing of Water". In: *Proceedings of the 5th Workshop on Ice Slurries of the IIR*.

Mokrani, A., C. Castelain, and H. Peerhossaini (1998). "Mesure du chaos dans les systemes conservatifs en vue de l'etude des transferts dans les systemes ouverts". In: *Revue generale de thermique* 37.6, pp. 459–474.

Monteiro, A.C.S. and P.K. Bansal (2010). "Pressure drop characteristics and rheological modeling of ice slurry flow in pipes". In: *international journal of refrigeration* 33.8, pp. 1523–1532.

Mouneer, T.A., M.S. El-Morsi, M.A. Nosier, and N.A. Mahmoud (2010). "Heat transfer performance of a newly developed ice slurry generator: A comparative study". In: *Ain Shams Engineering Journal* 1.2, pp. 147–157.

Murase, H. and T. Fujibayashi (1997). "Characterization of molecular interfaces in hydrophobic systems". In: *Progress in organic coatings* 31.1, pp. 97–104.

Murase, H, K Nanishi, H Kogure, T. Fujibayashi, K. Tamura, and N. Haruta (1994). "Interactions between heterogeneous surfaces of polymers and water". In: *Journal of Applied Polymer Science* 54.13, pp. 2051–2062.

Naphon, P. and S. Wongwises (2006). "A review of flow and heat transfer characteristics in curved tubes". In: *Renewable and Sustainable Energy Reviews* 10.5, pp. 463–490.

Niezgoda-Zelasko, B. and J. Zelasko (2007). "Generalized non-Newtonian flow of ice-slurry". In: *Chemical Engineering and Processing: Process Intensification* 46.10, pp. 895–904.

Norgaard, E., T.A. Sorensen, T.M. Hansen, and M. Kauffeld (2005). "Performance of components of ice slurry systems: pumps, plate heat exchangers, and fittings". In: *International Journal of Refrigeration* 28.1, pp. 83–91.

Oro, E., A. De Gracia, A. Castell, M.M. Farid, and L.F. Cabeza (2012). "Review on phase change materials (PCMs) for cold thermal energy storage applications". In: *Applied Energy* 99, pp. 513–533.

Owens, D.K. and R.C. Wendt (1969a). "Estimation of the surface free energy of polymers". In: *Journal of Applied Polymer Science* 13.8, pp. 1741–1747.

– (1969b). "Estimation of the surface free energy of polymers". In: *Journal of applied polymer science* 13.8, pp. 1741–1747.

Pawar, S.S. and V.K. Sunnapwar (2014). "Experimental and CFD investigation of convective heat transfer in helically coiled tube heat exchanger". In: *Chemical Engineering Research and Design* 92.11, pp. 2294–2312.

Petrenko, V.F. and R.W. Whitworth (2002). *Physics of Ice*. Published to Oxford Scholarship.

Pineiro, C., J. Barros-Velazquez, and S.P. Aubourg (2004). "Effects of newer slurry ice systems on the quality of aquatic food products: a comparative review versus flake-ice chilling methods". In: *Trends in Food Science and Technology* 15.12, pp. 575–582.

Pronk, P., T.M. Hansen, C.A. Infante Ferreira, and G.J. Witkamp (2005). "Time-dependent behavior of different ice slurries during storage". In: *International Journal of Refrigeration* 28.1, pp. 27–36.

Pronk, P., J.W. Meewisse, and C.A. Infante Ferreira (2001). "Heat transfer model for a fluidised bed ice slurry generator". In: *4th Workshop on Ice Slurries, Osaka, Japan, IIR*. Citeseer.

Pruppacher, H.R. (1967). "Some relations between the structure of the ice-solution interface and the free growth rate of ice crystals in supercooled aqueous solutions". In: *Journal of Colloid and Interface Science* 25.2, pp. 285–294.

Quarini, J. (2002). "Ice-pigging to reduce and remove fouling and to achieve clean-in-place". In: *Applied Thermal Engineering* 22.7, pp. 747–753.

Quist, A.S. and W.L. Marshall (1968). "Electrical conductances of aqueous sodium chloride solutions from 0 to 800 degree and at pressures to 4000 bars". In: *The Journal of Physical Chemistry* 72.2, pp. 684–703.

Raraty, L. and D. Tabor (1958). "The adhesion and strength properties of ice". In: *Proceedings of the Royal Society of London. Series A. Mathematical and Physical Sciences* 245.1241, pp. 184–201.

Rogers, G. and Yon R. Mayhew (1980). *Engineering Thermodynamics Work and Heat Transfer*. Longman Group Limited.

Ryzhkin, I.A. and V.F. Petrenko (1997). "Physical mechanisms responsible for ice adhesion". In: *The Journal of Physical Chemistry B* 101.32, pp. 6267–6270.

Saeki, H. et al. (2011). "Mechanical Properties Between Ice and Various Materials Used in Hydraulic Structures: The Jin S. Chung Award Lecture, 2010". In: *International Journal of Offshore and Polar Engineering* 21.02.

Saito, A., S. Okawa, and S. Koganezawa (1991). "Fundamental research on supercooling phenomenon on heat transfer surface". In: *Proceedings of the 1991 ASME JSME thermal engineering joint conference*.

Schmelzer, J.W.P. and O. Hellmuth (2013). *Nucleation Theory and Applications*. Joint Institute for Nuclear Research. URL: `http://theor.jinr.ru/meetings/2013/nta/NTA2013.pdf`.

Shapiro, A.H. (1977). "Steady flow in collapsible tubes". In: *Journal of Biomechanical Engineering* 99.3, pp. 126–147.

Shire, G.S.F. (2006). "The behaviour of ice pigging slurries". PhD thesis. University of Bristol, Queens School of Engineering.

Shire, G.S.F., G.L. Quarini, and T.S. Evans (2009). "Pressure drop of flowing ice slurries in industrial heat exchangers". In: *Applied Thermal Engineering* 29.8-9, pp. 1500–1506.

Smedsrud, L.H., T.M. Saloranta, P.M. Haugan, and T. Kangas (2003). "Sea ice formation on a very cold surface". In: *Geophysical research letters* 30.6.

Snoek, C., S. Joanis, and R. Gupta (1995). "Pressure drop characteristics of ice-water flows". In: *Two Phases Flow Model Exp*, pp. 655–63.

Stamatiou, E., J.W. Meewisse, and M. Kawaji (2005). "Ice slurry generation involving moving parts". In: *International Journal of Refrigeration* 28.1, pp. 60–72.

Tanino, M. (2000). "Development of active control method for supercooling releasing of water". In: *Proceedings of the 2nd Workshop on Ice Slurries of the IIR*. Vol. 127.

Teraoka, Y., A. Saito, and S. Okawa (2002). "Ice crystal growth in supercooled solution". In: *International Journal of Refrigeration* 25.2, pp. 218–225.

Thomason, S.B. (1987). "Experimental evaluation of parameters affecting turbulent flow freeze blockage of a tube". In: *International journal of heat and mass transfer* 30.10, pp. 2201–2205.

Van der Gun, M.A., J.W. Meewisse, and C.A. Infante Ferreira (2001). "Ice Production in a Fluidized Bed Crystalliser". In: *4th Workshop on Ice Slurries of the IIR, Osaka, Japan*, pp. 12–13.

Vargas, J.V. and A. Bejan (1995). "Fundamentals of ice making by convection cooling followed by contact melting". In: *International Journal of Heat and Mass Transfer* 38, pp. 2833–2841.

Vuarnoz, D., J. Sletta, O. Sari, and P.W. Egolf (2015). "Direct Injection Ice Slurry Generator". In: *Sixth Gustav Lorentzen Conference of the International Institute of Refrigeration on Natural Working Fluids*. Glasgow, Scotland.

Wang, H., H. Feng R.and Duan, and A. Chen (2016). "Investigation into the ice generator with double supercooled heat exchangers". In: *Applied Thermal Engineering* 98, pp. 380–386. ISSN: 1359-4311.

Wang, H., G. He, and R. Feng (2014). "An effective method for preventing ice-blockage in dynamic generation system with supercooling water". In: *International Journal of Refrigeration* 46, pp. 114–122.

Wang, J.M. and N. Kusumoto (2001). "Ice slurry based thermal storage in multi-functional buildings". In: *Heat and Mass Transfer* 37.6, pp. 597–604.

Weidemann, C., S. Vogt, and H. Nirschl (2014). "Cleaning of filter media by pulsed flow - Establishment of dimensionless operation numbers describing the cleaning result". In: *Journal of Food Engineering* 132, pp. 29–38.

Wettlaufer, J.S., M. G. Worster, and H.E. Huppert (1997). "Natural convection during solidification of an alloy from above with application to the evolution of sea ice". In: *Journal of Fluid Mechanics* 344, pp. 291–316. ISSN: 1469-7645.

Wijeysundera, N.E., M.N.A. Hawlader, C.W.B. Andy, and M.H. Hossain (2004). "Ice-slurry production using direct contact heat transfer". In: *International Journal of Refrigeration* 27.5, pp. 511–519.

Wilson, P.W. and A.D.J. Haymet (2009). "Effect of solutes on the heterogeneous nucleation temperature of supercooled water: an experimental determination". In: *Physical chemistry chemical physics* 11.15, pp. 2679–2682.

Winston, S., G. Hansson, A. Geernaert, G. Ewer, and M. Myszko (2011). *Slush Machine*. International Patent.

Work, A. and Y. Lian (2018). "A critical review of the measurement of ice adhesion to solid substrates". In: *Progress in Aerospace Sciences* 98, pp. 1–26.

Yamada, S., M. Shirakashi, M. Hattori, and A. Saito (2004). "Flow Patterns of Ice/Water Slurry in Horizontal Pipes". In: *Transactions of ASME* 126, pp. 436–441.

Yang, X. and S. Liu (2015). "Experimental Study on Ice Slurry Refrigeration System with Pre-Cooling Heat Exchanger". In: *Engineering* 7.05, p. 230.

Yun, X. (2017). "The formation of ice by coupled heat and mass transfer within subcooled aqueous media". PhD thesis. University of Bristol, Queens School of Engineering.

Yun, X., S. Brooks, Y. Cheng, A. Hales, E. Lucas, D. McBryde, and G. Quarini (2016). "Ice formation in the subcooled brine environment". In: *International Journal of Heat and Mass Transfer* 95, pp. 198–205.

Zeng, Q., K. Li, and T. Fen-Chong (2015). "Heterogeneous nucleation of ice from supercooled NaCl solution confined in porous cement paste". In: *Journal of Crystal Growth* 409, pp. 1–9.

Zhang, X., T. Inada, A. Yabe, S. Lu, and Y. Kozawa (2001). "Active control of phase change from supercooled water to ice by ultrasonic vibration 2. Generation of ice slurries and effect of bubble nuclei". In: *International Journal of Heat and Mass Transfer* 44.23, pp. 4533–4539.

Zhang, X., X.H. Li, and M. Chen (2016). "Role of the electric double layer in the ice nucleation of water droplets under an electric field". In: *Atmospheric Research* 178-179, pp. 150–154.

Zhang, X., L.M. Qiu, P. Zhang, L. Liu, and Z.H. Gan (2008). "Performance improvement of vertical ice slurry generator by using bubbling device". In: *Energy Conversion and Management* 49.1, pp. 83–88.

Zobrist, B., C. Marcolli, T. Peter, and Thomas Koop (2008). "Heterogeneous ice nucleation in aqueous solutions: the role of water activity". In: *The Journal of Physical Chemistry A* 112.17, pp. 3965–3975.

Zou, M., S. Beckford, R. Wei, C. Ellis, G. Hatton, and M.A. Miller (2011). "Effects of surface roughness and energy on ice adhesion strength". In: *Applied Surface Science* 257.8, pp. 3786–3792.